

Tectonostratigraphy of the Shyok Suture Zone in Ladakh, NW India.

by
Craig R. Martin

Submitted to the Department of Earth, Atmospheric and Planetary Science
in partial fulfillment of the requirements for the degree of

Doctor of Philosophy in Geology

at the

MASSACHUSETTS INSTITUTE OF TECHNOLOGY

June 2023

© Craig R. Martin 2023.

The author hereby grants to MIT a nonexclusive, worldwide, irrevocable, royalty-free license to exercise any and all rights under copyright, including to reproduce, preserve, distribute and publicly display copies of the thesis, or release the thesis under an open-access license.

Author.....
Department of Earth, Atmospheric, and Planetary Sciences

Certified by
Prof. Oliver E. Jagoutz
Full Professor
Thesis Supervisor

Accepted by
Prof. Rob van der Hilst
Chair, Department of Earth, Atmospheric and Planetary Sciences

Tectonostratigraphy of the Shyok Suture Zone in Ladakh, NW India

by
Craig R Martin

Submitted to the Department of Earth, Atmospheric and planetary sciences in June, 2023

in Partial Fulfillment of the Requirements for the Degree of

Doctor of Philosophy in Geology.

Abstract

This thesis explores the timing and nature of the tectonic collision between India, Eurasia, and an intra-oceanic arc in the western Himalaya. Chapter One presents the results of a geological mapping campaign in the Shyok-Nubra confluence region of Ladakh, in northwest India. It provides lithological descriptions of the major geological units in the Shyok suture zone, and also compiles tectonostratigraphic correlations with exposures in northern Pakistan to develop a tectonic reconstruction of the southern Eurasian margin in Jurassic-Paleocene time. Chapter Two presents U-Pb zircon dates that constrain the age of the significant tectonic boundaries between the Eurasian margin and the Kohistan-Ladakh arc. Chapter Three presents paleomagnetic results that constrain the latitude of the Kohistan-Ladakh arc in the Paleocene. Chapter Four presents paleomagnetic results that constrain the latitude of the Eurasian margin in the Late Cretaceous and discusses the paleogeography of the India-Eurasia collision. This thesis constrains the age of the Shyok suture zone using multiple lines of evidence and shows that the Shyok suture zone records final closure of the ocean between India and Eurasia in the Eocene.

Thesis Supervisor: Dr. Oliver E. Jagoutz

Title: Full Professor in Earth, Atmospheric, and Planetary Sciences Massachusetts Institute of Technology

Acknowledgments

I would like to express my deepest gratitude to all those who have contributed to the completion of this doctoral thesis. It would not exist without the support, guidance, and encouragement I have received along the way from my mentors, colleagues, friends, and family.

First and foremost, I am grateful to my advisor, Prof. Oliver Jagoutz, for his guidance, expertise, and mentorship throughout my time at MIT. Oli has always pushed me to think critically, develop testable and quantifiable hypotheses, and forged in me a determination to explore both the depth and breadth of my research interests. He has also encouraged me to be undaunted by diverse data types and methods, helping me become a more intellectually nimble geoscientist. I also want to thank Oli for his camaraderie and exuberance on the adventures and misadventures that the fieldwork for this thesis research has involved. It has been a privilege to work with and learn from you. I look forward to our future collaborations and adventures.

I want to thank the other members of my thesis committee for their support and mentorship. In particular, I would like to thank Prof. Ben Weiss for warmly welcoming me into the paleomagnetism fold and lending me his immense expertise during my thesis work in his lab. Ben's curiosity is boundless and infectious, and it has been an honor to be involved in the varied and exciting research his group engages in. I also want to thank Ben for the extra effort he makes to kindle a supportive and welcoming environment in his lab group. I'd like to thank Prof. Leigh Royden, for her ability to translate seemingly intractable tectonic problems into solvable mathematics equations, and Prof. Pete DeCelles of the University of Arizona, for his thoughtful and comprehensive reviews of my manuscripts. I'd also like to thank Prof. Rick Binzel for advising my second general project during my first two years at MIT and for continuing to guide me with wisdom and kindness ever since. Rick opened my eyes to strange and wonderful worlds at the edge of the solar system, and has been an inspirational teacher and mentor to me.

I would like to express my gratitude to the funding organizations that have supported this research, the National Science Foundation (NSF), Geological Society of America (GSA), and MIT International Student Travel Initiative (MISTI India).

I also want to thank those who have made the fieldwork for this thesis work possible. I am immensely grateful to Prof. Rajeew Upadhyay for sharing his knowledge and experience during our collaborations in Ladakh. This thesis would not have been possible without his assistance in the field, not to mention his uncanny ability to talk his way out of trouble. In addition, I thank C.P. Dorjay and the wonderful owners of Sia La Guesthouse in Leh for their logistical assistance. I want to thank the undergraduate and graduate student colleagues from MIT and Kumaun University who have joined me in Ladakh and helped me conduct the fieldwork for this thesis, including Santosh Joshi, Abhay-Jeet Joshi, Diwakar Bawari, Jigyasha Bisht, Jade Fischer, Megan Guenther, Zoe Levitt, Kate Przydzial, and Lucy Sandoe. Their good humor and steely determination ensured that the fieldwork was both productive and fun. I also want to thank Tsewang Dorjay and his family at Silok guesthouse in Khardung for graciously welcoming us and our copious sample collection into their home. For the same, I am also grateful to the owners of Nerpa guesthouse in Charasa and the people of Udmaru for offering shelter to a troupe of dusty geoscientists and lending us their donkeys. I would also like to thank the many drivers who have

ensured our safe passage on treacherous mountain roads, particularly Javid, for his enthusiasm and commitment to getting his ever-suffering car as close to the outcrops as possible.

This thesis would have been impossible without the assistance, mentorship, and collegiality in the lab from Claire Nichols, Athena Eyester, Jay Shah, and Eduardo Lima in the paleomagnetism lab, Jahan Ramezani in MIT's geochronology labs, Neel Chatterjee in the MIT Microprobe facility, and Daniel Sheehan at the MIT GIS Libraries. It also could never have happened without the help of the EAPS administrative staff, including Kayla Bauer, Roberta Allard, Brenda Carbone, and Mira Parsons, who have all gone to great lengths to help me, including managing customs clearance for large shipments of rocks from India, expensing the scrawled scraps of receipts that make it back from the field, and being eternally generous with their time. I would also like to thank the EAPS HQ staff, especially Megan Jordan and Brandon Milardo, who somehow kept me on track through many missed registration days due to my fieldwork.

My heartfelt thanks go out to all my fellow researchers and friends who have made my years in Boston fun and memorable. I want to thank my officemates and lab mates Josh Murray, Zach Molitor, Billy Shinevar, Ben Klein, Emilie Bowman, Herve Razeau, Tushar Mittal, Ze Liu, Liang Guo, and Hongze Bo, for their camaraderie and fortitude. I am also grateful to the many others who have enriched this experience, including Ekaterina Bolotskaya, Daniel Ortega-Arroyo, Fiona Clerc, Cailey Condit, Eli Mansbach, Caue Borlina, Clara Maurel, John Biersteker, Foteini Vervelidou, Susanna Hoyos, Patrick Beaudry, Max Collinet, Stephanie Brown, Marjorie Cantine, Adam Holt, Lizz Ultee, Kasturi Shah, Zara Essack, Jonathan Lin, Ellen Lalk, Joanna Millstein, and Li and Wynn Murphy, with special thanks to those of you who were unflinching in your commitment to the most important hour of the week. To my undergraduate professors, classmates, and friends from the University of St. Andrews, thank you for helping spark my passion for science, for providing good craic, and for continually standing by my side, however far away, for many years now. Also, the journalism crew: Anoushka Dalmia, Devyani Chhetri, Mita Kataria, Sammie Purcell, Kath Swindells, Robbie Vadala; and the TDI crew, including Emily Dhondt, Ian Beatty, Emer Martin, Lucas Spiro; and the many others who have been there with me along the way.

Finally, I want to thank my wonderful partner, Caitlin, my family back home in the UK, and Caitlin's family in the US. Their unwavering support, love, and encouragement have been my driving force, and I am truly grateful for them.

Table of Contents

1	Tectonostratigraphy and Age of the Shyok Suture Zone in Ladakh, NW India	15
1.1	Abstract	15
1.2	Introduction	16
1.3	Geological Background	19
1.4	Methods	25
	1.4.1 Geological Mapping	25
1.5	Results	26
	1.5.1 Lithological Descriptions	26
	<i>1.5.1.1 Shyok Suture Zone</i>	26
	<i>1.5.1.2 Ladakh Arc</i>	32
	<i>1.5.1.3 Karakoram Terrane</i>	35
	1.5.2 Structure	37
	<i>1.5.2.1 Faults</i>	37
	<i>1.5.2.2 Folding</i>	44
1.6	Discussion	46
	1.6.1 The Eurasian Forearc	46
	1.6.2 Post-Collision Sedimentation and Magmatism	51
	1.6.3 Structural Development of the Suture Zone	52
1.7	Conclusion	58
1.8	Figures and Captions	59
	References	79
2	Geochronology and Geochemistry	80
2.1	Abstract	80
2.2	Introduction	81
2.3	Methods	83
	2.3.1 Geochronology	83
	2.3.2 Geochemistry	84

2.4	Results	85
2.4.1	U-Pb Zircon Geochronology	85
	2.4.1.1 Detrital Zircon Geochronology	85
	2.4.1.2 Igneous Zircon Geochronology	88
2.4.2	Geochemistry	90
2.5	Discussion	93
2.5.1	Detrital Zircon Evidence	93
2.5.2	Structural Evidence	95
2.5.3	Magmatic Evidence	97
2.6	Conclusion	98
2.7	Figures and Captions	99
	References	113

3	Paleocene latitude of the Kohistan-Ladakh arc indicates multi-stage India-Eurasia collision	116
3.1	Abstract	117
3.2	Significance Statement	118
3.3	Introduction	119
3.4	Geology of the Khardung Volcanics	121
3.5	Rock Magnetism	123
3.6	Thermal Demagnetization	124
3.7	Paleomagnetism of the Khardung Volcanics	128
3.8	Discussion	131
3.9	Materials and Methods	135
	3.9.1 U-Pb Zircon Geochronology	135
	3.9.2 Paleomagnetism	137
3.10	Acknowledgments	139
3.11	Figures and Captions	140
	References	157

4	Paleomagnetic constraints on the age of the Shyok Suture Zone	162
4.1	Abstract	162
4.2	Plain Language Summary	163
4.3	Introduction	164
4.4	Geological Background	169
4.5	Materials and Methods	172
	4.5.1 Geochronology	172
	4.5.2 Paleomagnetism	173
4.6	Results	175
	4.6.1 U-Pb Geochronology	175
	4.6.2 Rock Magnetism	177
	4.6.3 Paleomagnetism	178
4.7	Discussion	185
	4.7.1 Age of the Shyok Suture Zone	185
	4.7.2 Paleomagnetic Reconstruction of the Neotethys	188
	4.7.2.1 <i>Paleomagnetic constraints on Eurasia</i>	189
	4.7.2.2 <i>Paleomagnetic Constraints on India</i>	190
	4.7.2.3 <i>Paleomagnetic Constraints on the KLA</i>	192
	4.7.2.4 <i>Synthesis</i>	193
4.8	Conclusion	194
4.9	Acknowledgments	195
4.10	Figures and Captions	196
	References	215
A	Ammonia-water Freezing in Pluto’s Subsurface Ocean as a Mechanism for Recent Cryovolcanism	224
A.1	Abstract	224
A.2	Introduction	226
A.3	Geology of Wright Mons, Hyecho Palus, and Cthulhu Regio	228

A.4	Modelling Freezing and Overpressure	230
A.5	The Effects of Ammonia	235
A.6	Results	237
A.7	Conclusion	239
A.8	Acknowledgments	241
A.9	Figures and Captions	242
	References	249
B	Geological Map of the Shyok Suture Zone	252

List of Figures

1-1	Regional tectonic map of the India-Eurasia collision.	59
1-2	Overview geological map of the Shyok suture zone.	60
1-3	Schematic tectonostratigraphic columns.	61
1-4	Detailed geological map of the Shyok suture zone.	62
1-5	Stratigraphy of the Hundri Formation.	63
1-6	Stratigraphy of the Saltoro Formation.	64
1-7	Panorama sketch and outcrop images of Udmaru normal faults.	65
1-8	Outcrop images of the Khalsar fault.	66
1-9	Stereographic projections of structural data stereonet.	67
1-10	Cross-sections A-A', B-B', C-C', and D-D'.	68
1-11	Images of upper Udmaru valley Murgi and Ensa Thrusts.	69
1-12	Schematic reconstruction of Cretaceous Shyok suture zone.	70
2-1	Map of U-Pb geochronology results.	99
2-2	U-Pb zircon analyses from the Hundri Formation.	100
2-3	U-Pb zircon analyses from the Saltoro Formation.	101
2-4	U-Pb zircon analyses from the Murgi conglomerate.	102
2-5	U-Pb zircon analyses from the Karakoram fault zone.	102
2-6	U-Pb zircon analyses from the Shyok volcanics	103
2-7	U-Pb zircon analyses from the Turtuk amphibolite.	103
2-8	U-Pb zircon analyses from the Khardung volcanics.	104
2-9	U-Pb zircon analyses from the Nubra-Siachen granites.	104
2-10	U-Pb zircon analyses from the Tirit-Hundar suite.	105
2-11	U-Pb zircon analyses from the Ladakh batholith.	105
2-12	U-Pb zircon analyses from the Chalunka and Hundar leucogranites.	106
2-13	U-Pb zircon analyses from the Shukur dikes.	106
2-14	Major element oxide discrimination diagrams.	107
2-15	Major element oxides versus silica.	108
2-16	Whole rock trace element spider diagrams.	109
2-17	Regional comparison of Shyok suture DZ spectra.	110
2-18	Age range of major geologic formations in the Shyok suture zone.	111
2-19	Age constraints of major fault zones in the Shyok suture zone.	112

3-1	Overview of India-Eurasia collision models.	140
3-2	Geological map of Khardung volcanics paleomagnetism section.	142
3-3	Field images of Khardung volcanics sampling site.	143
3-4	RL Microscopy and SEM images of Khardung volcanics.	144
3-5	Hysteresis curves for Khardung volcanics samples.	145
3-6	Day plot of Khardung volcanics samples.	146
3-7	Zijderfeld diagrams for Khardung volcanics thermal demagnetization.	147
3-8	Equal area projection of Khardung volcanics LCT magnetic components.	148
3-9	Equal area projections of Khardung conglomerate tests.	149
3-10	Khardung volcanics reversal test results.	150
3-11	Stratigraphy and magnetic reversals of the Khardung volcanics.	151
3-12	Quantile-Quantile analyses of Khardung volcanics VGPs.	152
3-13	Khardung volcanics VGPs compared to Eurasia and India APWP.	153
3-14	U-Pb Concordia diagrams of Khardung volcanics U-Pb zircon data.	154
3-15	Paleomagnetic mean directions for the Khardung volcanics.	155
3-16	Paleolatitude of the Kohistan-Ladakh arc.	156
4-1	Geologic maps and cross-section.	196
4-2	Field images of the Saltoro Formation.	198
4-3	U-Pb isotopic data of Saltoro Formation samples.	199
4-4	Detrital zircon spectra of Saltoro Formation samples.	200
4-5	Stratigraphy and geomagnetic reversal record of Saltoro Formation.	201
4-6	Hysteresis curves for Saltoro sediment and volcanic samples	202
4-7	Day plot of Saltoro formation hysteresis parameters.	203
4-8	Zijderfeld diagrams of Saltoro Formation thermal demagnetization.	204
4-9	Equal area projection of Saltoro Formation LCT site-mean directions.	205
4-10	Stereographic projections showing paleomagnetic results.	206
4-11	Reversal test for Saltoro formation site mean VGPs.	208
4-12	Results of E/I method unflattening of sedimentary samples.	209
4-13	Quantile-quantile plots of VGP longitudes and latitudes.	210
4-14	Paleolatitude of the Saltoro Formation.	211
4-15	Common mean test of Saltoro formation and Khardung volcanics.	212
4-16	Paleogeographic Reconstructions of the Neotethys Ocean.	213
4-17	Optical micrographs of Saltoro formation samples.	214
A-1	Topography map of Wright Mons.	242

A-2	Geological map of Wright Mons.	244
A-3	Schematic diagram of thick spherical elastic crust model.	245
A-4	Ammonia-water mixture phase diagram.	246
A-5	Evolution during freezing of two ammonia-water mixtures.	247
A-6	Modelled excess pressures generated during freezing of a subsurface ocean.	248

Chapter One

Tectonostratigraphy of the Shyok Suture Zone in Ladakh, NW India

1.1 Abstract

The events leading up to the India-Eurasia collision are preserved along the major suture zones that transect the Himalayan belt. The well-constrained 55 – 50 Ma age of the Indus suture zone (ISZ) has been widely used to infer the age of final continental collision between India and Eurasia. Yet, this interpretation assumes that all other major suture zones north of the Indus suture zone are older, which may not be the case throughout the Himalayan orogenic system. The age and kinematic development of the Shyok suture zone (SSZ) separating the Kohistan-Ladakh arc from the Karakoram terrane in NW India and Pakistan, to the north of the Indus suture zone, is poorly constrained. Available estimates for KLA-Eurasia collision span ages that are both younger and older than the Indus suture zone, leaving open the possibility that the Shyok suture zone, not the Indus, records final continental collision in the western Himalaya. This chapter presents the results of detailed geological mapping and structural analyses from the Shyok suture zone in Ladakh, NW India. It describes in detail the major geological units exposed in the suture zone and provides new constraints on the kinematics of the structures, constraining the kinematic development of the suture zone.

1.2 Introduction

The India-Eurasia collision has classically been understood to be a single-stage continent-continent collision in the Paleocene between India and Eurasia (Gansser, 1964; Hu et al., 2016; Yin and Harrison, 2000). However, others have proposed that it may have been a multi-stage process beginning with the accretion of an oceanic arc onto India in the Paleocene and continuing with the subduction of an additional oceanic plate or a major back-arc basin between India and Eurasia until the final continent-continent collision in the Eocene (Aitchison et al., 2007; Aitchison et al., 2000; Jagoutz et al., 2015; Kapp and DeCelles, 2019; Khan et al., 1997; Westerweel et al., 2019). The fundamental difference between the alternative collision scenarios is the timeframe over which intra-oceanic subduction operated outboard of Eurasia in the Neotethys Ocean. In single-stage collision models, after ~90 Ma, the pre-collisional Eurasian margin resembled a Cordilleran or Andean-style accretionary orogen with Neotethyan ocean crust subducting along a single subduction zone at the southern edge of the Eurasian continent (Yin and Harrison, 2000). In contrast, the multi-stage collision models envision a more complex Japan-Mariana-style southern margin of Eurasia in which intra-oceanic subduction operated significantly outboard from Eurasia until the Paleocene onset of collision. Resolving these alternative tectonic models has significant implications for understanding the Cretaceous-Oligocene plate motion of India (Jagoutz et al., 2015), the relative importance of slab-pull and plume-ridge-push forces in convergent tectonic systems (Cande and Stegman, 2011; Copley et al., 2010; Pusok and Stegman, 2020), and the relationships between chemical weathering of obducted ophiolites and climate (Jagoutz et al., 2016; Macdonald et al., 2019).

A fragmentary record of the tectonic events leading up to the India-Eurasia collision is preserved along the major Himalayan suture zones (see Figure 1-1). In particular, the very well-

constrained 50 – 54 Ma age of the Indus suture zone in northwest India and northern Pakistan has been widely inferred to constrain the timing of India-Eurasia continental collision (Garzanti et al., 1987; Najman et al., 2017). Indian continental lithosphere was metamorphosed to ultra-high-pressure conditions associated with subduction at 50 Ma, and Cretaceous volcanic arc detritus began to arrive in northern Indian margin sediments at 54 Ma around the same time that Indian margin sediments underwent a transition from marine to terrestrial facies (Garzanti et al., 1987; Kaneko et al., 2003; Najman et al., 2017). Elsewhere in the Himalayas, there is also significant evidence for a Paleocene onset of collision on the northern edge of India. Detrital zircons in Indian passive margin turbidites in Central Tibet record the first arc-like input at around 59 – 61 Ma (DeCelles et al., 2014; Hu et al., 2015; Wu et al., 2014), and the obduction of ophiolites onto India began at 65 – 60 Ma, at the start of the Paleocene (Beck et al., 1996; Catlos et al., 2019; Ding et al., 2005; Gnos et al., 1997).

The Indus suture zone separates India from the Kohistan-Ladakh arc (KLA), a huge remnant of an obducted oceanic island arc (Tahirkheli, 1979). In Pakistan, the Kohistan-Ladakh batholith intruded oceanic lithosphere, and no continental basement has been identified, suggesting that the KLA either initiated near the equator above an intra-oceanic subduction system (Bouilhol et al., 2013; Jagoutz et al., 2011; Jagoutz et al., 2015; Khan et al., 1997), or in the Eurasian forearc ophiolite separated from Eurasia by a back-arc basin (Bignold and Treloar, 2003; Coward et al., 1986; Khan et al., 1997; Rolland et al., 2000). The size and longevity of the basin that closed between the KLA and Eurasia are highly uncertain, with some envisaging a 1000 – 2000 km long oceanic plate (Jagoutz et al., 2015; Khan et al., 1997; Martin et al., 2020), and others a minor < 300 km wide back-arc basin (Coward et al., 1987; Petterson and Windley, 1985; Pudsey et al., 1985; Rolland et al., 2000; Treloar et al., 1989). Equally uncertain is the age of collision between

the KLA and Eurasia, with estimates ranging from 90 – 100 Ma (Borneman et al., 2015; Gaetani et al., 1990; Gaetani et al., 1993; Petterson and Windley, 1985) to as young as 40 Ma (Bouilhol et al., 2013; Brookfield and Reynolds, 1981; Martin et al., 2020).

Given that estimates of the collision age of the Shyok suture zone span times before and after the closure of the Indus suture zone, the possibility remains open that the Shyok suture zone, not the Indus suture zone, records the final closure of the Neotethys Ocean in the western Himalaya. In order to resolve this question and distinguish between the different models for the Eurasian margin prior to the India-Eurasia collision, it is necessary to determine the age of the Shyok suture zone and the nature of the basin that closed along it. In this study, we present a tectonostratigraphic framework of the Shyok suture zone based on detailed geologic mapping of a ~100 km along strike exposure of the structure in Ladakh, NW India. We synthesize the major lithologies exposed in the suture zone, as well as the significant structures and tectonic boundaries, and provide new age constraints obtained using U-Pb zircon geochronology.

1.3 Geological Background

The Himalaya-Karakoram-Tibet orogen is built from the deformed and thickened Indian lithosphere, remnants of intra-oceanic island arcs and ophiolites, and Gondwana-derived terranes that accreted onto Eurasia between the Triassic and Early Cretaceous (Allegre et al., 1984; Gansser, 1964; Kapp and DeCelles, 2019). In Tibet, the Eurasian accretionary orogen comprised the Gondwana-derived Lhasa and Qiangtang terranes, the Hoh-Xil/Songpan-Ganzi and Kunlun terranes of the pre-Triassic Eurasian margin (see Figure 1-1) (Kapp and DeCelles, 2019). These terranes are separated by the Kunlun, Jinsha, and Bangong suture zones (Kapp and DeCelles, 2019), and the Lhasa terrane is separated from northern Indian passive margin strata (Tethyan Himalaya) by the Yarlung-Tsangpo suture zone (Allegre et al., 1984; Burg et al., 1987). The Yarlung-Tsangpo suture zone is marked by Neotethyan ophiolites (Girardeau et al., 1985; Qian et al., 2020), arc remnants (Aitchison et al., 2000), and Cretaceous-Eocene Xigaze forearc basin strata (Ding et al., 2005; Einsele et al., 1994). It is overprinted by the south-dipping Great counter thrust system (Burg et al., 1987; Yin et al., 1999).

The Himalaya-Karakoram-Tibet orogenic belt is bisected by the right-lateral Karakoram fault, complicating the terrane correlation between Tibet and Central Asia (Robinson, 2015; Schwab et al., 2004). West of the Karakoram fault, the Eurasian accretionary orogen comprises the Gondwana-derived South Pamir and Karakoram terranes separated by the Tirich-Mir boundary zone, and the Eurasian Karakul–Mazar accretionary belt (which includes the Central and Northern Pamir terranes), separated from the Gondwanan terranes by the Rushan-Pshart suture (see Figure 1-1; Robinson, 2015; Schwab et al., 2004; Zanchi et al., 2000). As described above, in NW India and northern Pakistan, the Karakoram terrane is separated from the Indian passive-margin sedimentary rocks of the Himalaya by the Kohistan-Ladakh arc (KLA), a remnant of an intra-

oceanic island arc (see Figure 1-1; Tahirkheli, 1979). The KLA is separated from Indian passive margin sedimentary rocks and lower crustal eclogites by the Indus suture zone (ISZ) and from the Karakoram terrane by the Shyok suture zone (SSZ) (see Figure 1-1; Bard, 1980; Tahirkheli, 1979).

From west to east, the Shyok suture zone has been studied in Pakistan between Drosh and Hunza (Heuberger, 2004; Heuberger et al., 2007; Petterson and Windley, 1991; Petterson and Windley, 1985; Pudsey et al., 1985; Pudsey, 1986), around the Nanga Parbat syntaxis and in Baltistan between Gilgit and Skardu (Le Fort and Pecher, 2002; Robertson and Collins, 2002; Rolfo et al., 1997; Rolland et al., 2000; Rolland et al., 2002), and in the Shyok-Nubda area of Ladakh (see Figure 1-2 and Figure 1-3) (Rai, 1982; Rolland et al., 2000; Rolland et al., 2002; Srimal, 1986; Upadhyay et al., 1999). It is exposed at increasing metamorphic grade with proximity to the Nanga Parbat syntaxis, a half-window structure in which Indian continental crust is exhumed, bisecting the Kohistan and Ladakh arc segments (Pudsey et al., 1985; Tahirkheli, 1979). At its easternmost terminus, the Shyok suture zone merges into the Karakoram fault (Srimal, 1986) and, at its westernmost terminus into the Chaman fault (Treloar and Izatt, 1993).

In the Drosh area, the Shyok suture zone is overprinted by left-lateral strike-slip deformation. It is made up of tectonic slices comprising basaltic and andesitic volcanics, Cretaceous (107 – 111 Ma) gabbros and diorites, limestones, marbles, turbidites and clastic sedimentary facies, and serpentinites (Heuberger, 2004; Pudsey et al., 1985). The southern boundary of the suture at Drosh is a near-vertical thrust that separates the suture zone from 50 Ma KLA meta-gabbros and meta-diorites (Heuberger, 2004). The northern boundary of the suture zone is a complex anastomosing strike-slip fault zone containing bodies of serpentinite, marbles, and volcanics. North of this fault zone, the Karakoram terrane comprises Jurassic marbles, slates and quartzites, and 100 – 110 Ma plutonic rocks (Desio, 1977; Heuberger, 2004; Pudsey et al., 1985).

The strike-slip fault zone overprinting the suture zone can be traced northeast to the Yasin valley, where it becomes a north-dipping thrust zone with a less dominant left-lateral strike-slip overprint than Drosch (Pudsey et al., 1985). This thrust has since been referred to as the Main Karakoram thrust (MKT) in the Hunza area farther east (Rex et al., 1988). The thrust zone contains red sandstones, conglomerates interbedded with pyroclastic flows, and complex thrust sheets of calc-schists, serpentinites, epidotized volcanic rocks, sandstones, and marbles (Pudsey et al., 1985). South of the MKT in the Yasin valley is a folded but structurally coherent sequence of marine sedimentary rocks, including limestones, calcareous siltstones, and shales, that rest unconformably on top of a thick sequence of volcanics (Pudsey, 1986). The volcanic rocks are part of the Chalt volcanic group which crops out extensively across northern Pakistan and comprises basalts and basaltic andesites primarily, with some boninites near the base, and also tuffs, dacites, and rhyolites towards the top of the sequence (Pettersson and Treloar, 2004). The sedimentary rocks are known as the Yasin Group and consist of calcareous sandstones, shale, turbidites, and limestones that, close to the base of the stratigraphy, contain rudists of Aptian/Albian age (120 – 100 Ma) (Pudsey, 1986). The Chalt Volcanics and overlying Yasin Group are intruded by diorite and granite bodies that have been dated to between 68 Ma and 50 Ma using K-Ar dating of biotite and Rb-Sr dating techniques (Debon et al., 1987; Pudsey, 1986; Treloar et al., 1989). Pudsey et al. (1985) tentatively related the Chalt Volcanics and overlying Yasin Group sedimentary sequence to the Kohistan side of a back-arc basin on the Eurasian margin based on their position south of the MKT mélangé zones and the unconformity between the Yasin Group and Chalt Volcanics.

In the Hunza valley, the major components of the suture are similar to the Yasin area exposures, if somewhat more deformed and metamorphosed (Coward et al., 1986). South of Chalt village, the Chalt Volcanics are again overlain by Yasin Group limestones, calcareous sandstones,

chlorite-bearing slates, and phyllite, which are folded into tight north-vergent folds (Coward et al., 1986; Petterson and Treloar, 2004). The Chalt-Yasin sequence in the Hunza valley is bounded to the north by an intensely deformed thrust mélangé zone associated with the MKT (Coward et al., 1986; Rex et al., 1988). North of this structure are gneisses and other metamorphic and intrusive facies associated with the exposed Karakoram metamorphic complex (Coward et al., 1986; Desio, 1974). To the south, the Chalt Volcanics are intruded by the Matum Das tonalite (Coward et al., 1986; Petterson and Windley, 1985), which has been dated to 154.08 ± 0.85 Ma using CA-ID-TIMS U-Pb zircon geochronology (Jagoutz et al., 2019). The presence of intrusions into the Chalt volcanic group has led to the interpretation that the volcanics represent extrusive elements of the Kohistan arc (Coward et al., 1986; Jagoutz et al., 2019; Petterson et al., 1993; Petterson and Treloar, 2004; Petterson and Windley, 1985; Pudsey, 1986).

Le-Fort and Pecher (2002) mapped the Shyok suture zone on both sides of the Nanga Parbat syntaxis. In their map, the Chalt volcanic group and Matum Das plutons are separated from Kohistan arc diorites by a complicated deformed zone comprising multiple lithologies, including metasediment, amphibolite, and ultramafics that they called the Sinakkar Formation and Dobani ultramafics (Le Fort and Pecher, 2002). East of the Nanga Parbat syntaxis, there is a similar tectonic structure containing more ultramafic lenses (Dasu ultramafics) that marks the southern boundary of the Shyok suture zone (Rolfo et al., 1997). This structure separates amphibolite and banded amphibolite orthogneiss (Askor Amphibolite) to the south from an intensely folded belt of mafic metavolcanics (Turmik greenstone group), rudist bearing marbles (Pakora Limestone), psammites, and conglomerates (Desio, 1974; Le Fort et al., 1995; Le Fort and Pecher, 2002; Rolfo et al., 1997). The Turmik greenstones and Pakora Formation are intruded by a major undated dioritic-tonalitic plutonic complex in the Shigar valley (Le Fort et al., 1995). The suture zone is

overthrust by metamorphic rocks of the Karakoram terrane along a mylonitized thrust zone containing ultramafic lenses and reworked suture zone lithologies that extend eastwards to the Pakistan-India border areas (Le Fort et al., 1995; Robertson and Collins, 2002; Rolfo et al., 1997; Rolland et al., 2000).

At Khalpu, the easternmost accessible part of the Shyok suture zone in Pakistan, Jurassic metavolcanic rocks are separated from the Ladakh batholith by a shear zone that crosscuts dikes in the Ladakh batholith that were dated with Ar-Ar techniques to 40 – 44 Ma (Brookfield and Reynolds, 1990; Reynolds et al., 1983). The greenstone is separated from paragneiss and granite of the Karakoram terrane by a *mélange* zone containing serpentinite, chert, slate, and phyllite (Brookfield and Reynolds, 1990).

In Ladakh, NW India, the Shyok suture zone is exposed between the India-Pakistan border and its intersection with the right-lateral Karakoram fault at the confluence of the Shyok and Nubra Rivers. Pioneering early work in this area revealed that the suture zone is marked by pyroxenite, serpentinite, basalt, and marine sedimentary rocks that are thrust-bound against the Ladakh batholith and related felsic Khardung Volcanics by the Khalsar thrust in the south, and overthrust by the Karakoram batholith along the Main Karakoram thrust in the north (see Figure 1-3) (Rai, 1982; Sharma and Gupta, 1978; Srimal, 1986; Srimal et al., 1987; Thakur, 1981). These studies revealed that the Shyok suture zone comprises a folded sequence of pyroxenite, basalt, and basaltic andesite (the Shyok Volcanics and Bogdang ophiolite) which are unconformably overlain by Cretaceous rudist-bearing limestone and a sequence of marine clastic sedimentary strata (Hundri Formation) (Rai, 1982; Srimal, 1986; Upadhyay, 2014; Upadhyay et al., 1999). The Shyok Volcanics and Hundri Formations are intruded by a suite of plutons of various compositions (Borneman et al., 2015; Kumar et al., 2017; Rai, 1982; Upadhyay, 2003). A fault separates the

Shyok-Hundri sequence from red siliciclastic shale, mudstone, and conglomerate interbedded with intermediate volcanic horizons called the Saltoro Formation (Rai, 1982; Srimal, 1986; Upadhyay et al., 1999). A complex zone of sheared serpentinite, basalt, phyllite, slate, and marble is thrust over the Saltoro Formation, marking the boundary between the suture zone and the Karakoram terrane (Rai, 1982; Rolland et al., 2000; Srimal, 1986; Thakur, 1990).

1.4 Methods

1.4.1 Geological Mapping

In this study, we present a new detailed 1:200,000 scale geological map of the Shyok suture zone in the confluence area of the Shyok and Nubra Rivers in Ladakh, NW India (see Figure 1-4 and Appendix B for a high-resolution to-scale version). In this area, the Shyok suture zone is exposed over a 100 km along strike between the Karakoram fault and the Line of Actual Control (LAC), the de-facto border between Pakistan and India. Our mapping work, conducted during multiple field seasons since 2008, builds upon pioneering geological mapping efforts in this area by Rai (1982), Thakur and Misra (1984), Srimal (1986), and Upadhyay (1999), adopting much of the same formation names and terminology. Samples, observations, and structural data were collected along roadside outcrops and during donkey/porter-assisted expeditions to areas inaccessible by road. Due to the significant relief of the terrain and the military sensitivity of the region, some inaccessible areas were mapped by tracing contacts visible in Landsat and GoogleEarth® imagery from locations of ground truth.

1.5 Results

1.5.1 Lithological Descriptions

In the following section, we describe the major lithologies and structures of the Shyok suture zone in Ladakh, based on our geologic mapping work. We also introduce the age constraints for each formation that were published prior to this study.

1.5.1.1 Shyok Suture Zone

Changmar Complex: The Changmar Complex is a suite of pyroxenites, gabbros, and tonalites that intrude and underlie the lowermost exposures of the Shyok Volcanics (Saktura et al., 2021b; Srimal, 1986). The Changmar Complex is dismembered and heavily sheared by the Bogdang shear zone that separates it from granodiorites, gabbros, and amphibolite gneisses to the west. The Changmar Complex includes pyroxenite, serpentinite, and chlorite schist that occur as huge boudins between anastomosing shear planes in the Bogdang shear zone. The sheared ultramafic boudins are crosscut by 3 – 8 cm wide veins of calcite and graphite. The Changmar Complex also includes gabbro with pyroxene cumulate textures that intrude into fine-grained pillow basalt with intervening chert (Saktura et al., 2021b). Saktura et al. (2021b) obtained a SHRIMP U-Pb zircon age of 159.4 ± 0.9 Ma from the Changmar gabbro and 151.9 ± 1.5 Ma from a tonalite crosscutting the gabbro in a fallen block near Changmar.

Shyok Volcanics: The Shyok Volcanics are a thick succession of epidotized basalt that are situated throughout the Shyok valley from Changmar to Tirit and are particularly well exposed between Skuru and Waris Bridge, around Diskit and on the road between Waris Bridge and Udmaru (Rai, 1982; Srimal, 1986; Thakur, 1981). The Shyok Volcanics are mostly fine-grained

and massive, but are sometimes porphyritic, containing 3 – 5 mm plagioclase laths. The lowermost part of the volcanic stratigraphy comprises spectacular pillow basalts in which pillows are surrounded by chert and exhibit dark chilled margins and cores with zeolite and calcite-filled vesicles (Saktura et al., 2021b). Pillow basalts are present throughout the Shyok Volcanics at all structural levels, but become less common towards the top of the volcanic pile, where the flows are more massive and tend towards basaltic andesite compositions. The mafic and ultramafic pillow basalts near the base of the stratigraphy transition upward to more evolved compositions up section within the Shyok Volcanics (Saktura et al., 2021b). The base of the Shyok Volcanics is intruded by the Late Jurassic Changmar Complex gabbros (Saktura et al., 2021b) and the top is unconformably overlain by the Cretaceous Hundri Formation (Rai, 1982; Upadhyay, 2014). We group the Changmar pillow basalts with the overlying Shyok Volcanics due to the absence of structural or compositional discontinuity between them.

Hundri Formation: The Hundri Formation is a succession of marine sedimentary rocks that rest unconformably on top of the Shyok Volcanics (Rai, 1982; Srimal, 1986; Upadhyay, 2014). They are best exposed on the north side of the Shyok River around the village of Hundri and in the valley above Shukur Monastery (Upadhyay, 2014). The Hundri stratigraphy is complex and comprises a wide variety of sedimentary facies, including limestone, wackestone, bioclastic packstone, calcareous sandstone, quartz arenite, shale, and chert (Upadhyay, 2014). The stratigraphy is primarily composed of shallow marine calcareous facies that grade upward into sandstone and shale. There is also deep marine shale, chert, and turbidites, which are more dominant towards the south. Due to complex F₁ deformation and unmapped offsets within the

stratigraphy, the complete stratigraphy is not known. A schematic representation of the Hundri Formation stratigraphy is shown in Figure 1-5.

The lower part of the Hundri Formation comprises massive limestone horizons interbedded with wackestone and shale that transition upward to become interbedded with calcareous sandstone and bioclastic packstone (Upadhyay, 2014). These shallow-marine sedimentary rocks contain abundant Aptian-Albian age fauna, including rudists, crinoids, coral, bryozoa, gastropods, and foraminifera, which provided the only constraint on the depositional age prior to this study (Upadhyay, 2014; Upadhyay et al., 1999). The Hundri Formation is variously metamorphosed throughout the suture zone, from nearly unmetamorphosed around Hundri village to chlorite and muscovite schist around Diskit and Murgi villages.

Saltoro Formation: The Saltoro Formation (sometimes called Saltoro Molasse) is in faulted contact with the Hundri Formation and Shyok Volcanics, and its upper contact is truncated by the Murgi thrust (Rai, 1982; Srimal, 1986; Upadhyay et al., 1999). It is best exposed on the west side of the Nubra valley around the village of Charasa (see Figure 1-6), where it was described in detail by Upadhyay et al. (1999) and is also described in detail in Chapter 3. We also observed the Saltoro Formation in the upper Udmaru valley.

The Saltoro Formation is distinct from the Hundri Formation in that it comprises primarily siliciclastic deposits, including pebble and cobble conglomerate, planar cross-bedded sandstone, siltstone, and mudstone, and does not contain limestone or deep marine shale. The Saltoro Formation stratigraphy is interspersed with andesitic volcanic flows. The lowest levels of the Saltoro Formation are not visible in the type-section at Charasa, but are present in the Udmaru valley, where a lower stratigraphic section is exposed below a major angular unconformity

(Borneman et al., 2015). This lower stratigraphy comprises a >1500 m thick succession of heavily altered andesitic volcanic flows, andesite auto-breccia, and monolithic andesite conglomerate. The monolithic conglomerate transitions upward into poorly sorted, graded and cross-bedded pebble-conglomerates containing sub-rounded clasts of dominantly andesite volcanic lithologies along with some rare limestone and chert clasts. The volcanics and the overlying conglomerates are crosscut by numerous syn-sedimentary normal faults that terminate up section in the conglomerate pile (see Figure 1-7).

The lower Saltoro Formation stratigraphy is overlain by an angular unconformity that was originally interpreted by Borneman et al. (2015) as the contact between the Saltoro Formation and the Shyok Volcanics. The Shyok Volcanics and the Saltoro Formation are separated by a major fault lower in the Udmaru valley (see Figure 1-7). The angular unconformity is overlain by a sequence of conglomerates that blanket pre-existing paleotopography (Borneman et al., (2015)'s buttress unconformity). The conglomerates contain well-rounded, cobble-size clasts of a more varied range of lithologies than the conglomerates below the unconformity. The clasts include sandstones and pebble-conglomerate derived from the underlying stratigraphy, as well as andesite, limestone, chert, and some rare granite and basaltic clasts. Up section, more conglomerate horizons are interbedded with coarse sandstone and are overlain by a distinctive 40 – 60 m thick plagioclase-pyroxene bearing porphyritic andesite that serves as a useful marker horizon because it is also exposed in the Saltoro Formation stratigraphy at Charasa. The porphyritic andesite flow in Udmaru is overlain by more conglomerates, sandstones, and siltstones. The top of the Saltoro Formation stratigraphy in the Udmaru valley is truncated by the Murgi thrust.

The Saltoro Formation stratigraphy at Charasa contains significantly lower energy facies than in Udmaru, and there is a thicker sedimentary pile beneath the porphyritic andesite marker

horizon than in Udmaru (see Chapter 3). The lowermost strata consist of fine-grained sandstones interbedded with poorly sorted conglomerate containing various clasts, including extrusive volcanic lithologies, granite, sandstone, shale, limestone, and chert. The stratigraphy then progresses into very fine sandstone with planar crossbedding and siltstone and mudstone horizons (see Chapter 3). The porphyritic andesite flow is exposed at a stratigraphic level of 1510 m at Charasa Monastery and is overlain by sandstones, mudstones, and siltstones. The uppermost section of the Saltoro stratigraphy is dominated by high-Mg calc-alkaline volcanic flows consisting of andesitic and trachyandesitic compositions with plagioclase phenocrysts and/or vesicles (see Chapter 3). Close to their base, the volcanic flows are periodically interbedded with coarse black lithic sandstones with ripples and crossbedding that indicate the paleohorizontal, but towards the top of the section, the sedimentary horizons become scarce (see Chapter 3). The top of the Saltoro Formation is truncated by the Murgi thrust (Rai, 1982; Srimal, 1986). The Saltoro Formation stratigraphy is dated to between 92.9 ± 2.2 Ma and 74.6 ± 0.7 Ma using U-Pb zircon geochronology (Borneman et al., 2015; Chapter 3). The 74.6 ± 0.7 Ma age is derived from the base of the Saltoro Formation volcanic pile, which continues uninterrupted for 3600 m.

Shukur Dikes: The Shyok Volcanics, Hundri Formation, and the lower Saltoro Formation are crosscut by 1 – 5 m wide dikes that range in composition from andesite and trachyandesite to dacite and rhyolite. These dikes are spectacularly exposed, crosscutting the Shyok Volcanics, the cliffs beneath Shukur Monastery, and the Shyok-Hundri unconformity in the upper Shukur valley. They also crosscut the Saltoro Formation (Borneman et al., 2015). Two of the dikes were dated by Borneman et al. (2015) to 85.2 ± 3.8 Ma and 86.0 ± 0.7 Ma using LA-ICPMS U-Pb zircon geochronology.

Tirit-Hundar Plutonic Suite: The Shyok Volcanics and Hundri Formation are intruded by a varied suite of intrusive bodies, including gabbros, diorites, and granites (Rai, 1982; Srimal, 1986; Thakur, 1981). This group comprises the Tirit and Hundar granitoids (Kumar et al., 2017; Rao and Rai, 2009; Srimal, 1986; Upadhyay, 2008), as well as a coarse gabbro that is intruded by the Tirit granite at the Nubra-Shyok confluence south of Burma village, a dioritic body that intrudes the Hundri Formation cherts at the roadside between Diskit and Hundar, a plutonic body intruding the Shyok Volcanics above the Waris-Udmaru road, and a granodiorite at Waris village (Borneman et al., 2015). The Tirit granite crosscuts the Shyok Volcanics at the Tirit bridge and the Hundri Formation south of Burma, and is faulted against Karakoram granites to the east by the strike-slip Karakoram fault (Rai, 1982; Rao and Rai, 2009; Weinberg and Dunlap, 2000). Two different ages have been obtained from the Tirit granite using U-Pb zircon geochronology (Kumar et al., 2017; Upadhyay, 2008; Weinberg and Dunlap, 2000). There are likely two different intrusive bodies included within the Tirit granite, as various studies have reported different ages for samples from the same area. It was initially dated using whole-rock Rb-Sr and LA-ICPMS U-Pb zircon geochronology to between 74 – 67 Ma (Upadhyay, 2008; Weinberg and Dunlap, 2000) and subsequently to 109 – 105 Ma (Kumar et al., 2017). The Tirit granite also contains inherited grains of Permian to Paleoproterozoic age (Kumar et al., 2017). The Hundar granite intrudes cherts and quartzites of the Hundri Formation at the Hundar Monastery and is crosscut by the Khalsar fault in the Hundar Dog valley south of Hundar village. It has been dated using LA-ICPMS zircon geochronology to 67.3 ± 0.7 Ma by Kumar et al. (2017). Borneman et al. (2015) also obtained an 84.8 ± 0.7 Ma LA-ICPMS U-Pb zircon age from a granitic pluton intruding the Shyok Volcanics

in the cliffs between Udmaru and Waris and a 42.0 ± 1.7 Ma age for the granodiorite above the Waris thrust at Waris village.

Murgi Conglomerate: The Murgi Conglomerate is a thrust-bound 50 – 120 m thick wedge of conglomerate that overlies the Saltoro Formation and can be traced in satellite imagery as a continuous unit between outcrops south of Murgi village in the Nubra valley, through the upper Udmaru and Waris valleys, and on towards the Indo-Pakistan border area. It is a sheared polymictic conglomerate with lenses and channel fills of coarse sandstone and pebble-conglomerate. It contains rounded clasts that span a very wide array of lithologies, including serpentinite, gabbro, granite, rhyolite, andesite, limestone, marble, schist, slate, sandstone, pebble conglomerate, and chert. The clasts are imbricated with the S-C shear fabric and sometimes are frequently crosscut and displaced by shear planes (see Section XYZ Structure).

1.5.1.2 Ladakh Arc

Ladakh Batholith: Unlike in Kohistan, where there are spectacular exposures of mafic and ultramafic lower-crustal rocks (Bard, 1983; Jagoutz and Burg, 2009; Jagoutz and Schmidt, 2012), only the mid-upper arc crust is exposed in Ladakh (Bouilhol et al., 2013; Honegger et al., 1982; Jagoutz et al., 2019). The Ladakh arc batholith comprises predominantly large bodies of homogeneous granodiorite and biotite-granite, as well as some diorite, tonalite, and gabbroic intrusions (Bouilhol et al., 2013; Honegger et al., 1982; Raz and Honegger, 1989; Singh et al., 2007). It intrudes and is overlain by volcanic and sedimentary cover sequences, including the Khardung Volcanics and Darnok Group (Raz and Honegger, 1989), and the Dras Volcanics (Bhat et al., 2019; Frank, 1977; Gansser, 1964; Honegger et al., 1982; Wadia, 1937).

The Kohistan-Ladakh batholith was active from 118 – 25 Ma, with zircon ϵ_{Hf} and whole-rock Nd-Sr isotopic signatures indicating crustal contamination of the source region started after 50 Ma (Bouilhol et al., 2013; Jagoutz et al., 2019). It is possible that the Matum Das tonalite (U-Pb CA-ID-TIMS zircon age of 154.08 ± 0.85 Ma) records the initiation of KLA magmatism (Jagoutz et al., 2019), though this pluton maps north of the belt of sheared serpentinites indicated by Le-Fort and Pecher (2002) and is included in the suture zone in our regional interpretation (see Figure 1-2 and Figure 1-3). Based on our new field mapping, we revise our original interpretation (Jagoutz et al., 2019) and consider it more plausible that the Matum Das pluton is unrelated to the KLA and is instead related to magmatism in the Shyok suture zone. This interpretation explains the significant age gap of nearly 36 Ma between the Matum Das intrusion and the next oldest intrusion within the KLA at 118 Ma.

Darnok Group: Raz and Honegger (1989) reported intensely deformed metasedimentary rocks, including quartzites, schists, and marbles, that are intruded by gabbroic and dioritic plutons associated with migmatized amphibolites as part of a major anticline in the Ladakh range. These metasedimentary and metavolcanic rocks were also noted by Rolland et al. (2000), but they provided no further information regarding the age or tectonostratigraphic significance of these rocks. These metasedimentary units were likely part of the upper-crustal cover sequence of the arc, but no depositional age nor detrital zircon age spectra are available.

Khardung Volcanics: The Khardung Volcanics are a suite of rhyolitic volcanic flows that are best exposed on the Khardung-La road between Khardung and Khalsar, though they are also exposed in the Pachatang valley, where they are heavily intruded by Ladakh batholith granites,

and in tectonic slices in the Khalsar fault in the Hundar Dog valley south of Hundar village. The Khardung Volcanics on the Khardung-La road section are 5800 m thick and primarily comprise rhyolitic lava flows, with intervening welded tuff, ignimbrite, ash, and volcanoclastic conglomerates that are more frequent at the top of the stratigraphy (Bhutani et al., 2009; Lakhan et al., 2020; Martin et al., 2020; Saktura et al., 2021a; Weinberg and Dunlap, 2000). The base of the volcanic pile is not exposed because they are truncated by a fault at Khardung village (Saktura et al., 2021a), and the top of the stratigraphy is not exposed because it is truncated by the Khalsar Thrust (Saktura et al., 2021a; Srimal et al., 1987).

We subdivide the Khardung Volcanics into two map units; the lowermost exposed volcanic stratigraphy comprises massive 10 – 60 m thick lava flows of rhyolite, andesite, and dacite composition with intervening rhyolitic sills and dikes (Bhutani et al., 2009; Clift et al., 2002; Dunlap and Wysoczanski, 2002; Lakhan et al., 2020; Saktura et al., 2021a). This portion of the stratigraphy is more altered than the upper Khardung Volcanics and exhibits epidote alteration in the more mafic flows, and is crosscut by hydrothermal veins and deposits containing calcite and chert (Lakhan et al., 2020). The upper section is not metamorphosed and has experienced only minimal deuteric alteration (Martin et al., 2020). The upper Khardung Volcanics comprise 1 – 5 m thick rhyolitic lava flows interbedded with 5 – 8 m in thick tuff and ignimbrite horizons, as well as volcanoclastic conglomerate, 30 – 50 cm thick ash layers, and sandstone (Lakhan et al., 2020; Martin et al., 2020; Saktura et al., 2021a). The ignimbrite exhibits fiamme structures, volcanic bombs, imbrication, graded bedding, and other flow structures such as crossbedding.

The age of the Khardung Volcanics is very well constrained to between 70 – 52 Ma with LA-ICPMS U-Pb zircon geochronology (Lakhan et al., 2020; Saktura et al., 2021a), CA-ID-TIMS U-Pb zircon geochronology (Martin et al., 2020), and Ar/Ar dating techniques (Bhutani et al.,

2009). Flows near the bottom of the Khardung Volcanics stratigraphy were dated to 67.4 ± 1.1 Ma using LA-ICPMS U-Pb zircon geochronology by Dunlap and Wyczosanski (2002) and to 69.7 ± 0.4 Ma by Lakhan et al., (2020). As part of a paleomagnetic investigation, the age of the upper Khardung Volcanics stratigraphy was precisely constrained to between 66.100 ± 0.085 Ma and 61.636 ± 0.11 Ma using CA-ID-TIMS U-Pb zircon geochronology and also magnetostratigraphic boundaries corresponding to the C29 – C26 magnetochrons (Martin et al., 2020). The youngest ages from the Khardung Volcanics come from two samples collected above the Martin et al. (2020) sample section that were dated using LA-ICPMS U-Pb zircon geochronology to 51.9 ± 0.7 Ma and 52.2 ± 0.7 Ma (Saktura et al., 2021a). Ar-Ar ages of 56.4 ± 0.4 Ma and 52.0 ± 0.4 Ma were also obtained in this area by Bhutani et al. (2009).

Turtuk Complex: Around the village of Turtuk, there are deformed intermediate-mafic intrusive rocks, as well as amphibolites and banded orthogneisses. The contact relationships between these units are intrusive, and they are overprinted by right-lateral shearing associated with the Turtuk shear zone (see section 1.5.2.1).

1.5.1.3 Karakoram Terrane

Karakoram Metamorphic Complex: A strip of schist, marble, and quartzite, are exposed in the valleys on the eastern edge of the mapped area; these metasedimentary units are in faulted contact against leucogranites to the west and Cretaceous Karakoram granodiorites to the east (Phillips et al., 2013; Pundir et al., 2020; Ravikant et al., 2009; Van Buer et al., 2015). The metasedimentary rocks can be traced in satellite imagery extending into the Angmong footwall

Suite in the Pangong Lake area (Van Buer et al., 2015). Karakoram-related metasedimentary rocks are also exposed in the Saltoro ranges north of the Karakoram thrust zone in the uppermost Udmaru valley, where they comprise overturned dark quartzites, black slates, and grey marbles. The metasedimentary rocks are sheared and carried in the hanging wall of the steeply north-dipping thrust that bounds the northern limit of the Shyok suture zone (see Section 1.5.2.1). The marble can easily be traced northward and westward in satellite imagery and can be seen in the cliffs at the head of the Waris valley, but are inaccessible in that area due to the restricted access to valleys close to the Indo-Pakistan border.

Nubra-Siachen Granite and Karakoram Diorite: The Eastern boundary of the field area is dominated by a K-feldspar porphyritic granite that extends from Agham as far as Sasoma, which is intruded by a late-stage muscovite-garnet leucogranite body and leucogranite dikes (Phillips et al., 2004; Phillips et al., 2013). These granites have been dated using LA-ICPMS U-Pb zircon geochronology and have yielded ages of 15.9 ± 0.1 Ma, 13.7 ± 0.3 Ma, 13.6 ± 0.5 Ma (Horton and Leech, 2013; Phillips et al., 2004; Phillips et al., 2013). The leucogranite intrusions are separated from a major granodiorite and diorite body further to the east by a shear zone that carries the Karakoram metamorphic complex (see above). The granodiorites have been dated to using LA-ICPMS U-Pb zircon geochronology to 100.6 ± 1.5 Ma and 108.6 ± 1.7 Ma (Phillips et al., 2013; Ravikant et al., 2009).

1.5.2 Structure

1.5.2.1 Faults

Khalsar thrust: The southern boundary of the Shyok suture zone is the Khalsar thrust (Rai, 1982; Sharma and Gupta, 1978). It is a near vertical fault structure that separates the Shyok Volcanics, Hundri Formation, and Salto Formation against the Khardung Volcanics and the Ladakh batholith. It is exposed along the southern edge of Shyok River between Khalsar and Largyap and extends into the valleys south of Bogdang and Chalunka, where it separates heavily deformed and intruded amphibolites and mafic metavolcanics from Ladakh batholith biotite-granite and gabbro. Above Diskit, the Khalsar thrust truncates the faulted contact between the Salto Formation and Hundri Formation (see Figure 1-7 and Figure 1-10). The thrust zone contains ultramafic lenses along its length, including a 340 m wide serpentinite lens south of Thoise, and a 40 m wide pyroxenite body in the Darnok-Largyap valley. It is crosscut by the Chalunka granite and garnet-bearing leucogranite dikes (the only intrusive units crosscutting the Khalsar fault), as well as the Turtuk shear zone, and the Khardung thrust.

In Khalsar, the fault surface is oriented $304^{\circ}/74^{\circ}$ NE and comprises a 1-3 m wide zone of heavily sheared Hundri Formation phyllite and very friable fault gouge (see Figure 1-8 and Figure 1-9). Close to the fault surface, quartz-mica mineral elongation lineations are visible in the phyllite foliation plane plunging $72^{\circ}/023^{\circ}$ (see Figure 1-4 and Figure 1-9) and centimeter-scale asymmetrical folding and crenulations indicate a north-side up shear sense (see Figure 1-8c). In the Hundar valley, the Khalsar fault is a complex imbricated zone of multiple fault-bound slices comprising rhyolite from the Khardung Volcanics, Ladakh Batholith tonalite and biotite granite, and Hundri Formation quartzite and chert. In this area, the Khalsar fault shear planes are 0.4-2 m wide fault gouges surrounded by heavily fractured zones with numerous penetrative fault surfaces

planes exhibiting quartz slicken-lines with a north-side up shear sense. These fault planes trend between 95° - 130° and are variably dipping between 68° towards the south-southwest and 70° north-northeast, defining a complex but essentially vertical fault zone. The Hundar valley is also overprinted by 006° – 020° trending and 80° – 52° east-dipping right-lateral strike-slip fault planes with 30 – 50 m offsets that are unresolvable at the scale of our mapping.

Bogdang shear zone: The Bogdang shear zone is a major ~1 km wide anastomosing shear zone that separates the Changmar Complex from metamorphosed granodiorites, gabbros and orthogneisses of the Turtuk Complex (see Figure 1-4 and Figure 1-10). It is exposed at the roadsides in Bogdang village and south of Changmar where it truncates against the Turtuk shear zone. Westward it is traceable in satellite imagery extending to the northwest out of the accessible field area towards the LAC. The fault zone comprises meter-wide mylonetized zones of chlorite-schist surrounding 8 – 16 m wide asymmetrical boudins. The boudins comprise dismembered elements of the Changmar complex and comprise predominantly pyroxenite, with some gabbro, serpentinite, and basalt. The gabbroic boudins exhibit poikilitic cumulate textures with pyroxene chadacrysts and plagioclase oikocrysts that transition gradationally into pyroxenite at the meter scale. Some of the ultramafic boudins are crosscut by 5 – 20 cm wide calcite-graphite pegmatite veins, and which predate the penetrative ductile shear zones.

The chlorite-schist foliation within the Bogdang shear zone is complex, with foliation plane measurements trending between 102° – 140° and dipping between 84° – 47° towards the southwest and south-southwest (see Figure 1-9). Crenulation lineations in the chlorite schist plunge 64° – 70° towards 168 – 185° . Asymmetrical boudins, sigmoids, and asymmetrical folds suggest a normal (or overturned reverse) shear sense. The primary chlorite schist foliation of the Bogdang shear

zone is crosscut and disrupted by discrete fault planes that are east-west trending and vertical. These surfaces are mineralized with quartz and exhibit horizontal quartz-slicken-lines with slicken-steps that suggest a right-lateral strike-slip shear sense; these are likely related to the Turtuk shear zone, which crosscuts the Bogdang shear zone.

Turtuk shear zone: The Shyok River valley between Changmar and Turtuk follows a major right-lateral strike-slip fault zone. In Chalunka village, basalt intruded by gabbro is crosscut by multiple fault planes that increase in frequency towards the north. At the primary fault zone above Chalunka village, the basalt and gabbro transitions into a 5 – 8 m wide serpentinite-chlorite schist that separates them from a foliated granodiorite to the north. The shear zone at Chalunka is mineralized with calcite and sulfur.

On the border road west out of Turtuk towards Thang, the Turtuk shear zone is exposed as a 500 m wide shear zone separating a coarse-grained biotite granite to the south from amphibolite intruded by granodiorite and gabbro to the north. The biotite-granite has a strong foliation defined by feldspar and biotite close to the shear zone and becomes less foliated to the south towards Turtuk village. Within the shear zone there are meter-scale lenses of pyroxenite and gabbro similar to the Changmar Complex, and also amphibolite and granodiorite of the Turtuk Complex. Foliated garnet-bearing leucogranite dikes crosscut the amphibolite and granodiorites in the shear zone, suggesting that shearing occurred after their intrusion. The Turtuk shear zone crosscuts the Bogdang shear zone above south of Changmar village and is also exposed in the Largyap valley where it separates different structural levels of the Shyok Volcanics/Changmar Complex (Saktura, 2021b). The Turtuk shear zone is vertical trends 85° – 122° . Chlorite mineral elongation lineations and quartz slicken-line lineations are present on Turtuk shear zone fault planes with sub-horizontal

plunges between 0° – 32° (see Figure 1-9). Asymmetrical folding of garnet-bearing leucogranite dikes near Turtuk and slicken-step ridges on fault planes throughout the shear zone indicate a right-lateral sense of motion.

Khardung thrust: In the village of Khardung, granite and tonalite from the Ladakh Batholith contact rhyolite and andesite volcanic flows of the Khardung Volcanics along a south-dipping fault structure (Saktura et al., 2021a). The fault zone comprises a 4 m wide zone of brittle faults marked by 20 – 30 cm wide cataclasite zones. The primary fault planes trend 126° – 138° and dip toward the southwest at an angle of 47° – 57° , truncating at $\sim 80^{\circ}$ the rhyolitic sills and volcanic flows of the Khardung Volcanics, which are inclined $315^{\circ}/34^{\circ}$ NE (see Figure 1-9 and cross-section D-D' in Figure 1-10). To the east, this contact can be traced in satellite imagery into the Karakoram fault strike-slip shear zone near Agham and can be traced westward as far as the Hundar valley, where it appears to amalgamate into the complex imbricate fracture zone of the Khalsar thrust.

Karakoram thrust System: The Shyok suture zone is overprinted by a complex system of north-dipping thrust faults that place Karakoram metamorphic complex quartzite, slate, marble, and other metaplutonic rocks against lithologies from the Shyok suture zone (Rai, 1982). This thrust zone comprises three primary fault structures (the Murgu thrust, Waris thrust, and Ensa thrust) and an intensely sheared and isoclinally folded repetition of suture zone lithologies (Borneman et al., 2015; Rai, 1982). Between the Ensa thrust and the Murgu thrust, the broad scale structure is an isoclinal syncline comprising a heavily deformed but complete repetition of the Shyok suture zone sequence (see Section 1.5.2.2 Folding).

The Ensa thrust is the northernmost fault of the Karakoram thrust system and is best exposed at Ensa Monastery in the Nubra valley. The Ensa thrust is also exposed west of the Nubra valley, demarcating the primary ridgeline of the Saltoro Range. We accessed it in the slopes above the Udmaru glacier, where it presents as a steep boundary separating the Karakoram metamorphic complex metasedimentary rocks and metadiorite from Shyok suture zone serpentinite and basalt (see Figure 1-11), and it is traceable towards the west in satellite imagery, in the Patchhatang and Waris valleys and towards the India-Pakistan border areas.

At Ensa Monastery it is a 650 – 820 m wide zone of mylonitized basaltic and rhyolitic metavolcanics and granite sheets intruded parallel to the compositional layering of the volcanics. The mylonite foliation trends 277° – 313° and dips 28° – 54° towards the northeast with feldspar elongation lineations and quartz slicken-lines oriented parallel to the dip of the foliation, plunging 26° – 55° towards 15° – 45° . In the Udmaru valley, the Ensa thrust is slightly steeper, dipping 64° – 78° towards the northeast with a similar strike (see Figure 1-9). Meter-scale asymmetrical isoclinal folding, en-echelon tension gashes, and sigma porphyroblasts indicate a top-to-the-south (thrust) shear sense.

The Waris thrust is best exposed in the Waris area, where it emplaces the Waris granodiorite on top of mylonitized marble and chlorite-muscovite schist (Borneman et al., 2015). It is also exposed in the Udmaru valley, where it emplaces serpentinite, gabbro, and basalt on top of calc-silicate slate and in the mountains above Murgi village where it emplaces serpentinite on top of calcsilicate schist and marble. The Waris thrust strikes 290° and dips 28° – 31° towards the north-northeast and has dip-parallel quartz mineral elongation lineations and sigma porphyroblasts, indicating a top-to-the-south (thrust) shear sense. In the Udmaru valley, slate and

phyllite situated in the footwall of the Waris thrust exhibit strong S-C-C' fabrics indicating a top-to-the-south shear sense (see Figure 1-11b).

The base of the Karakoram thrust system is the Murgi thrust, which consists of two near-parallel thrust sheets above and below the Murgi conglomerate. The Murgi thrusts and the intervening conglomerates are best exposed on the roadside south of Murgi village in the Nubra valley but can also be accessed where they bisect the Udmaru, Patchhatang, and Waris valleys. The Murgi thrust emplaces the Murgi conglomerate on top of the Saltoro Formation in the Nubra and Udmaru valleys, and on top of Hundri Formation phyllites and cherts and limestones in the Waris valley. The hanging wall of the Murgi thrust comprises a repetition of the Shyok suture zone sequence, with serpentinite and listwanite (carbonized peridotite) close to the thrust surface, overlain by epidotized and sheared basalt, and then calcareous muscovite-mica schist, marble and slate. The Murgi thrust truncates normal faulting in the Saltoro Formation and is crosscut by a left-lateral strike slip fault with <100 m offset in the Udmaru valley.

Throughout the field area, the Murgi thrust maintains a very consistent trend of 284° – 308° , dipping 22° – 42° towards the northeast. Quartz slicken-lines and muscovite mineral elongation lineations on the foliation planes within from the hanging wall schists and metavolcanics are dip-parallel to the foliation plane, plunging 17° – 42° towards 016° – 046° . Between the two thrust sheets, Murgi conglomerate clasts are imbricated with the foliation and the bedding is overprinted by an S-C shear fabric displaying top-to-the-south shear sense.

Saltoro Extension: The contact between the Saltoro Formation on the underlying Shyok Volcanics and Hundri Formation is a brittle fault structure (termed Hundri fault by; Srimal, (1986)). In the Udmaru valley the fault separates the basal Saltoro Formation andesite breccias

from the epidotized pillow basalts of the Shyok Volcanics. On the slopes above Hundri and Shukur, it separates Saltoro Formation conglomerates and sandstones from calcareous phyllites and limestones of the Hundri Formation. The fault contact is folded by the F_1 anticline along the Shyok valley and crops out, dipping steeply towards the south in ridgelines south of Hundar and Diskit (see Figure 1-4). The Saltoro fault in the Udmaru valley trends towards 208° and dips 38° north-northeast.

Extensional deformation is common in the lowermost levels of the Saltoro Formation where numerous normal faults with < 30 m offset displace the volcanic layering in the lower Saltoro volcanics and propagate into the overlying Saltoro Formation conglomerates (see Figure 1-7c). Riedel shears on these structures in the Udmaru valley indicate normal shear sense (see Figure 1-7b). The offset on these normal faults decreases progressively until they terminate against the overlying stratigraphy, suggesting that extension occurred simultaneously with the sedimentation of the Saltoro Formation conglomerates. The extensional structures are restricted to the lower portion of the Saltoro stratigraphy beneath the angular unconformity that Borneman et al., (2015) originally described as an unconformity between the Saltoro Formation and the Shyok Volcanics. The faults truncate against the unconformity and are crosscut by the Khalsar thrust, the Murgi thrust, and the Shukur dikes (see Figure 1-7a).

Karakoram fault: At the confluence of the Nubra and Shyok valleys, the Shyok suture zone is sheared into the right-lateral Karakoram strike-slip fault zone (Phillips, 2008; Rai, 1982; Searle et al., 1998; Srimal, 1986). The Karakoram fault is a major orogen-scale structure separating Tibet from the Pamir/Karakoram (Gansser, 1964). It remains an active fault zone with recent faulting bisecting and displacing quaternary alluvial fan deposits, and with modern hydrothermal activity

and seismicity (Dutta et al., 2023; Houlié and Phillips, 2013; Kanna et al., 2018; Upadhyay, 2003; Valli et al., 2007). In our field area, the Karakoram fault is exposed on the eastern side of the Nubra valley between Panamik and Agham, where it splits into two strands on either side of the Pangong Complex (Searle et al., 1998; Phillips et al., 2008). It appears to extend on the western side of the Nubra valley north of Panamik to the edge of the field area, though we were not able to access it in this area and the granites north of Panamik are unfoliated.

The Karakoram fault comprises the entire Shyok suture zone stratigraphy sheared out into an intensely deformed 0.8 – 1 km wide strip that was originally grouped together as a single unit called the Nubra Formation by Phillips et al., (2008). From west to east the shear zone comprises Saltero Formation conglomerate, a band of strongly foliated dark-colored phyllite and schist, serpentinite lenses, mylonitized metabasalt, and a zone of high-grade sheared metasedimentary rocks. The Karakoram fault zone has a consistent northwest-southeast trend but has significant variations in dip along its exposure. Around Panamik, the Karakoram fault is vertical and has shallow 15° – 30° plunging slicken-line lineations. The Karakoram fault rotates towards the south at Sumur and Khalsar, where it dips 72° – 53° towards the northeast. In this area, there is a wide range of slicken-line and mineral elongation lineation orientations, suggesting a combination of strike-slip and thrust deformation.

1.5.2.2 Folding

The first-order fold structure (F_1) of the Shyok suture zone is a tens-of-kilometer wavelength anticline with an east-southeast to north-northwest trending fold axis. The large-scale map pattern of the depositional contact between Hundri Formation and Shyok Volcanics dips southward along the south side of the Shyok River and northward on the northern side of the Shyok

River, marking the limbs of the large-scale F_1 anticline. In the areas around Shukur and Hundri villages, the Hundri Formation stratigraphy and its basal contact with the Shyok Volcanics is folded by 1.5 – 2 km wavelength F_1 parasitic folds (and also 150 – 200 m wavelength second-order parasitic folds and 3 – 8 m wavelength third-order parasitic folds). The F_1 parasitic folds in this area have axes that plunge $2^\circ - 8^\circ$ east towards $087^\circ - 115^\circ$ (see Figure 1-9). The F_1 parasitic folds in this area have interlimb angles of $62 - 76^\circ$, northward vergence, and axial planes dipping $70^\circ - 80^\circ$ towards the south (see Figure 1-9). A similar wavelength north-verging anticline is also present in the Saloro Formation south of Charasa with a fold axis plunging 1° towards 061° and an axial plane trending towards dipping 58° towards the south-southeast (see Chapter 3).

The F_1 anticline is re-folded by gentle 50 – 60 km wavelength F_2 -folds with fold axes oriented broadly perpendicular to F_1 . Evidence for this F_2 folding is derived from the map patterns of the Hundri-Shyok contact along the Shyok River, and the precise fold axis orientations are unconstrained. At Thoise and Hundri villages, the Hundri Formation completely covers the underlying Shyok Volcanics, suggesting that this area is situated in the core of an F_2 -syncline. Eastward and westward from these villages, the deeper structural levels of the Shyok suture zone sequence are exposed, implying that these areas are in the cores of F_2 anticlines with axes situated around Changmar and Diskit villages.

1.6 Discussion

The results presented in this chapter, along with published geochronology and new U-Pb zircon ages from Chapter 2, enable us to characterize the tectonostratigraphy of the Shyok suture zone and constrain the relative timing and development of the major structures. In the following sections, we will synthesize the geology of the suture zone in Ladakh and develop tectonic and lithological associations along strike with its exposures in Pakistan. We will also discuss our interpretation of the kinematic development of the suture zone and its implications for understanding the age and tectonic development of the KLA-Eurasia collision.

1.6.1 The Eurasian Forearc

At the broadest scale, the geology of the Shyok suture zone in Ladakh comprises a Jurassic ophiolite with Cretaceous sedimentary cover that is tectonically emplaced between the Karakoram and Ladakh batholiths (Rai, 1982; Saktura et al., 2021b; Srimal, 1986; Thakur and Misra, 1984; Thanh et al., 2012). The Shyok Volcanics and the Changmar Complex together comprise the basement onto which Cretaceous marine sedimentary rocks were deposited (Rai, 1982; Rolland et al., 2000; Srimal, 1986; Upadhyay et al., 1999). The Shyok Volcanics are tholeiitic, meaning they formed from deep hydrous partial melting of the mantle wedge beneath an emergent subduction zone (See Chapter 2; Borneman et al., 2015; Rolland et al., 2000; Saktura et al., 2021b; Thanh et al., 2012). Their eruption is bracketed to the Late Jurassic by our 152.1 ± 1.2 Ma age from the uppermost Shyok Volcanic flows (LB19-22, see Chapter 2) and by the 159.4 ± 0.9 Ma Changmar gabbro which crosscuts the base of the volcanic stratigraphy (Saktura et al., 2021b). The Hundri Formation rests unconformably on the Shyok Volcanics (Upadhyay et al., 1999), and is structurally overlain by the Saltoro Formation. The Hundri Formation comprises a sequence of marine

sedimentary facies that were deposited between $\leq 115.9 \pm 2$ Ma (LB19-16) and $\leq 102.7 \pm 1.9$ Ma (LB19-35) (See Chapter 2). The Saltoro Formation comprises deltaic, estuarine, and fluvial sedimentary facies interlayered with andesite volcanic flows. They were deposited in an extensional basin environment starting at around $\leq 92.9 \pm 2.2$ Ma (LB18-18) and continued accumulating until 74.6 ± 0.7 Ma (LB19-56) (See Chapter 2).

Different studies have variably interpreted these formations as the remnant of a forearc sequence on the southern margin of the Karakoram terrane (Saktura et al., 2021b; Thanh et al., 2012), or a back-arc basin in association with the KLA (Pudsey, 1986; Rolland et al., 2000). Our results favor the interpretation that the Shyok suture zone formed in a forearc setting on the southern margin of Eurasia. This interpretation is supported by the long-lived deposition of Eurasia-derived sedimentary rocks interlayered with calc-alkaline arc volcanics, the entirely tectonic contact relationships between the suture zone ophiolite sequence and the KLA, and the anomalous age of the Changmar complex compared to the KLA batholith.

The gabbros and pyroxene cumulates of the Changmar Complex have similar geochemistry and age to the Matum Das gabbro and tonalite in Pakistan, which has been previously interpreted to record the initiation of the KLA (Saktura et al., 2021b; Jagoutz et al., 2019). The Matum Das Complex is 154.08 ± 0.85 Ma, similar to the 159.4 ± 0.9 age of the Changmar gabbro (Saktura et al., 2021b), and Matum Das intrudes the tholeiitic Chalt volcanics, which are compositionally similar to the Shyok Volcanics (Jagoutz et al., 2019; Petterson and Windley, 1991). The tholeiitic character of the Shyok and Chalt Volcanics is consistent with an ophiolitic setting. However, both the Changmar and Matum Das Complexes are anomalously old compared to the rest of the KLA batholith plutonic bodies and volcanic sequences, which are generally younger than 118 Ma, suggesting that they could be genetically distinct (Bouilhol et al., 2013; Jagoutz et al., 2019).

The Shyok Volcanics, Changmar Complex, and overlying sedimentary cover are separated from the Ladakh batholith by exclusively tectonic contacts (the Khalsar fault and the Bogdang shear zone). Srimal et al., (1986) and subsequently Saktura et al., (2021) interpreted intrusive relationships between the Chalunka granite and the Changmar Ophiolite as evidence that the Changmar-Shyok ophiolite represented a remnant of the oceanic basement into which the Ladakh arc batholith intruded. However, our geochronology results show that the Chalunka granite is 24.7 ± 0.4 Ma (see Chapter 2), so the intrusive relationship between it and the Changmar Complex indicates only that the KLA and the Changmar/Shyok ophiolite were structurally emplaced together before the end of the Oligocene, rather than demonstrating a genetic link prior to that time.

A major structural boundary, similar to the Khalsar thrust and Bogdang shear zone, separates the Matum Das Complex and the Chalt volcanics (and their correlatives) from KLA lithologies westward into Pakistan (see Figure 1-2 and Figure 1-3). There is an ultra-mafic-bearing shear zone between the Shyok Volcanics and Ladakh arc granodiorites in Khalpu (Brookfield and Reynolds, 1990), and between the Turmik Greenstone group and the Askor amphibolite in Dasu (Awais et al., 2022; Le Fort and Pecher, 2002; Rolfo et al., 1997; Rolland et al., 2000). Lefort and Pecher, (2002) continued the same contact zone west of the Nanga Parbat syntaxis along a sheared serpentinite-bearing shear zone (Dobani Ultramafic Unit) to the south of the Chalt Volcanics and Matum Das Complex near Jaglot (see Figure 1-2 and Figure 1-3). The continuation of this structure further westward around Yasin is unclear, and it may be obscured by subsequent plutonism that extensively disrupts the tectonic boundaries in that area (Jagoutz et al., 2011; Petterson et al., 1993; Petterson and Windley, 1985; Pudsey et al., 1985).

The Saltoro Formation conglomerates have previously been interpreted as a post-collision molasse unconformably resting on top of the Shyok Volcanics and Hundri Formations (Borneman et al., 2015; Rai, 1982; Srimal, 1986; Upadhyay et al., 1999). However, we interpret the Hundri and Saltoro Formations as related marine and terrestrial components of a long-lived Cretaceous forearc sedimentary basin at the southern edge of the Karakoram terrane (see Figure 1-12). The detrital zircon age spectra from both formations is consistent with detrital zircon age spectra from similar age sedimentary formations from Eurasian margin sources, including the Lhasa terrane, Central Pamir, Quiangtang terrane, and the Xigaze Forearc basin (see Figure 2-17) (Chapman et al., 2018a; He et al., 2019; Robinson et al., 2012; Xue et al., 2022). This provenance suggests that the Shyok suture zone sedimentary sequence and underlying Jurassic ophiolite were proximal to the Eurasian active margin from 115.9 – 74.6 Ma (Borneman et al., 2015). The overall stratigraphic progression of the Saltoro and Hundri Formations is also consistent with the shallowing upward paleo-bathymetry of classical forearc sedimentary basins (Dickinson and Seely, 1979). Finally, the presence of calc-alkaline andesite volcanics, indicative of shallow decompression melting (Schmidt and Jagoutz, 2017), interlayered with Saltoro Formation strata supports an arc-forearc depositional setting. The andesitic flows are distributed throughout the Saltoro Formation, underlying the lowermost sedimentary stratigraphy (i.e. $> 92.9 \pm 2.2$ Ma) and also extending above the uppermost sedimentary exposures (i.e. $< 74.6 \pm 0.7$ Ma), suggesting that sedimentation occurred in an environment with prolonged arc-volcanic activity. A forearc tectonic setting for the Saltoro volcanics is consistent with evidence for syn-sedimentary extension within the Saltoro Formation clastic deposits because forearc sequences can undergo periods of extension depending on the dynamics of the subducting slab (see Figure 1-7; Dickinson and Seely, 1979).

Similar and likely correlative sedimentary sequences are consistently observed throughout the Shyok suture zone. On the Kohistan side of the Nanga Parbat syntaxis, these include the Yasin Group limestone, schist, and conglomerate (Pudsey et al., 1985), and the Drosh and Purit Formations in Chitral (Heuberger, 2004; Heuberger et al., 2007). East of the Nanga Parbat syntaxis near Shigar, the Turmik greenstone group is interlayered with the Pakora Formation marble, calcareous schist, and quartzite-conglomerate, which likely correlate to the Hundri and Saltoro Formations (Reynolds et al., 1983; Rolfo et al., 1997; Rolland et al., 2000). In Pakistan, these units have previously been correlated with the KLA (Jagoutz et al., 2011; Petterson and Windley, 1985; Pudsey et al., 1985). However, this interpretation is tentative and is primarily based on their structural position south of the Karakoram thrust, which has been widely used to delineate the KLA-Karakoram boundary in that area, and the observation that plutonic bodies intrude the Chalt Volcanics (Pudsey, 1985; Burg et al., 2018; Robertson and Collins, 2002; Pettersen and Windley, 1985).

Arc magmatism was occurring in the Shyok suture zone over a prolonged period from the Late Cretaceous until the mid-Eocene, consistent with a long-lived arc-forearc origin for the Shyok suture zone sequence (see Figure 2-18). The Tirit-Hundar plutonic suite spans ages between (109 – 42 Ma). These include the 109 – 105 Ma and 76 – 74 Ma intrusions of the Tirit granite (Kumar et al., 2017; Upadhyay, 2008; Weinberg and Dunlap, 2000), the 84.8 ± 0.7 Ma Udmuru diorite/gabbro (Borneman et al., 2015), the 67.3 ± 0.7 Ma Hundar granite (Kumar et al., 2017), and a 59.1 ± 0.2 Ma diorite/gabbro body near Diskit (LB18-21; see Chapter 2), and the 42 ± 1.7 Ma Waris granodiorite that intrudes ultramafic volcanics in the footwall of the MKT and is crosscut by the Waris thrust (Borneman et al., 2015). We attribute the magmatism in the Shyok suture zone sequence, as well as the 93 – 85 Ma extension within the Saltoro Formation, to

southward movement of the arc-trench system during slab rollback, as has previously been inferred to explain the lack of 70 – 90 Ma magmatism in Tibet and the Pamir (Chapman and Kapp, 2017; Chapman et al., 2018a; Chapman et al., 2018b; Kapp and DeCelles, 2019).

1.6.2 Post-Collision Sedimentation and Magmatism

The youngest exposed Shyok suture zone sedimentary rocks are the $\leq 25.9 \pm 1.5$ Ma Murgi Conglomerates. The diversity of clast lithologies in the Murgi Conglomerate, and in particular the presence of serpentinite-bearing clasts, indicates that the suture zone ophiolite and other Shyok suture zone lithologies were exposed and eroded into a fluvial environment before the end of the Oligocene. These conglomerates were likely deposited in a post-collisional intermontane depositional environment like the Kailas conglomerate in the western Yarlung-Tsangpo suture zone, the Nima Redbeds in Bangong suture zone, and the Kargil/Indus Molasse in the Indus suture zone (DeCelles et al., 2011; DeCelles et al., 2007; Zhou et al., 2020). Since their deposition, the conglomerates were incorporated into a wedge between the upper and lower Murgi Thrusts.

There are three large Miocene magmatic bodies in the Shyok-Nubra confluence area that clearly postdate the collision. The 24.6 ± 0.4 Ma Chalunka granite crosscuts the Ladakh batholith and the suture zone forearc sequence and is crosscut by the right-lateral Turtuk Shear Zone. The 15 – 13.4 Ma Nubra-Siachen granites, and the associated Warshi Leucogranite body are separated from the suture zone by the Karakoram fault (Phillips et al., 2013; Ravikant et al., 2009). These bodies are the same age as other major Miocene granites in the Karakoram including the 25 – 13 Ma Baltoro Granite and were likely emplaced during large anatexis and melting as the orogenic crust thickened following the underthrusting of Indian lithosphere (Parrish and Tirrul, 1989; Scharer et al., 1990; Searle et al., 1989).

1.6.3 Structural Development of the Suture Zone

Constraining the kinematic development of the Shyok suture zone is essential to understand the age and nature of the KLA-Karakoram collision. In Ladakh, the Shyok suture zone is a complex structure that comprises multiple major fault structures and large-scale folds. Indeed, all the major contacts between the KLA and the Shyok forearc sequence are exclusively tectonic. The southern boundary of the suture zone is the Khalsar thrust which separates the Ladakh Batholith and Khardung Volcanics from the Shyok Volcanics, Hundri Formation, and Saltoro Formation (Rai, 1982). Further west, the Bogdang shear zone separates the Changmar Complex, Shyok Volcanics, and Hundri Formation from deformed gabbro, granodiorite, and amphibolite of the Turtuk Complex. The Karakorum terrane is thrust over the suture zone by the Karakoram thrust system, comprising a complex nappe-stack involving the Murgi, Waris, and Ensa thrusts, and the suture zone is overprinted by strike-slip deformation along the Turtuk shear zone and the Karakoram fault Zone. In the following section, I discuss the kinematics and age of each of these major structures and present a model for the structural development of the Shyok suture zone and the KLA-Eurasia collision.

The oldest structures in the Shyok suture zone are extensional and affect only the Shyok forearc sequence, particularly the lower stratigraphic levels of the Saltoro Formation. Their age is well-constrained by crosscutting relationships in the Udmaru area. An older bound is derived from the $\leq 92.9 \pm 2.2$ Ma depositional age of Saltoro Formation sandstones and conglomerates that unconformably overlie and truncate underlying faulted strata, and a younger bound is obtained from the 81.8 ± 0.5 Ma, 84.4 ± 0.9 Ma, and 85.0 ± 0.6 Ma Shukur Dikes that crosscut the faulting (see Figure 1-7; Chapter 2; Borneman, 2015). Extension in the Saltoro Formation at 93 – 85 Ma is

consistent with southward Neotethyan slab rollback and forearc extension at the southern Eurasian margin that has been proposed between 90 – 70 Ma to explain an absence of arc magmatism in Tibet and the Pamir during this period (Chapman and Kapp, 2017; Chapman et al., 2018a; Chapman et al., 2018b; Kapp and DeCelles, 2019).

The earliest compressional structure in the Shyok suture zone is the Khalsar thrust. We interpret the Khalsar thrust and the Bogdang shear zone as strands of the same original structure that have been displaced by right-lateral shearing along the Turtuk shear zone. This interpretation is supported by the observations that both the Khalsar fault and Bogdang shear zone emplaced the Shyok suture zone arc-forearc complex against elements of the Ladakh arc, and each has the same top-to-the-south shear sense, though the Bogdang shear zone is overturned. The Khalsar fault likely developed as a south-directed thrust carrying the Shyok forearc ophiolite sequence over the Ladakh arc before being tilted into its steep present-day orientation. Indeed, untilting the Khalsar thrust based on the bedding of the Khardung volcanics (mean bedding orientation: $222^{\circ}/39^{\circ}$ NE) rotates the Khalsar fault from its present-day north-northeast-dipping reverse fault geometry at Khalsar ($304^{\circ}/74^{\circ}$ NE) to a more typical thrust geometry with a north-dipping orientation of $283^{\circ}/25^{\circ}$ N.

The Khalsar fault truncates volcanic and sedimentary bedding at the top of the Khardung volcanic stratigraphy that has been dated to 51.9 ± 0.7 Ma (Saktura et al., 2021a), so this structure must have been active after the Ypresian. It is also crosscut by the undeformed Chalunka granite, which is 24.7 ± 0.4 Ma (see Chapter 2), placing a younger limit on the age. An Eocene-Oligocene age for the thrust contact between the Shyok forearc sequence and the KLA is consistent with observations from the comparable structures exposed further west (see Figure 1-3). At Khalpu, the southern boundary fault of the Shyok suture zone crosscuts 45 – 40 Ma dikes in the Ladakh

batholith that were dated with the Ar-Ar method (Brookfield and Reynolds, 1990), and a similar steep thrust crosscuts 49.80 ± 0.15 Ma KLA gabbros near Drosch that were dated using the U-Pb in zircon (Heuberger, 2004; Heuberger et al., 2007).

The Khardung fault intersects with the Khalsar fault in Hundar and was originally interpreted as a top-to-the-north reverse fault by Saktura et al., (2021a). However, the Khardung fault could equally have formed as an overturned north-side-down normal fault. Reconstructing the Khardung Fault by untilting the Khardung volcanics stratigraphy rotates it from a steep south-dipping reverse fault geometry ($130^\circ/51^\circ$ SW) to a steeply north-dipping normal fault geometry ($211^\circ/79^\circ$ NE). Either way, the Khardung fault crosscuts, and therefore postdates, the 59.8 ± 0.6 Ma sills in the lower Khardung volcanics (Saktura et al., 2021a), and appears to be truncated by the Khalsar fault at Hundar, restricting the age to the Paleocene between 59.8 ± 0.6 Ma and 51.9 ± 0.7 Ma.

The Shyok suture zone stratigraphy and F_1 folding are overthrust and truncated by the south-vergent thrusts of the Karakoram thrust system (Rai, 1982; Rolland et al., 2000; Srimal, 1986; Thakur and Misra, 1984). Combined, the Murgi, Waris, and Ensa thrusts have a classical fold and thrust belt geometry with a shallow-angle basal detachment (Murgi thrust) overridden by sheared nappes comprising repetitions of the Shyok suture zone units. The thrusts steepen higher in the nappe stack (e.g., Ensa Thrust) due to northward tilting during translation over the younger thrust ramps (e.g., Murgi Thrust).

The available age constraints are consistent with classical older-toward-the-top thrust-nappe models. However, only older-bound constraints are available because none of the thrust structures are crosscut by intrusive bodies precluding younger-bound age constraints. The Waris and Ensa thrusts crosscut, and therefore postdate, the undeformed 42.0 ± 1.7 Ma Waris

granodiorite (Borneman et al., 2015) and the basal Murgu thrust crosscuts, and therefore postdates the $\leq 25.9 \pm 1.5$ Ma Murgu Conglomerate (see Chapter 2). The Karakoram thrust zone extends westward from our field area and throughout northern Pakistan, where it sometimes overthrusts and obscures the suture zone forearc sequence entirely, truncating equivalent structures to the Khalsar thrust (Rolland et al., 2000; Rolland et al., 2002; LeFort and Pecher, 2002). In these areas, the Karakoram thrust system has been widely interpreted as a late Miocene structure that accommodates shortening due to the indentation of India after the continental collision (Rex et al., 1988; Searle and Rex, 1989).

The youngest fault structures in the Shyok suture zone are strike-slip faults. The Turtuk shear zone bisects and offsets the Khalsar thrust, the Bogdang shear zone, and crosscut garnet-bearing leucogranite dikes near Turtuk that were dated by Jagoutz et al., (2019) in Chalunka to 25.1 ± 1.3 Ma. Similar right-lateral strike-slip fault zones with comparable orientation to the Turtuk shear zone have also been identified, crosscutting the Main Karakoram thrust system and Shyok suture zone in Pakistan, including the Shigar fault and an unnamed right-lateral strike-slip fault at Khalpu, as well as left-lateral strike-slip zones west of the Nanga Parbat syntaxis (Maheo, 2004; Rolland, 2001; Cronin, 1989; Pettersen and Treloar; 1990; Pudsey et al., 1985). The strike-slip faults likely accommodate large-scale oroclinal bending around the Nanga Parbat Syntaxis related to the indentation of India into Eurasia (Coward et al., 1986). Orogen-scale bending and northeastward tilting of Ladakh during the uplift of the Nanga Parbat syntaxis may also explain the increasing metamorphic grade of suture zone exposures westward from our field area (Rolland, 2000; Coward et al., 1986). This is consistent with westward transition in deformation style along the Khalsar fault in our field area from broad anastomosing shear zones at Bogdang to predominantly brittle discrete fault surface at Khalsar.

The youngest strike-slip fault structure in the Shyok suture zone is the Karakoram fault which crosscuts all the other structures of the Shyok suture, including the Karakoram thrust system and both the Khalsar and Khardung thrusts. It crosscuts 13.4 ± 0.1 Ma Nubra-Siachen granites along the length of its exposure in Ladakh and remains active today, displacing quaternary alluvial fans (Horton and Leech, 2013; Phillips et al., 2004; Phillips et al., 2013).

Overall, our results enable us to develop a consistent model for the kinematic development of the Shyok suture zone since the Cretaceous. The Shyok suture zone forearc ophiolite and overlying forearc basin sedimentary cover sequences underwent extension between 93 Ma and 85 Ma. While periods of extension, compression, and extension are common in forearc basin sequences and not necessarily indicative of large-scale extension (Dickinson and Seely, 1979), the age of the Saltoro Formation extension is consistent with models of slab rollback and southward migration of the southern Eurasian magmatic arc, which have been proposed to explain the absence of magmatism in Tibet and the Pamir between 90 Ma and 70 Ma (Chapman and Kapp, 2017; Chapman et al., 2018a; Chapman et al., 2018b; Kapp and DeCelles, 2019).

The Khalsar fault is the major tectonic boundary in the Shyok suture zone separating the Eurasia-derived sedimentary sequences of the suture zone forearc sequence from elements of the Kohistan-Ladakh Arc. Our results suggest that it was active between 52 – 25 Ma based on crosscutting relationships with the uppermost Khardung volcanics and the Chalunka granite, making it also the oldest compressional structure of the suture zone. The east-west oriented axes of the F_1 folding are parallel to the Khalsar fault, suggesting that the folding may have begun contemporaneous with or developed shortly after the Khalsar fault, and indicating both the folding and the faulting are crosscut by the Chalunka granite. This suggests that obduction and compression of the Eurasian Forearc took place took place in the Eocene-Oligocene, after the

KLA-India collision and development of the Indus suture zone, consistent with paleomagnetic results suggesting that the KLA accreted onto India prior to final India-Eurasia collision (Martin et al., 2020; Chapter 3).

All other structures in the suture zone are post-Miocene age and therefore relate to the convergence of India and Eurasia after the onset of continental collision. The Karakoram Thrust system accommodated India-Eurasia convergence in the Miocene, emplacing deeper crustal levels of the Karakoram terrane over the suture zone and KLA. Finally, strike-slip deformation and associated F_2 folding accommodated the uplift and bending of the orogenic system around the Nanga Parbat Syntaxis (Coward et al., 1986).

1.7 Conclusion

This chapter presents detailed geologic mapping and structural observations, combined with U-Pb Zircon geochronology, from the Nubra-Shyok Confluence area of Ladakh, NW India. Our results demonstrate that the Shyok suture zone in Ladakh comprises a Jurassic ophiolite with Cretaceous sedimentary cover. The Shyok Volcanics and Changmar Complex form the ophiolitic basement onto which Cretaceous marine sedimentary and terrestrial strata were deposited in a forearc setting proximal to the Eurasian continental margin which underwent extension in the Late Cretaceous. The forearc sequence was thrust over the Kohistan-Ladakh arc in the Eocene-Oligocene along the Khalsar thrust and other correlative thrusts in northern Pakistan. Since all other compressional structures in the Shyok suture zone postdate the Khalsar Thrust, our results suggest that the KLA-Karakoram collision along the Shyok suture zone postdates the Paleocene 52 – 55 Ma KLA-India collision along the Indus suture zone (Bouilhol et al., 2013; Jagoutz et al., 2015; Martin et al., 2020). Therefore, the geology of the Shyok suture zone is consistent with recent paleomagnetic results suggesting that the Shyok suture zone, not the Indus, records the final closure of the Neotethys Ocean and continental collision between India and Eurasia (Martin et al., 2020). While it remains unclear whether the KLA formed proximal to the Eurasian margin and rifted southward or initiated near the equator in the Neotethys Ocean, the geology of the Shyok suture zone and the paleomagnetic results from Ladakh both show the India-Eurasia collision was a multi-stage process that began with the accretion of the KLA onto India in the Paleocene and concluded with continental collision along the Shyok suture zone.

1.8 Figures and Captions

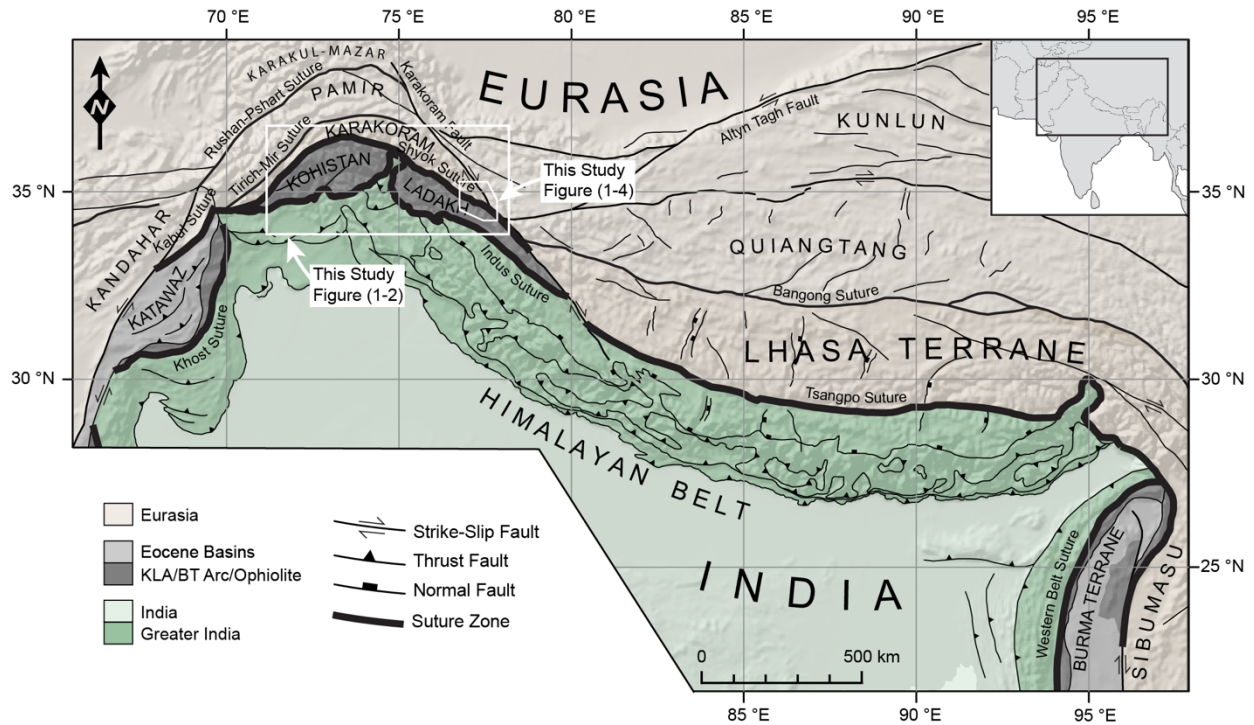


Figure 1-1: Tectonic map of the India-Eurasia collision showing India (light green), the Himalayan fold and thrust belt (dark green), intra-oceanic arc-derived terranes (grey), the major Himalayan suture zones (thick black line), and significant fault structures (thin black lines).

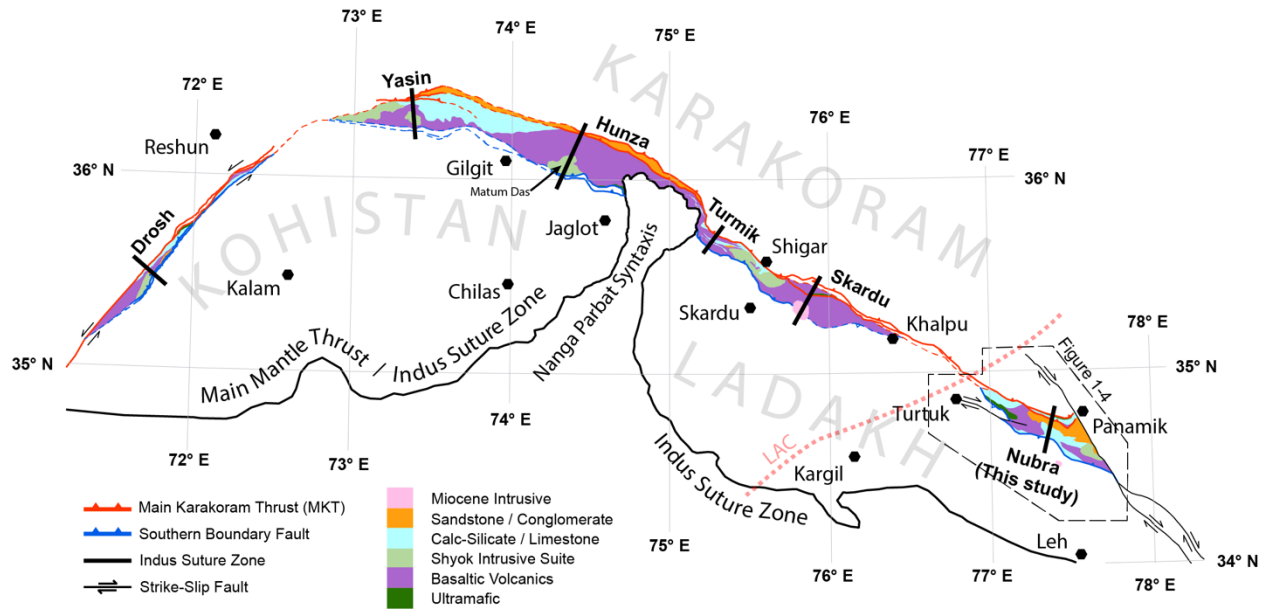


Figure 1-2: Geological map of the Shyok suture zone showing correlative structures and major lithological groupings. The Indus suture zone (ISZ) is marked using a black line, the steep north-side-up structures marking the contact between the Shyok suture zone and the Kohistan-Ladakh Arc are shown with blue lines, the Main Karakoram thrust system is shown with red lines. The locations the tectonostratigraphic columns shown in Figure 1-3 are marked on the map along with the settlement names referred to in the text.

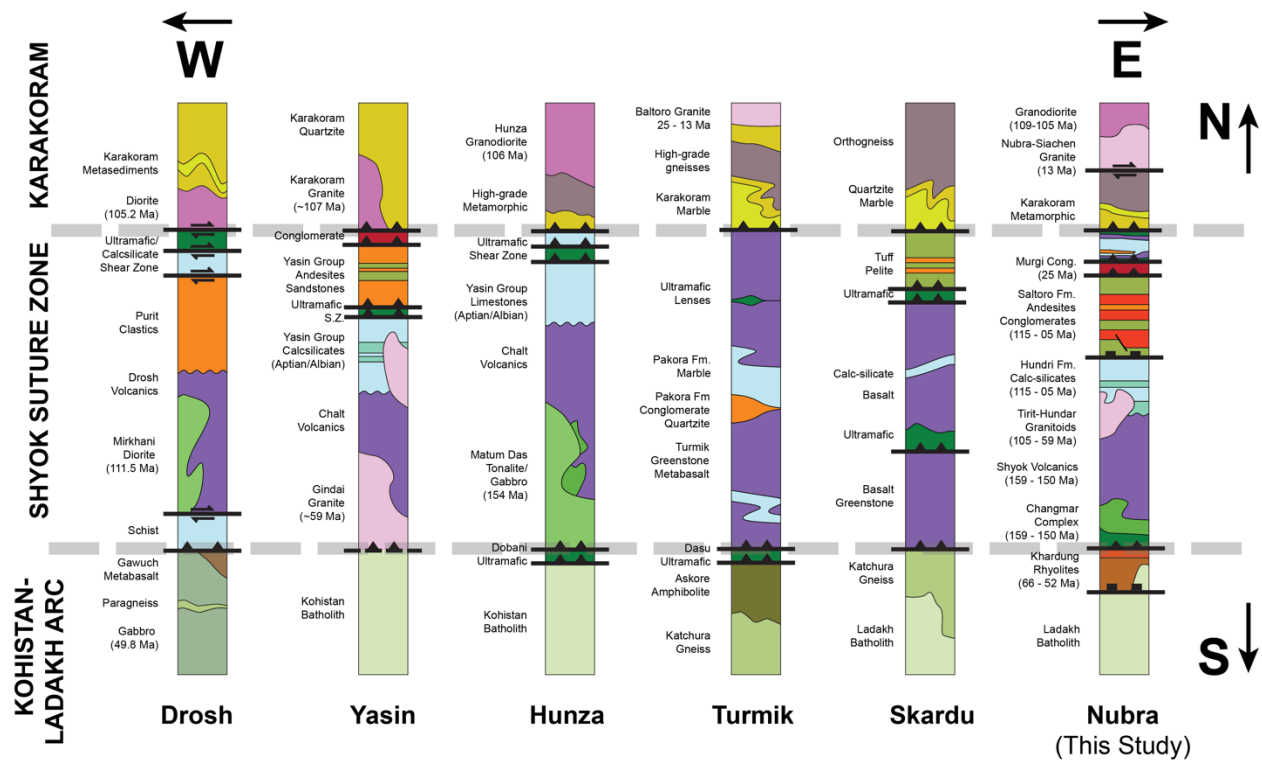


Figure 1-3: Schematic tectonostratigraphic columns detailing the major structures and lithologies in the Shyok suture zone. The columns are arranged from west to east across the page and the place names shown at the bottom of each column refer to the section lines marked in Figure 1-2. The columns are scaled such that the Shyok suture zone is the same width for effective comparison of different locations and does not reflect the actual thicknesses of any geological unit nor the true distance between structural boundaries. The faded dashed lines mark the boundaries between the Shyok suture zone lithologies and the Kohistan-Ladakh arc, and the location of the Main Karakoram thrust. Formation names, lithologies, and some significant age constraints discussed in the text are written on the left side of each column (see text for references).

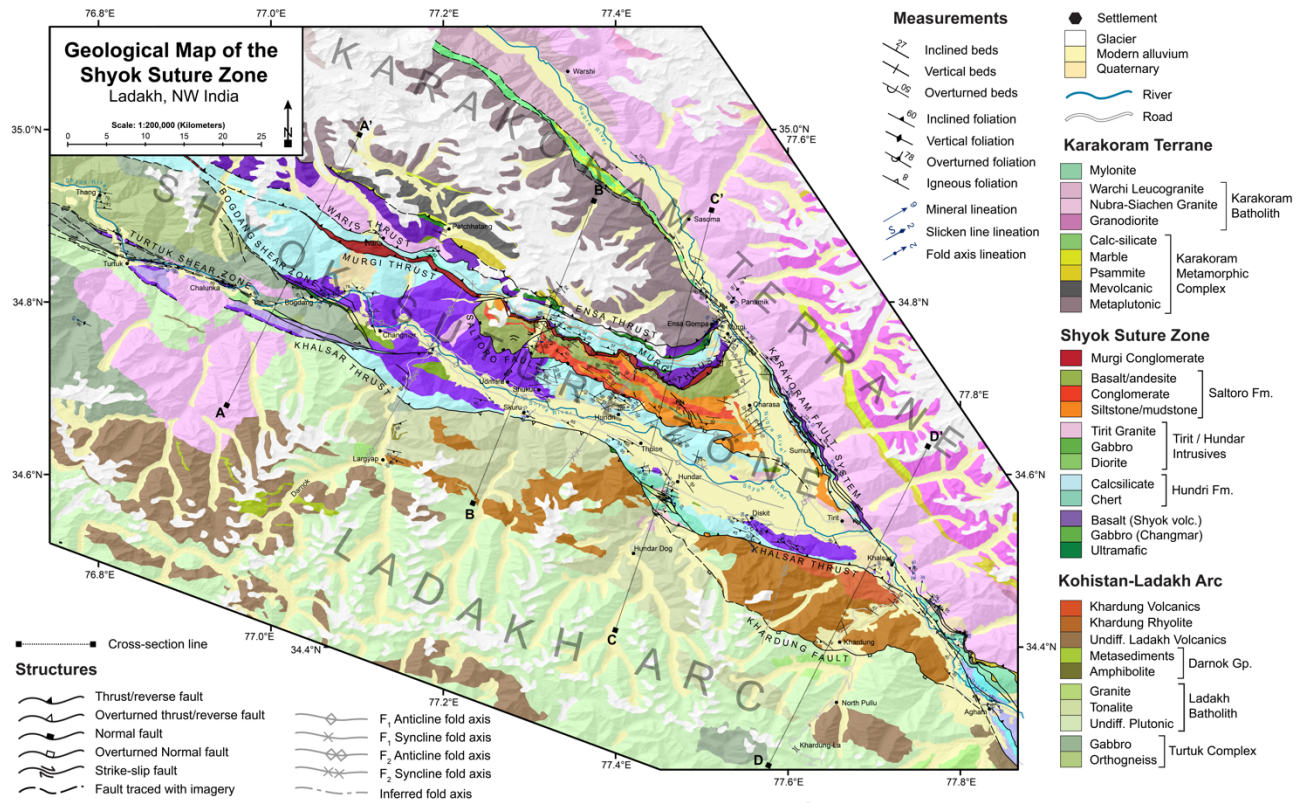


Figure 1-4: Detailed geological map of the Shyok suture zone in the Nubra-Shyok confluence area of Ladakh, NW India. The cross-sections A-A', B-B', C-C' and D-D' are shown in Figure 1-7 and a high-resolution to-scale version is included in Appendix B. Refer to the legend for the geological map units, structure symbols, and measurement symbols.

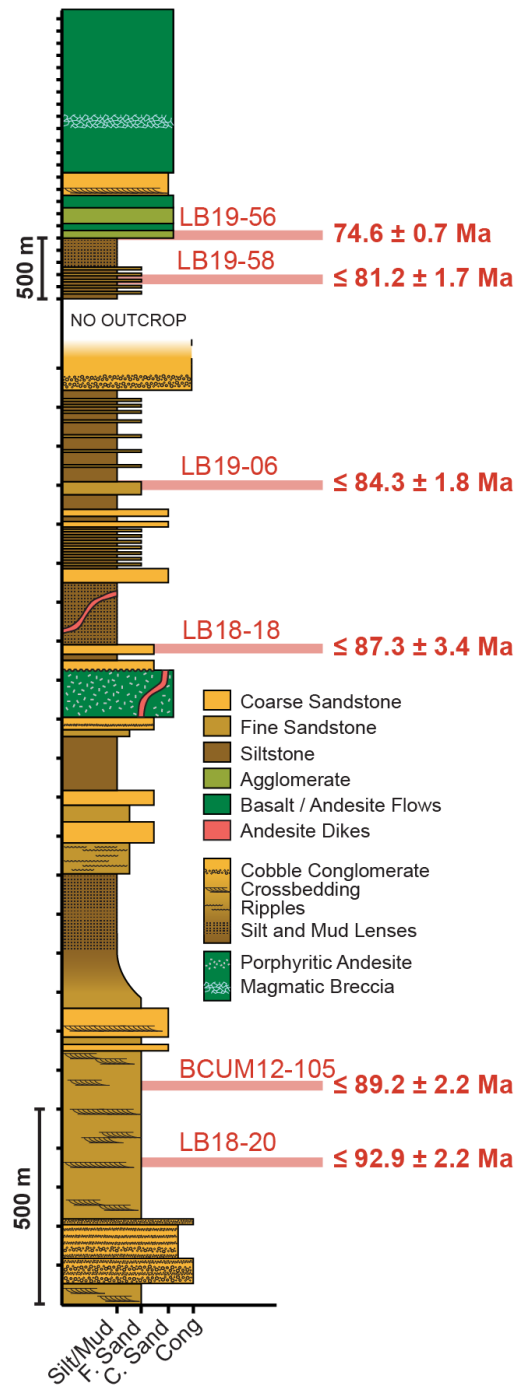


Figure 1-6: Stratigraphy of the Saltoro Formation from the exposures between Charasa and Murgi. the Y axis shows the measured vertical thickness, the X Axis shows the grain size of the sedimentary clasts. U-Pb zircon maximum depositional ages from Chapter 3 are shown in red.

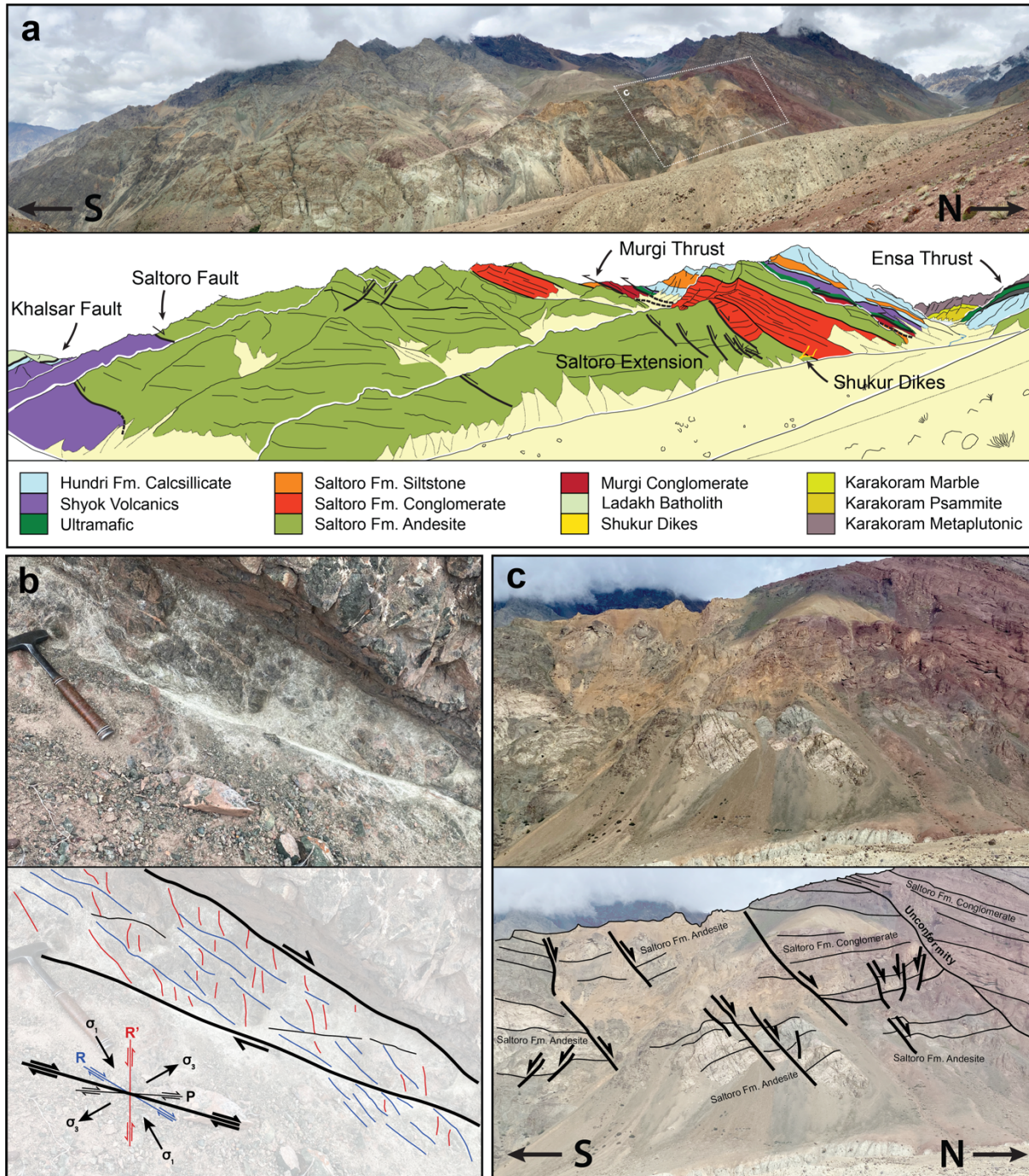


Figure 1-7: a) Panorama sketch of the Udmuru Valley showing the lower Saltoro Formation volcanics in faulted contact with the underlying Shyok Volcanics. The figure also shows the extensional faults in the Saltoro Formation, and the buttress unconformity at the base of the upper Saltoro Formation which is crosscut by the Shukur dikes. The Murgi thrust and overlying deformed repetition of the Shyok suture zone can be seen truncating the top of the Saltoro Formation to the right of the sketch. **b)** Reidel shear planes in the fault surface of a fault near the base of the Saltoro Formation in the Udmuru area. The orientation of R-type reidel shear planes is shown in blue, R'-type planes are shown in red and P-type planes are shown in black. **c)** Expanded view of the faulted

area in the lower Saltoro Formation. Saltoro Formation andesite layering and andesitic agglomerates are displaced by normal faults with 10 – 30 m displacements and are overlain by Saltoro Formation conglomerates, the normal faults do not extend above the angular unconformity.

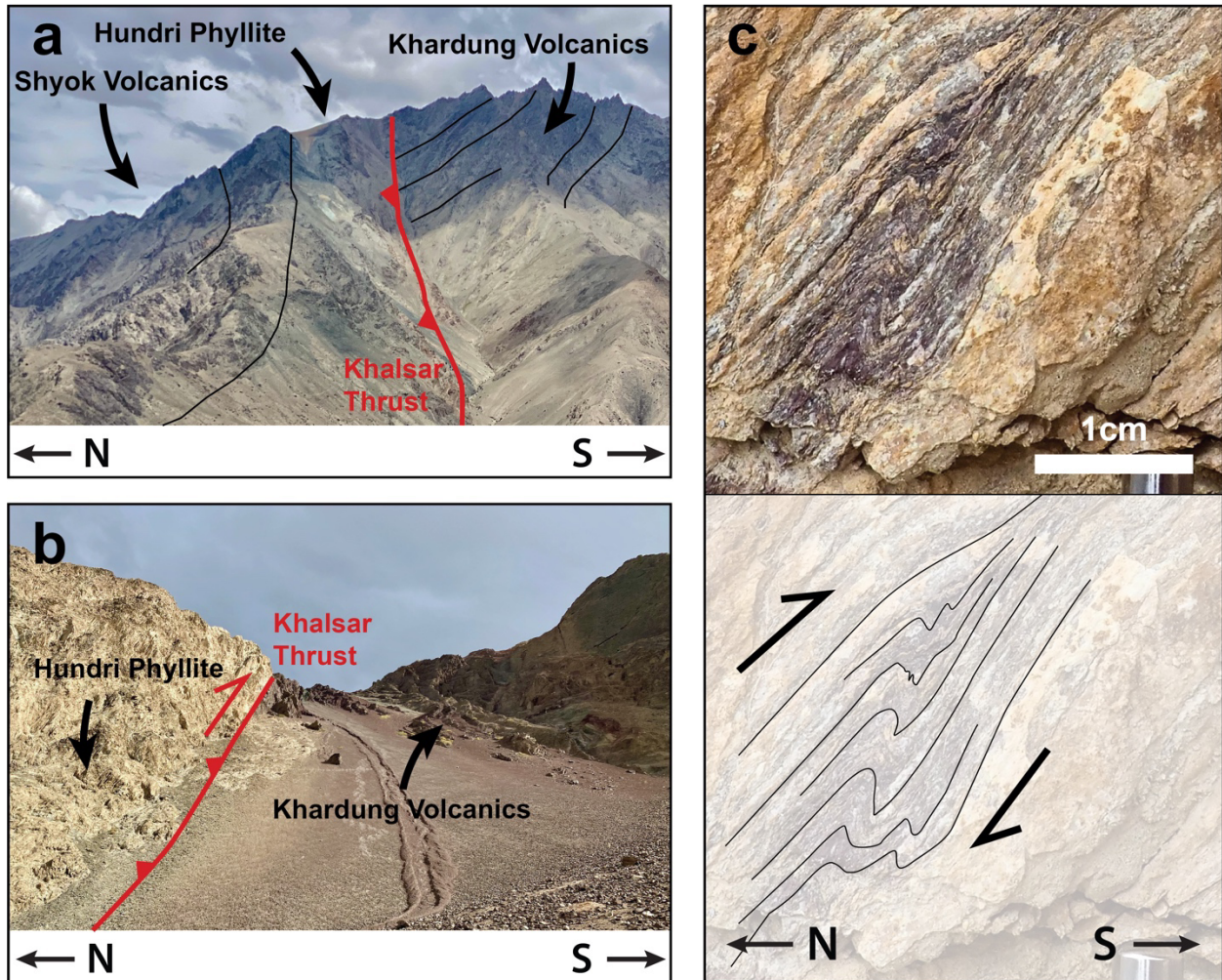


Figure 1-8: a) Exposure of Khalsar fault in the mountains south of Diskit, vertically bedded Shyok volcanics and Hundri Formation phyllites are thrust over northward inclined and unmetamorphosed Khardung volcanics stratigraphy. b) Outcrop image of Khalsar fault type locality bear Khalsar village showing Hundri Formation phyllites and calc-silicate slates thrust over Khardung volcanics tuffs and volcanogenic conglomerates. c) Asymmetrical folding in Hundri Formation phyllite from locality shown in panel B displaying top to the south shear sense.

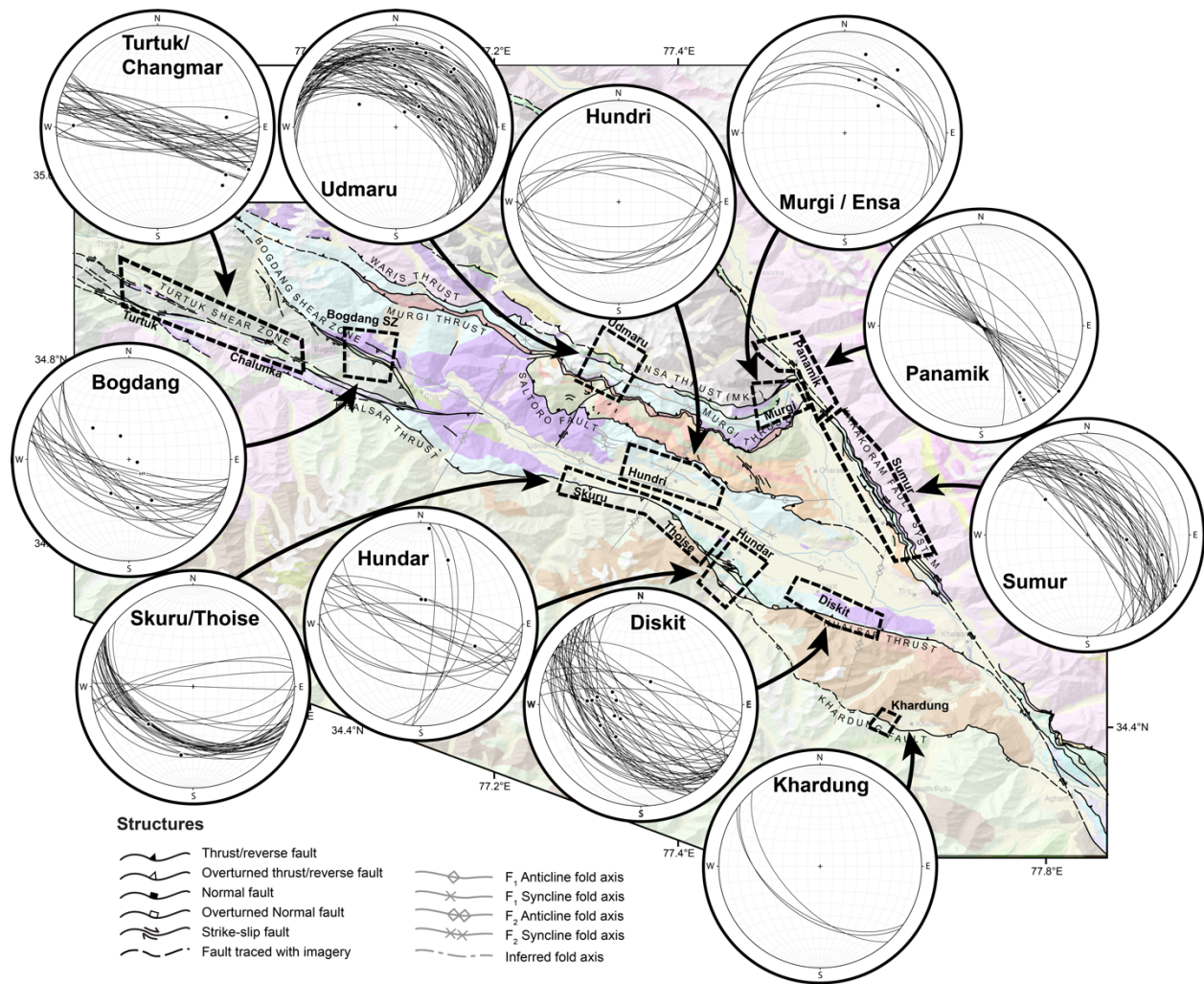


Figure 1-9: Stereographic projections of foliation and lineation data from the major structures of the Shyok Suture Zone. Each stereographic projection shows data from the corresponding area shown on the map using a dashed line. The stereonet labeled Hundri shows bedding data from the Hundri Formation and is presented to demonstrate F_1 folding.

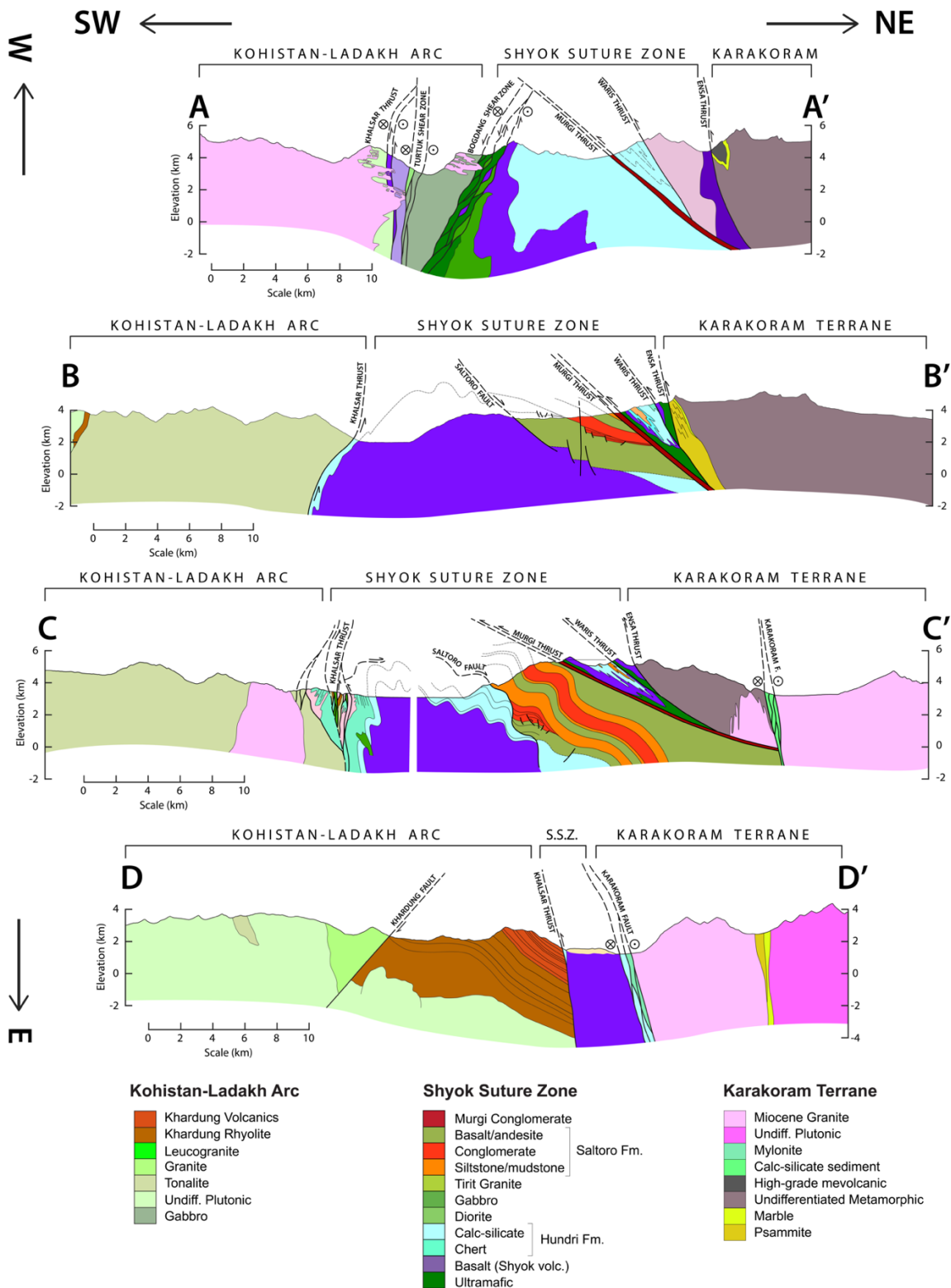


Figure 1-10: Structural cross-sections of Shyok suture zone at Bogdang, Hundar, Udmaru and Khardung. The cross-sections are ordered west to east down the page and the locations of the profile lines are shown on Figure 1-4 and Appendix B.

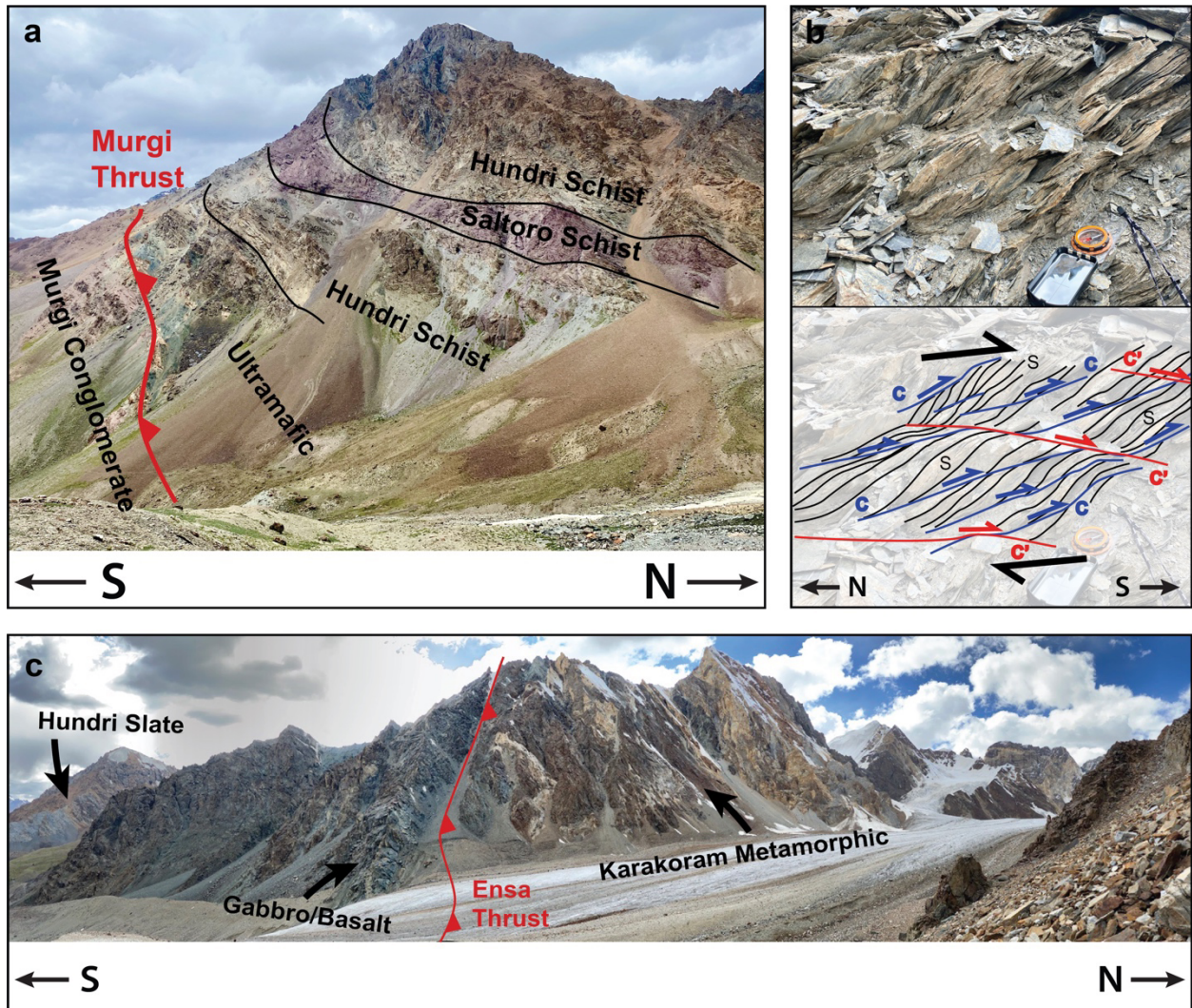


Figure 1-11: a) Sketch of Murgu thrust and overlying deformed Shyok suture zone stratigraphy. b) Sketch overlay of S-C-C' fabric in Hundri Formation phyllites and slates. The orientation of the S, C and C' planes indicate a top to the south shear sense. c) Panoramic image of Ensa thrust in the upper Udmaru valley above the Udmaru glacier. In the hanging wall (to the right of the fault) are marbles, schists and psammities of the Karakoram metamorphic complex, in the footwall, serpentinized ultramafic volcanics and gabbros from the Shyok suture zone complex.

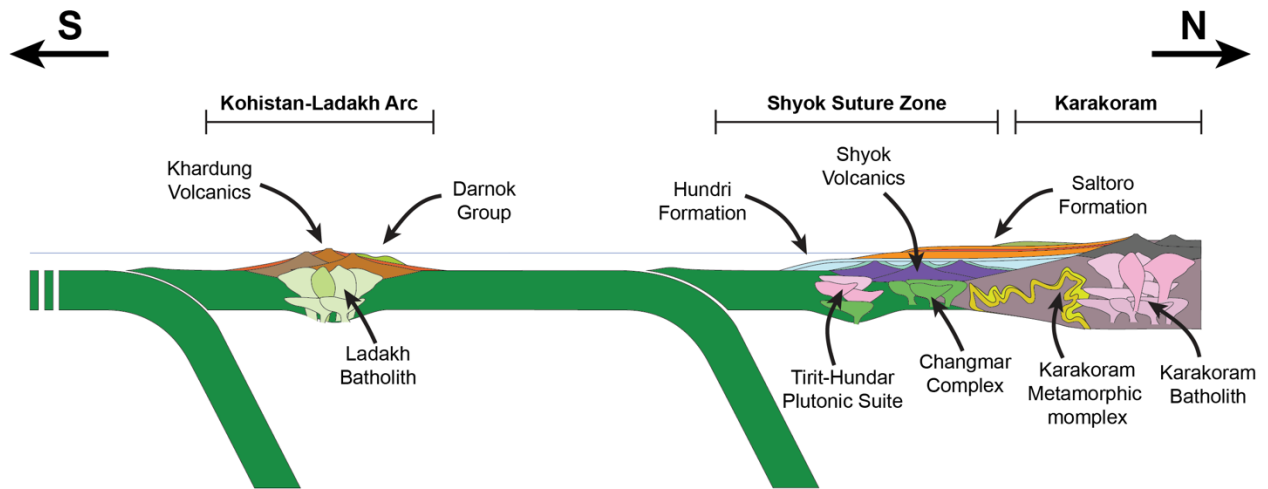


Figure 1-12: Simplified schematic representation of the 80 Ma tectonic environment along the Shyok Suture Zone (not to scale). The color scheme follows that of the geological map and cross-sections to show the terrane associations for each of the major suture zone formations.

References

- Aitchison, J.C., Ali, J.R. and Davis, A.M., 2007. When and where did India and Asia collide? *Journal of Geophysical Research: Solid Earth*, 112(B5).
- Aitchison, J.C., Davis, A.M., Liu, J., Luo, H., Malpas, J.G., McDermid, I.R., Wu, H., Ziabrev, S.V. and Zhou, M.-f., 2000. Remnants of a Cretaceous intra-oceanic subduction system within the Yarlung–Zangbo suture (southern Tibet). *Earth and Planetary Science Letters*, 183(1-2): 231-244.
- Allegre, C.J., Courtillot, V., Tapponnier, P., Hirn, A., Mattauer, M., Coulon, C., Jaeger, J.J., Achache, J., Scharer, U., Marcoux, J., Burg, J.P., Girardeau, J., Armijo, R., Gariépy, C., Gopel, C., Li, T.D., Xiao, X.C., Chang, C.F., Li, G.Q., Lin, B.Y., Teng, J.W., Wang, N.W., Chen, G.M., Han, T.L., Wang, X.B., Den, W.M., Sheng, H.B., Cao, Y.G., Zhou, J., Qiu, H.R., Bao, P.S., Wang, S.C., Wang, B.X., Zhou, Y.X. and Ronghua, X., 1984. Structure and Evolution of the Himalaya-Tibet Orogenic Belt. *Nature*, 307(5946): 17-22.
- Awais, M., Liu, X.C., Qasim, M. and Wu, F.Y., 2022. U (-Th)–Pb age and petrogenesis of Shigar leucogranites, Karakoram Metamorphic Complex, North Pakistan. *Geological Journal*, 57(10): 4052-4073.
- Bard, J., 1980. The Kohistan sequence: crust and mantle of an island arc. *Proc. Int. Committee Geodyn., Group 6 Meet.*, 13: 87-93.
- Bard, J.P., 1983. Metamorphism of an obducted island arc: example of the Kohistan sequence (Pakistan) in the Himalayan collided range. *Earth and Planetary Science Letters*, 65(1): 133-144.
- Beck, R.A., Burbank, D.W., Sercombe, W.J., Khan, A.M. and Lawrence, R.D., 1996. Late Cretaceous ophiolite obduction and Paleocene India-Asia collision in the westernmost Himalaya. *Geodinamica Acta*, 9(2-3): 114-144.
- Bhat, I.M., Ahmad, T. and Rao, D.S., 2019. The tectonic evolution of the Dras arc complex along the Indus Suture Zone, western Himalaya: Implications for the Neo-Tethys Ocean geodynamics. *Journal of Geodynamics*, 124: 52-66.
- Bhutani, R., Pande, K. and Venkatesan, T., 2009. ⁴⁰Ar–³⁹Ar dating of volcanic rocks of the Shyok suture zone in north–west trans-Himalaya: Implications for the post-collision evolution of the Shyok suture zone. *Journal of Asian Earth Sciences*, 34(2): 168-177.
- Bignold, S. and Treloar, P., 2003. Northward subduction of the Indian Plate beneath the Kohistan island arc, Pakistan Himalaya: new evidence from isotopic data. *Journal of the Geological Society*, 160(3): 377-384.
- Borneman, N.L., Hodges, K.V., Van Soest, M.C., Bohon, W., Wartho, J.A., Cronk, S.S. and Ahmad, T., 2015. Age and structure of the Shyok suture in the Ladakh region of northwestern India: Implications for slip on the Karakoram fault system. *Tectonics*, 34(10): 2011-2033.
- Bouilhol, P., Jagoutz, O., Hanchar, J.M. and Dudas, F.O., 2013. Dating the India-Eurasia collision through arc magmatic records. *Earth and Planetary Science Letters*, 366: 163-175.
- Brookfield, M. and Reynolds, P., 1981. Late Cretaceous emplacement of the Indus suture zone ophiolitic melanges and an Eocene-Oligocene magmatic arc on the northern edge of the Indian plate. *Earth and Planetary Science Letters*, 55(1): 157-162.

- Brookfield, M.E. and Reynolds, P., 1990. Miocene $^{40}\text{Ar}/^{39}\text{Ar}$ ages from the Karakorum Batholith and Shyok Melange, northern Pakistan, indicate late Tertiary uplift and southward displacement. *Tectonophysics*, 172(1-2): 155-167.
- Burg, J. P. (2018). Geology of the onshore Makran accretionary wedge: Synthesis and tectonic interpretation. *Earth-Science Reviews*, 185, 1210-1231.
- Burg, J.-P., Leyreloup, A., Girardeau, J. and Chen, G.-M., 1987. Structure and metamorphism of a tectonically thickened continental crust: the Yalu Tsangpo suture zone (Tibet). *Philosophical transactions of the Royal Society of London. Series A, Mathematical and Physical Sciences*, 321(1557): 67-86.
- Cande, S.C. and Stegman, D.R., 2011. Indian and African plate motions driven by the push force of the Reunion plume head. *Nature*, 475(7354): 47-52.
- Catlos, E.J., Pease, E.C., Dygert, N., Brookfield, M., Schwarz, W.H., Bhutani, R., Pande, K. and Schmitt, A.K., 2019. Nature, age and emplacement of the Spongtang ophiolite, Ladakh, NW India. *Journal of the Geological Society*, 176(2): 284-305.
- Chapman, J.B. and Kapp, P., 2017. Tibetan magmatism database. *Geochemistry, Geophysics, Geosystems*, 18(11): 4229-4234.
- Chapman, J.B., Robinson, A.C., Carrapa, B., Villarreal, D., Worthington, J., DeCelles, P.G., Kapp, P., Gadoev, M., Oimahmadov, I. and Gehrels, G., 2018a. Cretaceous shortening and exhumation history of the South Pamir terrane. *Lithosphere*, 10(4): 494-511.
- Chapman, J.B., Scoggin, S.H., Kapp, P., Carrapa, B., Ducea, M.N., Worthington, J., Oimahmadov, I. and Gadoev, M., 2018b. Mesozoic to Cenozoic magmatic history of the Pamir. *Earth and Planetary Science Letters*, 482: 181-192.
- Clift, P.D., Lee, J.I., Hildebrand, P., Shimizu, N., Layne, G.D., Blusztajn, J., Blum, J.D., Garzanti, E. and Khan, A.A., 2002. Nd and Pb isotope variability in the Indus River System: implications for sediment provenance and crustal heterogeneity in the Western Himalaya. *Earth and Planetary Science Letters*, 200(1-2): 91-106.
- Copley, A., Avouac, J.P. and Royer, J.Y., 2010. India-Asia collision and the Cenozoic slowdown of the Indian plate: Implications for the forces driving plate motions. *Journal of Geophysical Research: Solid Earth*, 115(B3).
- Coward, M., Butler, R., Khan, M.A. and Knipe, R., 1987. The tectonic history of Kohistan and its implications for Himalayan structure. *Journal of the Geological Society*, 144(3): 377-391.
- Coward, M.P., Rex, D.C., Asif Khan, M., Windley, B.F., Broughton, R.D., Luff, I.W., Petterson, M.G. and Pudsey, C.J., 1986. Collision tectonics in the NW Himalayas. *Geological Society, London, Special Publications*, 19(1): 203-219.
- Cronin, V. S. (1989). Kinematic model for evolution of a transtensional basin from transform fault whose initial displacement is purely strike-slip. *AAPG Bulletin (American Association of Petroleum Geologists);(USA)*, 73(CONF-8909166-).
- Debon, F., Le Fort, P., Dautel, D., Sonet, J. and Zimmermann, J., 1987. Granites of western Karakorum and northern Kohistan (Pakistan): a composite Mid-Cretaceous to upper Cenozoic magmatism. *Lithos*, 20(1): 19-40.
- DeCelles, P. G., Kapp, P., Ding, L., & Gehrels, G. E. (2007). Late Cretaceous to middle Tertiary basin evolution in the central Tibetan Plateau: Changing environments in response to tectonic partitioning, aridification, and regional elevation gain. *Geological Society of America Bulletin*, 119(5-6), 654-680.

- DeCelles, P., Kapp, P., Gehrels, G. and Ding, L., 2014. Paleocene-Eocene foreland basin evolution in the Himalaya of southern Tibet and Nepal: Implications for the age of initial India-Asia collision. *Tectonics*, 33(5): 824-849.
- DeCelles, P., Kapp, P., Quade, J. and Gehrels, G., 2011. Oligocene–Miocene Kailas basin, southwestern Tibet: Record of postcollisional upper-plate extension in the Indus-Yarlung suture zone. *Bulletin*, 123(7-8): 1337-1362.
- Desio, A., 1974. Karakorum mountains. Geological Society, London, Special Publications, 4(1): 255-266.
- Desio, A., 1977. The occurrence of blueschists between the middle Indus and the Swat Valleys as evidence of subduction (North Pakistan). *Atti della Accademia Nazionale dei Lincei. Classe di Scienze Fisiche, Matematiche e Naturali. Rendiconti*, 62: 653-661.
- Dickinson, W. and Seely, D., 1979. Structure and stratigraphy of forearc regions. *AAPG Bulletin*, 63(1): 2-31.
- Ding, L., Kapp, P. and Wan, X., 2005. Paleocene–Eocene record of ophiolite obduction and initial India-Asia collision, south central Tibet. *Tectonics*, 24(3).
- Dunlap, W.J. and Wysoczanski, R., 2002. Thermal evidence for early Cretaceous metamorphism in the Shyok suture zone and age of the Khardung volcanic rocks, Ladakh, India. *Journal of Asian Earth Sciences*, 20(5): 481-490.
- Dutta, A., Mishra, P., Absar, A., Malviya, V.P., Singh, P., Srivastava, A., Ray, B., Kumar, A. and Nitnaware, N., 2023. Tracing hydrothermal mineral thenardite in geysers/hot springs of North-western Himalayan belt, Ladakh Geothermal Province, India by hydrogeochemistry, fluid-mineral equilibria and isotopic studies. *Geochemistry*: 125973.
- Einsele, G., Liu, B., Dürr, S., Frisch, W., Liu, G., Luterbacher, H., Ratschbacher, L., Ricken, W., Wendt, J. and Wetzel, A., 1994. The Xigaze forearc basin: evolution and facies architecture (Cretaceous, Tibet). *Sedimentary Geology*, 90(1-2): 1-32.
- Frank, W., 1977. Geological observations in the Ladakh area (Himalayas). A preliminary report. *Schweiz Mineral. Petrogr. Mitt.*, 57: 89-113.
- Gaetani, M., Garzanti, E., Jadoul, F., Nicora, A., Tintori, A., Pasini, M. and Khan, K.S.A., 1990. The North Karakorum Side of the Central Asia Geopuzzle. *Geological Society of America Bulletin*, 102(1): 54-62.
- Gaetani, M., Jadoul, F., Erba, E. and Garzanti, E., 1993. Jurassic and Cretaceous Orogenic Events in the North Karakoram - Age Constraints from Sedimentary-Rocks. *Himalayan Tectonics*, 74: 39-52.
- Gansser, A., 1964. *Geology of the Himalayas*.
- Garzanti, E., Baud, A. and Mascle, G., 1987. Sedimentary Record of the Northward Flight of India and Its Collision with Eurasia (Ladakh Himalaya, India). *Geodinamica Acta*, 1(4-5): 297-312.
- Girardeau, J., Mercier, J.C. and Yougong, Z., 1985. Origin of the Xigaze ophiolite, Yarlung Zangbo suture zone, southern Tibet. *Tectonophysics*, 119(1-4): 407-433.
- Gnos, E., Immenhauser, A. and Peters, T., 1997. Late Cretaceous/early Tertiary convergence between the Indian and Arabian plates recorded in ophiolites and related sediments. *Tectonophysics*, 271(1-2): 1-19.
- He, J., Kapp, P., Chapman, J.B., DeCelles, P.G. and Carrapa, B., 2019. Structural setting and detrital zircon U–Pb geochronology of Triassic–Cenozoic strata in the eastern Central Pamir, Tajikistan. *Geological Society, London, Special Publications*, 483(1): 605-630.

- Heuberger, S., 2004. Kinematics of the Karakoram-Kohistan suture zone, chitral, NW Pakistan, ETH Zurich.
- Heuberger, S., Schaltegger, U., Burg, J.-P., Villa, I.M., Frank, M., Dawood, H., Hussain, S. and Zanchi, A., 2007. Age and isotopic constraints on magmatism along the Karakoram-Kohistan Suture Zone, NW Pakistan: Evidence for subduction and continued convergence after India-Asia collision. *Swiss Journal of Geosciences*, 100: 85-107.
- Honegger, K., Dietrich, V., Frank, W., Gansser, A., Thoni, M. and Trommsdorff, V., 1982. Magmatism and Metamorphism in the Ladakh Himalayas (the Indus-Tsangpo Suture Zone). *Earth and Planetary Science Letters*, 60(2): 253-292.
- Horton, F. and Leech, M.L., 2013. Age and origin of granites in the Karakoram shear zone and Greater Himalaya Sequence, NW India. *Lithosphere*, 5(3): 300-320.
- Houlié, N. and Phillips, R.J., 2013. Quaternary rupture behavior of the Karakoram Fault and its relation to the dynamics of the continental lithosphere, NW Himalaya–western Tibet. *Tectonophysics*, 599: 1-7.
- Hu, X.M., Garzanti, E., Moore, T. and Raffi, I., 2015. Direct stratigraphic dating of India-Asia collision onset at the Selandian (middle Paleocene, 59 +/- 1 Ma). *Geology*, 43(10): 859-862.
- Hu, X.M., Garzanti, E., Wang, J.G., Huang, W.T., An, W. and Webb, A., 2016. The timing of India-Asia collision onset - Facts, theories, controversies. *Earth-Science Reviews*, 160: 264-299.
- Jagoutz, O. and Burg, J.P., 2009. The link between the Kohistan arc granitoids and processes in the lower Kohistan arc crust. *Geochimica Et Cosmochimica Acta*, 73(13): A582-A582.
- Jagoutz, O. and Schmidt, M.W., 2012. The formation and bulk composition of modern juvenile continental crust: The Kohistan arc. *Chemical Geology*, 298: 79-96.
- Jagoutz, O., Bouilhol, P., Schaltegger, U. and Müntener, O., 2019. The isotopic evolution of the Kohistan Ladakh arc from subduction initiation to continent arc collision. *Geological Society, London, Special Publications*, 483(1): 165-182.
- Jagoutz, O., Macdonald, F.A. and Royden, L., 2016. Low-latitude arc-continent collision as a driver for global cooling. *Proceedings of the National Academy of Sciences of the United States of America*, 113(18): 4935-4940.
- Jagoutz, O., Muntener, O., Schmidt, M.W. and Burg, J.P., 2011. The roles of flux- and decompression melting and their respective fractionation lines for continental crust formation: Evidence from the Kohistan arc. *Earth and Planetary Science Letters*, 303(1-2): 25-36.
- Jagoutz, O., Muntener, O., Schmidt, M.W. and Burg, J.P., 2011. The roles of flux- and decompression melting and their respective fractionation lines for continental crust formation: Evidence from the Kohistan arc. *Earth and Planetary Science Letters*, 303(1-2): 25-36.
- Jagoutz, O., Royden, L., Holt, A.F. and Becker, T.W., 2015. Anomalously fast convergence of India and Eurasia caused by double subduction. *Nature Geoscience*, 8(6): 475-U78.
- Kaneko, Y., Katayama, I., Yamamoto, H., Misawa, K., Ishikawa, M., Rehman, H., Kausar, A. and Shiraishi, K., 2003. Timing of Himalayan ultrahigh-pressure metamorphism: Sinking rate and subduction angle of the Indian continental crust beneath Asia. *Journal of Metamorphic Geology*, 21(6): 589-599.

- Kanna, N., Gupta, S. and Prakasam, K., 2018. Micro-seismicity and seismotectonic study in Western Himalaya–Ladakh–Karakoram using local broadband seismic data. *Tectonophysics*, 726: 100-109.
- Kapp, P. and DeCelles, P.G., 2019. Mesozoic–Cenozoic geological evolution of the Himalayan–Tibetan orogen and working tectonic hypotheses. *American Journal of Science*, 319(3): 159-254.
- Khan, M.A., Stern, R.J., Gribble, R.F. and Windley, B.F., 1997. Geochemical and isotopic constraints on subduction polarity, magma sources, and palaeogeography of the Kohistan intra-oceanic arc, northern Pakistan Himalaya. *Journal of the Geological Society*, 154(6): 935-946.
- Kumar, S., Bora, S., Sharma, U.K., Yi, K. and Kim, N., 2017. Early Cretaceous subvolcanic calc-alkaline granitoid magmatism in the Nubra-Shyok valley of the Shyok Suture Zone, Ladakh Himalaya, India: Evidence from geochemistry and U–Pb SHRIMP zircon geochronology. *Lithos*, 277: 33-50.
- Lakhan, N., Singh, A.K., Singh, B.P., Sen, K., Singh, M.R., Khogenkumar, S., Singhal, S. and Oinam, G., 2020. Zircon U–Pb geochronology, mineral and whole-rock geochemistry of the Khardung volcanics, Ladakh Himalaya, India: Implications for Late Cretaceous to Palaeogene continental arc magmatism. *Geological Journal*, 55(5): 3297-3320.
- Le Fort, P. and Pecher, A., 2002. An Introduction to the geological Map of the Area between Hunza and Baltistan, Karakorum-Kohistan-Ladakh-Himalaya Region, Northern Pakistan (Scale 1: 150,000). *Geologica*, 6(1): 1-140.
- Le Fort, P., Lemennicier, Y., Lombardo, B., Pecher, A., Pertusati, P., Pognante, U. and Rolfo, F., 1995. Preliminary geological map and description of the Himalaya-Karakorum junction in Chogo Lungma to Turmik area (Baltistan, Northern Pakistan). *Journal of Nepal Geological Society*, 11: 17–38-17–38.
- Macdonald, F.A., Swanson-Hysell, N.L., Park, Y., Lisiecki, L. and Jagoutz, O., 2019. Arc-continent collisions in the tropics set Earth's climate state. *Science*, 364(6436): 181-184.
- Mahéo, G., Pêcher, A., Guillot, S., Rolland, Y., & Delacourt, C. (2004). Exhumation of Neogene gneiss domes between oblique crustal boundaries in south Karakorum (northwest Himalaya, Pakistan). *SPECIAL PAPERS-GEOLOGICAL SOCIETY OF AMERICA*, 141-154.
- Martin, C.R., Jagoutz, O., Upadhyay, R., Royden, L.H., Eddy, M.P., Bailey, E., Nichols, C.I. and Weiss, B.P., 2020. Paleocene latitude of the Kohistan–Ladakh arc indicates multistage India–Eurasia collision. *Proceedings of the National Academy of Sciences*, 117(47): 29487-29494.
- Najman, Y., Jenks, D., Godin, L., Boudagher-Fadel, M., Millar, I., Garzanti, E., Horstwood, M. and Bracciali, L., 2017. The Tethyan Himalayan detrital record shows that India-Asia terminal collision occurred by 54 Ma in the Western Himalaya. *Earth and Planetary Science Letters*, 459: 301-310.
- Parrish, R.R. and Tirrul, R., 1989. U-Pb age of the Baltoro granite, northwest Himalaya, and implications for monazite U-Pb systematics. *Geology*, 17(12): 1076-1079.
- Petterson, M. and Windley, B., 1991. Changing source regions of magmas and crustal growth in the Trans-Himalayas: evidence from the Chalt volcanics and Kohistan batholith, Kohistan, northern Pakistan. *Earth and Planetary Science Letters*, 102(3-4): 326-341.

- Petterson, M., Crawford, M. and Windley, B., 1993. Petrogenetic implications of neodymium isotope data from the Kohistan batholith, North Pakistan. *Journal of the Geological Society*, 150(1): 125-129.
- Petterson, M.G. and Treloar, P.J., 2004. Volcanostratigraphy of arc volcanic sequences in the Kohistan arc, North Pakistan: volcanism within island arc, back-arc-basin, and intra-continental tectonic settings. *Journal of Volcanology and Geothermal Research*, 130(1-2): 147-178.
- Petterson, M.G. and Windley, B.F., 1985. RbSr dating of the Kohistan arc-batholith in the Trans-Himalaya of north Pakistan, and tectonic implications. *Earth and Planetary Science Letters*, 74(1): 45-57.
- Phillips, R.J., 2008. Geological map of the Karakoram fault zone, eastern Karakoram, Ladakh, NW Himalaya. *Journal of Maps*, 4(1): 21-37.
- Phillips, R.J., Parrish, R.R. and Searle, M.P., 2004. Age constraints on ductile deformation and long-term slip rates along the Karakoram fault zone, Ladakh. *Earth and Planetary Science Letters*, 226(3-4): 305-319.
- Phillips, R.J., Searle, M.P. and Parrish, R.R., 2013. The geochemical and temporal evolution of the continental lithosphere and its relationship to continental-scale faulting: The Karakoram Fault, eastern Karakoram, NW Himalayas. *Geochemistry Geophysics Geosystems*, 14(3): 583-603.
- Pudsey, C., Coward, M., Luff, I., Shackleton, R., Windley, B. and Jan, M., 1985. Collision zone between the Kohistan arc and the Asian plate in NW Pakistan. *Earth and Environmental Science Transactions of the Royal Society of Edinburgh*, 76(4): 463-479.
- Pudsey, C.J., 1986. The Northern Suture, Pakistan: margin of a Cretaceous island arc. *Geological Magazine*, 123(4): 405-423.
- Pundir, S., Adlakha, V., Kumar, S. and Singhal, S., 2020. Closure of India–Asia collision margin along the Shyok Suture Zone in the eastern Karakoram: new geochemical and zircon U–Pb geochronological observations. *Geological Magazine*, 157(9): 1451-1472.
- Pusok, A.E. and Stegman, D.R., 2020. The convergence history of India-Eurasia records multiple subduction dynamics processes. *Science Advances*, 6(19): eaaz8681.
- Qian, Q., Hermann, J., Dong, F., Lin, L. and Sun, B., 2020. Episodic formation of Neotethyan ophiolites (Tibetan plateau): Snapshots of abrupt global plate reorganizations during major episodes of supercontinent breakup? *Earth-Science Reviews*, 203: 103144.
- Rai, H., 1982. Geological evidence against the Shyok palaeo-suture, Ladakh Himalaya. *Nature*, 297: 142-144.
- Rao, D. and Rai, H., 2009. Geochemical studies of granitoids from Shyok tectonic zone of Khardung-Panamik section, Ladakh, India. *Journal of the Geological Society of India*, 73: 553-566.
- Ravikant, V., Wu, F.-Y. and Ji, W.-Q., 2009. Zircon U–Pb and Hf isotopic constraints on petrogenesis of the Cretaceous–Tertiary granites in eastern Karakoram and Ladakh, India. *Lithos*, 110(1-4): 153-166.
- Raz, U. and Honegger, K., 1989. Magmatic and tectonic evolution of the Ladakh block from field studies. *Tectonophysics*, 161(1-2): 107-118.
- Rex, A.J., Searle, M.P., Tirrul, R., Crawford, M.B., Prior, D.J., Rex, D.C. and Barnicoat, A., 1988. The Geochemical and Tectonic Evolution of the Central Karakoram, North Pakistan. *Philosophical Transactions of the Royal Society a-Mathematical Physical and Engineering Sciences*, 326(1589): 229-255.

- Reynolds, P., Brookfield, M. and McNutt, R., 1983. The age and nature of Mesozoic-Tertiary magmatism across the Indus Suture Zone in Kashmir and Ladakh (NW India and Pakistan). *Geologische Rundschau*, 72: 981-1003.
- Robertson, A.H. and Collins, A.S., 2002. Shyok Suture Zone, N Pakistan: late Mesozoic–Tertiary evolution of a critical suture separating the oceanic Ladakh Arc from the Asian continental margin. *Journal of Asian Earth Sciences*, 20(3): 309-351.
- Robinson, A.C., 2015. Mesozoic tectonics of the Gondwanan terranes of the Pamir plateau. *Journal of Asian Earth Sciences*, 102: 170-179.
- Robinson, A.C., Ducea, M. and Lapen, T.J., 2012. Detrital zircon and isotopic constraints on the crustal architecture and tectonic evolution of the northeastern Pamir. *Tectonics*, 31(2).
- Rolfo, F., Lombardo, B., Compagnoni, R., Le Fort, P., Lemennicier, Y. and Pêcher, A., 1997. Geology and metamorphism of the Ladakh terrane and Shyok suture zone in the Chogo Lungma–Turmik area (northern Pakistan). *Geodinamica Acta*, 10(5): 251-270.
- Rolland, Y., Mahéo, G., Guillot, S., & Pêcher, A. (2001). Tectono-metamorphic evolution of the Karakorum Metamorphic complex (Dassu–Askole area, NE Pakistan): Exhumation of mid-crustal HT–MP gneisses in a convergent context. *Journal of metamorphic Geology*, 19(6), 717-737.
- Rolland, Y., Pecher, A. and Picard, C., 2000. Middle Cretaceous back-arc formation and arc evolution along the Asian margin: the Shyok Suture Zone in northern Ladakh (NW Himalaya). *Tectonophysics*, 325(1-2): 145-173.
- Rolland, Y., Picard, C., Pecher, A., Lapierre, H., Bosch, D. and Keller, F., 2002. The Cretaceous Ladakh arc of NW Himalaya—slab melting and melt–mantle interaction during fast northward drift of Indian Plate. *Chemical Geology*, 182(2-4): 139-178.
- Saktura, W.M., Buckman, S., Aitchison, J.C. and Zhou, R., 2021a. Paleogene magmatic flux and flux in the Ladakh Arc, NW Himalaya: chronostratigraphy of the Khardung Formation. *Lithos*, 388: 106053.
- Saktura, W.M., Buckman, S., Nutman, A.P. and Bennett, V.C., 2021b. Late Jurassic Changmar complex from the Shyok ophiolite, NW Himalaya: A prelude to the Ladakh arc. *Geological Magazine*, 158(2): 239-260.
- Scharer, U., Copeland, P., Harrison, T.M. and Searle, M.P., 1990. Age, Cooling History, and Origin of Postcollisional Leukogranites in the Karakoram Batholith - a Multisystem Isotope Study. *Journal of Geology*, 98(2): 233-251.
- Schmidt, M.W. and Jagoutz, O., 2017. The global systematics of primitive arc melts. *Geochemistry Geophysics Geosystems*, 18(8): 2817-2854.
- Schwab, M., Ratschbacher, L., Siebel, W., McWilliams, M., Minaev, V., Lutkov, V., Chen, F., Stanek, K., Nelson, B. and Frisch, W., 2004. Assembly of the Pamirs: Age and origin of magmatic belts from the southern Tien Shan to the southern Pamirs and their relation to Tibet. *Tectonics*, 23(4).
- Searle, M. and Rex, A., 1989. Thermal-Model for the Post-Collision Metamorphic Evolution of the Zaskar-Himalaya. *Journal of the Geological Society*, 146: 356-356.
- Searle, M., Rex, A., Tirrul, R., Rex, D., Barnicoat, A. and Windley, B., 1989. Metamorphic, magmatic, and tectonic evolution of the central Karakoram in the Biafo-Baltoro-Hushe regions of northern Pakistan.
- Searle, M., Weinberg, R. and Dunlap, W., 1998. Transpressional tectonics along the Karakoram fault zone, northern Ladakh: constraints on Tibetan extrusion. *Geological Society, London, Special Publications*, 135(1): 307-326.

- Sharma, K.K. and Gupta, K., 1978. Some observations on the geology of the Indus and Shyok valleys between Leh and Panamik, District of Ladakh, Jammu and Kashmir, India. *Recent researches in geology*, 7: 133-143.
- Singh, S., Kumar, R., Barley, M.E. and Jain, A., 2007. SHRIMP U–Pb ages and depth of emplacement of Ladakh Batholith, Eastern Ladakh, India. *Journal of Asian Earth Sciences*, 30(3-4): 490-503.
- Srimal, N., 1986. India-Asia collision: implications from the geology of the eastern Karakoram. *Geology*, 14(6): 523-527.
- Srimal, N., Basu, A.R. and Kyser, T.K., 1987. Tectonic inferences from oxygen isotopes in volcano-plutonic complexes of the India-Asia Collision Zone, NW India. *Tectonics*, 6(3): 261-273.
- Tahirkheli, R.K., 1979. Geology of Kohistan and adjoining Eurasian and Indo-Pakistan continents, Pakistan. *Geol. Bull. Univ. Peshawar*, 11(1): 1-30.
- Thakur, V. and Misra, D., 1984. Tectonic framework of the Indus and Shyok suture zones in eastern Ladakh, northwest Himalaya. *Tectonophysics*, 101(3-4): 207-220.
- Thakur, V., 1981. Regional framework and geodynamic evolution of the Indus-Tsangpo suture zone in the Ladakh Himalayas. *Earth and Environmental Science Transactions of The Royal Society of Edinburgh*, 72(2): 89-97.
- Thakur, V.C., 1990. Indus Tsangpo suture zone in Ladakh—its tectonostratigraphy and tectonics. *Proceedings of the Indian Academy of Sciences-Earth and Planetary Sciences*, 99: 169-185.
- Treloar, P. J., & Coward, M. P. (1991). Indian Plate motion and shape: constraints on the geometry of the Himalayan orogen. *Tectonophysics*, 191(3-4), 189-198.
- Treloar, P.J. and Izatt, C.N., 1993. Tectonics of the Himalayan collision between the Indian plate and the Afghan block: A synthesis. Geological Society, London, Special Publications, 74(1): 69-87.
- Treloar, P.J., Rex, D., Guise, P., Coward, M., Searle, M., Windley, B., Petterson, M., Jan, M. and Luff, I., 1989. K-Ar and Ar-Ar geochronology of the Himalayan collision in NW Pakistan: Constraints on the timing of suturing, deformation, metamorphism and uplift. *Tectonics*, 8(4): 881-909.
- Upadhyay, R., 2003. Earthquake-induced soft-sediment deformation in the lower Shyok River valley, northern Ladakh, India. *Journal of Asian Earth Sciences*, 21(4): 413-421.
- Upadhyay, R., 2003. Earthquake-induced soft-sediment deformation in the lower Shyok River valley, northern Ladakh, India. *Journal of Asian Earth Sciences*, 21(4): 413-421.
- Upadhyay, R., 2008. Implications of U–Pb zircon age of the Tirit granitoids on the closure of the Shyok suture zone, northern Ladakh, India. *Current science*: 1635-1640.
- Upadhyay, R., 2014. Palaeogeographic significance of Yasin-type rudist and orbitolinid fauna of the Shyok Suture Zone, Saltoro Hills, northern Ladakh, India. *Current Science*: 223-228.
- Upadhyay, R., Sinha, A.K., Chandra, R. and Rai, H., 1999. Tectonic and magmatic evolution of the eastern Karakoram, India. *Geodinamica Acta*, 12(6): 341-358.
- Valli, F., Arnaud, N., Leloup, P.H., Sobel, E.R., Maheo, G., Lacassin, R., Guillot, S., Li, H., Tapponnier, P. and Xu, Z., 2007. Twenty million years of continuous deformation along the Karakorum fault, western Tibet: A thermochronological analysis. *Tectonics*, 26(4).
- Van Buer, N.J., Jagoutz, O., Upadhyay, R. and Guillong, M., 2015. Mid-crustal detachment beneath western Tibet exhumed where conjugate Karakoram and Longmu-Gozha Co faults intersect. *Earth and Planetary Science Letters*, 413: 144-157.

- Wadia, D., 1937. The Cretaceous volcanic series of Astor-Deosai, Kashmir and its intrusions. *Rec. Geol. Surv. India*, 72(2): 151-161.
- Weinberg, R.F. and Dunlap, W.J., 2000. Growth and deformation of the Ladakh batholith, northwest Himalayas: Implications for timing of continental collision and origin of calc-alkaline batholiths. *Journal of Geology*, 108(3): 303-320.
- Westerweel, J., Roperch, P., Licht, A., Dupont-Nivet, G., Win, Z., Poblete, F., Ruffet, G., Swe, H.H., Thi, M.K. and Aung, D.W., 2019. Burma Terrane part of the Trans-Tethyan arc during collision with India according to palaeomagnetic data. *Nature Geoscience*, 12(10): 863-868.
- Wu, F.-Y., Ji, W.-Q., Wang, J.-G., Liu, C.-Z., Chung, S.-L. and Clift, P.D., 2014. Zircon U–Pb and Hf isotopic constraints on the onset time of India-Asia collision. *American Journal of Science*, 314(2): 548-579.
- Xue, W., Hu, X., Garzanti, E., Ma, A., Lai, W. and Li, C., 2022. Discriminating Qiangtang, Lhasa, and Himalayan sediment sources in the Tibetan Plateau by detrital-zircon UPb age and Hf isotope facies. *Earth-Science Reviews*: 104271.
- Yin, A. and Harrison, T.M., 2000. Geologic evolution of the Himalayan-Tibetan orogen. *Annual review of earth and planetary sciences*, 28(1): 211-280.
- Yin, A., Harrison, T.M., Murphy, M., Grove, M., Nie, S., Ryerson, F., Xiao Feng, W. and Zeng Le, C., 1999. Tertiary deformation history of southeastern and southwestern Tibet during the Indo-Asian collision. *Geological Society of America Bulletin*, 111(11): 1644-1664.
- Zanchi, A., Poli, S., Fumagalli, P. and Gaetani, M., 2000. Mantle exhumation along the Tirich Mir Fault Zone, NW Pakistan: pre-mid-Cretaceous accretion of the Karakoram terrane to the Asian margin. *Geological Society, London, Special Publications*, 170(1): 237-252.
- Zhou, R., Aitchison, J.C., Lokho, K., Sobel, E.R., Feng, Y. and Zhao, J.-x., 2020. Unroofing the Ladakh Batholith: constraints from autochthonous molasse of the Indus Basin, NW Himalaya. *Journal of the Geological Society*, 177(4): 818-825.

Chapter Two

Geochronology and Geochemistry

2.1 Abstract

The age of collision between the Kohistan Ladakh arc (KLA) and Karakoram terranes along the Shyok suture zone is a fundamental uncertainty that prevents consensus on tectonic models for the India-Eurasia collision. This study presents U-Pb zircon geochronology and whole rock major and trace element geochemistry analyses that constrain the age of significant tectonostratigraphic units of the suture zone and provide important information about the tectonic setting in which they formed. This study also provides constraints on the age of each of the significant fault structures in the suture zone, providing the basis for the tectonic-temporal reconstruction of the collision between the KLA and Eurasia, discussed in Chapter 1. The geochronology results show that the Shyok suture zone comprises a Jurassic ophiolite overlain by Cretaceous forearc basin strata with Eurasian provenance. The results also constrain the age of a suite of magmatic bodies intruding on the forearc sequence and the timing of the significant structural boundaries in the suture zone. These findings support multi-stage India-Eurasia collision models because they suggest that KLA-Eurasia collision post-dates collision along the Indus suture zone.

2.2 Introduction

Determining the age of the KLA-Eurasia collision requires robust age constraints for the primary lithologic units and major fault structures of the Shyok suture zone. Previous research has yielded conflicting interpretations of whether the Shyok suture zone complex (including the Changmar Ophiolite, Shyok Volcanics, Hundri Formation, and Saltoro Formation) formed in a forearc setting on the southern Eurasian margin (Saktura, 2021; Thanh, 2012), or in a back-arc environment in association with the KLA (Borneman et al., 2015; Rolland et al., 2000). Distinguishing between these tectonic interpretations and constraining the timeframe over which the sedimentary and volcanic units of the suture zone were formed is crucial to understanding the tectonic development of the KLA-Karakoram collision and the Cretaceous-Eocene tectonics of the Neotethys Ocean.

In this Chapter, we present U-Pb zircon geochronology and whole rock major and trace element geochemistry analyses, which constrain the tectonic setting of the Shyok suture zone complex. These results suggest that the Shyok suture zone comprises a forearc ophiolite and forearc basin sedimentary sequence that developed on the southern margin of Eurasia between the Jurassic and the Paleocene. The Eurasia-derived Saltoro and Hundri Formations were deposited in the mid to late-Cretaceous (115 – 75 Ma) on a Jurassic (159 – 151 Ma) ophiolite basement comprising ultramafic rocks and tholeiitic basalts. The Saltoro Formation strata are interlayered with arc-related calc-alkaline andesite volcanics, suggesting they were deposited in an active arc setting, proximal to subduction-related volcanism. Our results also provide constraints on the age of the structures separating Eurasian and KLA-related lithologies in the Shyok suture zone, representing a younger bound on the age of the KLA-Eurasia collision. The oldest fault structure in the Shyok suture zone in Ladakh comprises syn-sedimentary normal faults in the lower levels

of the Saltoro Formation. Our results constrain these structures to the Late Cretaceous between 93 Ma and 85 Ma. The age of the tectonic boundary between the Eurasian forearc and the KLA batholith (the Khalsar Fault) is 52 – 25 Ma, and all the other major thrust structures in the suture zone are post-Oligocene or Miocene age, suggesting that the Shyok suture zone closed after the Indus suture zone, and therefore records final India-Eurasia continental collision in the western Himalaya.

2.3 Methods

2.3.1 Geochronology

To extract zircons for U-Pb geochronology, rock samples collected during fieldwork were disaggregated by manual sledging, pulverized using a Shatterbox, and sieved into monomineralic, sand-sized particles. Magnetic and density separation techniques were used to obtain dense mineral concentrates from which zircon grains were randomly sampled and mounted in epoxy resin with natural reference standards FC1, R33, SLF, 91500, and GHR-1, and polished to expose the interiors of the grains. Zircons were imaged using backscattered electron (BSE) and cathodoluminescence (CL) using a scanning electron microscope (SEM) at MIT and the University of Maine. Using imagery to guide spot targeting, we dated samples with laser ablation inductively coupled plasma mass spectrometry (LA-ICPMS) at the Arizona Laserchron Center (ALC), the University of Florida, Rutgers University, and the University of Maine. Details of measurement protocols at the ALC are presented in Pullen et al. (2018), and protocols at the University of Florida are presented in Mueller et al. (2008). Data reduction was completed at Rutgers University and the University of Maine using the Iolite software package (Paton et al., 2011), at the University of Florida using in-house software (Calamari), and at the ALC using the AgeCalcML software package (Sundell et al., 2021). To minimize the chance of age underestimation due to lead loss (Vermeesch, 2021), we filtered our data using a 5% discordance cutoff and only included analyses with $^{204}\text{Pb}/^{206}\text{Pb} < 0.001$. The discordance filter used the discordance between the $^{206}\text{Pb}/^{238}\text{U}$ age and $^{207}\text{Pb}/^{235}\text{U}$ age for zircons with $^{206}\text{Pb}/^{238}\text{U}$ ages less than 1000 Ma, and the discordance between the $^{206}\text{Pb}/^{238}\text{U}$ age and $^{206}\text{Pb}/^{207}\text{Pb}$ age for zircons with $^{206}\text{Pb}/^{238}\text{U}$ ages greater than 1000 Ma. Concordia diagrams and detrital zircon spectra were produced using the AgeCalcML software package (Sundell et al., 2021).

2.3.2 Geochemistry

Block samples of volcanic rocks from the Shyok Volcanics and Saltoro Formations were collected in the field, and minimally altered samples were selected for whole-rock x-ray fluorescence (XRF) major element analysis at the Hamilton Analytical Laboratory (HAL). Samples were chipped in a hardened steel chipmunk, sub-sampled with a line pour, and ground to a very fine powder in a Rocklabs tungsten carbide or alumina ring mill. The powder was weighed with a Li-tetraborate only flux (Merck Spectromelt A-10) in the proportion of 1 part rock to 2 parts flux. Rock powder and flux were blended using a vortex mixer and fused in custom-machined graphite (Mersen grade UF-4S) crucibles at 1000 °C in an electronically controlled muffle furnace. The fused pellets were cleaned of residual carbon, and then reground to a fine powder in a WC ring mill and fused again at 1000 °C. The doubly fused pellets were lapped flat in four stages with progressively finer diamond laps to a surface finish of 15 microns before analysis using ultrasound in ethanol. Sample pellets were analyzed using a Thermo ARL Perform'X x-ray fluorescence spectrometer using a 45 kV accelerating voltage at 45 mA.

2.4 Results

2.4.1 U-Pb Zircon Geochronology

Maximum depositional ages and detrital zircon spectra were obtained from twelve sedimentary and metasedimentary samples, and crystallization ages were obtained from fifteen igneous samples in the Shyok suture zone (see Figure 2-1). We report maximum depositional ages for sedimentary samples determined using the $^{206}\text{Pb}/^{238}\text{U}$ age and 2-sigma uncertainty (95% confidence) of the youngest single zircon (YSG) analysis that passed the filtering criteria. For igneous samples, we report the weighted mean of $^{206}\text{Pb}/^{238}\text{U}$ dates from the youngest population of zircons in the sample that passed our filtration criteria. In brackets alongside each weighted mean age, we also report the mean square weighted deviation (MSWD) and the number of analyses (N) included in the mean (Wendt and Carl, 1991). Some igneous samples yielded analyses spanning a broad range of dates (i.e., multiple populations of inherited grains). To ensure that the reported age is as close as possible to the final crystallization age of the rock and that uncertainties are not artificially reduced by including zircons unrelated to the sample population (Spencer et al., 2016), the ages were determined using the youngest zircons in the sample, such that the MSWD was as close as possible to MSWD = 1.

2.4.1.1 Detrital Zircon Geochronology

Hundri Formation: Four samples were analyzed from Hundri Formation (see Figure 2-2), two from the type-section of the Hundri Formation near Hundri village, a calcareous sandstone (LB19-20) and a phyllite (LB19-16), One from the chert and quartzites at Hundar (LB19-35) and one from the deformed stratigraphy above the Murgi Thrust (LB19-55). Sample LB19-20 yielded a Cretaceous maximum depositional age of $\leq 103.8 \pm 2.8$ Ma, and sample LB19-16 yielded a

Cretaceous maximum depositional age of $\leq 115.9 \pm 2$ Ma. Each of these samples contained detrital zircons with complex age distributions spanning the mid-Cretaceous to the Mesoarchean with prominent peaks at 130 Ma, 150 – 155 Ma, 200 – 210 Ma, and 1140 – 1200 Ma. There was an absence of ages between 210 Ma and 410 Ma in sample LB19-20, while LB19-16 contained these ages. However, this absence could be due to the acceptance of fewer analyses from LB19-20 by our filtering procedure.

A sample of very fine-grained quartzite (LB19-35) from south of Hundar village was analyzed for comparison with the Hundri Formation. The quartzite is intruded by the 67.3 ± 0.7 Ma (U-Pb Zircon) granite body at Hundar bridge (Kumar et al., 2017), and both the quartzite and the granite are crosscut by strands of the Khalsar fault system. Sample LB19-35 yielded a Cretaceous maximum depositional age of $\leq 102.7 \pm 1.9$ Ma and contained detrital zircons with complex age distributions very similar to those from Hundri Formation samples LB19-20 and LB19-16. The Hundar quartzite contains detrital zircons spanning the mid-Cretaceous to the Mesoarchean with major peaks at 130 Ma, 150 – 155 Ma, 200 – 210 Ma, and 1140 – 1200 Ma.

A grey calcareous slate (LB22-55) from the heavily sheared meta-sediments from the deformed zone above the Murgi Thrust yielded a Cretaceous maximum depositional age of $\leq 100.7 \pm 5.5$ Ma. LB19-55 contained detrital zircons with complex age distributions with broad peaks around 150 – 170 Ma, 220 – 250 Ma, 860 – 980 Ma, 1810 – 1980 Ma, and 2410 – 2990 Ma.

Saltoro Formation: Two samples of heavily sheared Saltoro Formation sediments from the deformed zone above the Murgi Thrust were analyzed (see Figure 2-3). A red slate from the Udmaru valley (LB22-53) yielded a Cretaceous maximum depositional age of $\leq 79 \pm 1.1$ Ma. Near Murgi village in the Nubra valley, a sample of chlorite-mica schist containing rounded quartz

granules (LB19-13) yielded a Late Cretaceous maximum depositional age of $\leq 79.7 \pm 1.1$ Ma. Samples LB19-53 contained detrital zircons with a complex age distribution. There are too few analyses from LB19-53 to resolve well-defined peaks. Sample LB19-13 was dominated by an age peak at 83 – 85 Ma and a small subsidiary peak at 98 – 100 Ma. It yielded nine > 100 Ma zircons, including Jurassic, Devonian, and Proterozoic grains.

Murgi Conglomerate: Sample LB09-20.12 was collected from sheared polymictic conglomerate from the Murgi Formation, where it is exposed fault-bound by the Murgi Thrust in the Nubra valley (see Figure 2-4). Sample LB09-20.12 yielded a Late Oligocene maximum depositional age of $\leq 25.9 \pm 1.5$ Ma and contained detrital zircons spanning from the Oligocene to the Paleoproterozoic with a pronounced age peak between 150 and 170 Ma and a lesser peak at 440 – 540 Ma (Bouilhol and Jagoutz, 2014).

Karakoram Fault Quartzite: Sample LB18-12 was collected from a boudinaged quartzite horizon in phyllite from the Karakoram Shear Zone on the western bank of the Nubra valley north of Panamik bridge (see Figure 2-5). It yielded a Miocene maximum depositional age of $\leq 13.6 \pm 0.5$ Ma. The sample contained 20 concordant zircon grains with ages < 180 Ma, with a cluster of grains at 100 – 105 Ma and four zircons dated to between 400 – 500 Ma. There were abundant zircons between 500 – 1150 Ma that defined a broad multiphase spectrum, and also abundant Proterozoic and Archean zircons with a small peak in the age distribution at 2440 – 2520 Ma.

2.4.1.2 Igneous Zircon Geochronology

Shyok Volcanics: Two samples were dated from the Shyok Volcanics, samples LB19-22 and LB19-55 (see Figure 2-6). Sample LB19-22 was collected from a volcanoclastic horizon interbedded with limestones and basalt flows immediately below the unconformity between the Shyok Volcanics and the Hundri Formation in the Shukur valley and yielded a Late Jurassic age of 152.1 ± 1.2 Ma (MSWD = 0.93, N = 18). Sample LB19-55 was obtained from a highly sheared rhyolite interlayered with mylonitized mafic volcanics in the Ensa Thrust zone in the Nubra valley near Ensa Monastery. It yielded an age of 150.6 ± 2 Ma (MSWD = 0.16, N = 2).

Turtuk Amphibolite: Sample LB22-32 is from a felsic leucosome in the banded amphibolite gneiss at the roadside east of Turtuk village (see Figure 2-7), it yielded a weighted mean age of 147.0 ± 3.7 Ma (MSWD = 1.02, N = 5).

Khardung Volcanics: Sample LB19-60 is derived from rhyolitic volcanics intruded by the Ladakh batholith near Darnok (see Figure 2-8). It yielded a weighted mean age of 66.7 ± 0.3 Ma (MSWD = 1.14, N = 18).

Nubra-Siachen Granites: Two samples from the Nubra-Siachen granites were analyzed (see Figure 2-9). Sample LB18-09 was taken from an orthoclase-porphyritic granite that is exposed over a large area of the Nubra valley north of Panamik and is faulted against the Shyok suture zone by the Karakoram fault. It yielded a Miocene weighted mean age of 14.5 ± 0.1 Ma (MSWD = 0.6353, N = 6). Sample LB18-08 was collected from a garnet-bearing leucogranite pluton that

intrudes the Panamik porphyritic granite in the upper Nubra valley at Warshi, it yielded a Miocene weighted mean age of 13.46 ± 0.11 Ma (MSWD = 1.1651, N = 4).

Tirit-Hundar Intrusive Suite: Two samples from the Tirit-Hundar plutonic suite were analyzed (LB1821 and LB19-38) (see Figure 2-10). In the Diskit-Hundar area, sample LB18-21 is from a small diorite body that intrudes Hundri Formation cherts and quartzite; it yielded an age of 59.1 ± 0.2 Ma (MSWD = 0.96, N = 35). Sample LB19-38 is from a granite that intruded and assimilated Khardung Formation rhyolites; it was collected from a fault-bound slice within the Khalsar Fault zone in the Hundar valley and yielded a weighted mean age of 66.0 ± 0.2 Ma (MSWD = 1.01, N = 28).

Ladakh Batholith: Two samples were analyzed from plutonic bodies of the Ladakh batholith (LB19-27 and LB22-26) (see Figure 2-11). Sample LB19-27 is derived from a Ladakh batholith tonalite crosscut by the Khalsar fault in the Skuru valley; it yielded a weighted mean age of 65.6 ± 0.3 Ma (MSWD = 0.97, N = 12). In the Turtuk area, sample LB22-26 is from a deformed granodiorite that intrudes amphibolite and is crosscut by the Turtuk Shear Zone; it yielded an age of 121.5 ± 3.7 Ma (MSWD = 0.94, N = 4).

Hundar and Bogdang Leucogranites: The Hundar valley contains a garnet-calcite-bearing leucogranite that intrudes the Ladakh batholith tonalities. This body yielded a dominant age population with a weighted mean age of 61.8 ± 0.2 Ma (MSWD = 1.01, N = 18), comparable to the Khardung Volcanics and Ladakh batholith tonalite into which it intrudes but also contained a single zircon with a 27.1 ± 0.7 Ma core and a 15.4 ± 0.2 Ma rim. It is most likely that this young

grain represents the true crystallization age (see Figure 2-12). It could also be a contaminant derived from LB18-08, which contains abundant 13 – 24 Ma grains and was mounted on the same epoxy mount. The deformation related to the Bogdang Shear Zone and the Khalsar fault is crosscut by an undeformed granite/tonalite at Chalunka (LB11-O-35), which yielded an age of 24.3 ± 0.6 Ma. This granite is crosscut by garnet-bearing leucogranite dikes that were dated to 25.1 ± 1.3 Ma, overlapping within uncertainty (Jagoutz et al., 2019).

Shukur Dikes: We also dated two rhyolitic dikes that crosscut the Hundri Formation east of Hundri village (LB18-33) and in the Shukur valley (LB19-24). These yielded weighted mean ages of 84.4 ± 0.9 Ma (MSWD = 0.79, N = 3) and 81.8 ± 0.5 Ma (MSWD = 1.00, N = 9), respectively (see Figure 2-13).

2.4.2 Geochemistry

Whole rock major element compositions and trace element data were obtained for 16 samples using XRF. These included four samples collected from throughout the Shyok Volcanics (LB18-41, LB19-25, LB19-53, and LB18-34), seven samples from the Saltoro Volcanics (LB18-16, LB19-01, LB19-14, LB19-50, LB19-52, LB19-54, and LB19-56), and five from felsic dikes observed crosscutting the Hundri Formation, Shyok Volcanics, and Saltoro Formation (LB18-33, LB19-21, LB19-24, LB19-04, and LB19-57). The whole rock major element data are presented along with the available published data from the Shyok Volcanics (Rolland et al., 2000; Saktura et al., 2021b; Sivaprabha et al., 2022; Thanh et al., 2012) in Figures 2-14, Figure 2-15 and Figure 2-16.

Three of the Shyok Volcanics samples were of basaltic composition with SiO₂ concentrations between 46.83 wt.% and 52.37 wt.%, and total alkalis (Na₂O + K₂O) between 3.15 wt.% and 4.87 wt.%, while one sample (LB19-25) is a trachy-andesite composition with a SiO₂ content of 57.33 wt.% and 8.16 wt.% total alkali (see Figure 2-14). All Shyok Volcanics samples are characterized by TiO₂ concentrations of 0.55 – 1.06 wt.%, Al₂O₃ between 11.66 – 15.75 wt.%, FeO between 6.32 – 14.30 wt.%, MnO between 0.07 – 0.16 wt.%, low K₂O concentrations between 0.06 – 0.18 wt.%, and low P₂O₅ between 0.06 – 0.12 wt.%. Three samples had MgO concentrations between 4.87 – 7.75 wt.% and Na₂O concentrations of 2.97 – 4.78 wt.%, while the more silicic sample (LB19-25) had a lower MgO concentration of 1.01 wt. % and higher Na₂O concentration of 8.10 wt.%. Most of the Shyok Volcanics samples had CaO concentrations ranging between 2.96 wt.% and 6.68 wt.% except sample LB18-34 which had a much higher CaO concentration of 14.55 wt.%. Sample LB18-34 was the least silicic of the sample and was derived from pillow basalts at the base of the Shyok Volcanics. The Shyok Volcanics had XMg (molar Mg/(Mg + Fe)) between 0.21 – 0.63.

The Saltoro Volcanics are andesitic in composition with SiO₂ concentrations between 54.80 – 62.68 wt.% and total alkali concentrations of 5.68 – 7.06 wt.%. The samples from the Saltoro Volcanics are characterized by TiO₂ concentrations of 0.65 – 1.25 wt.%, Al₂O₃ between 14.81 – 16.92 wt.%, FeO between 2.32 – 7.99 wt.%, MnO between 0.01 – 0.17 wt.%, MgO between 1.67 – 3.80 wt.%, CaO between 2.89 – 5.77 wt.%, Na₂O between 2.92 – 7.20 wt.%, a range in K₂O between 0.15 – 2.77 wt.%, and P₂O₅ mostly between 0.18 – 0.21 wt.% with one sample (LB18-16) containing a higher P₂O₅ concentration 0.40 wt.%. The Saltoro Volcanics had XMg between 0.20 – 0.45.

The Shukur dikes span compositions between andesite–rhyolite with SiO₂ concentrations between 58.47 – 72.09 wt.% and total alkali concentrations of 5.55 – 8.24 wt.%. The dike samples are characterized by TiO₂ concentrations of 0.10 – 1.17 wt.%, Al₂O₃ between 13.37 – 18.76 wt.%, FeO between 0.91– 6.26 wt.%, MnO between 0.03 – 0.07 wt.%, MgO between 0.18 – 6.27 wt.%, CaO between 1.97 – 4.01 wt.%, Na₂O between 2.99 – 7.87 wt.%, a range in K₂O between 0.36 – 2.70 wt.%, and P₂O₅ between 0.06 – 0.27 wt.%. The Shukur Dikes have XMg between 0.14 and 0.45.

Overall, the Shyok Volcanics can be characterized as having largely arc tholeiite composition while the Saltoro Volcanics are calc-alkaline andesites (see Figure 2-14). This is supported by the fact that the Shyok Volcanics have a characteristically flat trace element profiles and very low K₂O and P₂O₅, while the Saltoro Volcanics have significantly higher K₂O and Higher P₂O₅, a more complex trace element profile, and lower CaO and MgO with higher SiO₂ (Schmidt and Jagoutz, 2017). The Saltoro Volcanics are also significantly more aluminous than the Shyok Volcanics.

2.5 Discussion

Previous studies have presented constraints on the age of collision between the KLA and Eurasia along the Shyok suture zone using a variety of approaches, including detrital zircon provenance (Borneman et al., 2015; Najman et al., 2017), isotopic changes in the KLA batholith melts (Bouilhol et al., 2013), and intrusive relationships between plutons and suture zone lithologies (Kumar et al., 2017). Each of these approaches has yielded important information regarding the development of the suture zone, but none provides a “smoking gun” constraint on the age of the KLA-Karakoram collision. As a result, significant debate remains surrounding the age of the collision and its significance regarding the final India-Eurasia continental collision (Hu et al., 2016; Kapp and DeCelles, 2019; van Hinsbergen, 2022). In the following sections, we summarize the available constraints on the age of the Shyok suture zone and combine them with our results to discuss the state of play concerning the age of the KLA-Eurasia collision.

2.5.1 Detrital Zircon Evidence

Detrital zircon age spectra reveal useful information about the dominant source terranes of different sedimentary formations through time. They can be extremely valuable for investigating the timing of collision between terranes with significantly different age and isotopic signatures. For example, the 54 - 60 Ma depositional age of the oldest Indian passive margin strata containing volcanic arc detritus has provided very robust constraints on the initiation of collision on the northern edge of India along the Indus suture zone in Ladakh and the Yarlung-Tsangpo suture in Tibet (DeCelles et al., 2014; Garzanti et al., 1987; Najman et al., 2017). However, similar approaches applied in the Shyok suture zone have produced less clear-cut results.

Borneman et al. (2015) interpreted the presence of Lhasa/Pamir/Quiangtang-derived detrital zircons and abundant ~105 – 90 Ma zircons in the Saloro Formation as indicating a > 93 Ma final closure of the Shyok suture zone. They interpreted the ~105 – 90 Ma zircons as uniquely indicating a KLA source, but since there is significant overlap in the age distribution of magmatism in both the KLA and the Karakoram/Pamir, it is not possible to uniquely attribute either as the source (Bouilhol et al., 2013; Chapman et al., 2018b). Their interpretation also assumed that the Shyok Volcanics and Hundri Formation, onto which the Saloro Formation was deposited, were related to the Kohistan-Ladakh arc, even though contacts between the Shyok Volcanics and the KLA are exclusively tectonic. Furthermore, our detrital zircon data supports that the Hundri Formation, too, has a Eurasia-derived detrital zircon signature (see Figure 2-17). A more plausible interpretation of the detrital zircon age spectra of the Hundri and Saloro Formations is that they both have Eurasia-derived grains because they were deposited in the Eurasian-Karakoram forearc.

Similar challenges affect the interpretation of isotopic signatures and age distributions of detrital zircons from Paleocene sediments deposited on the Indian plate that have been used to argue for a pre-Paleocene closure of the Shyok suture zone (Najman et al., 2017; Zhuang et al., 2015). Interpreting a uniquely Karakoram provenance for 200 – 220 Ma detrital zircons in Paleocene Indian passive margin strata does not provide a constraint on Shyok suture zone closure as proposed by Najman et al., (2017) since other potential sources for these grains cannot be ruled out, including reworked Late Triassic and Early Jurassic Indian passive margin sediments (Cao et al., 2018). In addition, Zhuang et al., (2015) used isotopic data from a compilation that includes Miocene age rocks to suggest that these were part of the source terrain responsible for changes in the isotopic composition of sediments deposited in the Ganges basin at ~50 Ma (when the Miocene rocks did not exist).

Detrital zircon provenance studies of sedimentary rocks deposited on the Indian plate provide strong evidence for a collision between the Indian plate and a volcanic arc and some Eurasian-derived source rocks at 60 – 55 Ma (DeCelles et al., 2014; Garzanti et al., 1987; Najman et al., 2017). However, these observations do not necessarily constrain final closure of the Shyok suture zone nor final India-Eurasia collision because the KLA provides a plausible source for Cretaceous arc-related detritus on the northern Indian passive margin. The KLA also provides a plausible source of other Eurasia-derived detrital zircons because it may have formed close to the Eurasian margin and subsequently rifted southward, could have joined with the Eurasian margin along strike, or be built on Eurasian crustal fragments (Kapp and DeCelles, 2019; Rolland et al., 2000; Saktura et al., 2022)

2.5.2 Structural Evidence

Constraining the age of the major tectonic boundaries within a suture zone provides a first-order constraint on the age of collision between two geologic terranes. In the Shyok suture zone, the primary boundary between KLA-related rocks and Eurasia-derived sedimentary rocks is the Khalsar Thrust/Bogdang Shear Zone. This structure separates the Jurassic-Cretaceous Eurasian arc-forearc sequence from the intrusive and extrusive elements of the Ladakh arc (Rai, 1982; Srimal et al., 1987). Our geochronology, published ages, and the crosscutting relationships observed during our geological mapping constrain the age of the Khalsar fault, and therefore the suturing of KLA and Eurasian terranes, to between 51.9 ± 0.7 Ma and 24.7 ± 0.4 Ma. There are limited constraints on the age of equivalent or comparable structures to the Khalsar Thrust west of our field area. However, the existing constraints are consistent with a < 50 Ma age. At Khalpu, the southernmost fault of the suture zone crosscuts dikes in the Ladakh batholith dated to 40 – 44 Ma

using the Ar-Ar method (Brookfield and Reynolds, 1990). In the Drosh area, the southern boundary thrust of the suture zone crosscuts 49.80 ± 0.15 Ma meta-gabbro and meta-diorite of the KLA (Heuberger et al., 2007).

All the other thrusts in the Shyok suture zone are significantly younger than the Khalsar Thrust. The Murgi Thrust marks the base of the Karakoram fault nappe stack and crosscuts the $< 25.9 \pm 1.5$ Ma post-collisional Murgi conglomerate. The Waris Thrust and Ensa Thrust are both younger than 40 Ma because they crosscut the Waris granodiorite (Borneman et al., 2015). The strike-slip deformation along the Turtuk Shear Zone crosscuts leucogranite dikes dated to $< 25.1 \pm 1.3$ Ma (Jagoutz et al., 2019). The only pre-Eocene fault structure in the Shyok suture zone is the extensional deformation along the Saltoro Fault and in the lower Saltoro Formation. The age of this syn-sedimentary extension is well-constrained by the $< 92.9 \pm 2.2$ Ma age of the overlying Saltoro Formation conglomerate, and the 85.0 ± 0.7 Ma age of the Shukur dikes crosscutting the faulting. Extension and compression in arc-forearc settings are common and are not an indicator of large-scale collision or rifting because small changes in the geometry of the subducting plate can initiate both tension and compression in the overriding arc lithosphere (Dickinson and Seely, 1979).

In summary, our results show no structural evidence of KLA-Eurasia collision along the Shyok suture zone in Ladakh before 51.9 ± 0.7 Ma. The oldest stitching granite dated in the Shyok suture zone is the 24.7 ± 0.4 Ma Chalunka granite, which crosscuts the Shyok Suture Ophiolite and the Turtuk Complex metagabbro and metadiorite. Future studies could further constrain the younger-bound age of the KLA-Eurasia collision by constraining the ages of other potential stitching granites elsewhere in the Shyok suture.

2.5.3 Magmatic Evidence

Shifts in the eHf and Nd isotopic signatures of KLA batholith melts at ~50 Ma in the southern Arc Batholith, and at ~40 Ma along the northern boundary of the batholith, were interpreted by Bouilhol et al. (2013) as indicative of two stages of collision affecting the KLA. They interpreted the 50 Ma isotopic change as the arrival of Indian continental lithosphere in the source region of KLA melts during arc-continent collision between India and the KLA. They attributed the 40 Ma isotopic change in the northern batholith as final collision between the KLA-India composite and Eurasia. Our results are consistent with this model because they suggest that magmatism in the Shyok suture zone arc-forearc sequence was very active from the Cretaceous until 42 ± 1.7 Ma (see Figure 2-18; Borneman et al., 2015). This suggests that subduction was taking place beneath the Shyok arc-forearc sequence until the Paleocene. However, it does not provide a strong constraint on collision timing because if the KLA had accreted onto Eurasia in the Cretaceous, northward subduction of Neotethyan oceanic lithosphere south of the KLA could still have resulted in magmatism in the suture zone. However, this magmatism does not crosscut the tectonic contacts between the KLA and Eurasia-derived suture zone lithologies until the 24.7 ± 0.4 Ma intrusion of the Chalunka granite. This suggests that KLA-Eurasia suturing did not pre-date Shyok suture zone magmatism. Instead, it is more likely that the magmatism in the Shyok suture zone is related to a second northward-directed subduction beneath the Karakoram terrane.

2.6 Conclusion

This study presents the U-Pb zircon geochronology results and whole-rock geochemistry that develop the tectonostratigraphic relationships of the Shyok suture zone in Ladakh, northwest India, and provide new time constraints on the development of the suture zone. Our results show that the Shyok suture zone comprises a Jurassic forearc ophiolite and Cretaceous forearc basin that is intruded by Cretaceous-Eocene arc magmatism, all of which formed on the southern Eurasian (Karakoram) margin. The earliest structure that emplaces these Eurasia-derived units against elements of the Kohistan-Ladakh arc is the Khalsar Thrust, which formed after 51.9 ± 0.7 Ma based on crosscutting relations with the Khardung Volcanics. The only pre-Eocene structures in the Shyok suture zone are extensional. All other major fault structures formed in the Oligocene – Miocene after ~ 25 Ma, overprinting the primary structures of the suture zone. These observations, combined with paleomagnetic evidence (see Chapters 2 and Chapter 3), together suggest that the Shyok suture zone post-dates the Indus suture zone, which is well constrained to $\sim 54 - 52$ Ma. Therefore, the geology of the western Himalaya is consistent with multi-stage India-Eurasia collision models in which the Kohistan-Ladakh arc was part of an intra-oceanic subduction system that operated south of the southern Eurasian margin throughout the closure of the Neotethys, until the arc accreted onto the northern margin of India in the Paleocene. Before the arrival of India, the Eurasian margin likely resembled the modern western margin of the Pacific, rather than an accretionary orogen like western margin of North America.

2.7 Figures and Captions

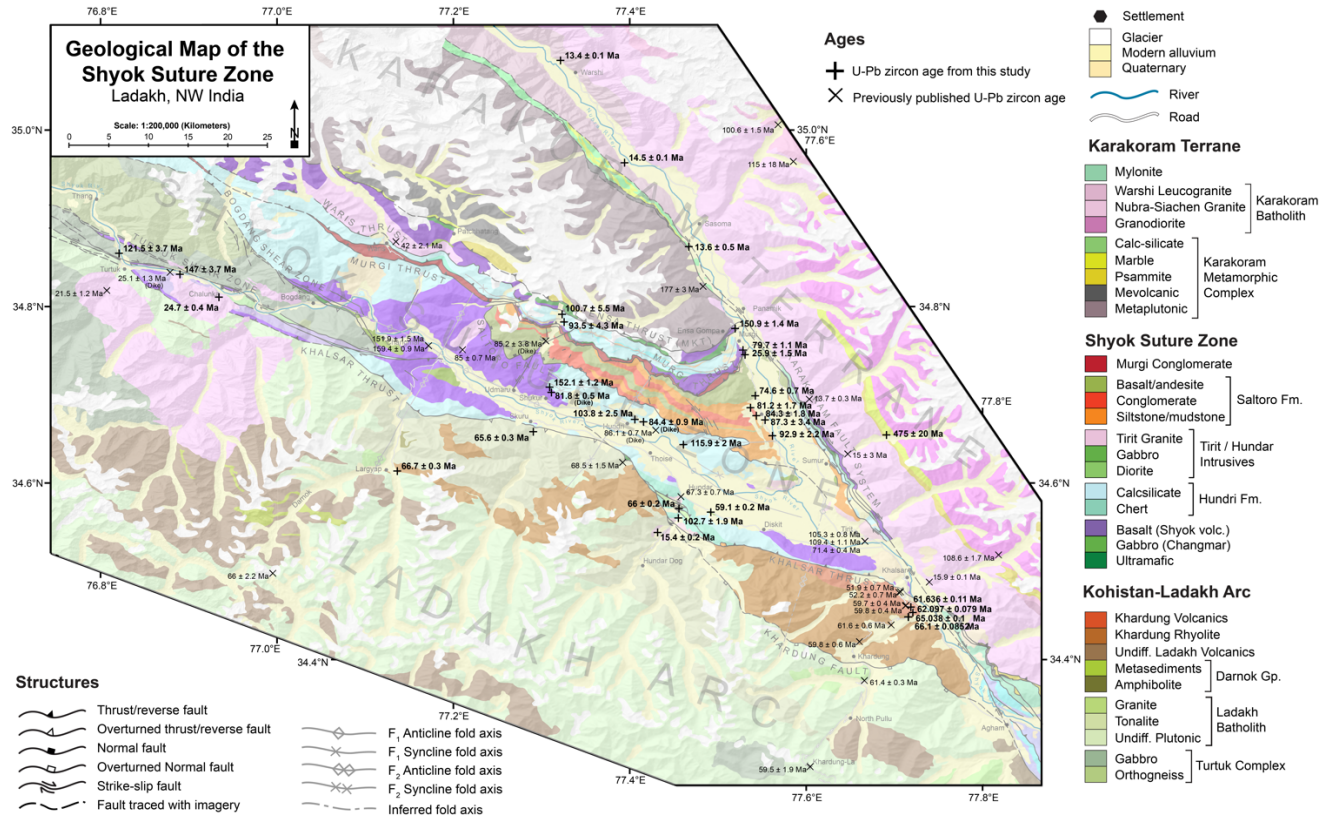
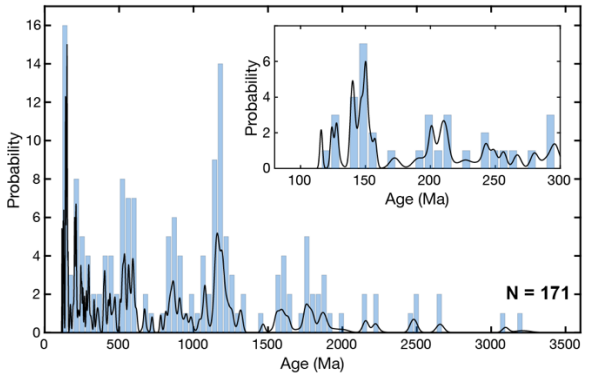
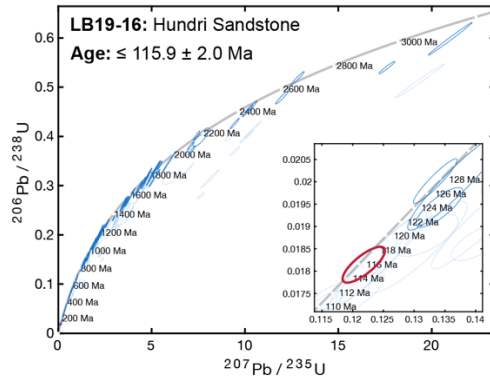
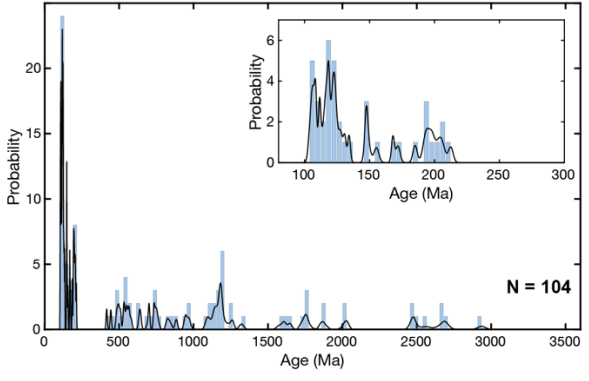
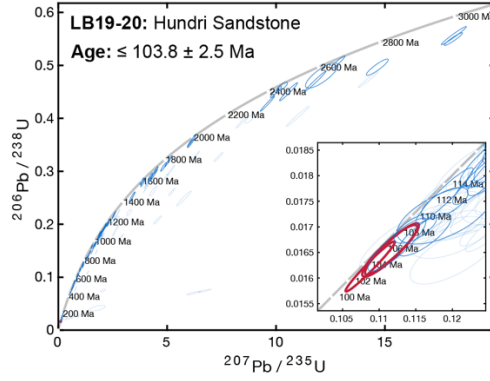
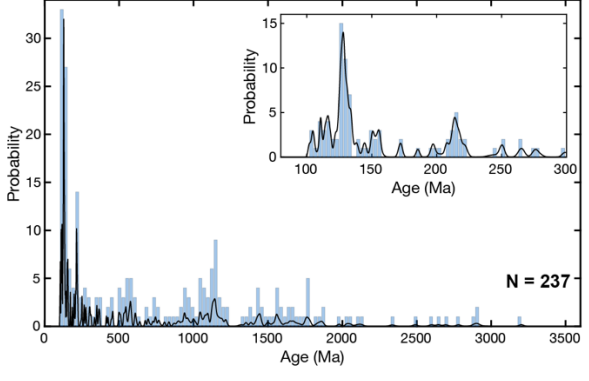
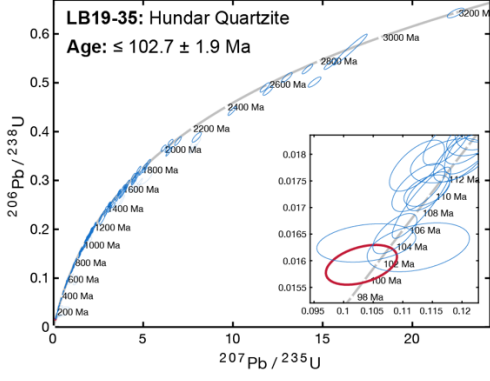
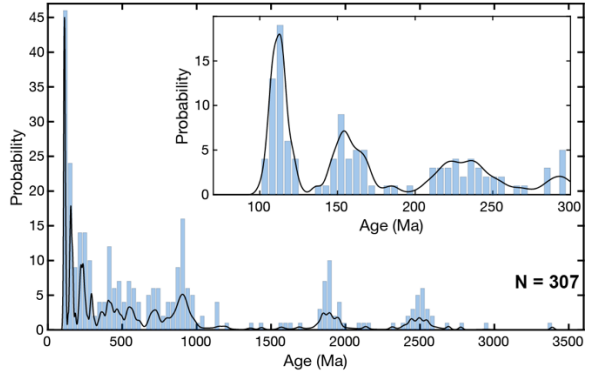
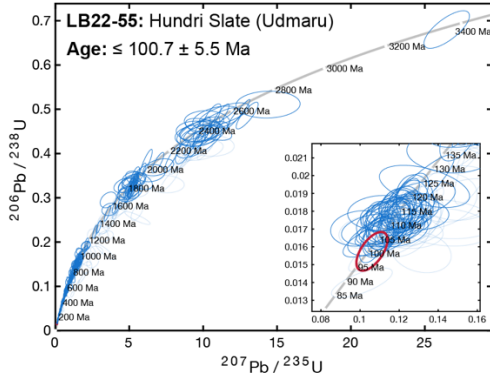


Figure 2-1: Summary figure showing all geochronology results presented in this thesis and further age constraints compiled from previously published work.



- Analyses used to determine age.
- Accepted analyses.
- Rejected analyses.

Figure 2-2: U-Pb zircon analyses for Hundri Formation samples LB19-55, LB19-35, LB19-20, and LB1916. Left column: Wetherhill concordia diagrams with insets showing the youngest analyses; red ellipses indicate the analyses used to determine the reported maximum depositional ages. Right Column: Histograms and probability density distributions of detrital zircon spectra for each sample.

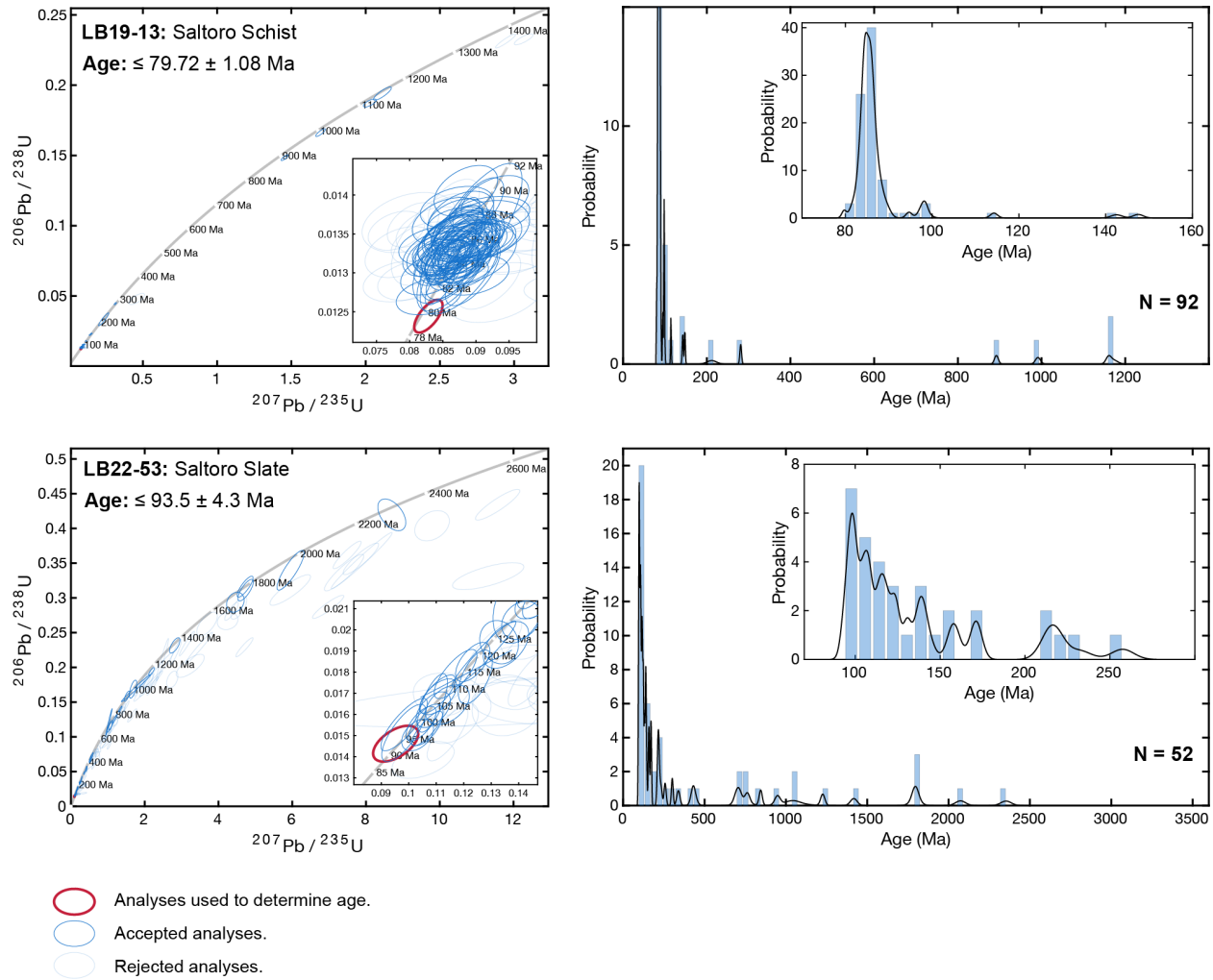


Figure 2-3: U-Pb zircon analyses for Saltoro Formation samples LB19-13 and LB19-53. Left column: Wetherhill concordia diagrams with insets showing the youngest analyses; red ellipses indicate the analyses used to determine the reported maximum depositional ages. Right Column: Histograms and probability density distributions of detrital zircon spectra for each sample.

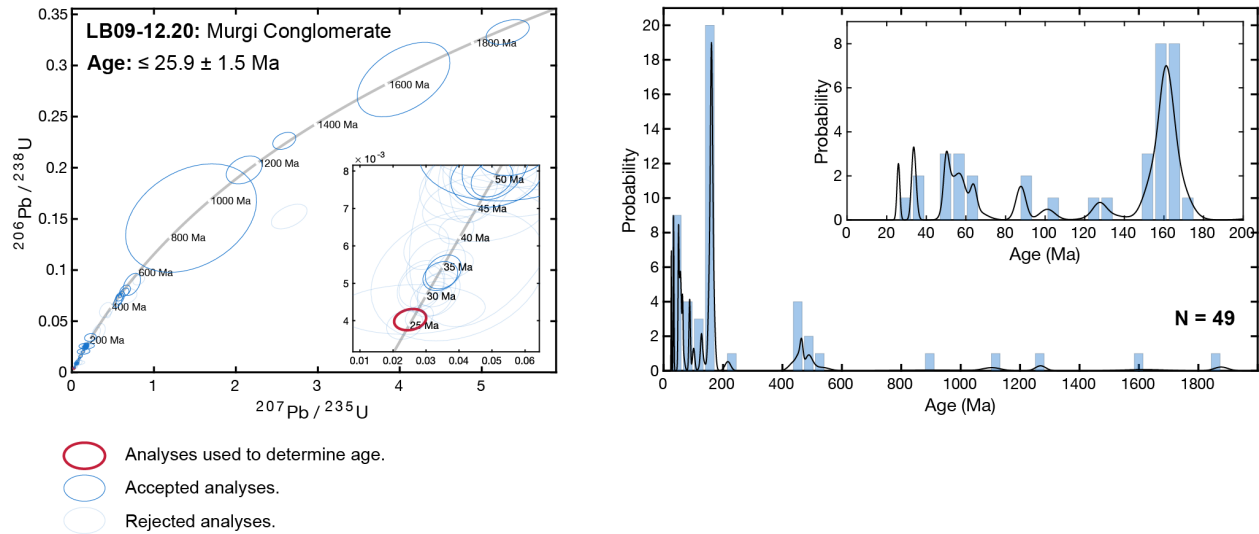


Figure 2-4: U-Pb zircon analyses for Murgi conglomerate sample LB09-12.20. Left column: Wetherhill concordia diagram with inset showing the youngest analyses; red ellipse indicates the analysis used to determine the reported maximum depositional age. Right Column: Histogram and probability density distribution of detrital zircon spectra for the sample.

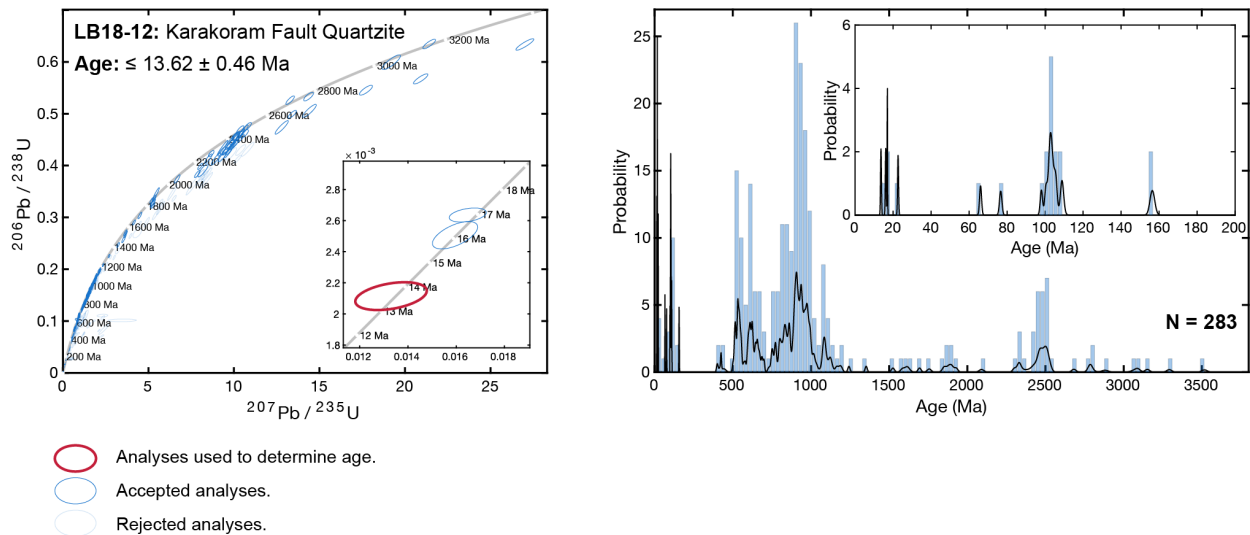


Figure 2-5: U-Pb zircon analyses for Karakoram fault zone quartzite sample LB18-12. Left column: Wetherhill concordia diagram with inset showing the youngest analyses; red ellipse indicates the analysis used to determine the reported maximum depositional age. Right Column: Histogram and probability density distribution of detrital zircon spectra for the sample.

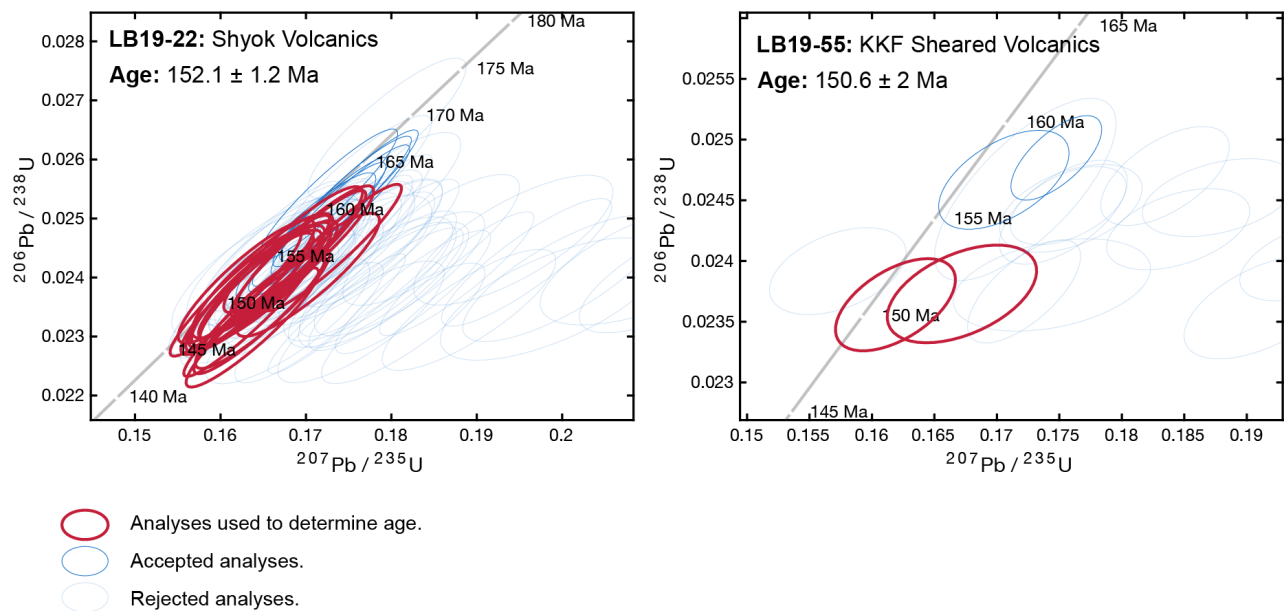


Figure 2-6: U-Pb zircon analyses for Shyok Volcanics samples LB19-22 and LB19-55. Wetherhill concordia diagrams are shown with red ellipses indicating the analysis used to determine the reported final crystallization age using a weighted mean.

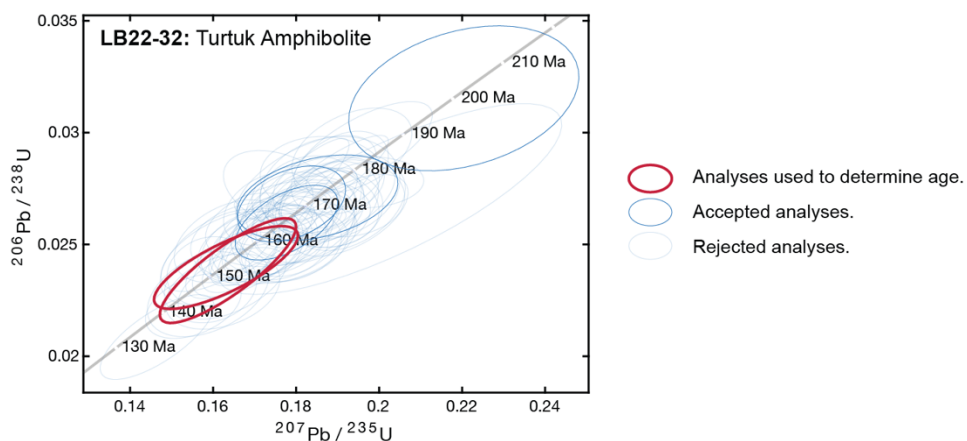


Figure 2-7: U-Pb zircon analyses for Turtuk Amphibolite (leucosome) sample LB19-32. Wetherhill concordia diagram is shown with red ellipses indicating the analysis used to determine the reported final crystallization age using a weighted mean.

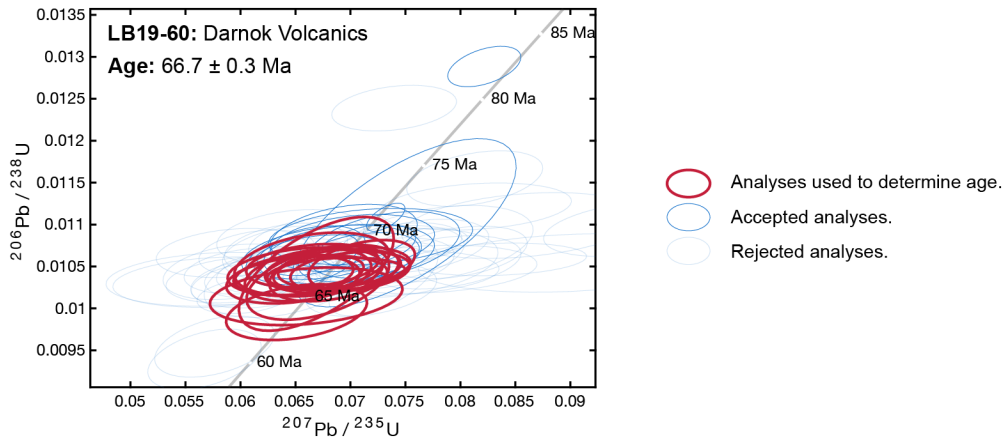


Figure 2-8: U-Pb zircon analyses for Khardung Volcanics rhyolite sample LB19-60 from the Darnok-Largyap area. Wetherhill concordia diagram is shown with red ellipses indicating the analysis used to determine the reported final crystallization age using a weighted mean.

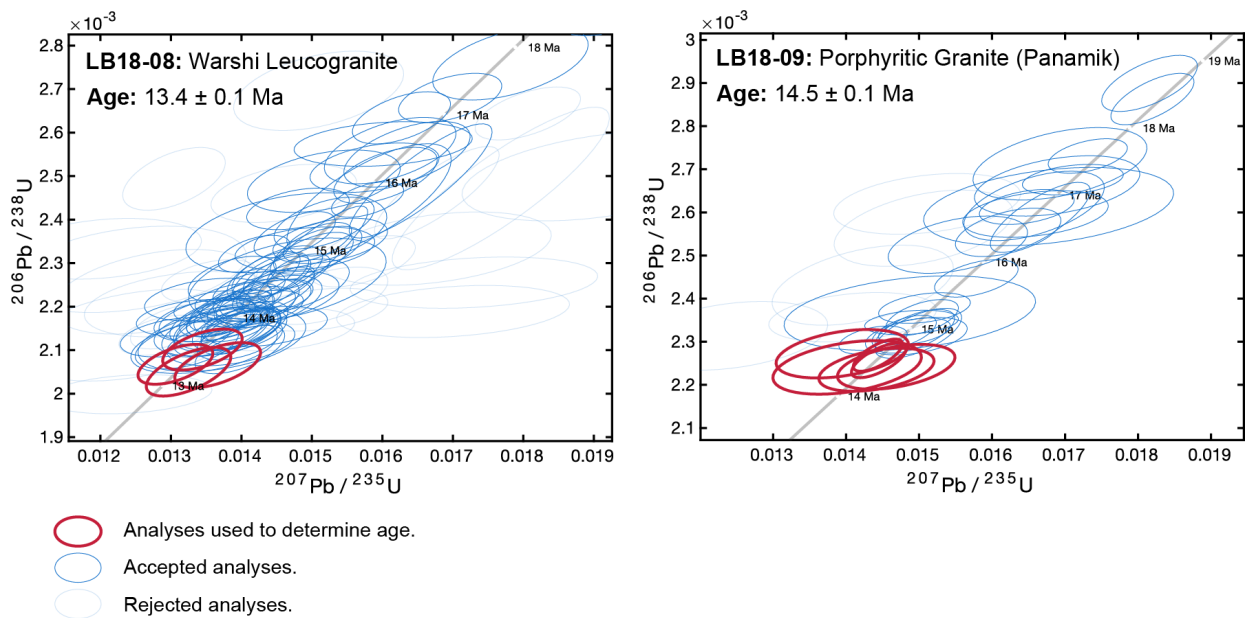


Figure 2-9 U-Pb zircon analyses for two Nubra-Siachen granites (samples LB18-08 and LB18-09) from the upper Nubra valley. Wetherill concordia diagrams are shown with red ellipses indicating the analysis used to determine the reported final crystallization age using a weighted mean.

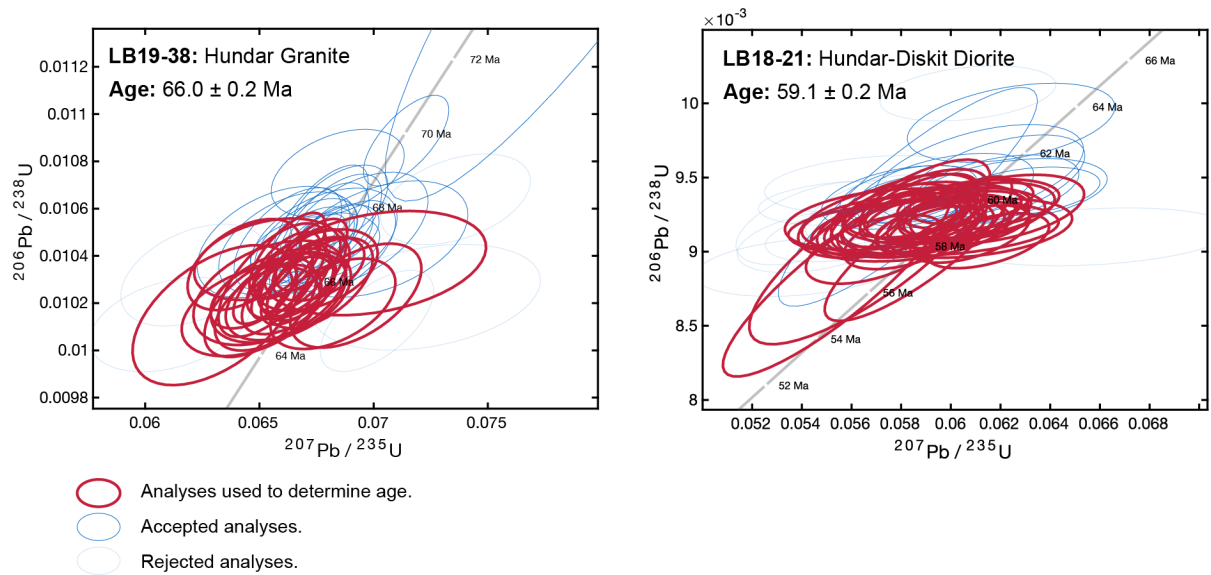


Figure 2-10: U-Pb zircon analyses for two Tirit-Hunder plutonic bodies (samples LB19-38 and LB18-21). Wetherhill concordia diagrams are shown with red ellipses indicating the analysis used to determine the reported final crystallization age using a weighted mean.

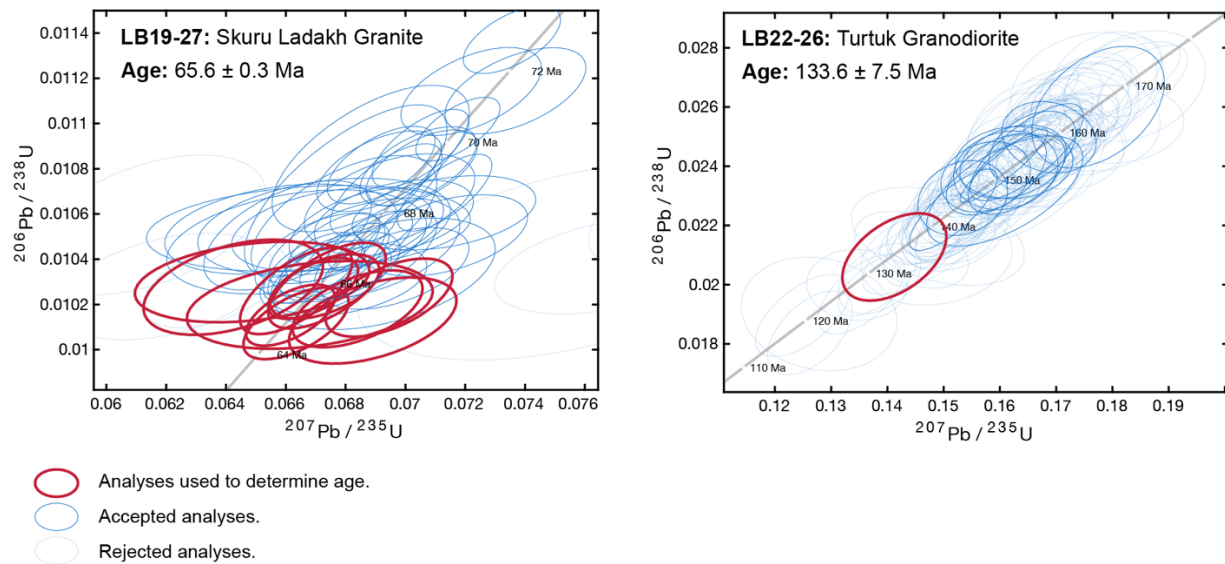


Figure 2-11: U-Pb zircon analyses for two Ladakh batholith plutonic bodies (samples LB19-27 and LB22-26). Wetherhill concordia diagrams are shown with red ellipses indicating the analysis used to determine the reported final crystallization age using a weighted mean.

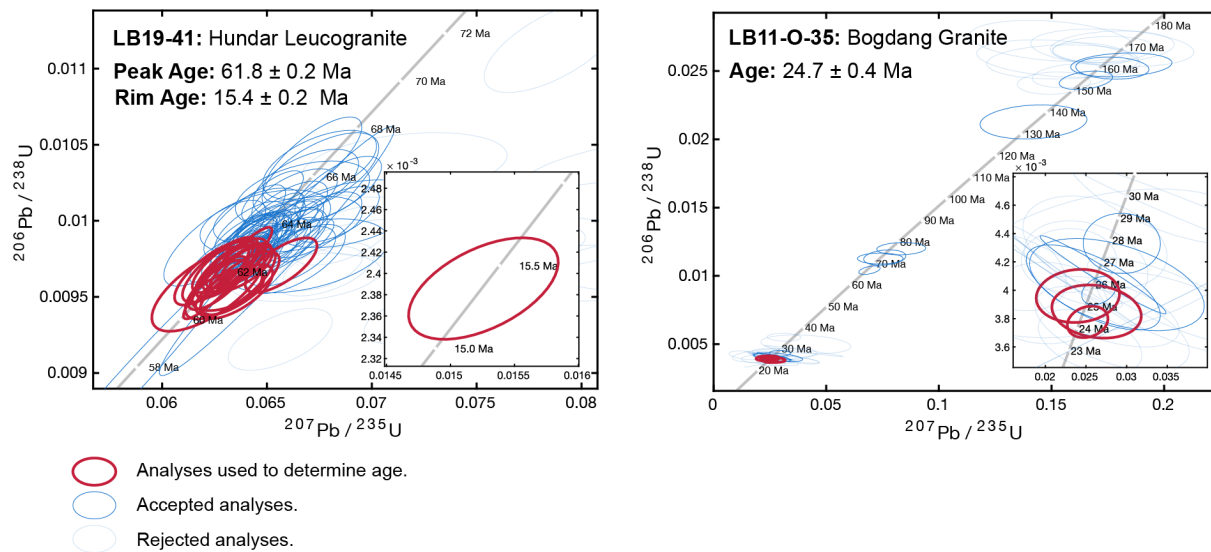


Figure 2-12. U-Pb zircon analyses for two post-collision leucogranites (samples LB19-41 and LB11-O-35). Wetherhill concordia diagrams are shown with red ellipses indicating the analysis used to determine the reported final crystallization age using a weighted mean.

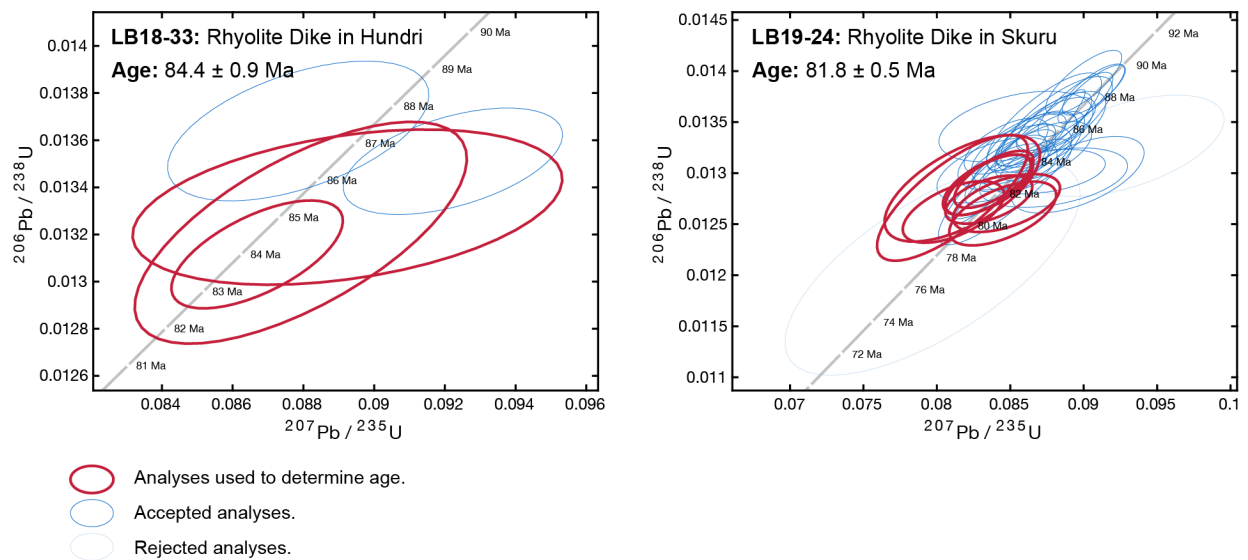


Figure 2-13. U-Pb zircon analyses for two Shukur dike samples (LB18-33 and LB19-24). Wetherhill concordia diagrams are shown with red ellipses indicating the analysis used to determine the reported final crystallization age using a weighted mean.

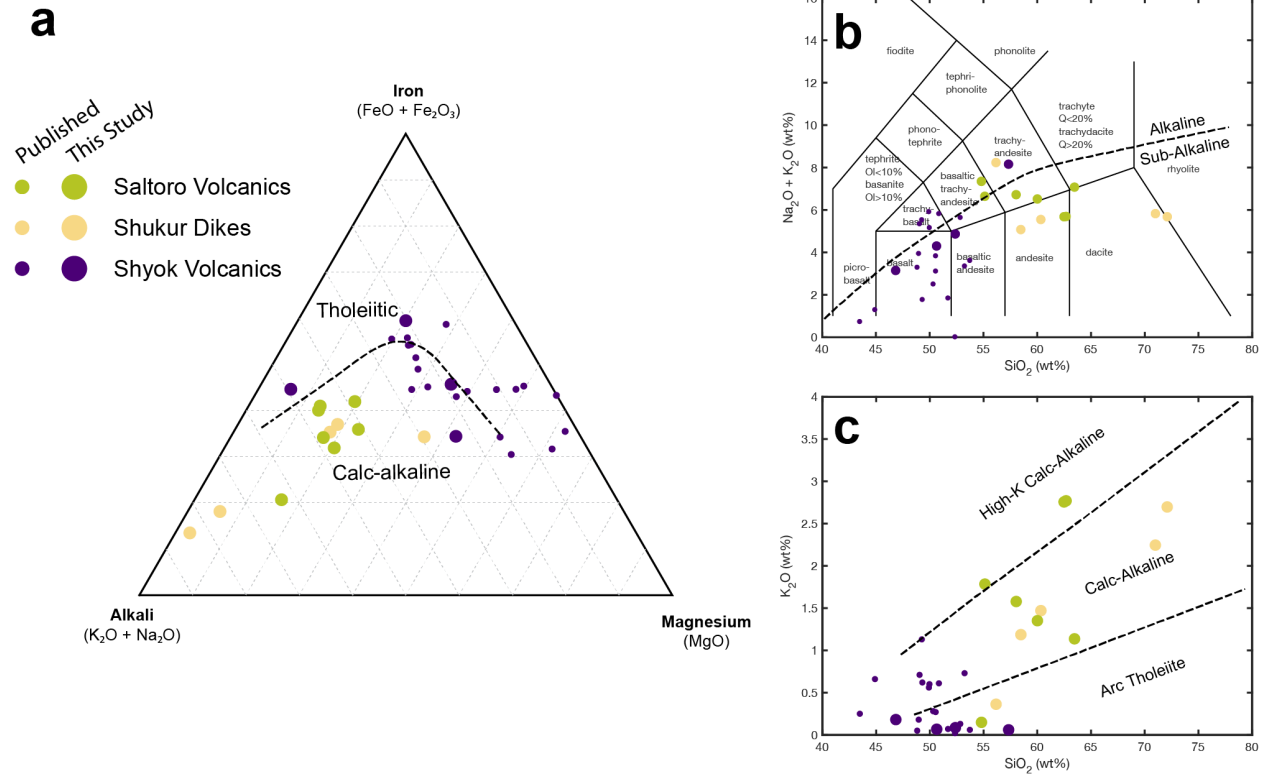


Figure 2-14: Major element discrimination diagrams showing whole-rock major element analyses from the Shyok Volcanics, the Saltoro Volcanics, and the Shukur dikes. **a)** Ternary AFM diagram with discrimination curve for tholeiitic versus calc-alkaline trends. **b)** Total alkali versus silica diagram showing alkaline versus sub-alkaline trends (Rickwood, 1989). **c)** Potassium versus silica diagram with fields for Arc Tholeiite, Calc-Alkaline, and High-K Calc-Alkaline trends (Rickwood, 1989).

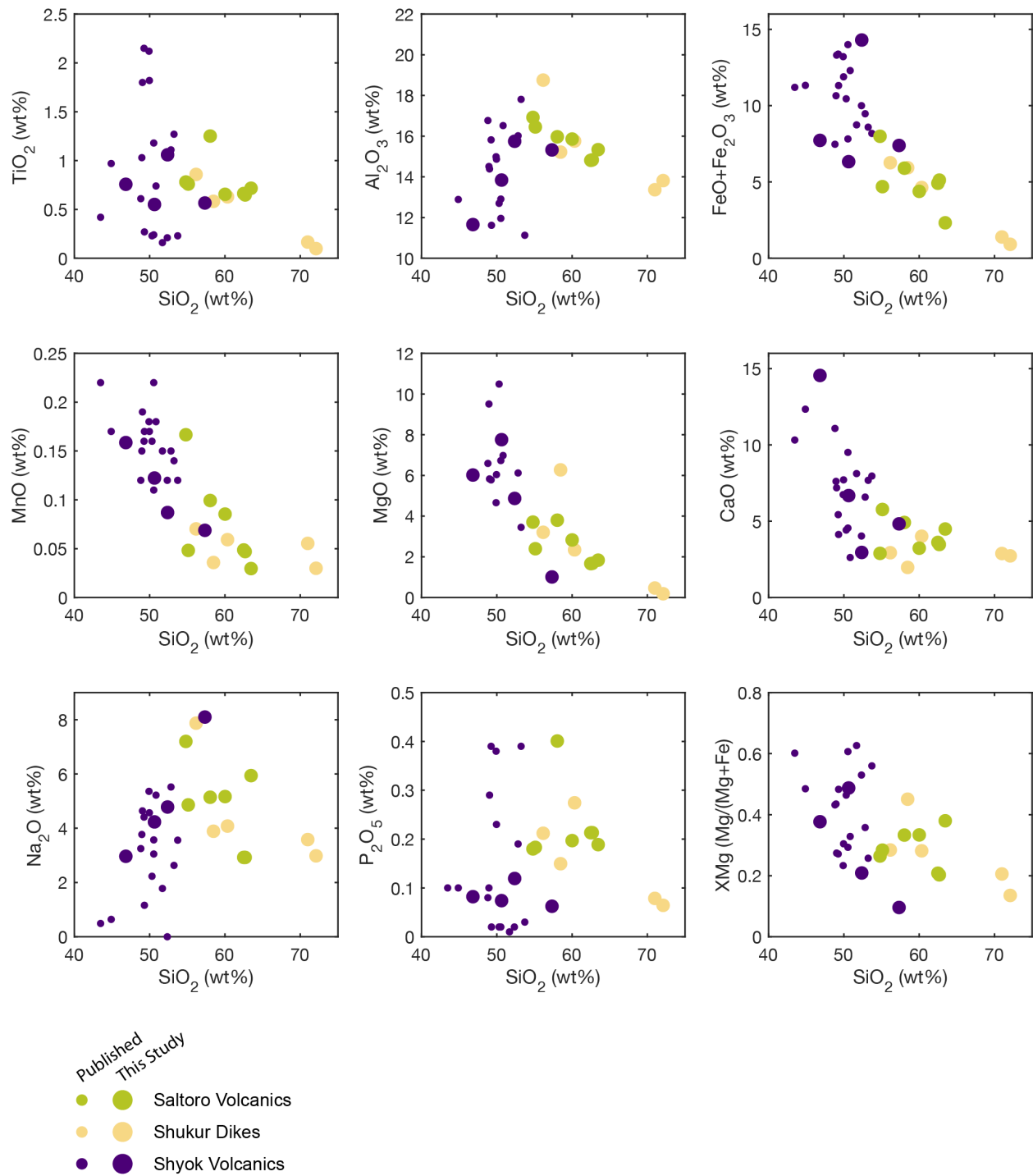


Figure 2-15: Major element oxides versus silica for the Shyok Volcanics, Saltoro Volcanics, and Shukur Dikes, from XRF analyses. Saltoro Formation andesites are consistently higher in SiO₂, Al₂O₃, and P₂O₅ and lower in FeO, MnO, MgO, and CaO.

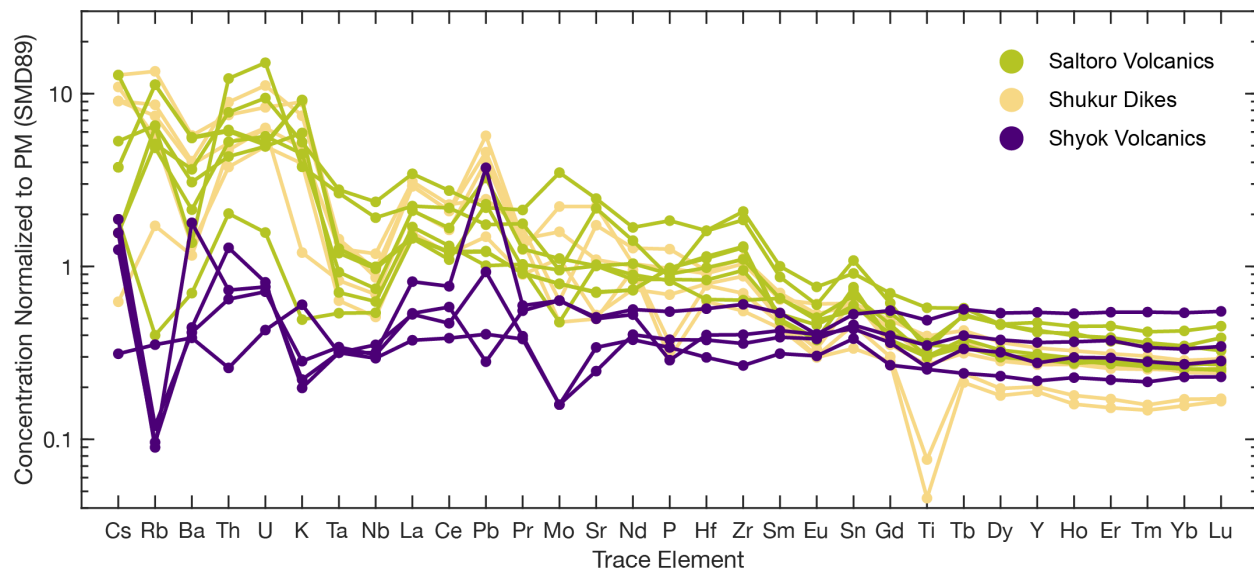


Figure 2-16: Whole rock trace element geochemistry analyses normalized to primitive mantle (Sun and McDonough, 1989) obtained using LA-ICPMS. The Shyok Volcanics have typically flat trace element curves typical of tholeiitic melts, while the Saltoro Volcanics show a sloped curve typical of calc-alkaline magmatic series (Schmidt and Jagoutz, 2017).

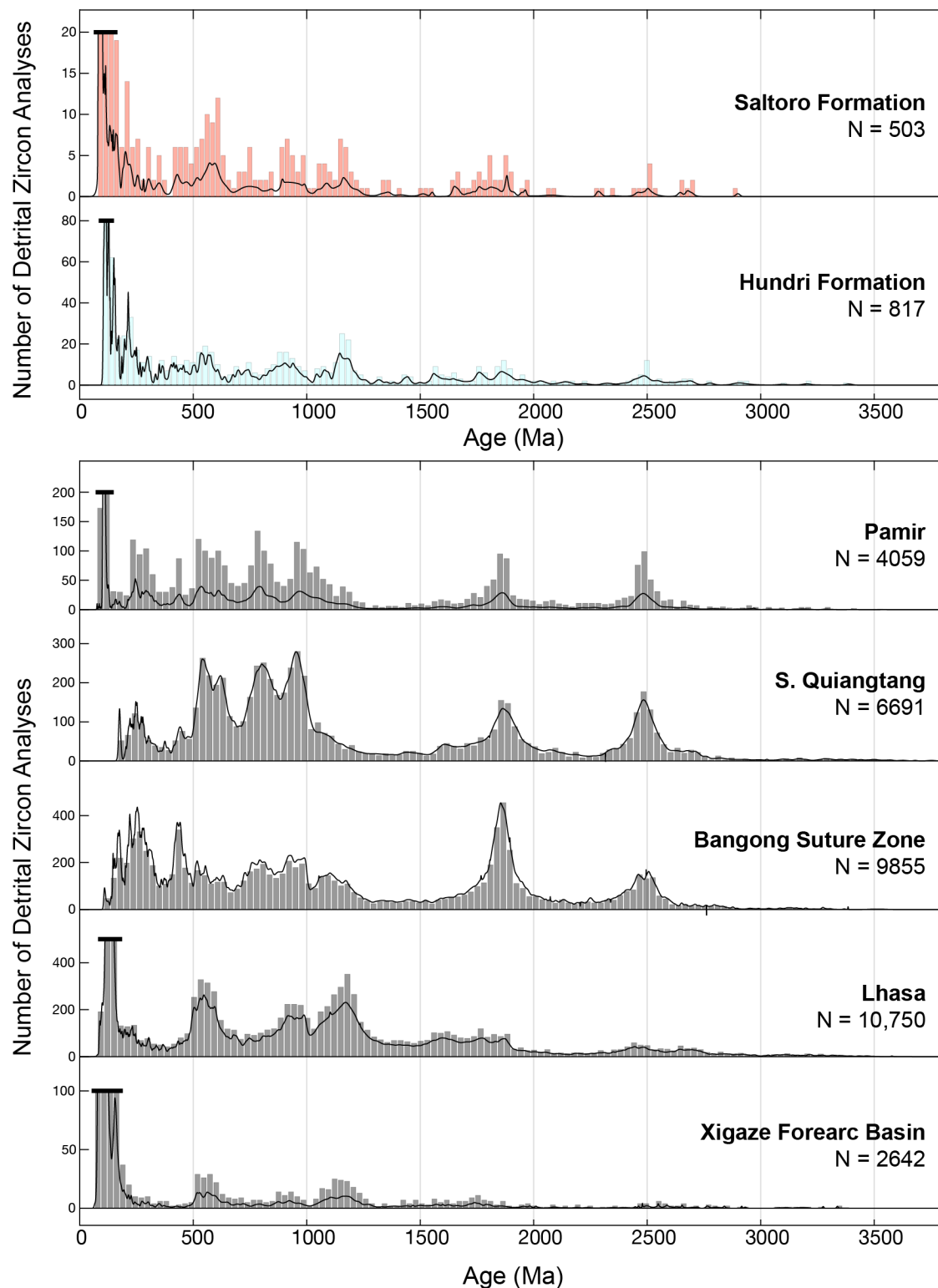


Figure 2-17: Comparison of detrital zircon spectra of the Hundri and Saltoro formations with zircon spectra for similar age sedimentary strata compiled from other major terranes that formed part of the southern Eurasian accretionary orogen in the Cretaceous (Chapman et al., 2018a; He et al., 2019; Xue et al., 2022).

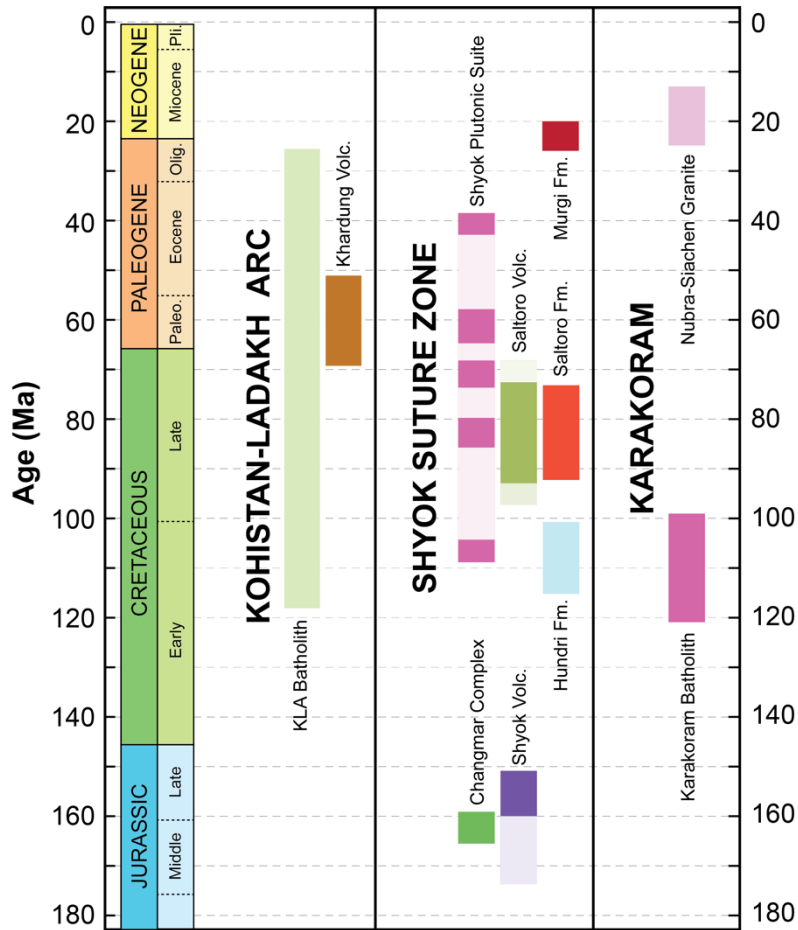


Figure 2-18. Summary timeline showing the age range of major geologic formations exposed in the Shyok suture zone. The column colors relate to the map colors of the geologic formations represented. The Kohistan-Ladakh batholith is shown in pale green; the Khardung Volcanics in brown; the magmatism of the Karakoram and Shyok forearc in dark pink; the Changmar complex in forest green; the Shyok Volcanics in purple; the Saltoro Volcanics in olive green; the Hundri Formation in pale blue; the Saltoro Formation in red; the Murgi Conglomerate in dark red; and post-collisional granites and leucogranites in light pink. Where ages are uncertain but likely extend, the bars are faded out.

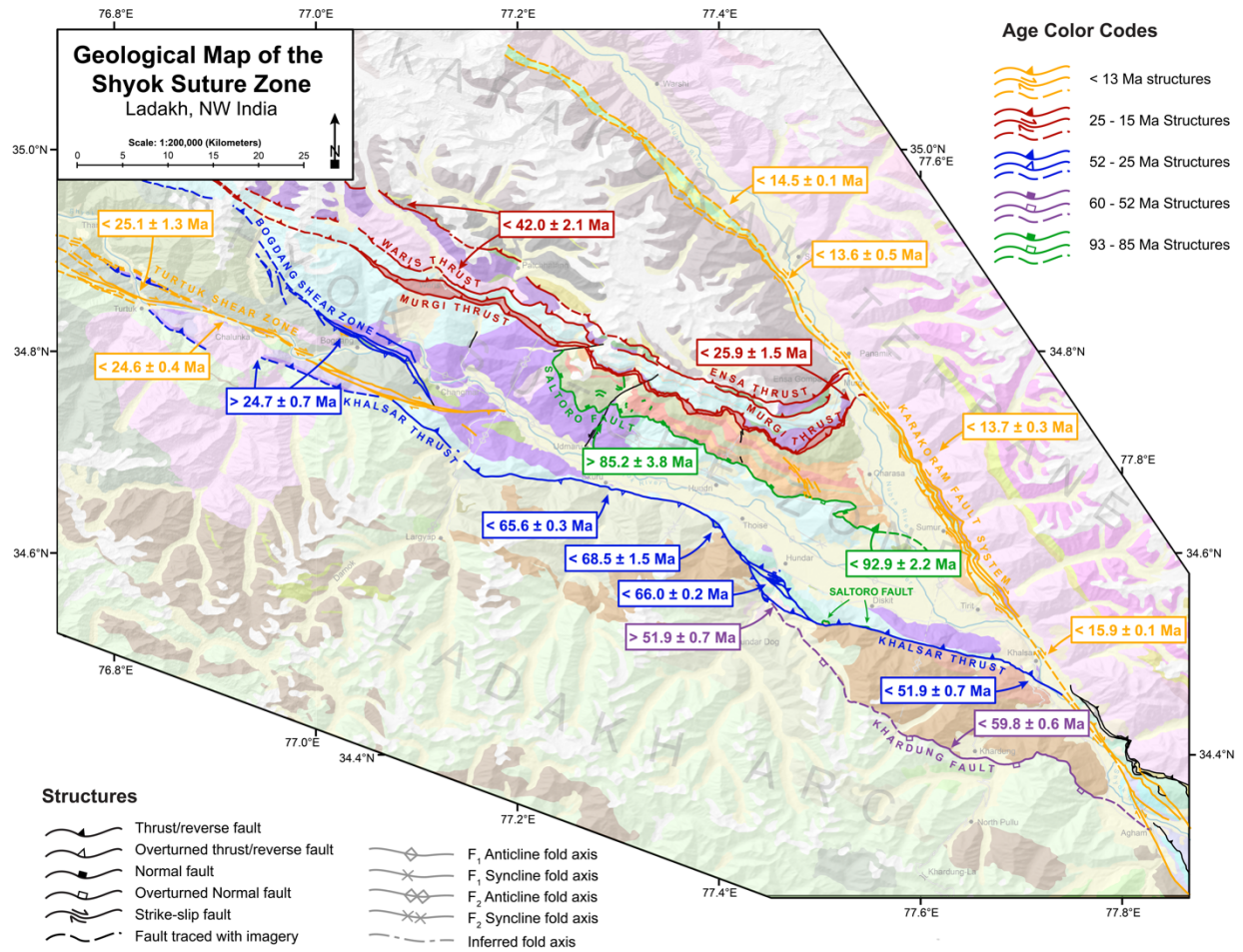


Figure 2-19. Geological map of the Shyok suture zone with the age constraints of the major fault structures overlaid with different colors for different age groups. The significant age constraints from crosscutting relationships are shown in the location from which they are derived.

References

- Borneman, N.L., Hodges, K.V., Van Soest, M.C., Bohon, W., Wartho, J.A., Cronk, S.S. and Ahmad, T., 2015. Age and structure of the Shyok suture in the Ladakh region of northwestern India: Implications for slip on the Karakoram fault system. *Tectonics*, 34(10): 2011-2033.
- Bouilhol, P. and Jagoutz, O., 2014. Redefining the Trans-Himalayan Batholith in the frame of the India-Eurasia collision, EGU General Assembly Conference Abstracts, pp. 10500.
- Bouilhol, P., Jagoutz, O., Hanchar, J.M. and Dudas, F.O., 2013. Dating the India-Eurasia collision through arc magmatic records. *Earth and Planetary Science Letters*, 366: 163-175.
- Brookfield, M.E. and Reynolds, P., 1990. Miocene $^{40}\text{Ar}/^{39}\text{Ar}$ ages from the Karakorum Batholith and Shyok Melange, northern Pakistan, indicate late Tertiary uplift and southward displacement. *Tectonophysics*, 172(1-2): 155-167.
- Cao, H., Huang, Y., Li, G., Zhang, L., Wu, J., Dong, L., Dai, Z. and Lu, L., 2018. Late Triassic sedimentary records in the northern Tethyan Himalaya: Tectonic link with Greater India. *Geoscience Frontiers*, 9(1): 273-291.
- Chapman, J.B., Robinson, A.C., Carrapa, B., Villarreal, D., Worthington, J., DeCelles, P.G., Kapp, P., Gadoev, M., Oimahmadov, I. and Gehrels, G., 2018a. Cretaceous shortening and exhumation history of the South Pamir terrane. *Lithosphere*, 10(4): 494-511.
- Chapman, J.B., Scoggin, S.H., Kapp, P., Carrapa, B., Ducea, M.N., Worthington, J., Oimahmadov, I. and Gadoev, M., 2018b. Mesozoic to Cenozoic magmatic history of the Pamir. *Earth and Planetary Science Letters*, 482: 181-192.
- DeCelles, P., Kapp, P., Gehrels, G. and Ding, L., 2014. Paleocene-Eocene foreland basin evolution in the Himalaya of southern Tibet and Nepal: Implications for the age of initial India-Asia collision. *Tectonics*, 33(5): 824-849.
- Dickinson, W. and Seely, D., 1979. Structure and stratigraphy of forearc regions. *AAPG Bulletin*, 63(1): 2-31.
- Garzanti, E., Baud, A. and Mascle, G., 1987. Sedimentary Record of the Northward Flight of India and Its Collision with Eurasia (Ladakh Himalaya, India). *Geodinamica Acta*, 1(4-5): 297-312.
- He, J., Kapp, P., Chapman, J.B., DeCelles, P.G. and Carrapa, B., 2019. Structural setting and detrital zircon U–Pb geochronology of Triassic–Cenozoic strata in the eastern Central Pamir, Tajikistan. *Geological Society, London, Special Publications*, 483(1): 605-630.
- Heuberger, S., Schaltegger, U., Burg, J.-P., Villa, I.M., Frank, M., Dawood, H., Hussain, S. and Zanchi, A., 2007. Age and isotopic constraints on magmatism along the Karakoram-Kohistan Suture Zone, NW Pakistan: Evidence for subduction and continued convergence after India-Asia collision. *Swiss Journal of Geosciences*, 100: 85-107.
- Hu, X.M., Garzanti, E., Wang, J.G., Huang, W.T., An, W. and Webb, A., 2016. The timing of India-Asia collision onset - Facts, theories, controversies. *Earth-Science Reviews*, 160: 264-299.
- Jagoutz, O., Bouilhol, P., Schaltegger, U. and Müntener, O., 2019. The isotopic evolution of the Kohistan Ladakh arc from subduction initiation to continent arc collision. *Geological Society, London, Special Publications*, 483(1): 165-182.

- Kapp, P. and DeCelles, P.G., 2019. Mesozoic–Cenozoic geological evolution of the Himalayan-Tibetan orogen and working tectonic hypotheses. *American Journal of Science*, 319(3): 159-254.
- Kumar, S., Bora, S., Sharma, U.K., Yi, K. and Kim, N., 2017. Early Cretaceous subvolcanic calc-alkaline granitoid magmatism in the Nubra-Shyok valley of the Shyok Suture Zone, Ladakh Himalaya, India: Evidence from geochemistry and U–Pb SHRIMP zircon geochronology. *Lithos*, 277: 33-50.
- Mueller, P. A., Kamenov, G. D., Heatherington, A. L., & Richards, J. (2008). Crustal evolution in the southern Appalachian orogen: Evidence from Hf isotopes in detrital zircons. *The Journal of Geology*, 116(4), 414-422.
- Najman, Y., Jenks, D., Godin, L., Boudagher-Fadel, M., Millar, I., Garzanti, E., Horstwood, M. and Bracciali, L., 2017. The Tethyan Himalayan detrital record shows that India-Asia terminal collision occurred by 54 Ma in the Western Himalaya. *Earth and Planetary Science Letters*, 459: 301-310.
- Paton, C., Hellstrom, J., Paul, B., Woodhead, J. and Hergt, J., 2011. Iolite: Freeware for the visualisation and processing of mass spectrometric data. *Journal of Analytical Atomic Spectrometry*, 26(12): 2508-2518.
- Pullen, A., Ibáñez-Mejía, M., Gehrels, G.E., Giesler, D. and Pecha, M., 2018. Optimization of a laser ablation-single collector-inductively coupled plasma-mass spectrometer (Thermo Element 2) for accurate, precise, and efficient zircon U-Th-Pb geochronology. *Geochemistry, Geophysics, Geosystems*, 19(10): 3689-3705.
- Rai, H., 1982. Geological evidence against the Shyok palaeo-suture, Ladakh Himalaya. *Nature*, 297: 142-144.
- Rickwood, P.C., 1989. Boundary lines within petrologic diagrams which use oxides of major and minor elements. *lithos*, 22(4): 247-263.
- Rolland, Y., Pecher, A. and Picard, C., 2000. Middle Cretaceous back-arc formation and arc evolution along the Asian margin: the Shyok Suture Zone in northern Ladakh (NW Himalaya). *Tectonophysics*, 325(1-2): 145-173.
- Saktura, W.M., Buckman, S., Nutman, A.P. and Bennett, V.C., 2021b. Late Jurassic Changmar complex from the Shyok ophiolite, NW Himalaya: A prelude to the Ladakh arc. *Geological Magazine*, 158(2): 239-260.
- Saktura, W.M., Buckman, S., Nutman, A.P. and Zhou, R., 2022. Jurassic–Cretaceous arc magmatism along the Shyok–Bangong Suture of NW Himalaya: formation of the peri-Gondwana basement to the Ladakh Arc. *Journal of the Geological Society*, 179(2).
- Schmidt, M.W. and Jagoutz, O., 2017. The global systematics of primitive arc melts. *Geochemistry Geophysics Geosystems*, 18(8): 2817-2854.
- Sivaprabha, S., Bhat, I.M., Ahmad, T., Tanaka, T., Balakrishnan, S., Asahara, Y. and Mukhopadhyay, D., 2022. Geochemical analysis of magmatic rocks from Shyok Suture Zone (SSZ) Trans-Himalaya, NW India: Insights for geodynamic evolution of the terrane. *Lithos*, 410: 106594.
- Spencer, C.J., Kirkland, C.L. and Taylor, R.J., 2016. Strategies towards statistically robust interpretations of in situ U–Pb zircon geochronology. *Geoscience Frontiers*, 7(4): 581-589.
- Srimal, N., Basu, A.R. and Kyser, T.K., 1987. Tectonic inferences from oxygen isotopes in volcano-plutonic complexes of the India-Asia Collision Zone, NW India. *Tectonics*, 6(3): 261-273.

- Sun, S.-S. and McDonough, W.F., 1989. Chemical and isotopic systematics of oceanic basalts: implications for mantle composition and processes. Geological Society, London, Special Publications, 42(1): 313-345.
- Sundell, K.E., Gehrels, G.E. and Pecha, M.E., 2021. Rapid U-Pb geochronology by laser ablation multi-collector ICP-MS. Geostandards and Geoanalytical Research, 45(1): 37-57.
- Thanh, N.X., Rajesh, V., Itaya, T., Windley, B., Kwon, S. and Park, C.-S., 2012. A Cretaceous forearc ophiolite in the Shyok suture zone, Ladakh, NW India: Implications for the tectonic evolution of the Northwest Himalaya. Lithos, 155: 81-93.
- van Hinsbergen, D.J., 2022. Indian plate paleogeography, subduction and horizontal underthrusting below Tibet: paradoxes, controversies and opportunities. National Science Review, 9(8): nwac074.
- Vermeesch, P., 2021. On the treatment of discordant detrital zircon U–Pb data. Geochronology, 3(1): 247-257.
- Wendt, I. and Carl, C., 1991. The statistical distribution of the mean squared weighted deviation. Chemical Geology: Isotope Geoscience Section, 86(4): 275-285.
- Xue, W., Hu, X., Garzanti, E., Ma, A., Lai, W. and Li, C., 2022. Discriminating Qiangtang, Lhasa, and Himalayan sediment sources in the Tibetan Plateau by detrital-zircon UPb age and Hf isotope facies. Earth-Science Reviews: 104271.
- Zhuang, G., Najman, Y., Guillot, S., Roddaz, M., Antoine, P.-O., Métais, G., Carter, A., Marivaux, L. and Solangi, S.H., 2015. Constraints on the collision and the pre-collision tectonic configuration between India and Asia from detrital geochronology, thermochronology, and geochemistry studies in the lower Indus basin, Pakistan. Earth and Planetary Science Letters, 432: 363-373.

Chapter Three

Paleocene latitude of the Kohistan-Ladakh arc indicates multi-stage India-Eurasia collision

Material from:

Martin et al., "Paleocene latitude of the Kohistan-Ladakh arc indicates multi-stage India-Eurasia collision," Proceedings of the National Academy of Sciences, published online 04 November 2020, copyright National Academy of Science 2020.

Reprinted with permission of PNAS

3.1 Abstract

We report paleomagnetic data showing that an intra-oceanic Trans-Tethyan subduction zone existed south of the Eurasian continent and north of the Indian subcontinent until at least Paleocene time. This system was active between 66 – 62 Ma at a paleolatitude of 8.1 ± 5.6 °N, placing it 600 – 2,300 km south of the contemporaneous Eurasian margin. The first ophiolite obductions onto the northern Indian margin also occurred at this time, demonstrating that collision was a multistage process involving at least two subduction systems. Collisional events began with collision of India and the Trans-Tethyan subduction zone in Late Cretaceous to Early Paleocene time, followed by the collision of India (plus Trans-Tethyan ophiolites) with Eurasia in mid-Eocene time. These data constrain the total post-collisional convergence across the India-Eurasia convergent zone to 1,350 – 2,150 km, and limit the north-south extent of northwestern Greater India to < 900 km. These results have broad implications for how collisional processes may affect plate reconfigurations, global climate, and biodiversity.

3.2 Significance Statement

We present paleomagnetic constraints on the latitude of an intra-oceanic subduction system that is now sutured between India and Eurasia in the western Himalaya. Our results demonstrate that the India-Eurasia collision was a multi-stage process involving at least two subduction systems rather than a single-stage collision event. This resolves the discrepancy between the amount of convergence and the observed crustal shortening in the India-Eurasia collision system, as well as the 10 – 15 Ma time lag between collision onset in India and the initiation of collision related deformation and metamorphism in Eurasia. The presence of an additional subduction system in the Neotethys ocean also explains the rapid India-Eurasia convergence rates in the Cretaceous and global climate variations in the Cenozoic.

3.3 Introduction

Classically, the India-Eurasia collision has been considered to be a single-stage event that occurred at 50 – 55 million years ago (Ma) (Garzanti et al., 1987; Hodges, 2000). However, plate reconstructions show thousands of kilometers of separation between India and Eurasia at the inferred time of collision (Patriat and Achache, 1984; Torsvik et al., 2012). Accordingly, the northern extent of Greater India was thought to have protruded up to 2,000 km relative to present-day India (Patzelt et al., 1996; Van Hinsbergen et al., 2011) (see Figure 3-1). Others have suggested that the India-Eurasia collision was a multi-stage process that involved an east-west trending Trans-Tethyan subduction zone (TTSZ) situated south of the Eurasian margin (Aitchison et al., 2000; Jagoutz et al., 2015; Zahirovic et al., 2012) (see Figure 3-1). Jagoutz et al. (2015) concluded that collision between India and the TTSZ occurred at 50 – 55 Ma and the final continental collision occurred between the TTSZ and Eurasia at 40 Ma (Bouilhol et al., 2013; Jagoutz et al., 2015). This model reconciles the amount of convergence between India and Eurasia with the observed shortening across the India-Eurasia collision system with the addition of the Kshiroda oceanic plate. Additionally, the presence of two subduction systems can explain the rapid India-Eurasia convergence rates (up to 16 mm a^{-1}) that existed between 135 Ma and 50 Ma (Jagoutz et al., 2015), as well as variations in global climate in the Cenozoic (Jagoutz et al., 2016).

While the existence of the TTSZ in the Cretaceous is not disputed, the two conflicting collision models make distinct predictions about its paleolatitude in Late-Cretaceous to Paleocene time; these can be tested using paleomagnetism. In the single-stage collision model, the TTSZ amalgamated with the Eurasian margin prior to $\sim 80 \text{ Ma}$ (Pettersen and Windley, 1985) at a latitude of $\geq 20^\circ \text{N}$ (Lippert et al., 2014; van Hinsbergen et al., 2019). In contrast, in the multi-stage model,

the TTSZ remained near the equator at $\leq 10^{\circ}\text{N}$, significantly south of Eurasia, until collision with India (Jagoutz et al., 2015) (see Figure 3-1).

No undisputed paleomagnetic constraints on the location of the TTSZ are available in the central Himalaya (Garzanti, 2008; Hu et al., 2016a; Zhang et al., 2014). Westerweel et al. (2019) showed that the Burma Terrane, in the eastern Himalaya, was part of the TTSZ and was located near the equator at 95 Ma, but they do not constrain the location of the TTSZ in the time period between 50 – 80 Ma, which is required to test the two collision hypotheses. In the western Himalaya, India and Eurasia are separated by the Bela, Khost and Muslimbagh ophiolites and the 60,000 km² intra-oceanic Kohistan Ladakh arc (Beck et al., 1996; Tapponnier et al., 1981) (see Figure 3-1). These were obducted onto India in the Late-Cretaceous to Early Paleocene (Beck et al., 1996), prior to the closure of the Eocene to Oligocene Katawaz sedimentary basin (Tapponnier et al., 1981) (see Figure 3-1). The Kohistan-Ladakh arc contacts the Eurasian Karakoram terrane in the north along the Shyok suture and the Indian plate in the south along the Indus suture (Tahirikheli, 1979) (see Figure 3-1). Previous paleomagnetic studies suggest that the Kohistan-Ladakh arc formed as part of the TTSZ near the equator in the early Cretaceous but provide no information on its location after 80 Ma (Ahmad et al., 2000; Klootwijk et al., 1979; Zaman et al., 2013; Zaman and Torii, 1999). While pioneering, these studies lack robust age constraints, do not appropriately average paleosecular variation of the geodynamo, and do not demonstrate that the measured magnetizations have not been reset during a subsequent metamorphic episode.

3.4 Geology of the Khardung Volcanics

The Khardung volcanics consist of rhyolitic lava flows, welded tuffs, ash and volcano-sedimentary conglomerates locally intruded by meter-scale dykes of intermediate composition. The volcanic stratigraphy is deposited onto and locally intruded by the plutonic rocks of the Ladakh batholith, and contacts metasedimentary and metavolcanic rocks of the Shyok suture zone along the Khalsar fault (see Figure 3-2). Rhyolite flows are 1 – 5 m thick and are typically very fine grained, often with chilled margins at their base and upper surface (see Figure 3-3). Some rhyolites exhibit vesicular or porphyritic textures but most are equigranular and massive. Four 30 – 60 m thick rhyolite units are exposed in the sampled section and have a slightly coarser grain size and no discernable internal flow or bedding structures. Throughout the section, volcano-sedimentary deposits are interbedded with the rhyolites becoming more frequent in the uppermost 300 m. These laterally extensive deposits are typically 30 – 50 cm thick with angular, poorly sorted, lithic clasts, < 0.5 – 5 mm in diameter. The sediments provide clear bedding planes to determine the paleohorizontal plane and often exhibit graded bedding, trough-crossbedding and localized channelization indicating that the sequence has not been overturned. The conglomerates sampled for our conglomerate tests are both ~ 4 m thick and contain sub-angular intermediate-rhyolitic clasts, 10 – 80 cm diameter, and supported in a matrix of fine-grained lithic sand and ash particles (see Figure 3-3). Ash-flow tuffs, typically 3 – 8 m thick with 5 – 15 cm volcanic bombs supported in very fine and glassy matrix, are also present in the uppermost 300 m of the section. The metamorphic overprint in the sediments is weak to absent with only minor deuteritic metamorphism related to the dewatering and degassing of the volcanic flows themselves. The preservation of cristobalite in the samples indicates that no significant post depositional metamorphism has affected these rocks.

Specimens cut from cores KH25-A and KH14-D were polished and imaged in reflected light with a Zeiss petrographic microscope and using backscattered scanning electron microscopy (BSEM) in the MIT Electron Microprobe Facility (see Figure 3-4). In KH14-D, the dominant opaque phase is up to 300 μm grain-size, cubic, pale-yellow colored and isotropic with a high reflectance and high polishing hardness, suggesting that it is pyrite (FeS_2) and possibly other iron sulfides. In sample KH25-A, the dominant opaque phase is mostly $< 5 \mu\text{m}$ grain-size and appears grey in reflected light, has low reflectivity, and usually has an irregular grain shape, suggesting that it is a secondary alteration product. Wavelength-dispersive x-ray spectroscopy (WDS) showed that these grains are FeOOH (either goethite or lepidocrocite). While not observed with electron or optical microscopy, the peak unblocking temperatures of our specimens strongly suggest that magnetite (Fe_3O_4) is present and is the dominant magnetization carrier. The lack of detection of magnetite using microscopy is expected given that hysteresis experiments (see Figure 3-5) suggest that the magnetite grains present are single domain (S-D) and therefore very small ($< 500 \text{ nm}$) and so would be difficult to detect given the maximum resolution of the BSEM images ($100 - 200 \text{ nm}$). In addition, the magnetic moment to volume ratio of our specimens ($\sim 5 \times 10^{-8} \text{ Am}^2$ and $\sim 1 \times 10^{-7} \text{ Am}^2$, for KH14-D and KH25-A respectively) suggests that magnetite grains are present in very low concentration ($< 1 \text{ ppb}$) and so would easily evade detection given the limited field of view of the Electron Microprobe.

3.5 Rock Magnetism

The domain state of magnetite in a representative subset of bedded volcanic samples (KH01B, KH03F, KH14A and KH25A) was characterized by acquiring hysteresis curves. Hysteresis curves were measured in the Ross Laboratory, MIT Department of Materials Sciences and Engineering on an ADE model 1660 vibrating sample magnetometer (VSM). Hysteresis loops were acquired for applied fields of -1 to 1 T and were corrected by removing any paramagnetic or diamagnetic signals (see Figure 3-5). The corrected curves were used to ascertain the saturation magnetization (M_s), the saturation remanent magnetization (M_{rs}), the coercivity of remanence (H_{cr}) and the coercivity (H_c) for each sample (Table 2-2). The ratio of M_{rs}/M_s and H_{cr}/H_c were calculated to assess the domain state of magnetite on a Dunlop-Day plot (Day et al., 1977; Dunlop, 2002) (see Figure 3-6).

All of the samples plot in the pseudo-single domain (PSD) range on the Day plot suggesting they have reliable paleomagnetic recording properties. Samples KH01B and KH03F show ‘wasp-waisted’ hysteresis behavior, indicative of a mixture of single-domain and PSD carriers (Roberts et al., 1995). Samples KH14A and KH25A are approaching the sensitivity limit of the VSM but their hysteresis parameters also indicate a PSD state. These observations are consistent with the position of each sample on the Day plot; KH01B and KH03F have higher M_{rs}/M_s ratios and lower H_{cr}/H_c ratios placing them closer to the SD region.

3.6 Thermal Demagnetization

Most specimens contained a low temperature and low coercivity overprint (LTC) that was removed in AF steps and thermal steps below 200 °C (see Figure 3-7). These components align with the present-day magnetic field direction in the study location and are interpreted to represent a recent overprint, either due to viscous remanent magnetization (VRM) (Pullaiah et al., 1975), or chemical remanent magnetization (CRM) carried by goethite (see Figure 3-8). In most of the specimens, stable, origin-trending, high temperature magnetization components with blocking temperatures consistent with magnetite were isolated in the thermal demagnetization steps between 500 °C and 580 °C (HT1, see Figure 3-7 and Dataset S1). In a small subset of the specimens, stable, high-temperature components with blocking temperatures consistent with hematite were also isolated in the thermal steps between 600 °C and 680 °C (HT2, see Figure 3-7 and Dataset S1). Samples from one site (KH06) had stable, origin-trending, magnetization components that were isolated in the thermal demagnetization steps between 200 °C and 350 °C that could be carried by titanomagnetite, pyrrhotite or goethite (LT2, see Figure 3-7 and Dataset S1).

To test if the high temperature magnetic components (HT1 and HT2) represent a later overprinting magnetization, we conducted two conglomerate tests (Van der Voo, 1990) using 46 clast specimens from an intraformational conglomerate unit at site KH12 (near the top of the section) and 23 clasts from another intraformational conglomerate unit at site KP3 (near the bottom of the section) (see Figure 3-9). To test the randomness of clast magnetization directions, we performed a Watson (1956) test on the distribution of tilt-corrected HT1 and HT2 components from the clast specimens. In the Watson (1956) test, for the clast magnetization directions to be considered randomly distributed, the magnitude of the unit-vector sum (R) of the clast magnetizations should be less than a critical value R_0 which is defined as a function of the number

of clasts (n). The distribution of tilt-corrected HT1 magnetization directions from $n = 46$ igneous clasts at site KH12 yielded $R = 6.305$, which is considerably less than the 95% confidence critical value $R_0 = 10.947$. Likewise, the same test for the HT2 directions ($n = 30$) from the clasts at site KH12 yields $R = 7.572$, less than the 95% confidence critical value $R_0 = 8.840$. The distribution of tilt-corrected HT1 components from igneous clasts at site KP3 ($n = 18$) yielded $R = 5.359$, which is less than the 95% critical value $R_0 = 6.848$. These results demonstrate that to 95% confidence we cannot distinguish the distributions of the HT1 and HT2 magnetization directions among clasts in these conglomerates from a random distribution. This means that the conglomerate test passes, and both HT1 and HT2 magnetizations are not regional nor local overprints and therefore can be considered primary remanent magnetizations throughout our studied section.

We interpret the HT1 component to represent a primary thermoremanent magnetization (TRM) acquired as the volcanic flows cooled below the magnetite Curie temperature. It is plausible that HT2 components either represent a primary TRM that was acquired as flows containing hematite cooled through 680 °C, or a chemical remnant magnetization (CRM) acquired during deuteric alteration converting magnetite to hematite. The most likely explanation for the contemporaneous formation of a magnetite TRM and hematite CRM in the Khardung volcanics is deuteric auto-metamorphism during dewatering and degassing of the water-rich felsic flows as they cooled. In either case, TRM or CRM, the fact that the HT2 magnetization directions pass the conglomerate test, and are almost exclusively near-parallel to HT1 directions from the same samples specimens, suggests that even if they are a CRM they were acquired very soon after the flows were formed and can still be considered primary. Primary site-mean directions were calculated from the HT magnetization directions that dominated the NRM using Fisher statistics

(Fisher, 1953) and corrected for bedding tilt. Three sites were excluded from further analysis due to their large site-mean uncertainties ($\alpha_{95} > 15^\circ$) (Butler, 1998).

A bootstrap reversal test demonstrated that the two populations of site-mean directions are statistically antipodal to each other and are therefore highly likely to be the result of reversals in polarity of Earth's geodynamo (Tauxe, 2010) (see Figure 3-10). The antipodal populations of site-mean directions correlate to all but one of the expected geomagnetic polarity chrons (see main text Figure 3-11). It is unsurprising that the C27n chron is not observed because it is relatively short in duration (< 250 kyr). Either there were no eruptions in that time or that we did not sample the flows in which it is preserved. Additionally, since our oldest age constraint is a maximum deposition age rather than an absolute deposition age, we conservatively assume that the two lowermost paleomagnetic sites are part of the C29n chron despite the age placing them within the opposite polarity C29r chron. It is also possible that these two sites actually correlate to C30n and C29r is not observed. If this is the case, it would only increase the number of magnetic polarity chrons preserved, strengthening our reversal test and increasing the time range included in our dataset. The passed reversal and conglomerate tests demonstrate that the section has not been overprinted by subsequent events that would have obliterated the reversal record (Van der Voo, 1990).

The time-averaged paleomagnetic pole was determined using northern hemisphere virtual geomagnetic poles because they are more likely to have a Fisher distribution than site-mean paleomagnetic directions (Deenen et al., 2011). We used the quantile-quantile method (Fisher and Lewis, 1983) to assess whether the distribution of VGPs is indeed Fisher-distributed (see Figure 3-12). We obtain the test statistics $M_u = -0.904$ and $M_e = 0.533$ that are less than their respective critical values [$M_u (critical) = 1.207$, $M_e (critical) = 1.095$ for $n = 18$], indicating that the Khardung VGP

distribution is consistent with a Fisher model (see Figure 3-12). Northern hemisphere VGP positions for each site and the paleomagnetic mean pole for the Khardung volcanics are shown in Table 2-3 and Figure 3-13.

3.7 Paleomagnetism of the Khardung Volcanics

Paleocene volcanic rocks from the Kohistan-Ladakh arc provide an unrivaled opportunity to use paleomagnetism to reconstruct the paleolatitude of the TTSZ shortly before onset of collision and test the two conflicting models. We sought to determine the paleolatitude of the Paleocene Khardung volcanics on the northern margin of the Kohistan-Ladakh arc in Ladakh, India. The ~3,000 m thick stratigraphy of the Khardung volcanics formed between 70 Ma and 60 Ma (Dunlap and Wysoczanski, 2002; Lakhan et al., 2020) and comprises rhyolitic and andesitic lava flows, tuffs, ignimbrites, agglomerate and minor clastic sediments at the top of the section (see Figure 3-2 and Figure 3-3).

Zircons from ash layers and lava flows distributed throughout the upper 1,000 m of the exposed section were dated using U-Pb CA-ID-TIMS geochronology (Table 2-1 and Figure 3-14). The U-Pb ages are consistently younger from the bottom to the top of the stratigraphy indicating that there are no major repetitions or duplications caused by unidentified fault zones. Zircons separated from a rhyolite flow (LB13-17) sampled from the bottom part of the studied section yield a Th-corrected $^{206}\text{Pb}/^{238}\text{U}$ weighted mean eruption/deposition age of 65.038 ± 0.12 Ma (2σ external uncertainty) and zircons from the intermediate ash layer (KA1) yield a Th-corrected $^{206}\text{Pb}/^{238}\text{U}$ weighted mean eruption/deposition age of 62.097 ± 0.079 Ma. Two samples yielded inherited zircon populations, such that only a maximum depositional age could be constrained from the youngest zircon in the sample. The rhyolite flow sampled from the top of the section (LB-13-16) has a Th-corrected $^{206}\text{Pb}/^{238}\text{U}$ zircon maximum depositional age of 61.636 ± 0.11 Ma and the interlayered ash horizon (KA4D) at the bottom of the sampled stratigraphy has a Th-corrected $^{206}\text{Pb}/^{238}\text{U}$ zircon maximum depositional age of 66.100 ± 0.085 Ma. Based on these results the

absolute time within our sampled section is 61.64 – 66.10 Ma, a time span of 4.46 million years (Ma) (see Figure 3-15).

We obtained a total of 191 oriented 2.2-cm diameter cores from 21 sites across the dated section. At each site, the orientations of multiple bedding planes were measured and a site-specific mean was calculated and applied to the magnetic data to correct for bedding tilt (see Figure 3-11). The sites used to estimate the paleolatitude each consist of 5 – 13 core samples from single flows that should have acquired a near-instantaneous (a few hours) thermoremanent magnetization (TRM) from the local magnetic field as they cooled. For most samples, low coercivity/low temperature (LCT) overprints were removed using alternating field demagnetization steps between 1 mT and 20 mT and thermal demagnetization steps between 100 °C and 300 °C (see Figure 3-7 and Figure 3-8). Stable high temperature magnetization components consistent with magnetite were isolated in the thermal demagnetization steps between 500 °C and 580 °C. In a small subset of the samples, stable, high-temperature components unblocking between 600 °C and 680 °C consistent with hematite were also present, oriented parallel to the magnetite component (see SI Appendix, Figure 3-7 and Dataset S1).

We confirmed the absence of significant post-eruption remagnetization using a reversal test and two conglomerate tests consisting of 69 cores from clasts from two intraformational conglomerate units near the top and bottom of the sampled section (Van der Voo, 1990) (Figure 3-9 and Figure 3-10). The high-temperature magnetization directions from the clasts in the conglomerate units are random with $\geq 95\%$ certainty (Watson and Williams, 1956), therefore indicating a lack of total remagnetization since deposition. The paleomagnetic measurements of the bedded volcanics define two antipodal populations (see Figure 3-11) extending over three geomagnetic polarity reversals that correlate to chrons C29n, C28r, C28n, C27r and C26r, showing

that they have not been overprinted (Barnet et al., 2019) (see Figure 3-15). Our successful conglomerate tests and reversal test unequivocally demonstrate that the HT1 and HT2 directions in the samples are primary (Buchan, 2013; Van der Voo, 1990).

We obtain a Fisher mean paleomagnetic pole located at a latitude of 64.0°N and a longitude of 266.4°E with an 95% confidence angle of $A_{95} = 5.6^{\circ}$ (see Figure 3-13). Secular variation should have been successfully averaged by our measurements given the > 4 million year (Ma) time span recorded within the section (including three reversals) and the fact that the value of A_{95} is within the observed range for the modern geomagnetic field ($5.3^{\circ} < A_{95} < 13.3^{\circ}$, for $N = 18$) (Buchan, 2013; Deenen et al., 2011; Van der Voo, 1990). The measured paleomagnetic pole constrains the paleolatitude of the Kohistan-Ladakh arc to $8.1 \pm 5.6^{\circ}\text{N}$ at $61.64 - 66.10$ Ma, significantly south of the Eurasian margin which was situated at $21.2 \pm 2.1^{\circ}\text{N}$ at the same time (van Hinsbergen et al., 2019). This constrains the location of the TTSZ to $600 - 2300$ km south of the Eurasian margin in the Paleocene (see Figure 3-16).

3.8 Discussion

Our results indicate that until at least ~ 61.6 Ma, and probably until 50 – 55 Ma, the Neotethys ocean was subducted along two separate subduction systems, an active continental system at the southern Eurasian margin, and the TTSZ located in the equatorial Neotethys (Aitchison et al., 2000; Jagoutz et al., 2015; Zahirovic et al., 2012) (see Figure 3-16). These findings support multi-stage tectonic evolution models for the western Himalaya in which the India-TTSZ-Eurasia collision began with collision between the TTSZ and the northern margin of India in the Late Cretaceous to Paleocene, and ended with final continental collision in the mid-Eocene (Bouilhol et al., 2013; Jagoutz et al., 2015) (see Figure 3-16).

The termination of intra-oceanic subduction during the first stage of collision resulted in the Late Cretaceous/Early Paleocene obduction of the Bela, Muslimbach and Khost ophiolites onto the north-western margin of India (Beck et al., 1996), as well as the formation of the 50 – 55 Ma Indus suture zone between the Kohistan-Ladakh arc and India (Bouilhol et al., 2013). It also caused a reduction in the rate of northward motion of India at 52 ± 4 Ma (Jagoutz et al., 2015). The final India-TTSZ-Eurasia continent-continent collision occurred along the Shyok-Tsangpo suture, not the Indus-Tsangpo, and the age of this final collision is constrained to 40.4 ± 1.3 Ma by geochemical and isotopic changes in the Kohistan-Ladakh batholith (Bouilhol et al., 2013). This explains why the India-Eurasia convergence rate continued to decrease until 40 – 45 Ma (Cande et al., 2010).

Recent Cretaceous age estimates for the Kohistan-Ladakh arc-Eurasia collision based on sediment provenance interpretations of detrital zircon U-Pb age data (Borneman et al., 2015; Najman et al., 2017) are incompatible with our results. We note that Borneman et al. (2015) report that Eurasia-derived detrital zircons were deposited on Kohistan-Ladakh arc rocks at 80 Ma despite

previous work showing that the sediments they sampled were deposited on the Eurasian margin, not the Kohistan-Ladakh arc (Thanh et al., 2012; Upadhyay et al., 1999; Weinberg and Dunlap, 2000). Similarly, Najman et al. (2017) interpret a uniquely Eurasian provenance for seven 200 – 220 Ma grains from Paleocene Indian passive margin sediments, but these could have been reworked from Late Triassic and Early Jurassic Indian passive margin sediments which contain similar age populations (Cai et al., 2016; Guangwei et al., 2010). Unlike our paleomagnetic data, these detrital zircon provenance investigations are limited by the fact that the vast area of Greater Indian landmass, now lost beneath Tibet, likely contributed detritus of unknown age to passive margin sediments before the collision.

Geological evidence for a multi-stage collision history of the Himalaya is best preserved in the western Himalaya where the Kohistan-Ladakh arc and other ophiolite bodies clearly demarcate the TTSZ and east of the Namche Barwa syntaxis where the TTSZ is represented by the Burma Terrane (Westerweel et al., 2019). The exposure of the Kohistan-Ladakh arc is ~ 200 km wide in north-east Pakistan but reduces to < 20 km in south-western Tibet where it disappears at the intersection of the great counter thrust system and the Karakoram fault (Murphy et al., 2000)(see Figure 3-1). In south-central Tibet the record of the TTSZ is fragmentary due to the large-scale back-thrusting along the great counter thrust system that obscures the complex evolution of the Tsangpo suture zone (Burg and Chen, 1984; Kapp and DeCelles, 2019; Yin et al., 1999). It is not surprising that the geological record of the multiple stages of the India-TTSZ-Eurasia collision is limited in the central part of the Himalayan belt, where shortening and under-thrusting were presumably highest.

The dismembered ophiolites in the Tsangpo suture zone could have formed in the TTSZ (Aitchison et al., 2000; Hébert et al., 2012), or in the forearc of the continental margin (Hu et al.,

2016b; Zhang et al., 2014). While the Xigaze ophiolite likely formed on the southern edge of Eurasia, it has recently been suggested that it moved southward in the Cretaceous during back arc extension after 85 - 90 Ma becoming part of the TTSZ (Kapp and DeCelles, 2019). However, subduction along the TTSZ initiated in the Jurassic, ~154 Ma (Jagoutz et al., 2019), and not in the Cretaceous. Alternatively, if the TTSZ and Xigaze units are unrelated, fragments of the TTSZ could remain unidentified in the accretionary mélangé south of the Xigaze ophiolite or elsewhere in the less well studied areas of the suture zone. Regardless, our results require that a major oceanic basin existed in between India and Eurasia at the same time Cretaceous arc detritus was deposited in Indian passive margin sediments in south-eastern Tibet at 58.5 – 60 Ma (DeCelles et al., 2014), making the TTSZ the likely sedimentary source rather than Eurasia.

The near-equatorial location of the TTSZ in the Paleocene implies that a significant proportion of the 2,800 – 3,600 km India-Eurasia convergence since 50 – 55 Ma (Molnar and Stock, 2009) can be accounted for by pre-collisional subduction of the Kshiroda oceanic plate beneath Eurasia until ~ 40 Ma rather than by thickening and extrusion of Indian and Eurasian continental crust. Indeed, the extrusion of south-east Asia started later, at ~ 36 Ma (Leloup et al., 2001), and metamorphism and melting in the High Himalaya began after 40 Ma (Burg and Bouilhol, 2019). Comparison of our data to the well-constrained paleolatitudes of the Eurasian margin and India (Lippert et al., 2014; van Hinsbergen et al., 2019) suggests that the Kshiroda plate was 1450 ± 850 km wide, at the time of the TTSZ-India collision (see Figure 3-16). Therefore, the convergence accommodated by deformation in the Himalayan orogen was 1350 – 2150 km, similar to the 1050 – 1950 km combined Eurasian and Indian shortening observed across western and eastern Tibet and the Himalayan fold and thrust belt (Van Hinsbergen et al., 2011). Our results also constrain the size of Greater India in the western Himalaya to < 900 km, consistent

with the observed ~ 600 km extent of Indian continental lithosphere under-thrusting beneath Eurasia (Li et al., 2008), and reconstructions of Greater India based on Cretaceous paleomagnetic data (van Hinsbergen et al., 2019).

In conclusion, we present robust and reliable paleomagnetic data constraining the location of the TTSZ to 8.1 ± 5.6 °N in the Paleocene, 600 – 2,300 km south of the Eurasian margin. Our results require that two subduction zones were active throughout the closure of the Neotethys until the Paleocene. We have also shown that the India-Eurasia collision was a multi-stage process that began with the accretion of the TTSZ onto India in the Late-Cretaceous to Paleocene and ended with continent-continent collision in the Eocene at ~ 40 Ma. The north-south extent of Greater India in the west was ~ 900 km and the final collision occurred along the Shyok-Tsangpo suture zone, not the Indus-Tsangpo. The combined activity of both Neotethyan subduction systems explains the anomalously rapid motion of India in the Late Cretaceous (Jagoutz et al., 2015) and the low-latitude obduction of ophiolites associated with the two stages of India-Eurasia collision caused the global cooling observed throughout the Cenozoic (Jagoutz et al., 2016). Our study demonstrates that the peripheries of the Himalayan belt provide crucial insight into the geological evolution of the India-TTSZ-Eurasia collision system that is difficult to discern in the central part of the orogen.

3.9 Materials and Methods

3.9.1 U-Pb Zircon Geochronology

Zircons were separated from each sample using standard crushing and density separation techniques. U-Pb geochronology was completed using the chemical abrasion-isotope dilution-thermal ionization mass spectrometry (CA-ID-TIMS) technique at MIT, following methods slightly modified from Mattinson (2005) and outlined in the appendix to Eddy et al. (2016). Zircons were first annealed at 900 °C and 1 atm for 60 hours. Subsequently, individual zircons were loaded into Teflon™ microcapsules with 100 – 125 µl of 29M HF. The microcapsules were then loaded into a Parr dissolution vessel and held at 215 °C for 12 – 13 hours. The resulting solutions were discarded and each individual zircon was repeatedly rinsed in H₂O, and 6N HCl. After rinsing, approximately ~ 0.01 g of EARTHTIME ²⁰²Pb-²⁰⁵Pb-²³³U-²³⁵U isotopic tracer (McLean et al., 2015) and 75-100 µl of 29M HF were added to each microcapsule. The microcapsules were then re-loaded into a Parr dissolution vessel and held at 215 °C for 48 – 60 hours for total digestion. The solutions were subsequently dried down and dissolved in 6N HCl at 180°C for ~12 hours to convert the samples to chloride form. Uranium and Pb were purified from the dissolved sample with AG-1 X8 200-400 mesh anion exchange resin using methods modified from Krogh (1972). Samples were first loaded onto 50 µl anion exchange columns in 50 – 75 µl of 3N HCl and rinsed dropwise to remove trace elements. Then Pb and U were eluted using 200 µl of 6N HCl and 250 µl of H₂O, respectively. Samples were dried down with a microdrop of 0.05M H₃PO₄ prior to analysis via TIMS.

All of the data presented in this study was analyzed on the IsotopX Phoenix TIMS or the VG Sector 54 TIMS at MIT. Lead was run as a metal and measured by peak hopping on a Daly photomultiplier. Uranium was analyzed as UO₂ and was measured statically on a series of faraday

cups. Measured ratios were corrected assuming an $^{18}\text{O}/^{16}\text{O}$ of 0.00205 ± 0.00004 (2σ), corresponding to the modern atmospheric value Nier (1950). Corrections for mass dependent fractionation of U was done using the known ratio of $^{233}\text{U}/^{235}\text{U}$ in the ET535 isotopic tracer and assuming a $^{238}\text{U}/^{235}\text{U}$ of 137.818 ± 0.045 (2σ), which represents the mean value of $^{238}\text{U}/^{235}\text{U}$ measured in natural zircon (Hiess et al., 2012). Corrections for Pb fractionation were done using an α (% amu) calculated from repeat runs of the NBS 981 Pb isotopic standard for the IsotopX Phoenix TIMS and an α calculated from 53 Pb measurements on the Sector 54 TIMS of the ET2535 isotopic tracer, which contains a known $^{202}\text{Pb}/^{205}\text{Pb}$ ratio.

A well-known problem in the measurement of small amounts of Pb by TIMS is the effect of isobaric interferences. Known isobaric interferences include BaPO_4 and Tl and were corrected by measuring masses 201 and 203, assuming that they represent $^{201}\text{BaPO}_4$ and ^{203}Tl , and using the natural abundances of $^{202}\text{BaPO}_4$, $^{204}\text{BaPO}_4$, $^{205}\text{BaPO}_4$, and ^{205}Tl to correct the measurements of masses 202, 204, and 205. These corrections were often minor and have no effect on our data interpretations.

A correction for common Pb (Pb_c) was done by assuming that all Pb_c is from laboratory contamination and using the measured ^{204}Pb and a laboratory Pb_c isotopic composition to subtract the appropriate mass of Pb_c from each analysis. We consider the assumption that all measured Pb_c is from laboratory contamination to be robust, because the typical Pb_c seen in zircon analyses (< 1 pg) is comparable to the mass of Pb_c seen in procedural blanks. One hundred forty nine procedural blanks were used to quantify the Pb_c isotopic composition at MIT of $^{206}\text{Pb}/^{204}\text{Pb} = 18.13 \pm 0.96$ (2σ), $^{207}\text{Pb}/^{204}\text{Pb} = 15.28 \pm 0.60$ (2σ), $^{208}\text{Pb}/^{204}\text{Pb} = 37.04 \pm 1.77$ (2σ).

A correction for initial secular disequilibrium in the ^{238}U - ^{206}Pb system due to the exclusion of Th during zircon crystallization, e.g. (Schärer, 1984), was made for each analysis using a ratio

of zircon/melt partition coefficients (f_{ThU}) of 0.119. This value was determined from coexisting zircon rims/surfaces and high-SiO₂ glass from a dacitic lava from Mt. St. Helens (Claiborne et al., 2018). We view this as the best available analogue for silicic, hydrous, arc magmatism. Nevertheless, we have applied a generous uncertainty of ± 1 (2σ) for the calculated [Th/U]_{Magma}.

All data reduction was done with the Tripoli and ET_Redux software packages (Bowring et al., 2011) using the algorithms presented in McLean et al. (McLean et al., 2011). The U decay constants are from Jaffey et al. (1971). All isotopic data is presented in Table 2-1. Our age interpretations for each sample include weighted mean eruption/deposition ages for those samples that contain a coherent age population (LB13-17 and KA1) and maximum depositional ages for samples that did not include a coherent population (KA4D and LB13-16). These samples may have incorporated xenocrysts during eruption/deposition and we conservatively use the youngest grain as a maximum age. All uncertainties within the text are reported as external 2σ to aid in comparison with other geochronologic datasets produced by other techniques within the orogenic belt.

3.9.2 Paleomagnetism

Core samples were drilled in the field using a water-cooled electric hand drill. Cores were oriented in the field using an ASC Industries pomerooy orienting fixture and extracted from the outcrop using non-magnetic brass tools. One paleomagnetic specimen was cut from each core sample at MIT using an ASC Scientific dual blade rock saw. Measurements of the natural remanent magnetization (NRM) were obtained in the MIT Paleomagnetism Laboratory using a 2G Enterprises Superconducting Rock Magnetometer equipped with an automated sample handler (Kirschvink et al., 2008) inside a mu-metal magnetically shielded room with < 200 nT DC field. The specimens were subjected to stepwise alternating field (AF) and thermal demagnetization. AF

steps were applied in increments of 4 mT up to 20 mT and followed by thermal steps starting at 100 °C and increasing up to 600 °C or 680 °C in variable interval sizes from a maximum of 100 °C and minimum of 5 °C close to the Curie temperatures of the suspected principal magnetic carriers, magnetite (580 °C) and hematite (680 °C). Stable components of magnetization were isolated using principal component analysis (PCA) (Kirschvink, 1980) (see SI Appendix, Figure 3-6 for examples of typical sample demagnetizations and Dataset S1 for all fitting data). The domain state of magnetite was assessed using hysteresis curves (see Figure 3-5 and Figure 3-14) that were measured for a representative subset of bedded volcanic samples (KH01B, KH03F, KH14A and KH25A) on an ADE model 1660 vibrating sample magnetometer (VSM) in the Ross Laboratory, MIT Department of Materials Sciences and Engineering.

Site-mean magnetization directions were calculated using Fisher (1953) statistics and corrected for bedding tilt (see Figure 3-15 and Table 2-3). We calculated Northern hemisphere virtual geomagnetic pole (VGP) positions for each site (Table 2-3 and Figure 3-12) then we took the Fisher (1953) mean of the VGP data to obtain the overall paleomagnetic mean pole and associated A95 error envelope. We used the quantile-quantile method (Fisher and Lewis, 1983) to show that the VGP distribution is consistent with a Fisher model (see Figure 3-10).

To test for post-depositional remagnetization, we performed two conglomerate tests and a reversal test (Van der Voo, 1990). The conglomerate test samples consisted of cores from 46 clasts from an intraformational conglomerate unit at site KH12 (near the top of the section) and 23 clasts from another intraformational conglomerate unit at site KP3 (near the bottom of the section) (see Figure 3-8). We performed a Watson (1956) test for randomness on the distribution of tilt-corrected magnetic components from the clast specimens in each conglomerate unit. Both sets of conglomerate clast magnetization directions passed the conglomerate test, indicating that the clast

magnetization directions were primary (see SI Appendix, Information for further details). We used the bootstrap reversal test of Tauxe (2010) to demonstrate that the two populations of site-mean magnetization directions from the volcanic sequence are antipodal to each other, therefore passing the reversal test (see Figure 3-9). All paleomagnetic data-reduction and interpretation was carried out using the PmagPy software package (Tauxe et al., 2016).

3.10 Acknowledgements

We thank Jade Fischer, Benjamin Klein and Claire Bucholz for field assistance; C.P. Dorjay for logistical assistance; Tsewang Dorjay, Stanzin Khando and their family for accommodation at the Silok guesthouse in Khardung village, Ladakh. We also thank Athena Eyster, Caue Borlina, Jay Shah and Eduardo Lima for assistance with paleomagnetic and rock magnetic experiments at the MIT Paleomagnetism Laboratory and MIT Ross Laboratory, and Neel Chatterjee for assistance in the MIT Electron Microprobe Facility. This work was funded by the NSF Tectonics Program and financially supported by MIT's student travel program MISTI Indi

3.11 Figures and Captions

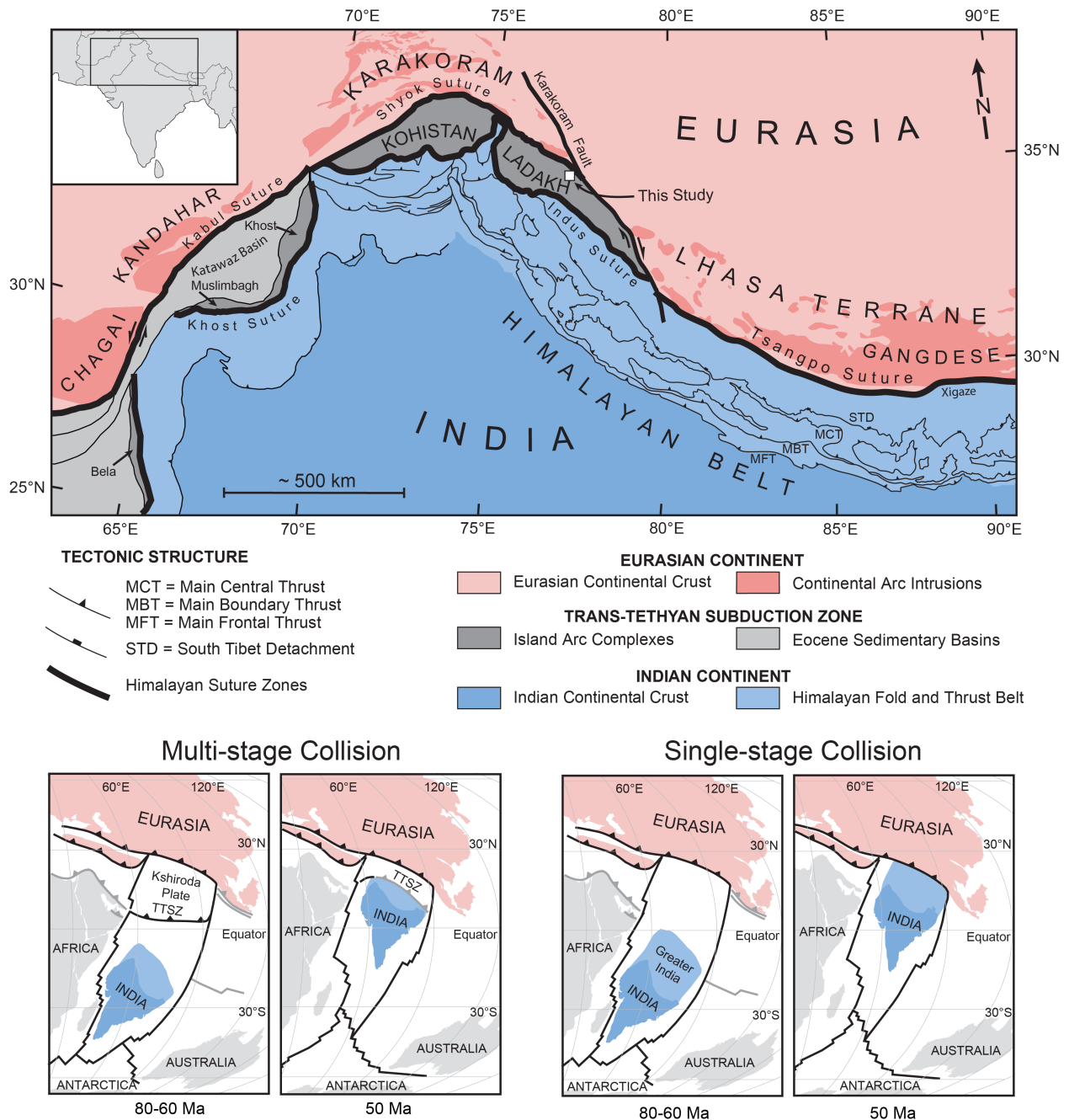


Figure 3-1: The first panel is an overview map of tectonic structure of the Karakoram-Himalaya-Tibet orogenic system. Blue represents India, red represents Eurasia and the Kohistan-Ladakh arc (KLA) is shown in grey. The different shades of blue highlight the deformed margin of the Indian plate that has been uplifted to form the Himalayan belt and the zones of darker red in within the Eurasian plate highlight the Eurasian continental arc batholith. Thick black lines denote the suture

zones which separate Indian and Eurasian terranes. The tectonic summary panels illustrate the two conflicting collision models and their differing predictions of the location of the Kohistan-Ladakh arc. India is shown in blue, Eurasia is shown in red, and the other nearby continents are shown in grey. Active plate boundaries are shown with black lines and recently extinct boundaries are shown with grey lines. Subduction zones are shown with triangular tick marks.

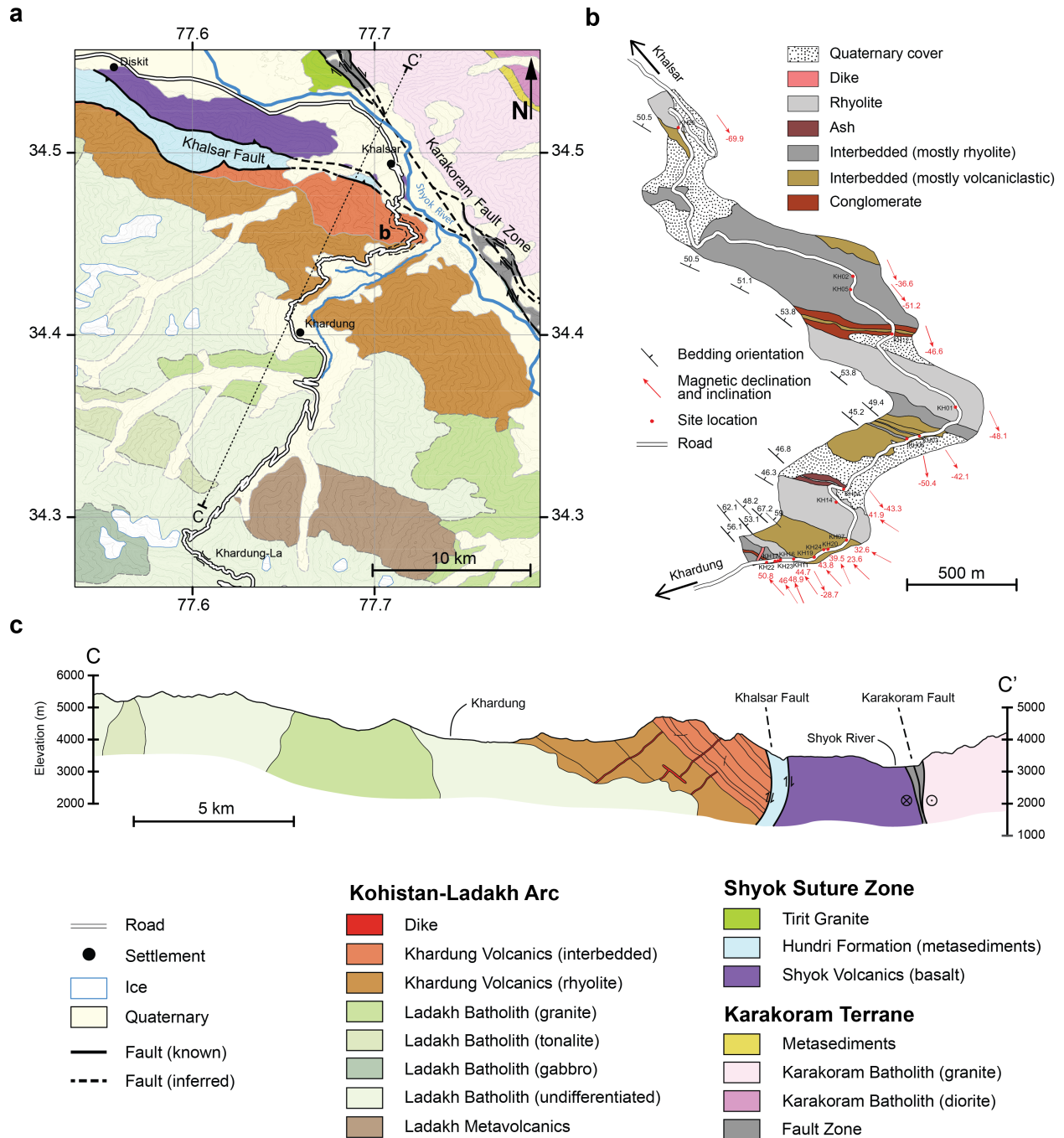


Figure 3-2: **a)** Geological map of the area around Khardung village extending from the Khardung-La pass to the Shyok river valley. **b)** Detailed geological map of the road cut transect where the paleomagnetic sampling was conducted. The map is annotated with the site locations, site-mean bedding orientations and paleomagnetic declinations and inclinations in geographic coordinates at each site. **c)** Geologic cross-section of the study area showing the structural setting of the Khardung volcanics.

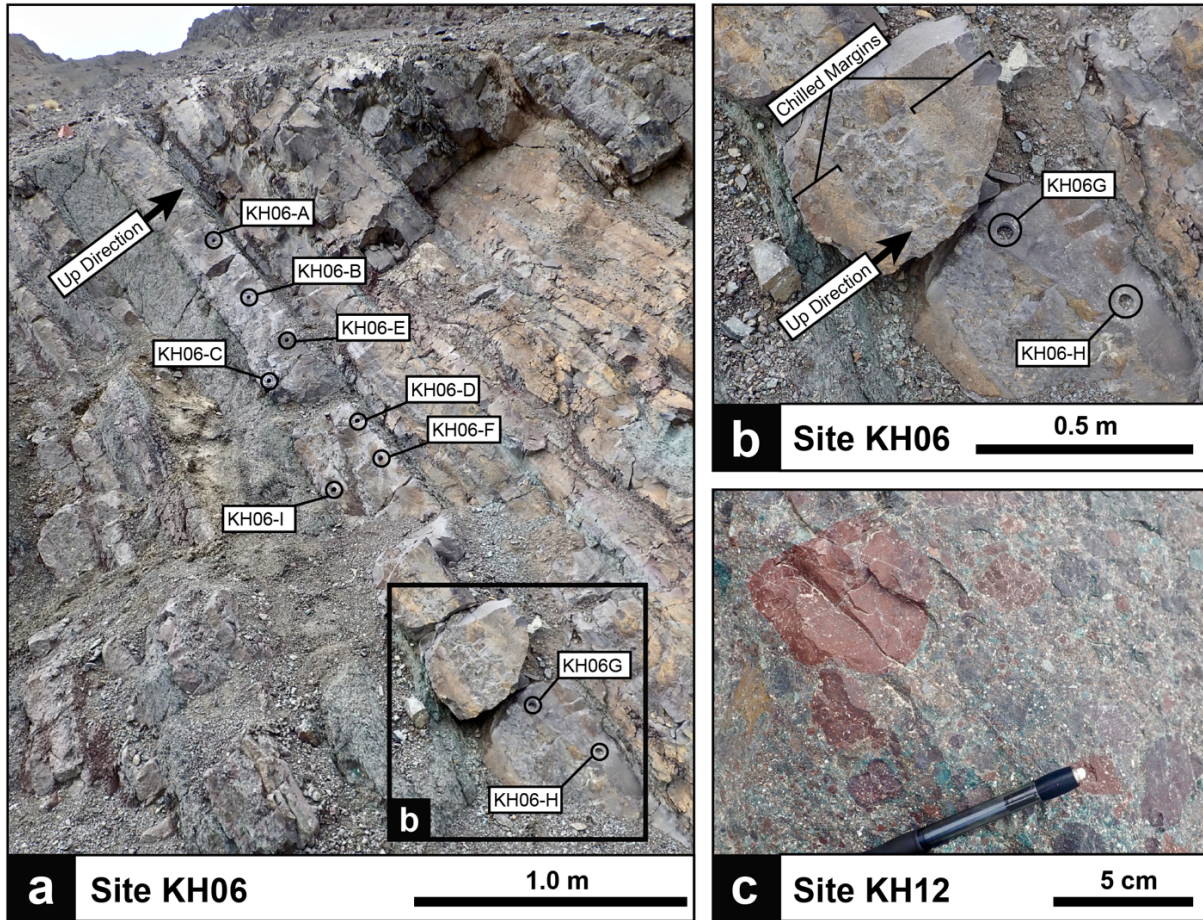


Figure 3-3: a) Lava flow interbedded with tuff and ash at site KH06 with locations of drill cores highlighted and up direction indicated. b) Blow up of lava flow sampled at site KH06 showing chilled lower and upper surfaces of the flow. c) conglomerate clasts that were drilled at site KH12 for a conglomerate test, transported clasts are exclusively rhyolitic and andesitic volcanic lithologies similar to other flows in the Khardung section.

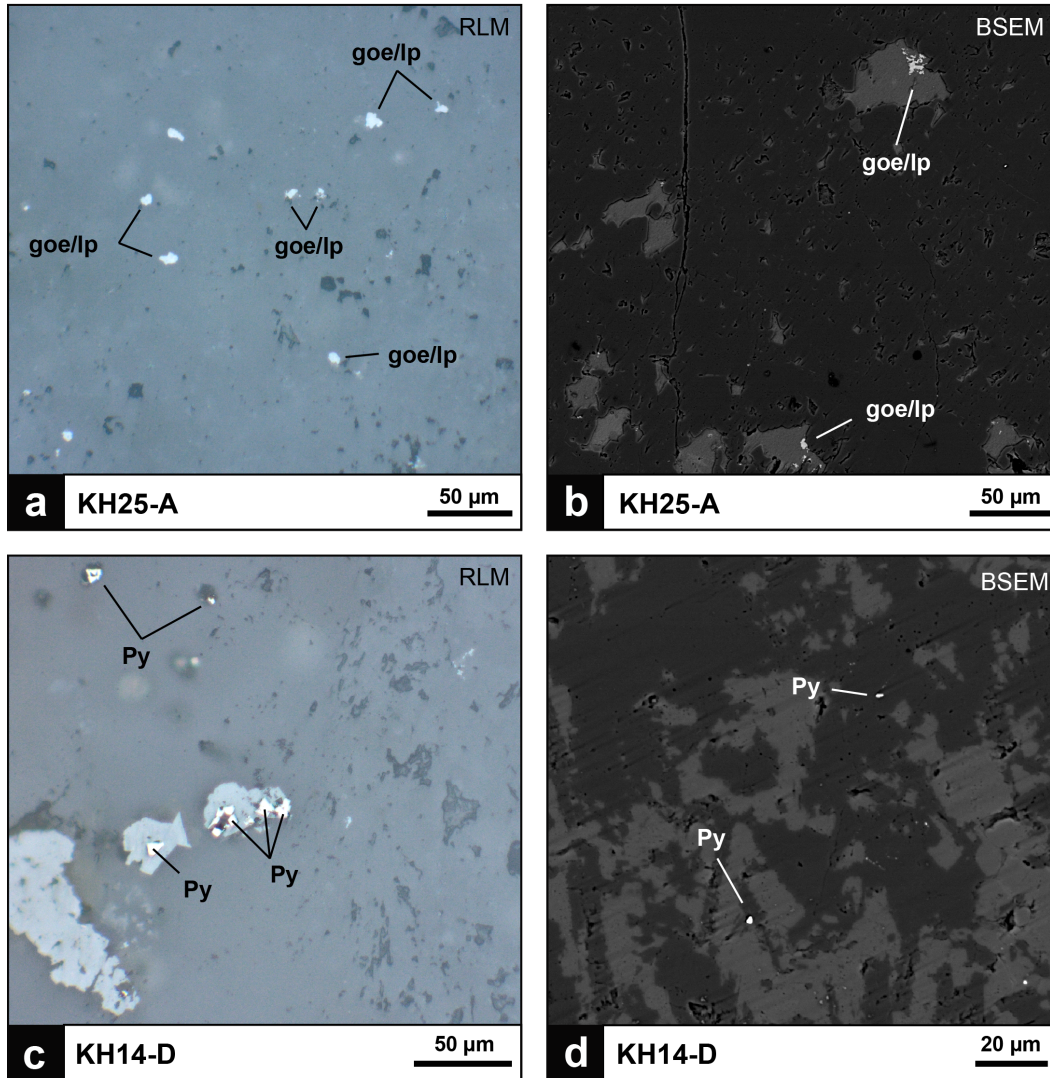


Figure 3-4: **a)** Reflected light microscope image of core sample KH25-A with goethite/lepidocrocite grains indicated. **b)** Backscattered scanning electron microscope (BSEM) image of KH25-A showing irregular goethite/lepidocrocite grains. **c)** Reflected light microscope image of core sample KH14-D showing pyrite. **d)** BSEM image of KH14-D.

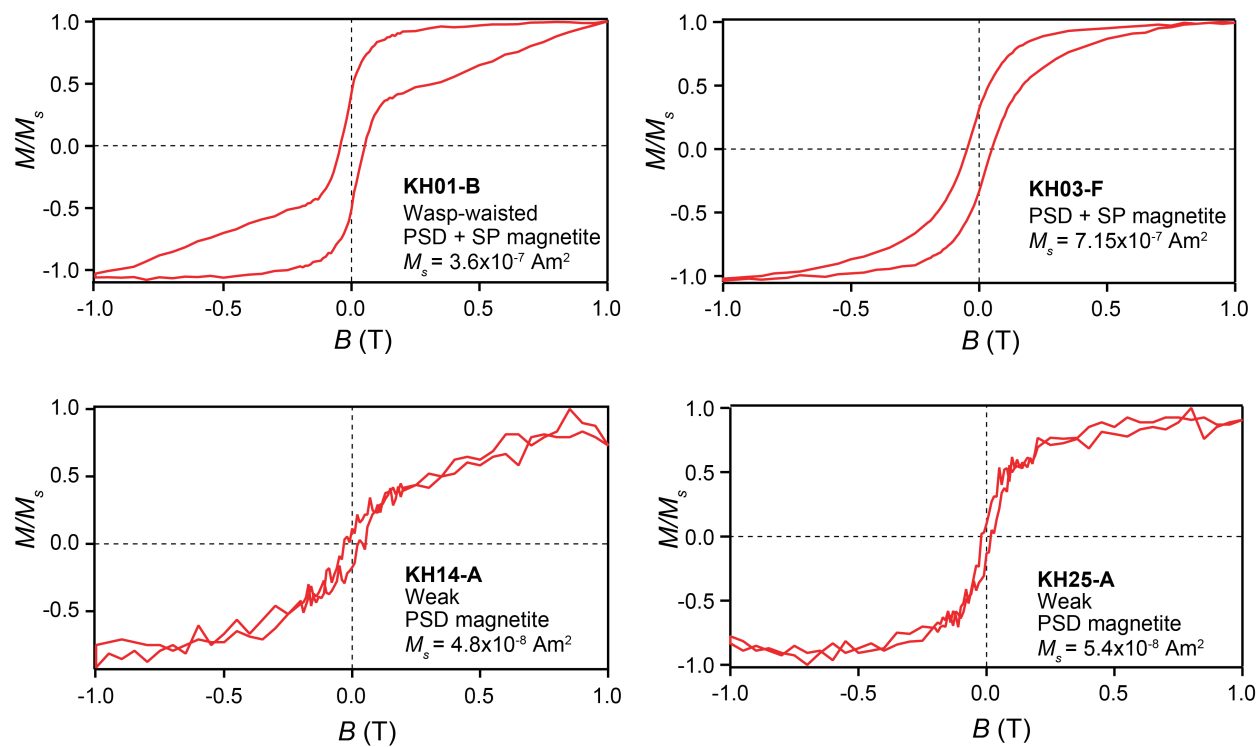


Figure 3-5: Hysteresis curves for the representative rhyolite samples KH01-B, KH03-F, KH14-A and KH25-D. Hysteresis loops were acquired for applied fields of $B = -1.0 - 1.0$ T and were corrected by removing any paramagnetic or diamagnetic signals. The corrected curves were used to ascertain the saturation magnetization (M_s), the saturation remanent magnetization (M_{rs}), the coercivity of remanence (H_{cr}) and the coercivity (H_c) for each sample.

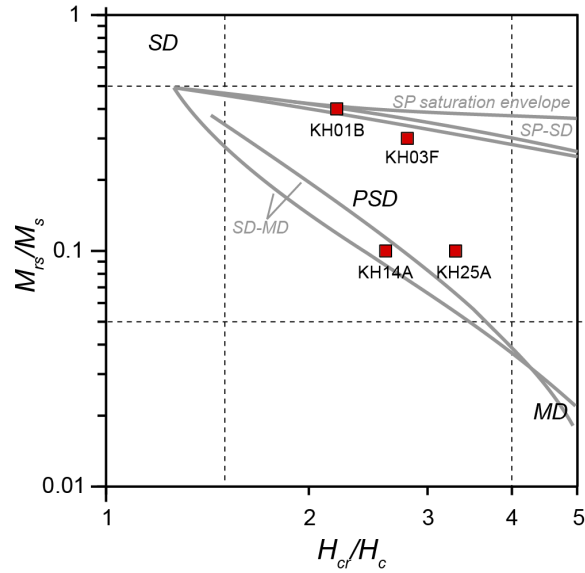


Figure 3-6: Day plot showing the ratio of saturation remanent magnetization (M_{rs}) over saturation magnetization (M_s), and the ratio of coercivity of remanence (H_{cr}) and coercive force (H_c) determined from hysteresis data for the representative samples KH01-B, KH03-F, KH14-A and KH25-D (see Table 2-2). Regions are denoted to show the different domain states magnetite: MD = multidomain, PSD = pseudo-single domain, SD = Single domain. All of our samples are in pseudo-single domain field indicating that they are reliable paleomagnetic recorders (Day et al., 1977; Dunlop, 2002).

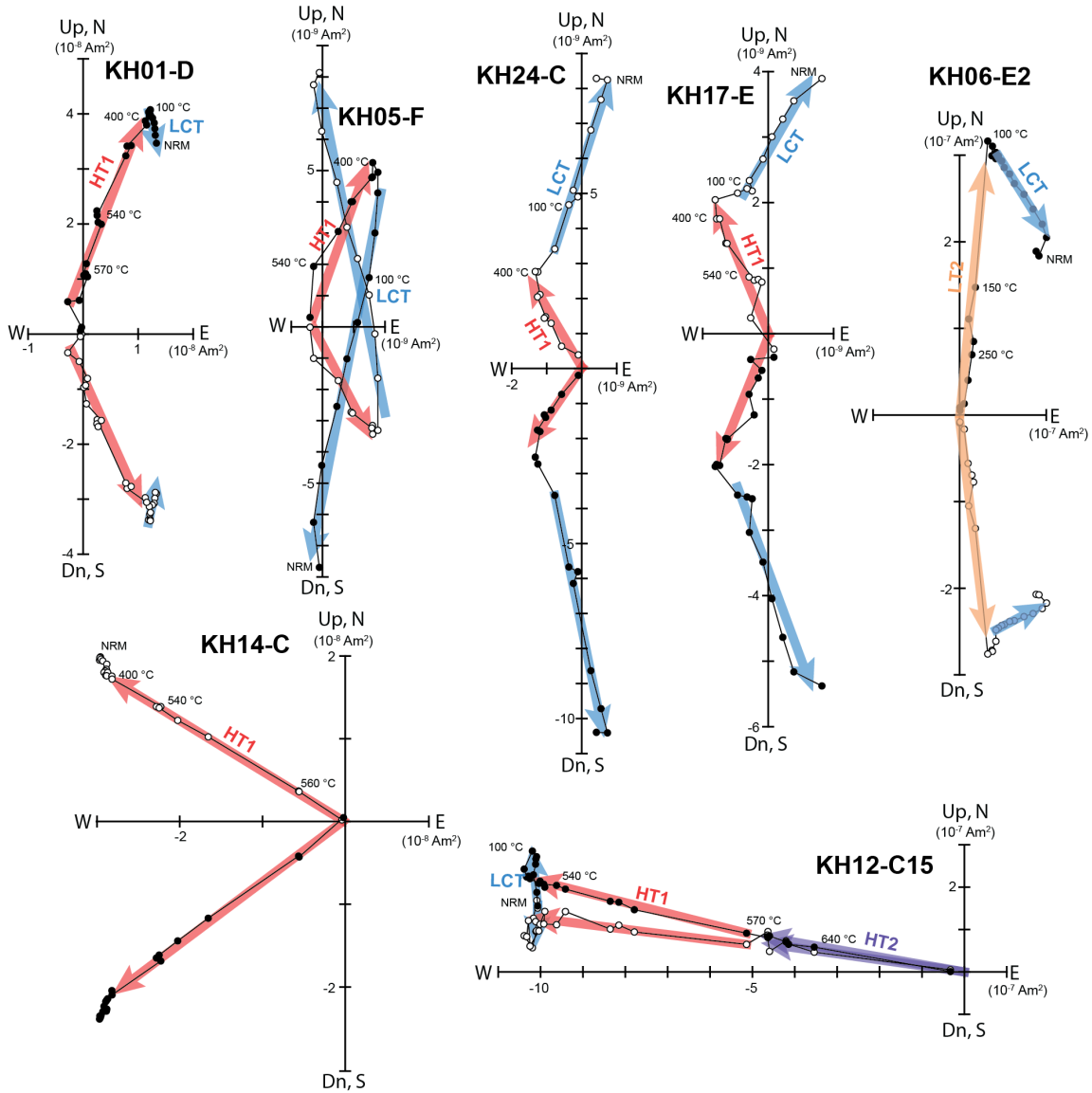


Figure 3-7: Zijderveld diagrams showing AF and thermal demagnetization of a representative set of specimens. Data is presented in geographic coordinates. Closed symbols represent north-south-east-west projections and open symbols represent up-down-east-west projections.

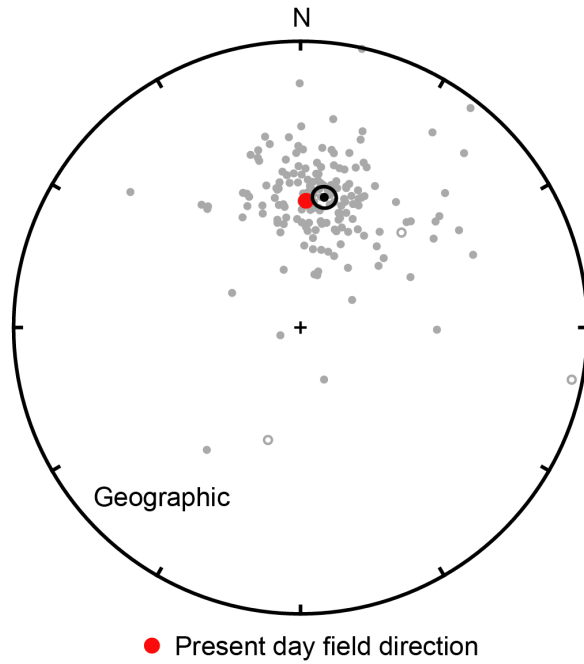


Figure 3-8: Equal area projection showing the LCT directions. The mean direction of the LCT components is almost equivalent to the modern-day field direction. Negative inclinations are projected onto the upper hemisphere and shown with open symbols, filled symbols represent positive inclinations.

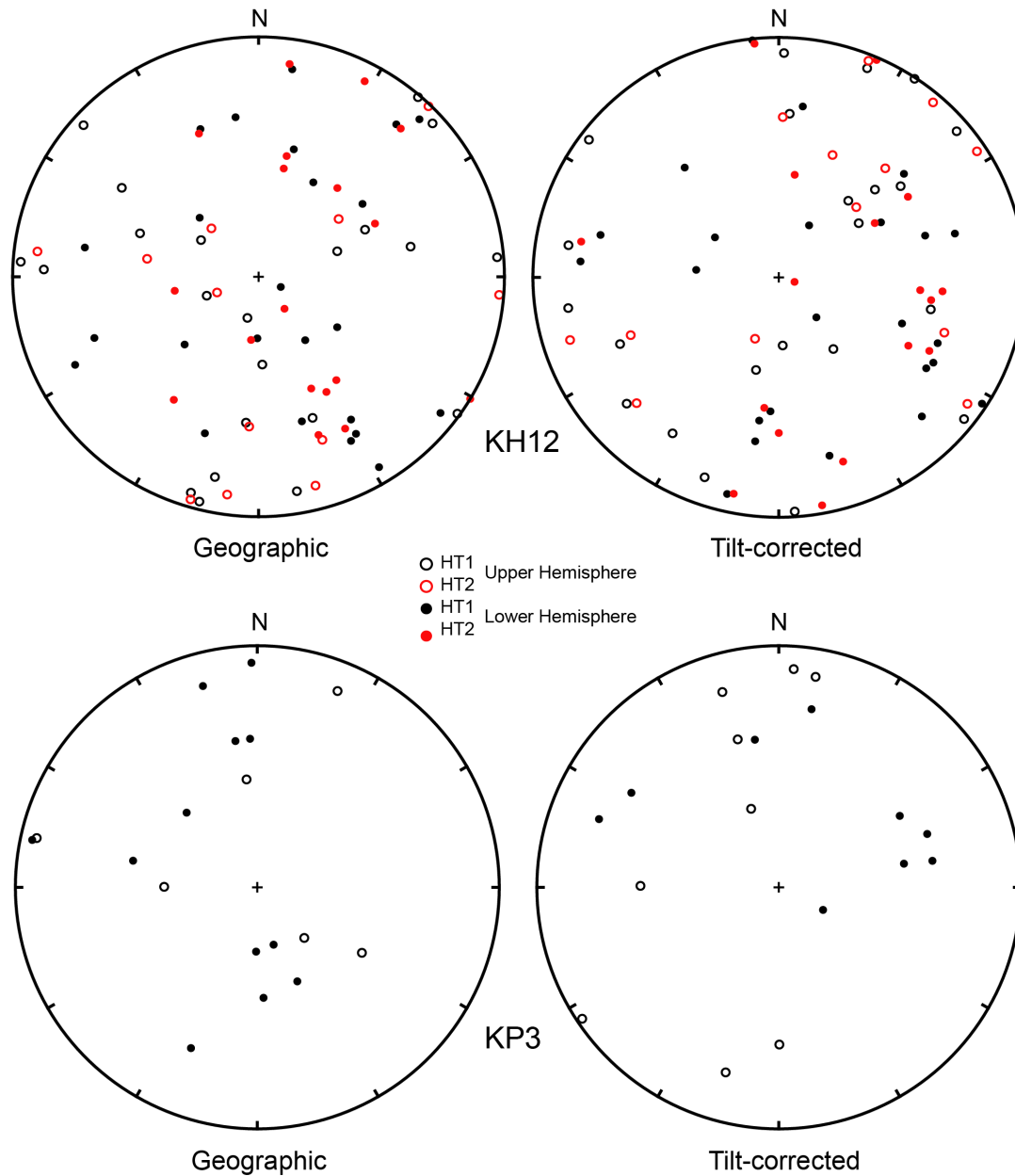


Figure 3-9: Equal area projection showing the HT1 and HT2 conglomerate test results. The HT1 directions of conglomerate clasts are shown in black and HT2 directions are shown in red. Negative inclinations are projected onto the upper hemisphere and shown with open symbols, while filled symbols represent positive inclinations projected onto the lower hemisphere. Both HT1 and HT2 directions are random with > 95% certainty.

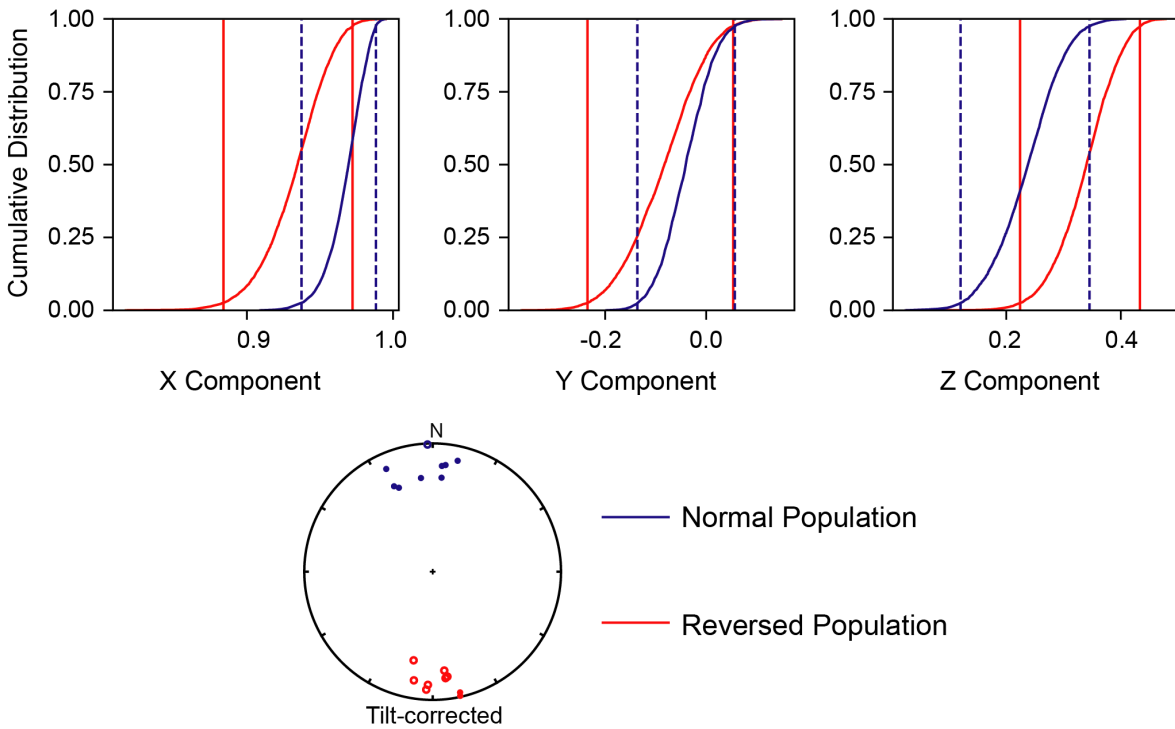


Figure 3-10: Cumulative distributions of Cartesian components of bootstrapped means from 500 pseudo-samples from tilt-corrected site-mean data (Tauxe et al., 2016). The 95% confidence intervals for the two populations overlap in X, Y, and Z. The two populations can be considered antipodal to one another because they share a common mean.

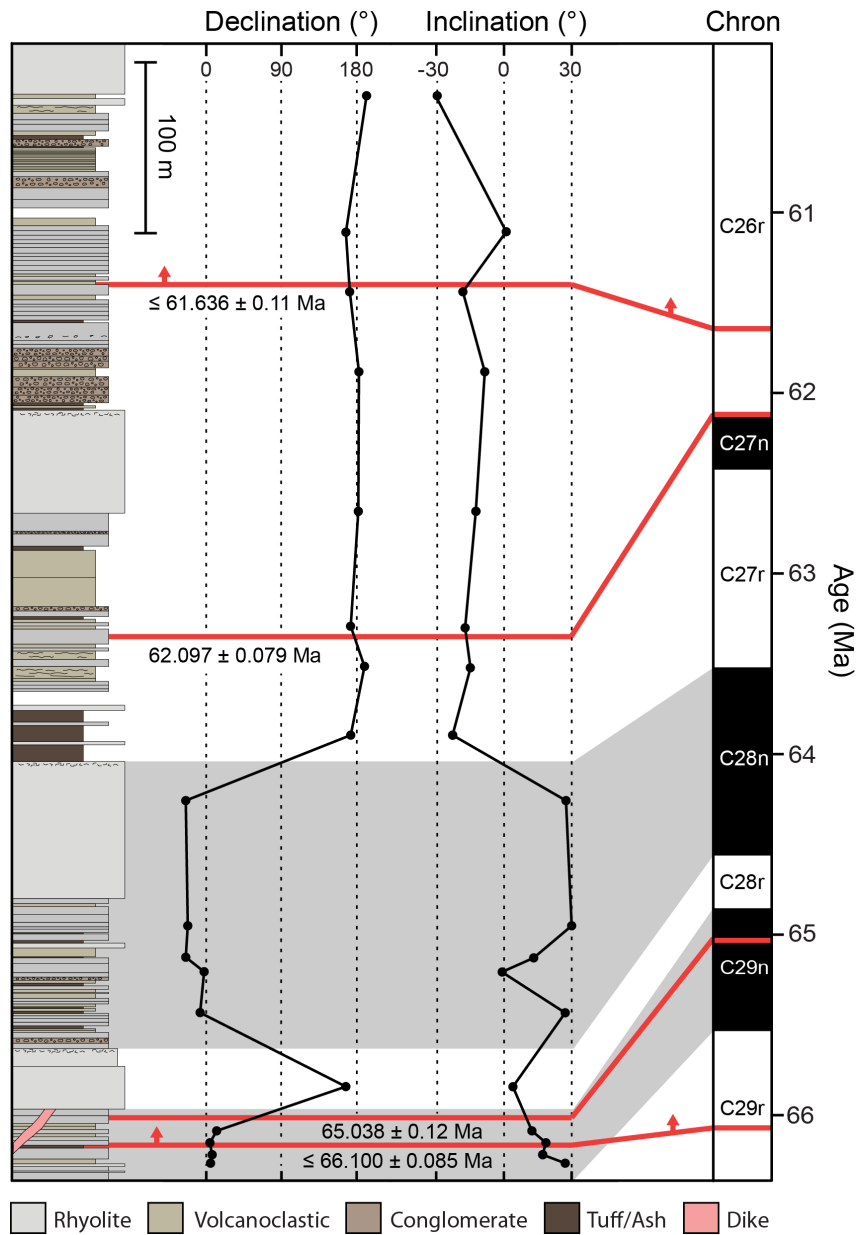


Figure 3-11: Stratigraphic column of upper 1,000 m of Khardung volcanics where we collected paleomagnetic and geochronology samples. Rock types are denoted by the color of the blocks (grey = rhyolite, yellow = volcanoclastic, light brown = conglomerate, dark brown = tuff/ash, red = intermediate dike) and the horizontal extent of the blocks represents the relative erosive prominence of the units in the field and BIS refers to small breaks in the section due to no exposure. The site-mean declinations and inclinations are plotted against stratigraphic height and our four U-Pb ages (2σ external uncertainty) are shown as red lines, up arrows indicate maximum depositional ages. The grey shaded regions show the correlation of the magnetic reversals in the sequence to the documented C29r, C29n, C28, C28n and C26r chrons which have been plotted with their age in right hand column (Barnet et al., 2019).

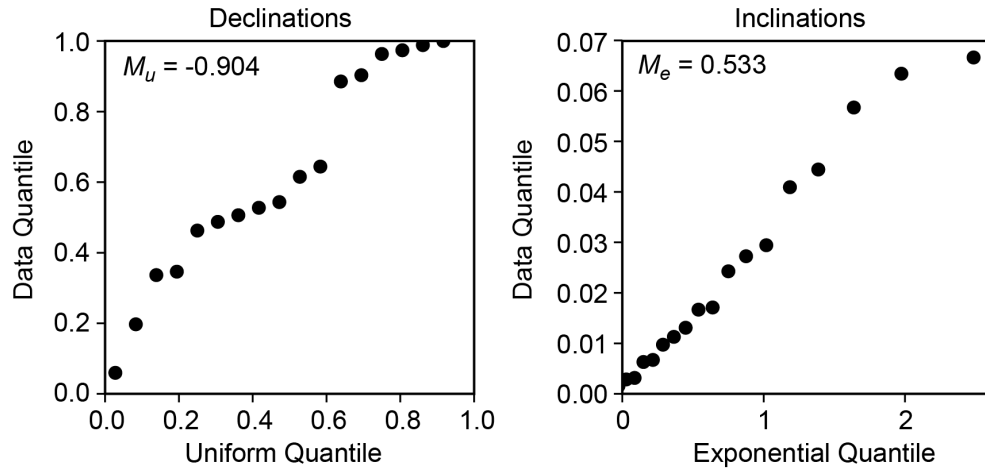


Figure 3-12: Quantile-quantile plots of longitudes and latitudes (in data coordinates) plotted against an assumed uniform and exponential distribution respectively. The data are Fisher distributed because the statistical parameters M_u and M_e are both less than the critical values.

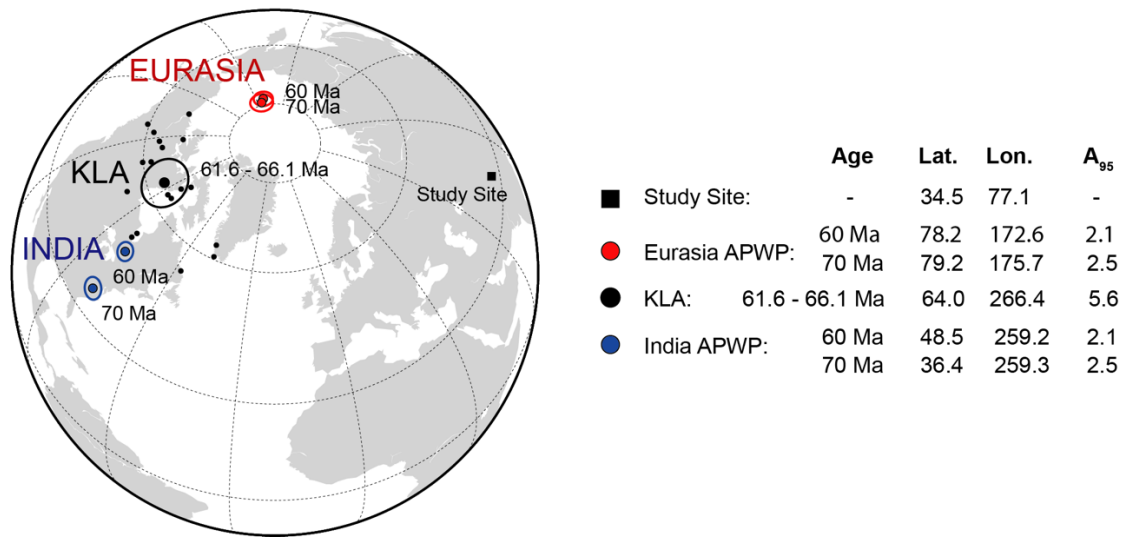


Figure 3-13: Northern hemisphere virtual geomagnetic poles (VGPs) and mean paleomagnetic pole for the KLA compared to contemporaneous apparent polar wander path (APWP) poles for India and Eurasia (Torsvik et al., 2012). The poles do not coincide so the KLA was not moving rigidly with either India or Eurasia at 61.6 – 66.1 Ma.

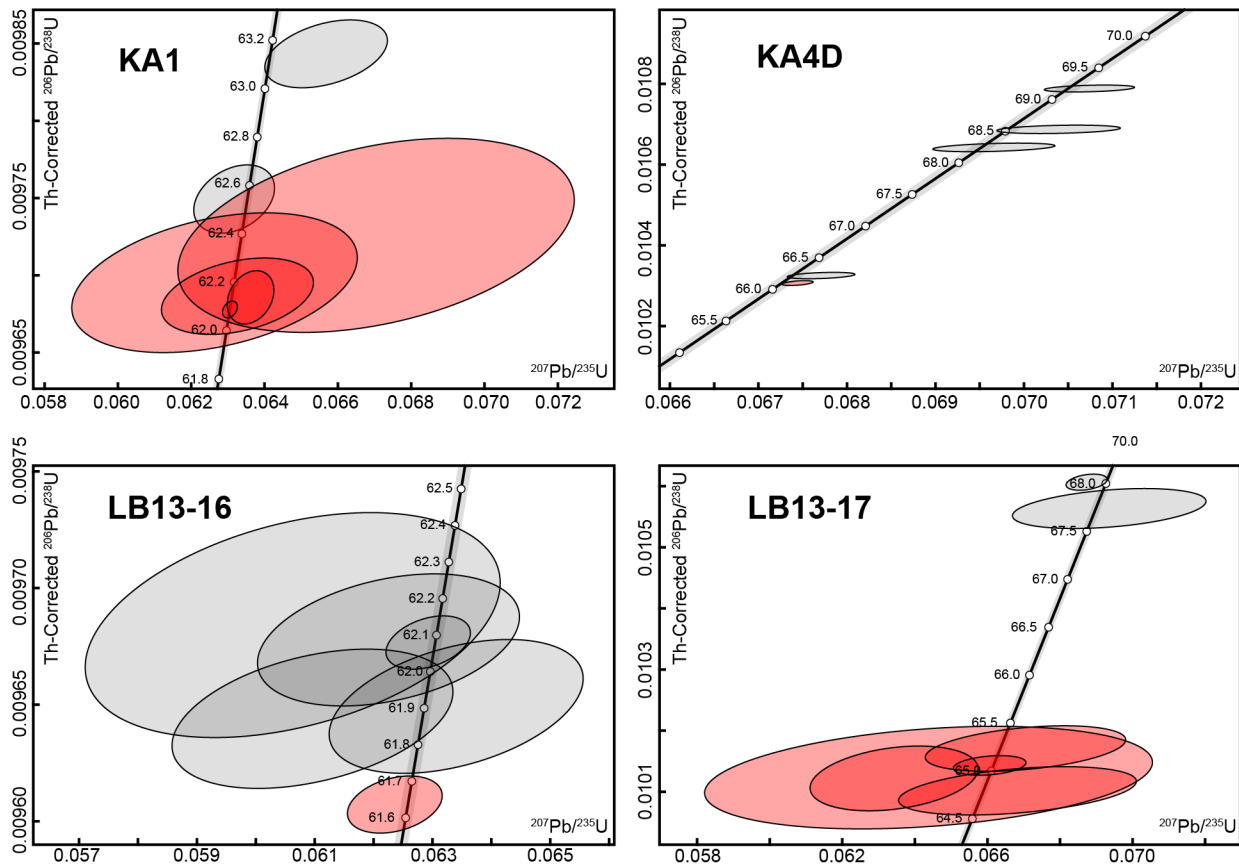


Figure 3-14: U-Pb concordia plots and weighted mean Th-corrected $^{206}\text{Pb}/^{238}\text{U}$ dates for KA1, KA4D, LB13-16 and LB13-17. Zircon grains contributing to the reported ages for each sample are shown in red. The dates from all of these samples are interpreted to represent the age of eruption/deposition.

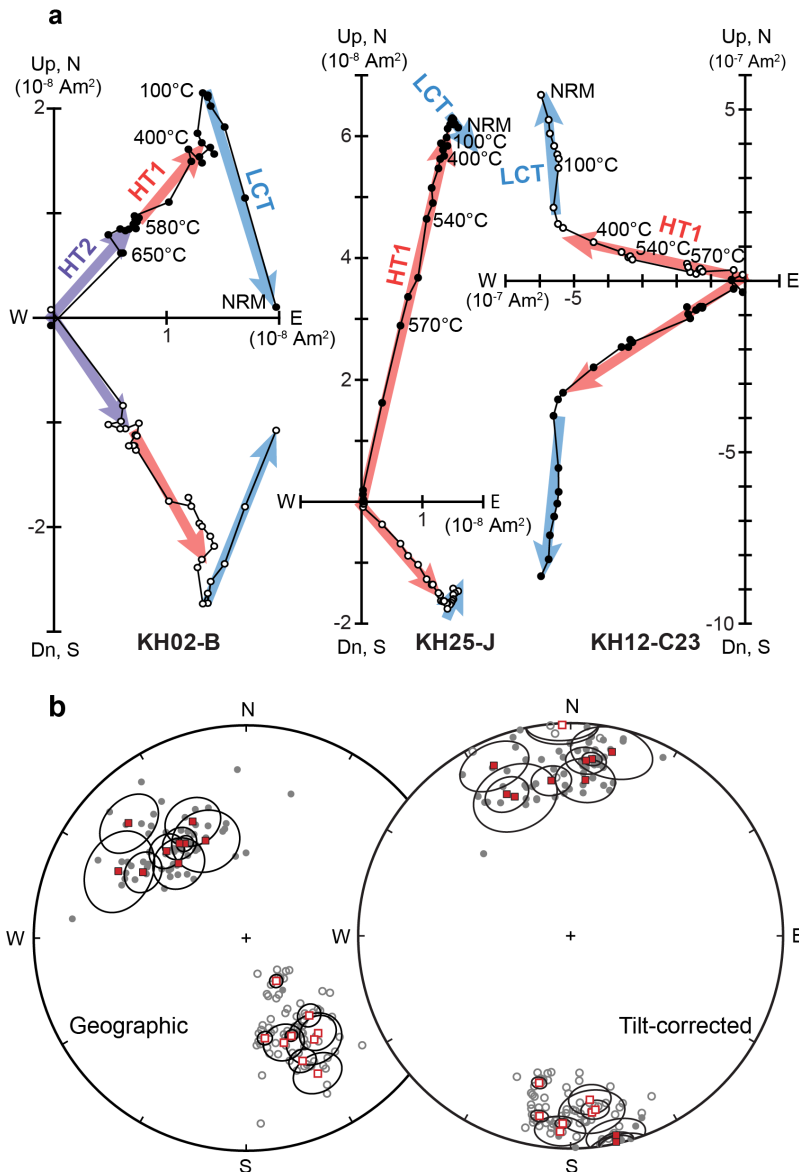


Figure 3-15: a) Orthographic projection diagrams showing AF and thermal demagnetization of three representative samples KH02-B, KH25-J and conglomerate clast KH12-C23. Data are presented in geographic coordinates; closed symbols represent north-south-east-west projections and open symbols represent up-down-east-west projections. Interpretations are shown with colored arrows: each arrow reflects a direction vector corresponding to components inferred from PCA. LCT = low coercivity/low temperature overprint, HT1 = high temperature magnetite, HT2 = high temperature hematite. **b)** Stereographic equal area projections showing HT1 directions for each sample (grey circles) and their site-means (red squares) with associated 95% confidence angles (black ellipses). Data are presented in geographic coordinates (left) and after tilt correction (right). Upward directions are denoted with open symbols and downward directions are denoted with filled symbols.

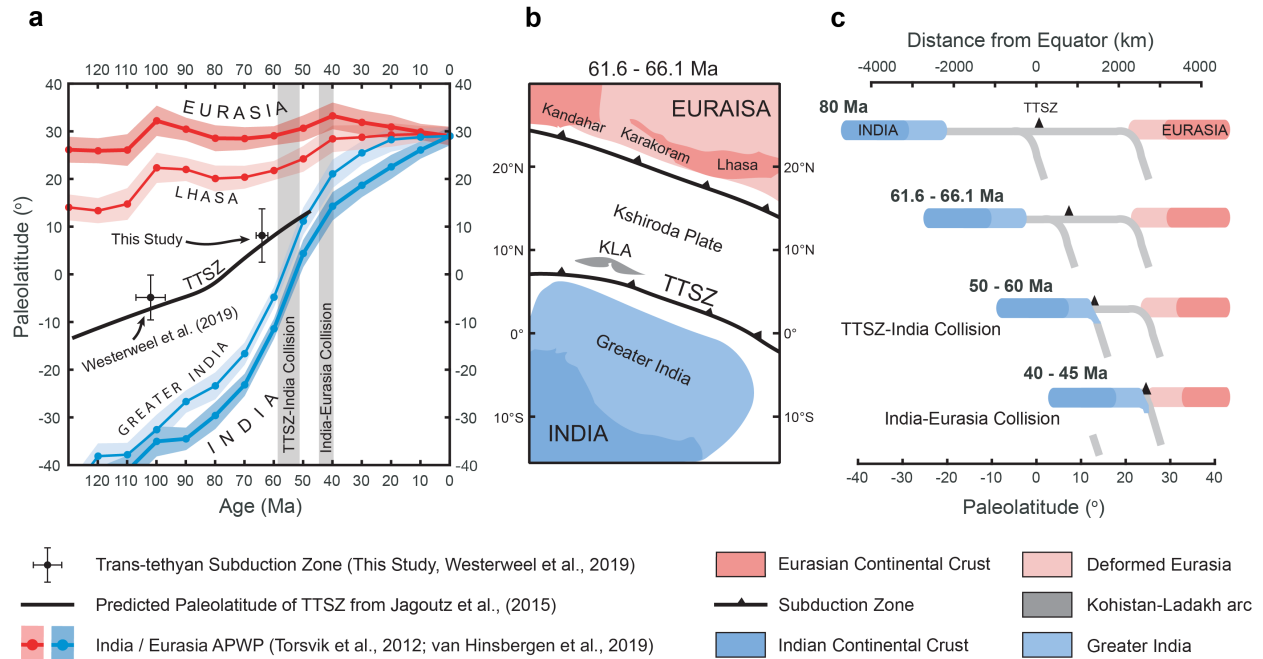


Figure 3-16: a) Paleolatitude of the TTSZ constrained at the Kohistan-Ladakh arc (KLA; this study) and the Burma Terrane (Westerweel et al., 2019) compared to paleomagnetic plate reconstructions of Indian and Eurasian terranes (Torsvik et al., 2012; van Hinsbergen et al., 2019) and the predicted location of the TTSZ (Jagoutz et al., 2015) throughout the closure of the Neotethys ocean. **b)** Paleogeographic map of the location of Kohistan-Ladakh arc relative to India and Eurasia in the Paleocene. The position of the Kohistan-Ladakh arc is reconstructed using our paleomagnetic pole from the Khardung volcanics and the locations of Indian and Eurasian tectonic blocks are from the plate reconstruction of van Hinsbergen et al. (van Hinsbergen et al., 2019). **c)** Cross-section illustration showing the plate tectonic configuration of the India-TTSZ-Eurasia collision at 80 Ma, 61.6 – 66.1 Ma (constrained by our data), 50 – 60 Ma and 40 – 45 Ma.

References

- Ahmad, M.N., Yoshida, M. and Fujiwara, Y., 2000. Paleomagnetic study of Utror Volcanic Formation: Remagnetizations and postfolding rotations in Utror area, Kohistan arc, northern Pakistan. *Earth, planets and space*, 52(6): 425-436.
- Aitchison, J.C., Davis, A.M., Liu, J., Luo, H., Malpas, J.G., McDermid, I.R., Wu, H., Ziabrev, S.V. and Zhou, M.-f., 2000. Remnants of a Cretaceous intra-oceanic subduction system within the Yarlung–Zangbo suture (southern Tibet). *Earth and Planetary Science Letters*, 183(1-2): 231-244.
- Barnet, J.S., Littler, K., Westerhold, T., Kroon, D., Leng, M.J., Bailey, I., Röhl, U. and Zachos, J.C., 2019. A high-Fidelity benthic stable isotope record of late Cretaceous–early Eocene climate change and carbon-cycling. *Paleoceanography and Paleoclimatology*, 34(4): 672-691.
- Beck, R.A., Burbank, D.W., Sercombe, W.J., Khan, A.M. and Lawrence, R.D., 1996. Late Cretaceous ophiolite obduction and Paleocene India-Asia collision in the westernmost Himalaya. *Geodinamica Acta*, 9(2-3): 114-144.
- Borneman, N.L., Hodges, K.V., Van Soest, M.C., Bohon, W., Wartho, J.A., Cronk, S.S. and Ahmad, T., 2015. Age and structure of the Shyok suture in the Ladakh region of northwestern India: Implications for slip on the Karakoram fault system. *Tectonics*, 34(10): 2011-2033.
- Bouilhol, P., Jagoutz, O., Hanchar, J.M. and Dudas, F.O., 2013. Dating the India-Eurasia collision through arc magmatic records. *Earth and Planetary Science Letters*, 366: 163-175.
- Bowring, J.F., McLean, N.M. and Bowring, S., 2011. Engineering cyber infrastructure for U-Pb geochronology: Tripoli and U-Pb Redux. *Geochemistry, Geophysics, Geosystems*, 12(6).
- Buchan, K.L., 2013. Key paleomagnetic poles and their use in Proterozoic continent and supercontinent reconstructions: A review. *Precambrian Research*, 238: 93-110.
- Burg, J. and Chen, G., 1984. Tectonics and structural zonation of southern Tibet, China. *Nature*, 311(5983): 219-223.
- Burg, J.-P. and Bouilhol, P., 2019. Timeline of the South Tibet–Himalayan belt: The geochronological record of subduction, collision, and underthrusting from zircon and monazite U–Pb ages. *Canadian Journal of Earth Sciences*, 56(12): 1318-1332.
- Butler, R.F., 1998. *Paleomagnetism: Magnetic domains to geologic terranes*. Electronic edition, 23.
- Cai, F., Ding, L., Laskowski, A.K., Kapp, P., Wang, H., Xu, Q. and Zhang, L., 2016. Late Triassic paleogeographic reconstruction along the Neo–Tethyan Ocean margins, southern Tibet. *Earth and Planetary Science Letters*, 435: 105-114.
- Cande, S.C., Patriat, P. and Dymant, J., 2010. Motion between the Indian, Antarctic and African plates in the early Cenozoic. *Geophysical Journal International*, 183(1): 127-149.
- Claiborne, L.L., Miller, C.F., Gualda, G.A., Carley, T.L., Covey, A.K., Wooden, J.L. and Fleming, M.A., 2018. Zircon as magma monitor: Robust, temperature-dependent partition coefficients from glass and zircon surface and rim measurements from natural systems. *Microstructural geochronology: Planetary records down to atom scale*: 1-33.
- Day, R., Fuller, M. and Schmidt, V., 1977. Hysteresis properties of titanomagnetites: grain-size and compositional dependence. *Physics of the Earth and planetary interiors*, 13(4): 260-267.

- DeCelles, P., Kapp, P., Gehrels, G. and Ding, L., 2014. Paleocene-Eocene foreland basin evolution in the Himalaya of southern Tibet and Nepal: Implications for the age of initial India-Asia collision. *Tectonics*, 33(5): 824-849.
- Deenen, M.H., Langereis, C.G., van Hinsbergen, D.J. and Biggin, A.J., 2011. Geomagnetic secular variation and the statistics of palaeomagnetic directions. *Geophysical Journal International*, 186(2): 509-520.
- Dunlap, W.J. and Wysoczanski, R., 2002. Thermal evidence for early Cretaceous metamorphism in the Shyok suture zone and age of the Khardung volcanic rocks, Ladakh, India. *Journal of Asian Earth Sciences*, 20(5): 481-490.
- Dunlop, D.J., 2002. Theory and application of the Day plot (Mrs/Ms versus Hcr/Hc) 1. Theoretical curves and tests using titanomagnetite data. *Journal of Geophysical Research: Solid Earth*, 107(B3): EPM 4-1-EPM 4-22.
- Eddy, M.P., Bowring, S.A., Umhoefer, P.J., Miller, R.B., McLean, N.M. and Donaghy, E.E., 2016. High-resolution temporal and stratigraphic record of Siletzia's accretion and triple junction migration from nonmarine sedimentary basins in central and western Washington. *Bulletin*, 128(3-4): 425-441.
- Fisher, N.I. and Lewis, T., 1983. Estimating the common mean direction of several circular or spherical distributions with differing dispersions. *Biometrika*, 70(2): 333-341.
- Fisher, R.A., 1953. Dispersion on a sphere. *Proceedings of the Royal Society of London. Series A. Mathematical and Physical Sciences*, 217(1130): 295-305.
- Garzanti, E., 2008. Comment on "When and where did India and Asia collide?" by Jonathan C. Aitchison, Jason R. Ali, and Aileen M. Davis. *Journal of Geophysical Research-Solid Earth*, 113(B4).
- Garzanti, E., Baud, A. and Mascle, G., 1987. Sedimentary Record of the Northward Flight of India and Its Collision with Eurasia (Ladakh Himalaya, India). *Geodinamica Acta*, 1(4-5): 297-312.
- Guangwei, L., Xiaohan, L., Alex, P., Lijie, W., Xiaobing, L., Feixin, H. and Xuejun, Z., 2010. In-situ detrital zircon geochronology and Hf isotopic analyses from Upper Triassic Tethys sequence strata. *Earth and Planetary Science Letters*, 297(3-4): 461-470.
- Hébert, R., Bezard, R., Guilmette, C., Dostal, J., Wang, C. and Liu, Z., 2012. The Indus–Yarlung Zangbo ophiolites from Nanga Parbat to Namche Barwa syntaxes, southern Tibet: First synthesis of petrology, geochemistry, and geochronology with incidences on geodynamic reconstructions of Neo-Tethys. *Gondwana Research*, 22(2): 377-397.
- Hiess, J., Condon, D.J., McLean, N. and Noble, S.R., 2012. $^{238}\text{U}/^{235}\text{U}$ systematics in terrestrial uranium-bearing minerals. *Science*, 335(6076): 1610-1614.
- Hodges, K.V., 2000. Tectonics of the Himalaya and southern Tibet from two perspectives. *Geological Society of America Bulletin*, 112(3): 324-350.
- Hu, X.M., Garzanti, E., Wang, J.G., Huang, W.T., An, W. and Webb, A., 2016a. The timing of India-Asia collision onset - Facts, theories, controversies. *Earth-Science Reviews*, 160: 264-299.
- Hu, X.M., Wang, J.G., BouDagher-Fadel, M., Garzanti, E. and An, W., 2016b. New insights into the timing of the India-Asia collision from the Paleogene Quxia and Jialazi formations of the Xigaze forearc basin, South Tibet. *Gondwana Research*, 32: 76-92.
- Jaffey, A., Flynn, K., Glendenin, L., Bentley, W.t. and Essling, A., 1971. Precision measurement of half-lives and specific activities of U^{235} and U^{238} . *Physical review C*, 4(5): 1889.

- Jagoutz, O., Bouilhol, P., Schaltegger, U. and Müntener, O., 2019. The isotopic evolution of the Kohistan Ladakh arc from subduction initiation to continent arc collision. *Geological Society, London, Special Publications*, 483(1): 165-182.
- Jagoutz, O., Macdonald, F.A. and Royden, L., 2016. Low-latitude arc-continent collision as a driver for global cooling. *Proceedings of the National Academy of Sciences of the United States of America*, 113(18): 4935-4940.
- Jagoutz, O., Royden, L., Holt, A.F. and Becker, T.W., 2015. Anomalously fast convergence of India and Eurasia caused by double subduction. *Nature Geoscience*, 8(6): 475-U78.
- Kapp, P. and DeCelles, P.G., 2019. Mesozoic–Cenozoic geological evolution of the Himalayan-Tibetan orogen and working tectonic hypotheses. *American Journal of Science*, 319(3): 159-254.
- Kirschvink, J., 1980. The least-squares line and plane and the analysis of palaeomagnetic data. *Geophysical Journal International*, 62(3): 699-718.
- Kirschvink, J.L., Kopp, R.E., Raub, T.D., Baumgartner, C.T. and Holt, J.W., 2008. Rapid, precise, and high-sensitivity acquisition of paleomagnetic and rock-magnetic data: Development of a low-noise automatic sample changing system for superconducting rock magnetometers. *Geochemistry, Geophysics, Geosystems*, 9(5).
- Klootwijk, C., Sharma, M.L., Gergan, J., Turkey, B., Shah, S.K. and Agarwal, V., 1979. Extent of Greater India .2. Paleomagnetic Data from the Ladakh Intrusives at Kargil, Northwestern Himalayas. *Earth and Planetary Science Letters*, 44(1): 47-64.
- Krogh, H., Maeland, J. and Tönder, O., 1972. Indirect haemagglutination for demonstration of antibodies to stratum corneum of skin. *International Archives of Allergy and Immunology*, 42(4): 493-502.
- Lakhan, N., Singh, A.K., Singh, B.P., Sen, K., Singh, M.R., Khogenkumar, S., Singhal, S. and Oinam, G., 2020. Zircon U–Pb geochronology, mineral and whole-rock geochemistry of the Khardung volcanics, Ladakh Himalaya, India: Implications for Late Cretaceous to Palaeogene continental arc magmatism. *Geological Journal*, 55(5): 3297-3320.
- Leloup, P.H., Arnaud, N., Lacassin, R., Kienast, J.R., Harrison, T.M., Trong, T.T.P., Replumaz, A. and Tapponnier, P., 2001. New constraints on the structure, thermochronology, and timing of the Ailao Shan-Red River shear zone, SE Asia. *Journal of Geophysical Research-Solid Earth*, 106(B4): 6683-6732.
- Li, C., Van der Hilst, R.D., Meltzer, A.S. and Engdahl, E.R., 2008. Subduction of the Indian lithosphere beneath the Tibetan Plateau and Burma. *Earth and Planetary Science Letters*, 274(1-2): 157-168.
- Lippert, P.C., Van Hinsbergen, D.J. and Dupont-Nivet, G., 2014. Early Cretaceous to present latitude of the central proto-Tibetan Plateau: A paleomagnetic synthesis with implications for Cenozoic tectonics, paleogeography, and climate of Asia. *Geological Society of America Special Papers*, 507: 1-21.
- Mattinson, J.M., 2005. Zircon U–Pb chemical abrasion (“CA-TIMS”) method: combined annealing and multi-step partial dissolution analysis for improved precision and accuracy of zircon ages. *Chemical Geology*, 220(1-2): 47-66.
- McLean, N.M., Bowring, J.F. and Bowring, S.A., 2011. An algorithm for U-Pb isotope dilution data reduction and uncertainty propagation. *Geochemistry, Geophysics, Geosystems*, 12(6).
- McLean, N.M., Condon, D.J., Schoene, B. and Bowring, S.A., 2015. Evaluating uncertainties in the calibration of isotopic reference materials and multi-element isotopic tracers

- (EARTHTIME Tracer Calibration Part II). *Geochimica et Cosmochimica Acta*, 164: 481-501.
- Molnar, P. and Stock, J.M., 2009. Slowing of India's convergence with Eurasia since 20 Ma and its implications for Tibetan mantle dynamics. *Tectonics*, 28(3).
- Murphy, M., Yin, A., Kapp, P., Harrison, T., Lin, D. and Jinghui, G., 2000. Southward propagation of the Karakoram fault system, southwest Tibet: Timing and magnitude of slip. *Geology*, 28(5): 451-454.
- Najman, Y., Jenks, D., Godin, L., Boudagher-Fadel, M., Millar, I., Garzanti, E., Horstwood, M. and Bracciali, L., 2017. The Tethyan Himalayan detrital record shows that India-Asia terminal collision occurred by 54 Ma in the Western Himalaya. *Earth and Planetary Science Letters*, 459: 301-310.
- Nier, A.O., 1950. A redetermination of the relative abundances of the isotopes of carbon, nitrogen, oxygen, argon, and potassium. *Physical Review*, 77(6): 789.
- Patriat, P. and Achache, J., 1984. India–Eurasia collision chronology has implications for crustal shortening and driving mechanism of plates. *Nature*, 311(5987): 615-621.
- Patzelt, A., Li, H., Wang, J. and Appel, E., 1996. Palaeomagnetism of Cretaceous to Tertiary sediments from southern Tibet: evidence for the extent of the northern margin of India prior to the collision with Eurasia. *Tectonophysics*, 259(4): 259-284.
- Petterson, M.G. and Windley, B.F., 1985. RbSr dating of the Kohistan arc-batholith in the Trans-Himalaya of north Pakistan, and tectonic implications. *Earth and Planetary Science Letters*, 74(1): 45-57.
- Pullaiah, G., Irving, E., Buchan, K. and Dunlop, D., 1975. Magnetization changes caused by burial and uplift. *Earth and Planetary Science Letters*, 28(2): 133-143.
- Roberts, A.P., Cui, Y. and Verosub, K.L., 1995. Wasp-waisted hysteresis loops: Mineral magnetic characteristics and discrimination of components in mixed magnetic systems. *Journal of Geophysical Research: Solid Earth*, 100(B9): 17909-17924.
- Schärer, U., 1984. The effect of initial²³⁰Th disequilibrium on young UPb ages: the Makalu case, Himalaya. *Earth and Planetary Science Letters*, 67(2): 191-204.
- Tahirkheli, R.K., 1979. Geology of Kohistan and adjoining Eurasian and Indo-Pakistan continents, Pakistan. *Geol. Bull. Univ. Peshawar*, 11(1): 1-30.
- Tapponnier, P., Mattauer, M., Proust, F. and Cassaigneau, C., 1981. Mesozoic Ophiolites, Sutures, and Large-Scale Tectonic Movements in Afghanistan. *Earth and Planetary Science Letters*, 52(2): 355-371.
- Tauxe, L., 2010. *Essentials of paleomagnetism*. Univ of California Press.
- Tauxe, L., Shaar, R., Jonestrask, L., Swanson-Hysell, N., Minnett, R., Koppers, A., Constable, C., Jarboe, N., Gaastra, K. and Fairchild, L., 2016. PmagPy: Software package for paleomagnetic data analysis and a bridge to the Magnetism Information Consortium (MagIC) Database. *Geochemistry, Geophysics, Geosystems*, 17(6): 2450-2463.
- Thanh, N.X., Rajesh, V., Itaya, T., Windley, B., Kwon, S. and Park, C.-S., 2012. A Cretaceous forearc ophiolite in the Shyok suture zone, Ladakh, NW India: Implications for the tectonic evolution of the Northwest Himalaya. *Lithos*, 155: 81-93.
- Torsvik, T.H., Van der Voo, R., Preeden, U., Mac Niocaill, C., Steinberger, B., Doubrovine, P.V., van Hinsbergen, D.J., Domeier, M., Gaina, C. and Tohver, E., 2012. Phanerozoic polar wander, palaeogeography and dynamics. *Earth-Science Reviews*, 114(3-4): 325-368.
- Upadhyay, R., Sinha, A.K., Chandra, R. and Rai, H., 1999. Tectonic and magmatic evolution of the eastern Karakoram, India. *Geodinamica Acta*, 12(6): 341-358.

- Van der Voo, R., 1990. The reliability of paleomagnetic data.
- Van Hinsbergen, D.J., Kapp, P., Dupont-Nivet, G., Lippert, P.C., DeCelles, P.G. and Torsvik, T.H., 2011. Restoration of Cenozoic deformation in Asia and the size of Greater India. *Tectonics*, 30(5).
- van Hinsbergen, D.J., Lippert, P.C., Li, S., Huang, W., Advokaat, E.L. and Spakman, W., 2019. Reconstructing Greater India: Paleogeographic, kinematic, and geodynamic perspectives. *Tectonophysics*, 760: 69-94.
- Watson, G.S. and Williams, E.J., 1956. On the construction of significance tests on the circle and the sphere. *Biometrika*, 43(3/4): 344-352.
- Weinberg, R.F. and Dunlap, W.J., 2000. Growth and deformation of the Ladakh batholith, northwest Himalayas: Implications for timing of continental collision and origin of calc-alkaline batholiths. *Journal of Geology*, 108(3): 303-320.
- Westerweel, J., Roperch, P., Licht, A., Dupont-Nivet, G., Win, Z., Poblete, F., Ruffet, G., Swe, H.H., Thi, M.K. and Aung, D.W., 2019. Burma Terrane part of the Trans-Tethyan arc during collision with India according to palaeomagnetic data. *Nature Geoscience*, 12(10): 863-868.
- Yin, A., Harrison, T.M., Murphy, M., Grove, M., Nie, S., Ryerson, F., Xiao Feng, W. and Zeng Le, C., 1999. Tertiary deformation history of southeastern and southwestern Tibet during the Indo-Asian collision. *Geological Society of America Bulletin*, 111(11): 1644-1664.
- Zahirovic, S., Müller, R.D., Seton, M., Flament, N., Gurnis, M. and Whittaker, J., 2012. Insights on the kinematics of the India-Eurasia collision from global geodynamic models. *Geochemistry, Geophysics, Geosystems*, 13(4).
- Zaman, H., Otofujii, Y.-i., Khan, S.R. and Ahmad, M.N., 2013. New paleomagnetic results from the northern margin of the Kohistan Island Arc. *Arabian Journal of Geosciences*, 6(4): 1041-1054.
- Zaman, H. and Torii, M., 1999. Palaeomagnetic study of Cretaceous red beds from the eastern Hindukush ranges, northern Pakistan: palaeoreconstruction of the Kohistan–Karakoram composite unit before the India–Asia collision. *Geophysical Journal International*, 136(3): 719-738.
- Zhang, L.-L., Liu, C.-Z., Wu, F.-Y., Ji, W.-Q. and Wang, J.-G., 2014. Zedong terrane revisited: An intra-oceanic arc within Neo-Tethys or a part of the Asian active continental margin? *Journal of Asian Earth Sciences*, 80: 34-55.

Chapter Four

Paleomagnetic Constraints on the Age of the Shyok Suture Zone

Submitted to JGR Solid Earth.

4.1 Abstract

The India-Eurasia collision is a key case study for understanding the influence of plate tectonic processes on Earth's atmosphere, hydrosphere and biosphere. However, the timing of the final India-Eurasia continental collision is debated due to significant uncertainty in the age of the collision between the Kohistan-Ladakh arc and Eurasia along the Shyok suture zone. Here, we present paleomagnetic results that constrain the Eurasian Karakoram terrane in the present-day western Himalaya to a paleolatitude of $20.0 \pm 6.2^\circ\text{N}$ between 93 – 75 million years ago (Ma). Our results show that the Karakoram terrane was situated on the southern margin of Eurasia in the Late-Cretaceous, at a comparable latitude to the Lhasa terrane in Tibet. Our results also show that the ocean basin that separated the Kohistan-Ladakh arc from the Eurasian continent had a north-south extent of ~ 1320 km until < 61.6 Ma, placing an older limit on the age of final closure of the Shyok suture zone. We show that the Paleocene collision event affecting India, which has been widely interpreted to represent final India-Eurasia collision, instead records the arc-continent collision between the Kohistan-Ladakh arc and the northern edge of India prior to final India-Eurasia collision. Final India-Eurasia collision occurred after the closure of the oceanic basin between the Kohistan-Ladakh arc and Eurasia, likely at around 45 – 40 Ma when widespread metamorphism and deformation occurred throughout the Himalaya.

4.2 Plain Language Summary

We use the magnetism of rocks from the western Himalaya to determine the latitude of the southern edge of Eurasia before the India-Eurasia continental collision. The results show that the Shyok suture zone, a geological boundary where a major ocean basin once existed, was formed < 61 million years ago. This age constraint means that a volcanic island chain called the Kohistan-Ladakh arc was situated significantly outboard of the Eurasian continent before the start of the India-Eurasia collision. The Kohistan-Ladakh arc collided with India 65 – 50 million years ago, resulting in the delivery of sediment from the arc to the northern edge of India and the thrusting of oceanic rocks on top of India. Final collision between India and Eurasia occurred 45 – 40 million years ago, ~15 million years later than previously thought, causing widespread heating and deformation in the Himalaya and Tibet.

4.3 Introduction

Collisions of continental plates are among the most significant tectonic events on Earth, affecting global plate configurations, climate and biological diversity. However, causally linking hydrosphere-biosphere processes and tectonic motion requires a detailed understanding of the tectonic events leading up to and during continental collisions. Robust reconstructions of pre-collisional configurations of the colliding plates are also essential for understanding the deformation mechanisms accommodating the shortening of continental plates during collision and orogenesis.

The classical case-study for investigating these processes is the Himalaya-Karakoram-Tibet orogenic belt in south Eurasia, which has conventionally been thought to be a single-stage collision between India and Eurasia in the Paleocene related to the closure of the Neotethys ocean (Gansser, 1964). However, in recent years, multiple studies have questioned this classical interpretation and suggested a more protracted multi-stage collision (Aitchison & Davis, 2004; Aitchison et al., 2000; Bouilhol, 2013) similar to other ancient systems, such as the Appalachian system. Multiple evidences indicate that a major collision affected the northern Indian passive margin at 65 – 50 Ma, yet it is disputed whether this event dates the terminal India-Eurasia collision (DeCelles et al., 2014; Garzanti et al., 1987; Kaneko et al., 2003) or an earlier India-arc accretion (Aitchison et al., 2000; Jagoutz et al., 2015). Additionally, it has been proposed that the Indian plate rifted in the Late Cretaceous and the Paleocene event relates to collision between Eurasia and a rifted India-derived fragment (Van Hinsbergen et al., 2012; Yuan et al., 2021).

Multiple observations support and contradict each of these interpretations. The classical single-stage collision model requires that a vast amount of north-south India-Eurasia convergence (>3000 km) be accommodated by continental shortening (Molnar & Stock, 2009). This is 1000 –

2000 km more convergence than geologic observations suggest has been accommodated by deformation within Tibet (Van Hinsbergen et al., 2011) and in the Himalaya fold and thrust belt (DeCelles et al., 2002). Additionally, major faults accommodating the collision, including the Red River shear zone, the Altyn Tagh fault, and the Gangdese/Kailash thrust, were mostly active after 40 Ma (Cowgill et al., 2003; Leloup et al., 2001; Yin et al., 1999), and major collision-related metamorphism and melting in the Greater Himalayan Crystalline (GHC) belt is younger than 45 – 40 Ma (Burg & Bouilhol, 2019). If the 65 – 50 Ma event indeed represents the final collision, the system did not respond up to 15 Ma after. Similarly, the Greater India rifting hypothesis predicts an Eocene-Oligocene suture zone south of the Tethyan Himalaya for which there is no geological evidence (Searle, 2019).

The India-arc accretion model reinterprets the Paleocene collision event as the accretion of a trans-Tethyan intra-oceanic subduction zone/arc system (TTSZ) onto India prior to the final India-Eurasia collision at 40 – 45 Ma (Aitchison et al., 2000; Bouilhol et al., 2013; Jagoutz et al., 2015). This model postulates that the subduction of an oceanic plate between India and Eurasia after the Paleocene onset of arc-continent collision provides a plausible mechanism to accommodate excess convergence not accounted for in geological estimates (Martin et al., 2020). The oceanic lithosphere would not be represented in shortening estimates because it was subducted into the mantle (Cloos, 1993). Geological evidence for this model derives from the western and eastern peripheries of the system (Ladakh, Pakistan and Myanmar), but may not be supported by the geology of the central part of the system (Wang et al., 2017). Although, it is common in many ancient continental collision systems (e.g., the Appalachian-Caledonide) for field relations vary significantly along strike and for crucial elements of the tectonic system to be missing or minimally exposed along strike (Waldron et al., 2022).

Of particular importance in this discussion is constraining the relative locations and motions of the active southern margin of Eurasia, the trans-Tethyan intra-oceanic subduction zone, and the pre-collision extent of the Indian continental lithosphere. Unfortunately, the narrow suture zones that transect the central Himalayan belt preserve only fragmentary records. In the central and eastern Himalaya, Indian passive margin sediments are directly juxtaposed against elements of the southern-Eurasian active margin along major post-Miocene backthrusts that overprinted the complex Tsangpo suture zone (Burg & Chen, 1984). In the western Himalaya, Indian and Eurasian terranes are separated from one another by the Kohistan-Ladakh arc (KLA), a large remnant of the trans-Tethyan intra-oceanic subduction system that operated in the Neotethys prior to the continental collision (Tahirkheli, 1979). The southern boundary between the KLA and India is delineated by the Indus suture zone, and in the north, the Shyok suture zone separates the KLA from the Karakoram terrane, part of southern Eurasia since the Jurassic (Tahirkheli, 1979; Zanchi et al., 2000).

Crucially, a prediction of the Paleocene arc-continent accretion model is that the age of collision along the Indus suture zone reflects arc-continent accretion onto India prior to final collision. Therefore, the model requires that the final closure of the Shyok suture occur after the collision between the KLA and India along the Indus suture zone, making it younger than 55 – 50 Ma (Garzanti et al., 1987; Kaneko et al., 2003). Unfortunately, the closure age of the Shyok suture zone has remained an open question. Previous estimates range from >80 Ma (Borneman et al., 2015; Petterson & Windley, 1985) to as young as 40 Ma (Bouilhol et al., 2013; Brookfield & Reynolds, 1981), spanning periods before and after the closure of the Indus suture zone.

Previous Cretaceous age constraints for the Shyok suture zone have been based on detrital zircon provenance investigations seeking to distinguish Karakoram-, KLA- and India-derived

detrital zircon populations to constrain the timing of sediment co-deposition from converging terranes as a proxy for collision (Borneman et al., 2015; Najman et al., 2017). These approaches are limited by the fact that vast areas of Indian and Eurasian source rocks are now lost due to erosion or under-thrusting and could have contributed detrital zircon populations of unknown age. This challenge is compounded by the potential for zircon transport over thousands of kilometers during along-trench sediment transport (Malatesta et al., 2013), or in airborne ash particles during large eruptions (Barham et al., 2016). The 40.4 ± 1.3 Ma age estimate derived from changes in the isotopic composition of KLA arc-magmas is an indirect constraint that is reliant on complex magmatic processes taking place at depth (Bouilhol et al., 2013). Another indirect constraint includes the >84 Ma age of an unconformity in which undeformed sediments sit atop deformed and metamorphosed Jurassic strata in Pakistan, which was interpreted as bracketing deformation related to the KLA-Eurasia collision (Gaetani et al., 1990; Gaetani et al., 1993). However, the fining upwards sequence of marine sediments above the unconformity (Gaetani et al., 1990) suggests a subsiding marine basin north of the KLA at this time rather than a post-collisional terrestrial environment.

To provide additional constraints on the age of Shyok suture zone, we compare two paleomagnetic poles obtained from rocks just 15 km apart on either side of the Shyok suture zone in Ladakh, northwest India. Our new paleomagnetic results are derived from Late Cretaceous volcanic and sedimentary rocks deposited in a forearc setting on the Eurasian Karakoram margin. The results yield a significantly different paleolatitude from that derived from the volcanic rocks of the KLA (Martin et al., 2020), precluding final closure of the Shyok suture zone until after 61 Ma. Our results confirm that an ocean basin with a north-south extent of around ~ 1320 km existed between India and Eurasia as collision was beginning on the northern edge of India in the

Paleocene. While the pre-Paleocene paleogeography of the KLA and the extent of intra-oceanic subduction in the Neotethys ocean during the Cretaceous remains uncertain, our results show that the Paleocene collision event in the Himalayan was the accretion of the KLA onto India prior to final continental collision.

4.4 Geological Background

The Shyok suture zone (see Figure 4-1) is a complex zone that records not only the collision between the KLA and Eurasia, but also significant strike-slip faulting and thrusting associated with the indentation of India into Eurasia (Coward et al., 1986). We studied the Shyok suture zone at its easternmost exposure where it is well exposed and accessible in the border area of northern Ladakh, northwest India. There, the Shyok suture is dominated by a 152 – 159 Ma forearc ophiolite comprising ultramafics (pyroxenites and serpentinites), gabbros, diorites and pillow basalts (Changmar/Bogdang Ophiolite) that are overlain by a thick sequence of subduction-related basalt and basaltic andesite volcanics (Shyok volcanics) (Rolland et al., 2000; Saktura et al., 2021; Srimal, 1986; Thanh et al., 2012). The ophiolite and volcanics are unconformably overlain by the middle to late-Cretaceous Hundri Formation, which is composed of shallow-marine limestones, shales and cherts (Srimal, 1986; Upadhyay, 2014).

To the south, the ophiolitic and forearc units are in faulted contact (Srimal, 1986) with either the Khardung volcanics or the Ladakh Batholith, which comprise the extrusive and intrusive elements, respectively, of the KLA (Dunlap & Wysoczanski, 2002). The Khardung volcanics are composed of rhyolite, dacite, tuff and volcano-sedimentary flows that are now in thrust contact with, but thought to be originally deposited onto and intruded by, the plutonic rocks of the Ladakh batholith (Bhutani, 2009; Dunlap & Wysoczanski, 2002). The volcanics have an age range of 66 – 61 Ma (Lakhan et al., 2020; Martin et al., 2020), and may extend to as young as 52 Ma at their uppermost exposure (Saktura et al., 2021). A shallowly north-dipping thrust-reactivated normal fault (Saltoro fault) separates the marine forearc sediments of the Hundri Formation from the fluvial and estuarine sediments and volcanics of the Saltoro Formation (Srimal, 1986; Upadhyay et al., 1999). The Saltoro Formation comprises a fault-bound wedge that is tilted towards the north-

west and is truncated at its upper contact by a complex set of late-stage south-vergent thrusts representing the eastern extent of the Karakoram thrust system (Rai, 1982; Rex et al., 1988; Rolland et al., 2000; Searle et al., 1989). The tilt of the Saltoro Formation strata steepens to vertical towards the south, where the strata are locally folded into a north-verging anticline-syncline pair.

We studied an approximately 4830 m thick exposure of the Saltoro Formation on the western bank of the Nubra valley near the village of Charasa (see Figure 4-1). The Saltoro Formation is an ideal target for paleomagnetic investigation because the paleohorizontal is easy to determine and it comprises unmetamorphosed volcanic flows and clastic sediments. The base of the Saltoro stratigraphy is not exposed in the study area, but the lowermost 220 m of the exposed sediments comprise primarily fine-grained fluvial sandstones interbedded with poorly sorted conglomerates containing a variety of well-rounded pebble- and cobble-size clasts of almost entirely extrusive volcanic lithologies, as well as rare granite, sandstone, shale, limestone and chert clasts (see Figure 4-2a). Over the next 560 m of the stratigraphy, the conglomerates grade upwards into 0.3 – 2 m thick layers of very fine sandstone with planar crossbedding interbedded with 1 – 5 cm thick siltstone and mudstone horizons. The dominant grain size continues to decrease for a further 720 m up section, becoming characterized by mudstones and siltstones intercalated with paleosol horizons and interbedded with fine-grained fluvial sandstones. Periodically, coarse sandstone beds are interspersed within the finer grained sediment indicating periods of high sediment transport and stronger flow conditions. Throughout the lower stratigraphy, cross-stratification and asymmetrical ripples indicate a southwestward paleo-flow direction (see Figure 4-2b).

At a stratigraphic level of 1510 m above the lowermost exposed strata, in the distinctive promontory upon which the Charasa Monastery is situated, there is a 50 – 120 m thick, internally

homogeneous and laterally continuous plagioclase-pyroxene porphyritic andesite flow. Phenocrysts vary in size from 0.5 – 2 cm and are sometimes clustered together into glomerocrysts. The upper surface of this volcanic unit contains weathering cracks that are filled with the overlying coarse sandstone (see Figure 4-2c). The Charasa Monastery volcanic flow is overlain by a 715 m thick section of sediments comprising fine-grained grey and red mudstones interbedded with medium to coarse-grained sandstones and topped by a 40 m thick conglomerate that marks the start of a break in section due to quaternary cover. Above the break, 480 m of mudstones and shales give way to massive volcanoclastic tuffs and agglomerates. The agglomerates have 2 – 15 cm diameter subangular clasts in a fine-grained welded matrix and are increasingly interbedded with very fine-grained black basalts and basaltic andesites up section towards the north.

Volcanic flows dominate the 1870 m thick uppermost section of exposed Saltero stratigraphy. The andesitic and trachyandesitic volcanics are very fine-grained, unfoliated, and sometimes contain 1 – 5 mm long plagioclase phenocrysts and/or vesicles. Some of the volcanic flows are locally epidotized and exhibit spectacular auto-brecciation (see Figure 4-2d), suggesting that some flows were erupted into lacustrine or shallow marine environments. In places, the basalts are interbedded with black medium-coarse lithic sandstones and sandy paleosol horizons. The presence of major volcanic flows conformably bedded with the sedimentary horizons throughout the Saltero stratigraphy indicates that the sediments were accumulating in close proximity to active volcanic centers. The Saltero Formation is crosscut by small 0.5 – 3 m wide intermediate and felsic dikes.

4.5 Materials and Methods

4.5.1 Geochronology

To extract zircons for U-Pb geochronology that could constrain the age range of our paleomagnetic results, we collected oriented block samples from throughout our paleomagnetic sample section. The rock samples were disaggregated by manual sledging, pulverized using a Shatterbox and sieved into monomineralic, sand-sized particles. Magnetic and density separation techniques were used to obtain heavy mineral concentrates from which zircon grains were randomly sampled and mounted in epoxy resin with natural reference standards and polished to expose the interiors of the grains. Zircons were imaged using backscattered electron (BSE) and cathodoluminescence (CL) using a scanning electron microscope (SEM) at MIT. Using the imagery to guide spot targeting, samples were dated with laser ablation inductively coupled plasma mass spectrometry (LA-ICP-MS) at the University of Florida and Rutgers University. Details of measurement protocols are in Mueller et al. (2008). Data reduction was completed at Rutgers University using the Iolite software package (Paton et al., 2011) and at the University of Florida using in-house software (Calamari). In order to minimize the chance of age underestimation due to lead loss (Vermeesch, 2021), we filtered our data using a 5% discordance cutoff and only included analyses with $^{204}\text{Pb}/^{206}\text{Pb} < 0.001$. The discordance filter used the discordance between the $^{206}\text{Pb}/^{238}\text{U}$ age and $^{207}\text{Pb}/^{235}\text{U}$ age for zircons with $^{206}\text{Pb}/^{238}\text{U}$ ages less than 1000 Ma and the discordance between the $^{206}\text{Pb}/^{238}\text{U}$ age and $^{206}\text{Pb}/^{207}\text{Pb}$ age for zircons with $^{206}\text{Pb}/^{238}\text{U}$ age greater

than 1000 Ma. Concordia diagrams and detrital zircon spectra (Figures 3-3 and 3-4) were produced using the AgeCalcML software package (Sundell et al., 2021).

4.5.2 Paleomagnetism

We collected 7 – 10 oriented core samples from 29 horizons distributed throughout the Saltero Formation stratigraphy near Charasa for paleomagnetic analysis. Core samples were collected in the field using a water-cooled electric hand drill and oriented using an ASC Industries Pomeroy orienting fixture. Nonmagnetic brass tools were used to extract cores from the outcrop to prevent damaging the remanent magnetization of samples during sample collection. Optical microscopy was used to identify magnetic carriers and textural relationships within the samples. One specimen was cut from each core sample using an ASC Scientific dual-blade rock saw. The natural remanent magnetization was measured on a 2G Enterprises Superconducting Rock Magnetometer equipped with an automated sample handler (Kirschvink et al., 2008) inside a mu-metal magnetically shielded room in the MIT Paleomagnetism Laboratory applying a <200-nT DC field. Specimens were subjected to stepwise alternating field (AF) and thermal demagnetization. AF steps were applied in increments of 2 mT up to 12 mT followed by thermal steps starting at 100 °C and increasing up to 600 °C or 680 °C in variable interval sizes at a maximum of 100 °C and minimum of 2 °C close to the Curie temperatures of the suspected principal magnetic carriers (magnetite: 580 °C, and hematite: 680 °C). Stable components of magnetization were isolated using principal component analysis (PCA) (Kirschvink, 1980).

The domain state of magnetite was assessed using hysteresis curves acquired for applied fields of -1 to 1 T and corrected by removing any paramagnetic or diamagnetic signals. Samples

were analyzed using an ADE model 1660 vibrating sample magnetometer (VSM) in the Ross Laboratory, MIT Department of Materials Sciences and Engineering.

Site-mean magnetization directions were calculated using Fisher statistics (Fisher, 1953) and corrected for bedding tilt. Corrections for inclination-shallowing of sedimentary magnetization directions were made using the elongation-inclination method of Tauxe and Kent (2004). Northern hemisphere virtual geomagnetic pole (VGP) positions for each site were determined and the Fisher mean (Fisher, 1953) of the VGP data was used to obtain the overall paleomagnetic mean pole and associated A95 error envelope. We used the quantile–quantile method (Fisher & Lewis, 1983) to show that the final VGP distribution is consistent with a Fisher model. All paleomagnetic data processing and plotting were done using the PmagPy software package (Tauxe et al., 2016).

4.6 Results

4.6.1 U-Pb Geochronology

Detrital zircons from four sedimentary samples, comprising three medium-fine grained sandstones (LB19-06, LB18-18, and LB18-20) and one siltstone (LB19-54), were analyzed along with one sample of welded tuff (LB19-56) to bracket the age of deposition/eruption of the paleomagnetic sampling section (see Figures 3-3, 3-4, 3-5). In the subsequent section, we report the $^{206}\text{Pb}/^{238}\text{U}$ age and 2σ uncertainty of the youngest individual zircon in each sample (Coutts et al., 2019; Dickinson & Gehrels, 2009). In cases where the youngest grain had a large 2σ uncertainty we report the $^{206}\text{Pb}/^{238}\text{U}$ age of the zircon with the smallest 2σ uncertainty that was within error of the youngest zircon in the same sample. The age of the tuff sample records the time of magma cooling and eruption while the detrital zircon ages are maximum depositional ages because the true depositional age is by definition an unknown amount younger than the youngest zircons in the sample. Nevertheless, the presence of volcanic flow horizons within the Saltero stratigraphy indicates that active volcanic centers were proximal to the sedimentary catchment area, so maximum depositional age is likely well-approximated by the youngest grains in the sample.

At the base of our sampled section, sample LB18-20 yielded a maximum depositional age $\leq 92.9 \pm 2.2$ Ma. This age is identical within error to the $\leq 92.43 \pm 0.24$ Ma age (calculated using the weighted mean of the youngest mode of a probability density plot for number, $N = 97$) reported near the bottom of the Saltero section by Borneman et al. (2015). For comparison with our data, we passed the data from Borneman et al. (2015) (sample BCUM12-105) through the same quality filter applied to our data and yielded a maximum depositional age $\leq 89.2 \pm 2.2$ Ma. Due to the potential problems with depositional age overestimation associated with using the weighted mean

of the youngest peak (Coutts et al., 2019; Vermeesch, 2021), we believe our treatment of their data provides a more reliable estimate of the depositional age.

Sample LB18-18 is from a fine-grained sandstone deposited immediately above the andesitic flow exposed at the Charasa Monastery. It yielded a maximum depositional age $\leq 85.3 \pm 3.4$ Ma. Sample LB19-06 is from a medium-grained sandstone interbedded with mudstones in the middle portion of the sampled Saloro section. It yielded a maximum depositional age $\leq 84.3 \pm 1.8$ Ma. A small break in exposure due to quaternary glacial cover separates LB19-06 from the overlying sediments, volcanoclastics and thick volcanic flow succession that defines the uppermost exposures of the Saloro Formation stratigraphy. LB19-58 is a fine-grained siltstone near the base of this upper exposure and yielded a maximum depositional age $\leq 81.2 \pm 1.7$ Ma. The youngest age constraint on the sampled section comes from the welded tuff sample (LB19-56) that yielded a well-defined population of igneous grains along with a few xenocrysts. The U-Pb zircon age of the tuff is 74.6 ± 0.7 Ma. This provides a younger bound on most of our paleomagnetic samples, with five paleomagnetic sites situated higher in the stratigraphy where no viable sample for U-Pb geochronology was available.

The U-Pb zircon depositional and eruption ages of our samples are consistently younging up-section (see Figure 4-5), suggesting that there are no major structural breaks or unconformities throughout the section. The results also suggest that the time interval recorded in our paleomagnetic sampling section is 18.3 million years in the Late Cretaceous between 92.9 ± 2.2 Ma and 74.6 ± 0.7 Ma. This interval spans sufficient time for the paleomagnetic data to reliably average paleosecular variation of the geodynamo (Deenen et al., 2011).

All the sedimentary samples (LB18-20, LB18-18, LB19-06, LB19-54) contained detrital zircons with broad, multi-peaked age distributions ranging from the Late Cretaceous to the

Mesoarchean with the vast majority of the grains of Cretaceous and Jurassic age (see Figure 4-4). The presence of zircons from a broad range of sources suggests a complex continental provenance with a mixture of various basement sources and more recent active sources, consistent with a Eurasian margin provenance.

4.6.2 Rock Magnetism

Hysteresis curves were acquired for a representative subset of volcanic samples (SA24-7, SA27-5, and SA28-7) and for representative sedimentary samples (SA16-1, SA17-2, SA19-3, and SA22-5) exhibiting different component combinations as determined by their thermal demagnetization results (see Figure 4-6). The hysteresis curves were corrected for paramagnetic and diamagnetic signals and used to determine the saturation magnetization (M_s), the saturation remanent magnetization (M_{rs}), the coercivity of remanence (H_{cr}) and the coercivity (H_c) for each sample (see Table 3-2). The domain state of magnetite was assessed using a Dunlop-Day plot (see Figure 4-7) by calculating the ratio of M_{rs}/M_s and H_{cr}/H_c (Day et al., 1977; Dunlop, 2002).

The sedimentary samples with magnetite and the absence of hematite (SA16-1 and SA17-2) plot in the pseudo-single domain (PSD) range on the Day plot, suggesting that they have reliable paleomagnetic recording properties. The andesite samples (SA24-7, SA27-5, and SA28-7) all plot in the field of PSD and multi-domain (MD) mixtures on the Day plot suggesting that there are both reliable paleomagnetic recorders and less reliable recorders in the sample. Two of the samples (SA22-5 and SA19-3) did not contain magnetite, so are not displayed on the Day plot.

4.6.3 Paleomagnetism

The sample set contains a broad spectrum of lithologies exhibiting a range of different magnetic components characterized by different unblocking temperatures and relative magnitude (see Figure 4-8). Almost all specimens exhibited a low temperature and low coercivity overprint (LCT) that was removed during the AF steps and during thermal steps below 200 °C. Prior to any structural corrections, and regardless of site lithology, these components mostly aligned within $\alpha 95\%$ confidence with the present-day magnetic field direction in the study location (see Figure 4-9). The LCT components are interpreted as a recent overprint, likely due to viscous remanent magnetization (VRM) (Pullaiah et al., 1975).

The majority of the sedimentary sites (SA02 – SA11, SA14, and SA23) exhibited two high temperature components (see Figure 4-8). Components with unblocking temperatures consistent with magnetite were isolated in thermal demagnetization steps between 450 °C and 580 °C (HT1), and origin-trending components with unblocking temperatures consistent with hematite were isolated in thermal demagnetization steps between 640 °C and 680 °C (HT2). A subset of the sedimentary sites (SA12, SA13, SA15, SA16, and SA21) had origin-trending HT1 components, but no HT2 components. Two sites (SA17 and SA18) had origin-trending components consistent with magnetite that were isolated between 450 °C and 550 °C (HT1) and antipodally directed components with unblocking temperatures consistent with pyrrhotite (Curie temperature: 320 °C) that were isolated between 300 °C and 400 °C (LT). One site (SA22) was unique in that it had only components consistent with hematite that were isolated between 600 °C and 640 °C (HT2a) and highly stable origin-trending components that were isolated between 640 °C and 680 °C. Samples from site SA19 had only LCT components and no high-temperature components and samples from SA09 had LCT components, but became highly unstable at temperatures exceeding 640 °C and

were excluded from further analysis. Samples from site SA20 were also excluded because the high temperature magnetization directions from these samples were not sufficiently clustered to achieve a site-mean directional uncertainty of $\alpha_{95} < 16^\circ$ (Van der Voo, 1990).

Sites SA24, SA25, SA27, SA28, and SA29 comprise andesitic lava flows and SA26 is a welded ignimbrite. In addition to LCT components with the same direction and unblocking temperature range as sedimentary samples, these sites exhibited origin-trending high-temperature magnetization components with unblocking temperatures consistent with magnetite that were isolated in thermal demagnetization steps between 540 °C and 580 °C (HT1). All of the volcanic sites except SA29 also contained origin-trending components with unblocking temperatures consistent with hematite that were isolated between 620 °C and 680 °C (HT2). In volcanic or sedimentary samples exhibiting HT1 and HT2 directions with very similar orientations, we selected the best-defined site-mean direction, depending on which had the lowest α_{95} site-mean uncertainty, as the characteristic remanent magnetization (ChRM) direction to be used in subsequent calculations of the paleomagnetic pole for the Saltero Formation.

To conclusively test whether the high-temperature magnetization components (both HT1 and HT2) exhibited by our sample suite reflect the orientation of Earth's magnetic field at the time the rocks formed, we conducted a conglomerate test on specimens from 30 primarily andesitic clasts (see Figure 4-10f) in a cobble-conglomerate unit (site SA01) near the base of the sampled section (see Figure 4-5). The magnetization directions of large, transported sedimentary clasts in a conglomerate should be randomly distributed when they are deposited, whereas a magnetic overprint would produce clast magnetization directions aligning with the magnetic field at the time of overprinting (i.e., not randomly distributed) (Van der Voo, 1990). We performed a Watson test to determine whether the magnetization directions of both HT1 and HT2 components from the

clasts in site SA01 were randomly distributed (Watson, 1956). For the suite of clast HT1 and HT2 magnetization directions, we obtained resultant vectors of $R_{HT1} = 4.33$ and $R_{HT2} = 3.18$ respectively. Since R_{HT1} and R_{HT2} are both less than the critical value of $R_0 = 8.80$ for $N = 30$ directions, we cannot rule out the null hypothesis that the magnetization directions are randomly distributed with 95% confidence. The conglomerate test is therefore successful, indicating that both the HT1 and HT2 high-temperature magnetization directions recorded by our samples have not been overprinted subsequent to deposition.

Additional strong evidence for the primary origin of magnetization comes from directions from sites stratigraphically above SA17 that are antipodally reversed compared to those from sites SA16 and the underlying stratigraphy. These sites define a reversal of Earth's geodynamo situated at the expected stratigraphic location for the C34n to C34r reversal at 83.65 Ma (see Figure 4-5) (Gradstein et al., 2020). Sample LB19-06 was collected from 160 m up section of the reversal and its depositional age is within error of the reversal age suggesting that our age determinations fall very close to the true maximum depositional ages of the sediments sampled throughout the Saltoro section. The normal and reversed populations pass a bootstrap reversal test (Tauxe, 2010) demonstrating that they are indeed antipodally reversed (see Figure 4-11). The presence of a magnetic reversal in the stratigraphy in the expected location is strong evidence for primary magnetization because a regional magnetic overprinting event would have obliterated the reversal record, remagnetizing all samples to the same polarity (Van der Voo, 1990). Our geochronology suggests one other normal polarity magnetochron (C33n) is expected within the sampled stratigraphic section. However, it is not present in our paleomagnetic results. This is not surprising

because C33n is a relatively short magnetochron and it is expected to be within the large sampling gap between SA18 and SA25, where there is very limited exposure due to quaternary cover.

To identify and correct for possible compaction related shallowing of inclination in our sedimentary paleomagnetic datasets, we used the elongation/inclination (E/I) method (Tauxe & Kent, 2004). Application of the E/I method to $N = 19$ sedimentary site-mean directions yielded a flattening factor of $f = 0.510$, which we used to correct the sedimentary site-mean direction data before determination of the paleopole (see Figure 4-10c and Figure 4-12). The E/I correction applied here uses less than the optimum $N \geq 100$ suggested by Tauxe and Kent, (2004), but we do not believe this limits the reliability of our shallowing correction. Artificially increasing N by using sample level data ($n = 155$) yields an almost identical flattening factor of $f = 0.515$ and resulted in an insignificant ($< 0.5^\circ$) difference on the final paleomagnetic pole and paleolatitude. The alternative corrections modified the mean inclination of uncorrected sedimentary sites from $I_{(uncorrected)} = 20.6 \pm 7.8^\circ$ to a site-E/I corrected inclination of $I_{(Site\ corrected)} = 35.32 \pm 8.9^\circ$, and a sample-E/I corrected inclination of $I_{(Sample\ corrected)} = 34.4 \pm 8.8^\circ$, which are easily within error of one another (see Figure 4-10c). Furthermore, both corrections yield inclinations that are within error of the volcanic sites ($I_V = 32.2 \pm 10.5^\circ$), which require no shallowing correction. This suggests the E/I correction performed here appropriately removes the effects of inclination shallowing in the dataset.

After the corrections are applied for bedding tilt and inclination shallowing in sedimentary sites, the site-mean magnetization directions from the Saloro Formation fall into two groups with distinct mean declinations (see Figure 4-10d). Sites SA25 – SA29 at the top of the sampled stratigraphy have a mean normal-polarity declination of $D = 3.56 \pm 11.00^\circ$, while samples stratigraphically beneath SA25 have a mean normal-polarity declination of $D = 304.40 \pm 8.47^\circ$,

which we interpret as corresponding to an anti-clockwise vertical axis rotation (VAR) of $59.2 \pm 19.5^\circ$ between sites SA18 and SA25. We considered a number of other possible causes for this rotation, including incorrect structural correction due to either angular unconformity, rotation along an unidentified fault surface or an unidentified plunging fold. Any of these reorientation processes would be expected to produce different bedding orientations over the transition between the rotated and unrotated sites. However, the mean bedding orientation across this interval is almost identical (see Figure 4-10g). The rotation, therefore, must have occurred around a vertical axis during the deposition of the Saltoro Formation rather than during subsequent deformation. This rotation likely occurred during extension of the Eurasian margin (Karakoram and South Pamir) in the Late Cretaceous due to slab rollback (Chapman et al., 2018). It is also important to note that the vertical axis rotation in our data has no effect on our E/I flattening correction. Accurate determination of the flattening factor using the E/I method relies on the assumption that there are no sources of scatter within the data other than paleo-secular variation (PSV) of the geodynamo (Vaes et al., 2021). Since all of the sedimentary sites are situated in the rotated lower portion of the stratigraphy, there is no differential rotation between the sedimentary sites and no effect on the shallowing correction.

After a correction was made for the vertical axis rotation, northern hemisphere virtual geomagnetic poles (VGP) were used to determine the paleopole. VGPs are more likely to have a Fisher distribution than site-mean paleomagnetic directions (Deenen et al., 2011). To assess whether the final distribution of VGPs is Fisher distributed, we used the quantile-quantile method of Fisher and Lewis (1983) and obtained a longitude-test statistic of $M_u = -0.923$ and a colatitude-test statistic of $M_e = 0.534$, each of which are less than the respective critical values for 95% confidence of $M_{u(critical)} = 1.207$ and $M_{e(critical)} = 1.094$ for $N = 25$. This indicates the Saltoro VGP

distribution is consistent with a Fisherian model (see Figure 4-13). The time-averaged mean paleomagnetic pole for the Saltero Formation is situated at $P_{Lon} = 244.0^\circ$ E and $P_{Lat} = 75.0^\circ$ N with a 95% uncertainty bound of $A_{95} = 6.2^\circ$ and precision parameter $K = 22.9$. The corresponding paleolatitude of the Saltero Formation is $20.0 \pm 6.2^\circ$ N in the time period between 92.9 ± 2.2 Ma and 74.6 ± 0.7 Ma (see Figure 4-14).

We compared the Saltero Formation paleopole to the well-established reliability criteria to determine paleopole reliability, and it meets all the applicable criteria (Meert et al., 2020; Van der Voo, 1990). The Saltero Formation paleopole has a very well constrained U-Pb zircon age and the >18.3 million years spanned by the Saltero stratigraphy is easily long enough to achieve appropriate sampling of paleosecular variation (PSV) of the geodynamo, and the A_{95} uncertainty for the Saltero Formation paleopole is comfortably within the acceptable range to reliably average paleosecular variation (PSV) of the geodynamo ($10.8^\circ \geq A_{95} \geq 3.3^\circ$ for $N = 25$) defined by Deenen et al. (2014). The number of samples used to calculate the paleopole ($n = 207$) exceeds the minimum criterion of $n \geq 25$, the precision parameter ($K = 22.9$) is in the range $70 \geq K \geq 10$, and the number of sites ($N = 25$) is well above the required threshold of $N \geq 8$ (Deenen et al., 2014; Meert et al., 2020). The separation of the natural remanent magnetization into constituent components was achieved using modern demagnetization techniques. The magnetic carriers were constrained with rock magnetic analyses and microscopy. There is good structural control, and inclination shallowing of sedimentary data was corrected using the E/I method. Finally, a primary origin of remanence was confirmed by both a successful conglomerate test and the presence of a geomagnetic reversal at the expected stratigraphic level that passes a bootstrap reversal test.

Overall, this suggests that the paleomagnetic pole that we obtained from the Saltero Formation is of high reliability and can be used in paleomagnetic reconstructions with confidence.

4.7 Discussion

4.7.1 Age of the Shyok Suture Zone

Our results from the Saltoro Formation constrain the paleolatitude of the Karakoram terrane in the western Himalaya to $20.0 \pm 6.2^\circ$ N at 92.9 – 74.6 Ma. This latitude is significantly different from that of the KLA, which is constrained by paleomagnetic results from the Khardung volcanics to a paleolatitude of $8.1 \pm 5.6^\circ$ N between 66.1 – 61.6 Ma (Martin et al., 2020). These results conflict with a postulated Late Cretaceous (85-93 Ma) formation age of the Shyok suture (Borneman et al., 2015; Gaetani et al., 1993; Petterson & Windley, 1985). If the Khardung volcanics formed after the accretion of the KLA and closure of the Shyok suture (Pundir et al., 2020; Saktura et al., 2021), then their paleolatitude would be indistinguishable from that of the Saltoro Formation because the two are situated just 15 km apart across the Shyok suture zone. Instead, the Saltoro and Khardung Formations do not share a common paleopole, and were separated by 11.9° latitude (equivalent to 1320 km). This significant separation between the KLA and Karakoram places a maximum age limit of 61 Ma for final closure of the Shyok suture zone. This constraint is substantiated by a common mean test (Tauxe et al., 1991) performed using the VGP distributions of both the Khardung volcanics and the Saltoro Formation, which demonstrates with 95% certainty that the paleomagnetic datasets define different paleopoles (see Figure 4-15). The constraint is also unaffected by the challenges associated with comparing individual study mean paleomagnetic poles to a reference pole from an apparent polar wander path (APWP) that was recently highlighted by Rowley, (2019) because it derives from the direct comparison of two paleopoles from nearby locations.

A post-61 Ma age for the Shyok suture zone is consistent with early studies that interpreted that the Shyok suture zone closed in the Eocene-Oligocene (Andrews-Speed & Brookfield, 1982;

Brookfield & Reynolds, 1981; Sharma, 1987). This early interpretation was only abandoned when Pettersen and Windley (1985) posited that the SSZ formed in the Late Cretaceous (85 – 104 Ma) based on the Rb-Sr whole rock ages of granitoid intrusions and the presence or absence of a pervasive gneissic fabric (i.e., younger intrusions undeformed, older deformed). However, Jagoutz et al. (2009) demonstrated using modern U-Pb zircon ages that no relationship exists between the presence or absence of gneissic fabric and the intrusion age of felsic plutons in Kohistan.

The age of the Shyok suture zone was further obfuscated by Borneman et al. (2015), who suggested a 92 – 85 Ma age based on the depositional age of the Eurasia-derived Saltoro Formation sediments and the 85.2 ± 3.8 Ma U-Pb zircon age of a felsic dike crosscutting what they interpreted as an unconformity between Saltoro sediments and the Shyok volcanics. Contrary to previous work interpreting the Shyok volcanics and Saltoro sediments as part of the southern margin of Eurasia (Rai, 1982; Sharma, 1987; Thanh et al., 2012), they asserted that the Shyok volcanics and Saltoro Formations were part of the KLA and interpreted the presence of Eurasia-derived zircons in the Saltoro Formation as an age constraint for the KLA-Eurasia collision. Additionally, the dike dated by Borneman et al. (2015) does not crosscut a Shyok/Saltoro unconformity as postulated, but rather an angular unconformity within the Saltoro Formation in which clastic sediments are deposited on one of the many andesitic volcanic flows that are common within the Saltoro stratigraphy. Bornemann et al. (2015) interpreted that the Saltoro fault becomes an unconformity along strike. However, within the study area of Bornemann et al. (2015) the Saltoro fault is spectacularly exposed at a lower structural level separating the Saltoro Formation andesites, agglomerates and sediments from typical pillow basalts of the Shyok volcanics (see Figure 4-1b). Thus, the rationale

for the Late Cretaceous formation age of the Shyok suture zone proposed by Borneman et al. (2015) is not supported by the field relationships.

Indeed, the development of an angular unconformity and normal faulting near the base of the Saltoro Formation, its fining upward stratigraphy, and the presence of dikes and volcanic horizons throughout the section suggests that the Karakoram margin was undergoing extension and subsidence at around 93 – 83 Ma, not compressional orogenesis. The anti-clockwise vertical axis rotation of the Saltoro stratigraphy in our paleomagnetic results also occurred at ~ 83 Ma, so may be related to this extension. Late Cretaceous Karakoram extension is also supported by the presence of an angular unconformity in northern Pakistan where deformed Jurassic strata of the Karakoram block are overlain by a fining upward marine transgression of subaerial alluvial fan deposits that are overlapped by Campanian age (83.6 – 72.1 Ma) marine wackestones and mudstones (Tupop Fm. and Durband Fm.; Gaetani et al., 1993). This field evidence for Cretaceous extension along the Karakoram margin is consistent with the magmatic evolution of the Karakoram and south Pamir, which has been recently interpreted to suggest extension between 80 – 70 Ma due to Neotethyan slab rollback (Chapman et al., 2018). It is also consistent with the postulated back-arc extension and rifting of the Xigaze forearc southward from the Eurasian forearc due to a retreating subduction zone (Kapp and DeCelles, 2019; their Scenario 2). Rifting of the Xigaze and Karakoram forearc sediments southward from the Eurasian margin could provide an additional mechanism for delivering Eurasian derived sediments to the Indian margin during a Paleocene India-arc collision (An et al., 2021; DeCelles et al., 2014) without requiring full closure of the Neotethys ocean.

The difference in age between our paleomagnetic results and those of Martin et al. (2020) leaves open the possibility that the Karakoram terrane moved southward towards the KLA between

75 Ma – 66 Ma, resulting in a >61 Ma closure of the Shyok suture zone. However, the absence of a younger suture zone north of the Shyok suture zone makes this scenario unlikely. Furthermore, this southward motion of the Karakoram block relative to Eurasia would be required to occur at a rapid ~14 cm/year and is not supported by paleomagnetic evidence from elsewhere in the Himalaya, which indicates that the Eurasian margin remained at a quite stationary paleolatitude of ~18 – 22 °N from the Early Cretaceous until the Eocene (Lippert et al., 2014; van Hinsbergen et al., 2019).

In summary, both geologic and paleomagnetic records suggest that the final closure of the Shyok suture zone occurred in the Paleogene, most likely in the Eocene at around 45 – 40 Ma as constrained by the appearance of an evolved crustal signature in the ϵ_{Hf} , ϵ_{Nd} and $^{87}\text{Sr}/^{86}\text{Sr}$ isotopic record of KLA magmas at 40.4 ± 1.3 Ma (Bouilhol et al., 2013). An Eocene final collision is consistent with the onset of regional metamorphism and deformation in response to a continental collision at 45 – 40 Ma (Burg & Bouilhol, 2019; Cowgill et al., 2003; Leloup et al., 2001; Yin et al., 1999). In addition, crustal shortening estimates from across Tibet and the Himalaya fold and thrust belt are in good agreement with the amount of India-Eurasia convergence that occurred after 40 Ma (DeCelles et al., 2002; Martin et al., 2020; Van Hinsbergen et al., 2011).

4.7.2 Paleomagnetic Reconstruction of the Neotethys

Reconciling the various conflicting India-Eurasia collision models relies on a robust understanding of the relative positions of the leading edge of India, the KLA and any other trans-Tethyan subduction system remnants, and the southern margin of Eurasia through time. Our results represent the only reliable Cretaceous paleomagnetic constraint from the Karakoram terrane in the western Himalaya and so provide an important constraint on the location of the Eurasian margin

in the western extent of the belt. They suggest that the Karakoram terrane and the Lhasa block (the southernmost Eurasian tectonic block in Tibet) comprised contiguous elements of the southern Eurasian margin at $\sim 20^\circ\text{N}$ in the Campanian. To aid the discussion of our results in the broader context of the paleo-reconstructions of India, the Trans-Tethyan-subduction system and Eurasia we will review reliable paleomagnetic constraints from each of the three tectonic plates, and then synthesize the results to derive a coherent picture of the tectonic evolution of the Neotethyan realm based on reliable and robust paleomagnetic data. The compilation of paleomagnetic poles for our synthesis is presented in Table 3-4.

4.7.2.1 Paleomagnetic Constraints on Eurasia

The most reliable paleomagnetic data show that the Lhasa terrane was situated at a constant $\sim 18 - 22^\circ\text{N}$ latitude from the Early Cretaceous until the Eocene, throughout the closure of the Neotethys ocean (Dupont-Nivet et al., 2010; Lippert et al., 2014; van Hinsbergen et al., 2019). Reliable Cretaceous paleomagnetic results from volcanic and sedimentary successions across Tibet yield paleolatitudes around $16 - 20^\circ\text{N}$ (Bian et al., 2017; Chen et al., 2012; Li et al., 2017; Ma et al., 2017; Ma et al., 2014; Yang et al., 2015). The majority of Late Cretaceous to Eocene paleomagnetic data are derived from the Eocene Linzizong volcanics and underlying Cretaceous sediments that are well exposed in the Linzhou area near Lhasa in Eastern Tibet. Paleomagnetic studies of these units have yielded a large range of paleolatitudes between $5^\circ\text{N} - 24^\circ\text{N}$ (Achache et al., 1984; Cao et al., 2017; Chen et al., 2010; Chen et al., 2014; Dupont-Nivet et al., 2010; Liebke et al., 2010; Lippert et al., 2014; Sun et al., 2010; Sun et al., 2012; Tan et al., 2010; Tong et al., 2022; Yi et al., 2021). However, careful paleomagnetic and rock magnetic analyses have demonstrated that the spread in paleolatitudes is the result of a low-latitude bias caused by a

combination of uncorrected inclination shallowing in sedimentary sites and partial remagnetization after tilting (Huang et al., 2013; W. T. Huang et al., 2015). Lippert et al. (2014) rigorously filtered Linzizhong volcanic data to mitigate these effects and their analysis yielded an Eocene paleolatitude of 21.1 ± 4.1 °N between 56 – 47 Ma (for a reference location on the Tsangpo suture zone at 29.0 °N and 88.0 °E). The only other Eocene constraints on the Lhasa Terrane are from Xigaze forearc basin sediments exposed near Zedong in west-central Tibet, which yield a paleolatitude of 24.2 ± 5.9 °N between 57 – 54 Ma (Meng et al., 2012; Tong et al., 2022). These results are consistent with those of Lippert et al. (2014), although the datasets have significant scatter and have not been corrected for inclination shallowing.

The reliable paleomagnetic record from across the southern Eurasian margin, including our results, are in very close agreement with the paleolatitude of Makran (part of the Eurasian margin minimally affected by collision) reconstructed using the Eurasian apparent polar wander path of Torsvik (2012) (see Figure 4-14). Since Makran is part of the present day southern Eurasian margin in Iran, where effects related to the Indian-Eurasia collision are minor, its restored paleolatitude provides a reasonable approximation of the pre-collisional Eurasian margin eastward into the Karakoram and Tibet.

4.7.2.2 Paleomagnetic Constraints on India

Owing to the dearth of volcanic rocks that are considered the optimum target for paleomagnetism, and the widespread thermal and chemical overprint in the Tethys Himalaya sediments (Appel et al., 2012; Crouzet et al., 2003; Dannemann et al., 2022; Huang et al., 2017; Schill et al., 2002; Xu et al., 2022), the location of the northern edge of India is more challenging to constrain than the Eurasian margin. Results from Paleocene Limestones of the Tingri and

Zongpu Formations were originally interpreted as suggesting the Tethys Himalaya were situated 2000 – 3000 km north of cratonic India at the onset of collision (Besse et al., 1984; Patzelt et al., 1996; Tong et al., 2008; Yi et al. 2011), but these successions have since been shown to be remagnetized (Huang et al., 2017; Liebke et al., 2013).

The best paleomagnetic data from the northern Indian margin derive from basaltic flows that were erupted between 140 – 125 Ma, while India was still proximal to Gondwana (Bian et al., 2019; Ma et al., 2016; Yang et al., 2015). Although these represent valuable constraints on Indian plate motion, they are of limited utility in constraining the size of Greater India in the run-up to collision due to the significant rotation of India since Gondwana breakup (Zhang & Huang, 2017).

Recent, high quality paleomagnetic data from 76 – 74 Ma shales in south-central Tibet suggest that the Tethyan Himalaya was situated at a paleolatitude 19.4 ± 1.8 °S, corresponding to a Greater India with a latitudinal extent of 715 ± 374 km (Yuan et al., 2022; Yuan et al., 2021). Yuan et al. (2022; 2021) also obtained a 62.5 – 59.2 Ma paleomagnetic pole from clastic successions at Mulbala and Sangdanlin with a paleolatitude of 14.1 ± 1.9 °N, suggesting a western Greater India extent of 1342 ± 484 km, leading them to infer rifting of the Tethyan Himalaya northward between 74 – 63 Ma. This paleolatitude is slightly north of the 8.1 ± 5.6 °N of the KLA at 66 – 61 Ma (Martin et al., 2020), suggesting convergence between the Tethyan Himalaya and the KLA in the Paleocene (Yuan et al., 2022). In the absence of geologic evidence for a Greater India basin and rifting of northern India between 74 – 63 Ma (Searle, 2019), more constraints are needed to substantiate the extent to which the inferred extension is real or an artifact of the rapid motion of India in the Paleocene and the inherent scatter in paleomagnetic data. Reconstructing Greater India based on the Wallaby-Zenith Fracture zone off western Australia and the fit of India

into Gondwana (Ali & Aitchison, 2005) predicts paleolatitudes of the Tethyan Himalaya that are in very good agreement with the reliable paleomagnetic data (see Figure 4-14).

4.7.2.3 Paleomagnetic Constraints on the KLA

The only reliable paleomagnetic constraint on the position of the KLA is the 8.1 ± 5.6 °N paleolatitude of the Khardung volcanics reported by Martin et al. (2020). The paleomagnetic record is presently unable to resolve the paleogeography of the KLA prior to 66 Ma because paleomagnetic studies from Cretaceous rocks from Kohistan either yielded overprinted remanences (Ahmad et al., 2001; Ahmad et al., 2000) or fall short of modern reliability standards (Klootwijk et al., 1984; Klootwijk et al., 1979; Zaman et al., 2013; Zaman & Torii, 1999). This leaves open the possibility that the KLA formed near to or collided with the Eurasian margin before ~93 Ma and subsequently rifted southward to a near equatorial latitude (comparable to the present-day Sea of Japan) before collision with India in the Paleocene (Kapp & DeCelles, 2019; Rolland et al., 2002). Alternatively, the KLA could have formed part of a long-lived intra-oceanic subduction system (similar to the present-day Izu-Bonin-Mariana arc) operational outboard of the Eurasian margin throughout the closure of the Neotethys since ~156 Ma (Jagoutz et al., 2019; Jagoutz et al., 2015). It is notable, however, that the available paleomagnetic studies all yielded equatorial paleolatitudes, which would be consistent with long-lived intra-oceanic subduction in the Neotethys.

In addition to the KLA in the western Himalaya, the Burma Terrane, which separates India from the Eurasian Sibumasu block (see Figure 4-1a) in the eastern Himalaya, has also been proposed to be part of a trans-Tethyan intra-oceanic subduction zone south of the Eurasian margin (Licht et al., 2020; Westerweel et al., 2019). Westerweel et al. (2019) concluded that this terrane

was situated at a latitude of 5.0 ± 4.7 °S between 97 – 87 Ma and was subsequently rotated into its present-day orientation due to Paleocene collision with the northeast corner of India.

4.7.2.4 Synthesis

The most reliable paleomagnetic data from the southern edge of Eurasia show that it did not diverge significantly from around 18 – 22 °N between 140 – 40 Ma throughout the closure of the Neotethys ocean (van Hinsbergen et al., 2019). Our results and analysis of the available paleomagnetic constraints shows that the Karakoram terrane was a constituent part of the Eurasian margin at ~20 °N in the Campanian and that the Eurasian margin and KLA had significantly different latitudes at 66 – 61 Ma when geologic evidence from the Indian margin records the onset of collision (Beck et al., 1995; Tapponnier et al., 1981). Reliable paleomagnetic data from the Tethyan Himalaya show that the northern edge of India was situated far south of Eurasia at ~8 – 14 °N (Yuan et al., 2022; Yuan et al., 2021), at a comparable latitude to the KLA (Martin et al., 2020) at this time. The robust paleomagnetic records of the Himalaya are therefore consistent with the India-arc accretion model for the India-Eurasia collision (see Figure 4-16). Future paleomagnetic work will establish the pre-Paleocene paleogeography of the KLA and the Burma terrane and determine whether they are relics of a long-lived intra-oceanic subduction zone in the Neotethys (Jagoutz et al., 2015), the product of a rifted back-arc derived from the Eurasian margin (Kapp & DeCelles, 2019), or a complex combination of the two.

4.8 Conclusion

Determining the age of final closure of the Shyok suture zone has been a crucial challenge hindering the resolution of multiple conflicting tectonic models for the India-Eurasia collision. Our results resolve this challenge by providing an independent paleomagnetic upper bound on the final closure of the Shyok suture zone at < 61 Ma. These data constrain the Karakoram terrane to a paleolatitude of 20.0 ± 6.2 °N between 93 – 75 Ma, equivalent to that of the Lhasa block, indicating that Lhasa and the Karakoram terrane were contiguous elements of the southern Eurasian margin in the Late Cretaceous (Zanchi et al., 2000). The obduction of ophiolites onto northern India at 60 – 65 Ma (Beck et al., 1995; Tapponnier et al., 1981) and the delivery of arc-detritus to the Indian passive margin sediments at 61 – 58 Ma (An et al., 2021; DeCelles et al., 2014) occurred during arc-continent collision between the KLA and India prior to final India-Eurasia collision (Aitchison et al., 2000; Bouilhol et al., 2013; Jagoutz et al., 2015). This conclusion is independent of whether the KLA moved southward to its Paleocene latitude from the Eurasian margin due to slab rollback and the opening of a back-arc basin after 93 Ma, or if it formed above a long-lived intra-oceanic subduction zone outboard of the Eurasian margin. The final India-Eurasia continental collision occurred later than previously thought, at 45 – 40 Ma (Bouilhol et al., 2013), causing widespread metamorphism at 40 Ma (Burg & Bouilhol, 2019) and the initiation of major faults that accommodated Eurasian shortening after 36 Ma (Cowgill et al., 2003; Leloup et al., 2001; Yin et al., 1999). While evidence for arc-continent accretion events prior to final continental collision may be absent from the central part of the Himalaya, they are clear at the western and eastern peripheries of the belt. It is essential that tectonic models for the India-Eurasia collision incorporate evidence from these areas in addition to the classical exposures in central Tibet.

4.9 Acknowledgments

We thank Megan Guenther for field assistance; C. P. Dorjay for logistical assistance and Nerpa guesthouse for the hospitality they provided us in Charasa village, Ladakh. We also thank Jay Shah and Eduardo Lima for assistance with paleomagnetic and rock magnetic experiments at the MIT Paleomagnetism Laboratory and MIT Ross Laboratory; Jacob Setera, Laura C. Mulrooney and George Kamenov for assistance with LA-ICPMS analyses at Rutgers University and the University of Florida; and Neel Chatterjee for assistance in the MIT Electron Microprobe Facility. This work was funded by the National Science Foundation (NSF) under Grant No. EAR-1902179, financially supported by the AGeS program (NSF Grant Nos. EAR-1759200 and EAR-1759353) and also by the MIT International Science and Technology Initiatives India (MISTI India) student travel program.

4.10 Figures and Captions

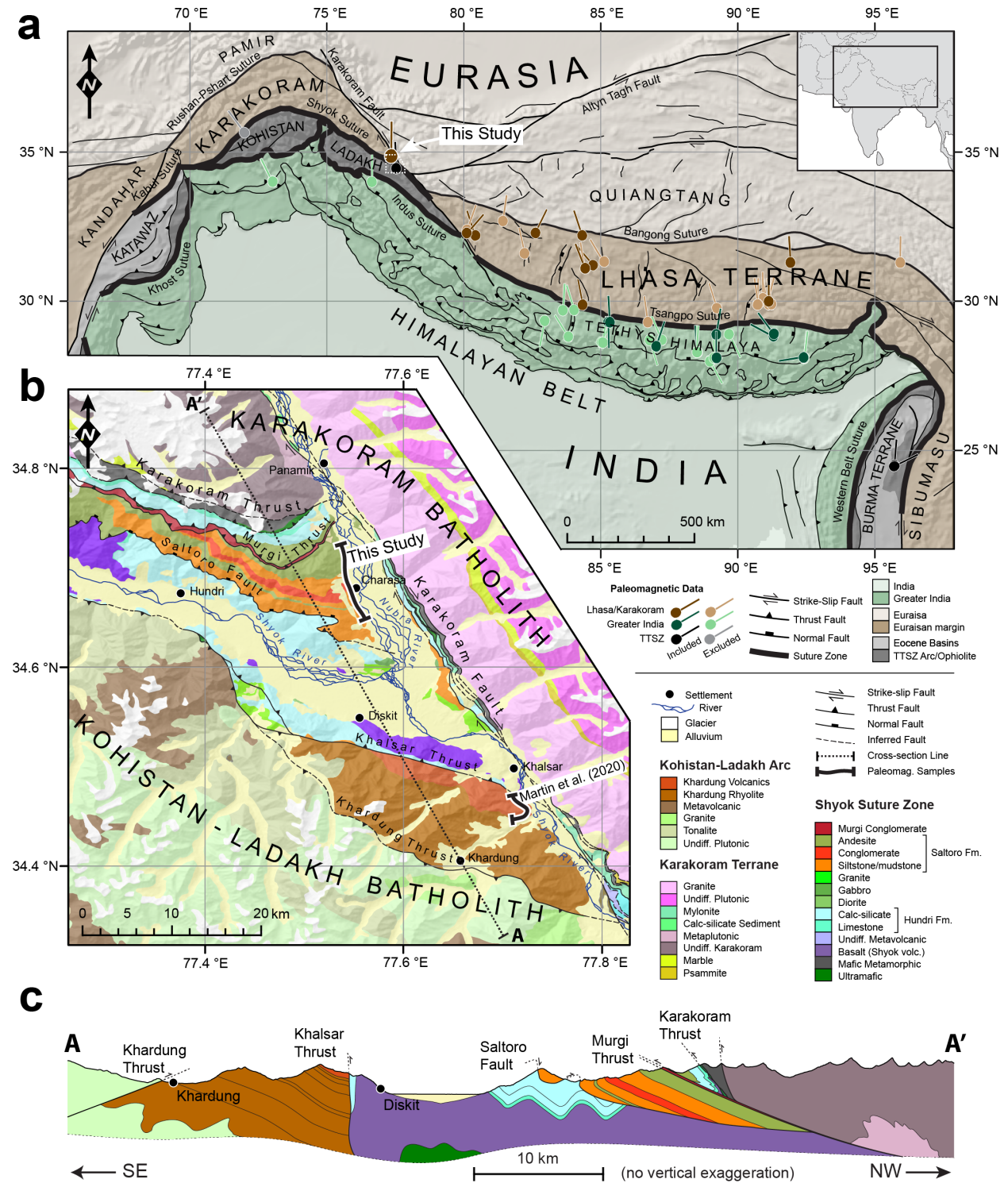


Figure 4-1: Geologic maps of the Himalaya and Nubra-Shyok confluence area in Ladakh NW India. **a)** Tectonic map showing the architecture of the Himalayan orogenic belt from Afghanistan to Myanmar with Indian derived terranes (green), Eurasian tectonic blocks (brown), and intra-oceanic arc remnants (dark grey) shown in contact with each other along major faults (narrow black lines) and suture zones (thick black lines). Paleomagnetic study locations and the mean paleomagnetic declination are overlaid on the terranes where they were derived with darker shading indicating the most reliable paleomagnetic studies. **b)** Detailed geological map of the Shyok suture zone in the Shyok-Nubra confluence area, Ladakh, northwest India. The major structures and tectonostratigraphic units of the Shyok suture zone are overlaid with the locations of the paleomagnetic sampling sections for the Saltoro Formation (this study) and the Khardung volcanics (Martin et al., 2020). **c)** Geological cross-section at 1:1 scale for the line marked A – A' that is oriented southeast to northwest (330°) from the Kohistan-Ladakh Batholith near the village of Khardung across the Shyok suture zone to the Karakoram terrane.

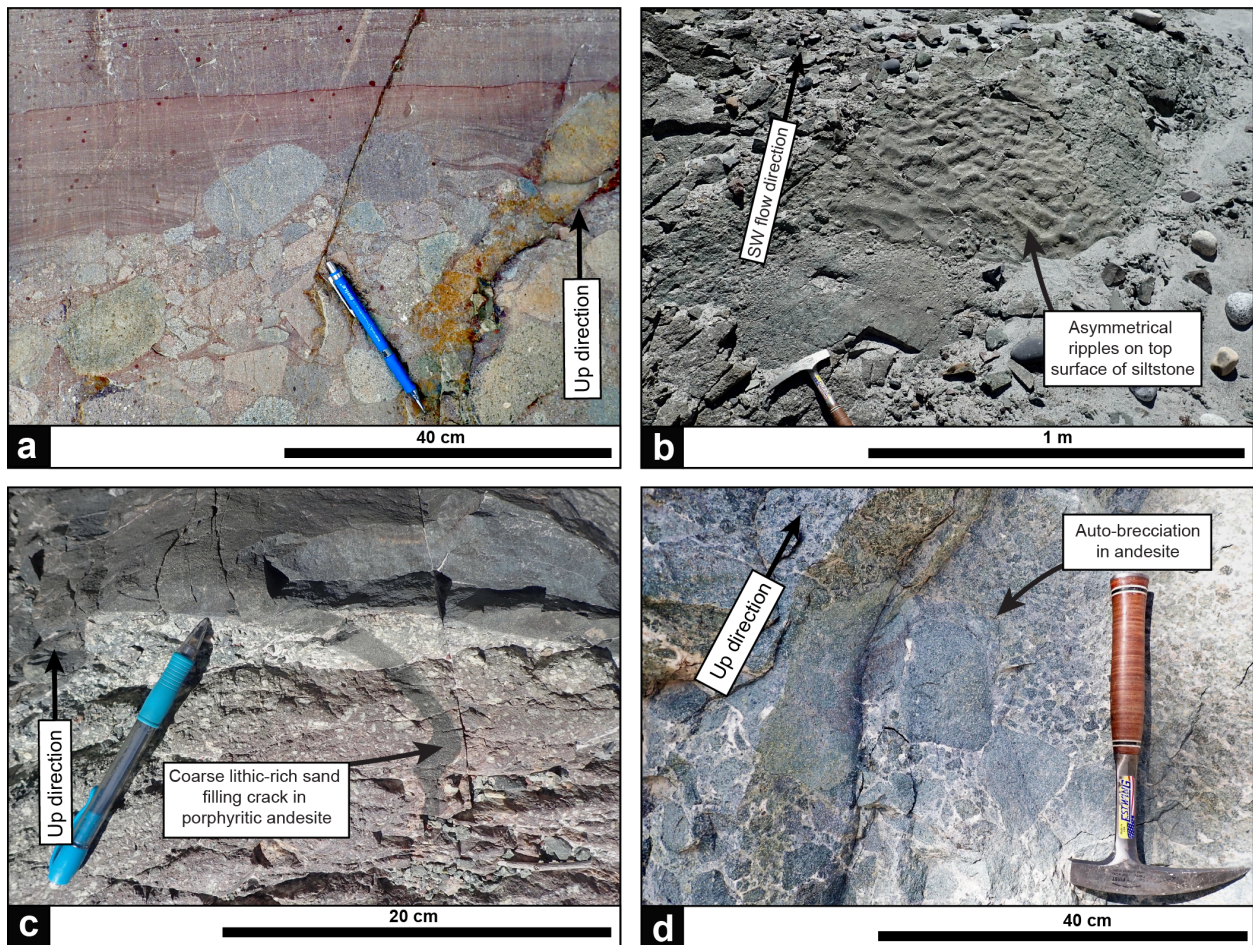


Figure 4-2: Images depicting a range of Saltoro Formation rock types. a) Upper contact of clast-supported conglomerate overlain by laminated silty sandstone. Conglomerate clasts of mostly volcanic origin are poorly sorted and range in size from small pebbles to cobbles with variable shapes from sub-rounded to sub-angular. Sandy and silty laminations in the sandstone can be seen onlapping against the pebbles at the contact indicating the paleo-up direction. b) Asymmetrical ripples in upper surface of tilted siltstone bed exposed near Charasa Monastery indicating an estuarine or low-energy fluvial environment with a southwestward flow direction. c) A coarse lithic-rich sandstone infills cracks in the underlying plagioclase-pyroxene porphyritic andesite. d) An example of magmatic brecciation in a basaltic flow near the top of the Saltoro stratigraphy, suggesting that some of the flows were erupted into water or flowed into water rich environments.

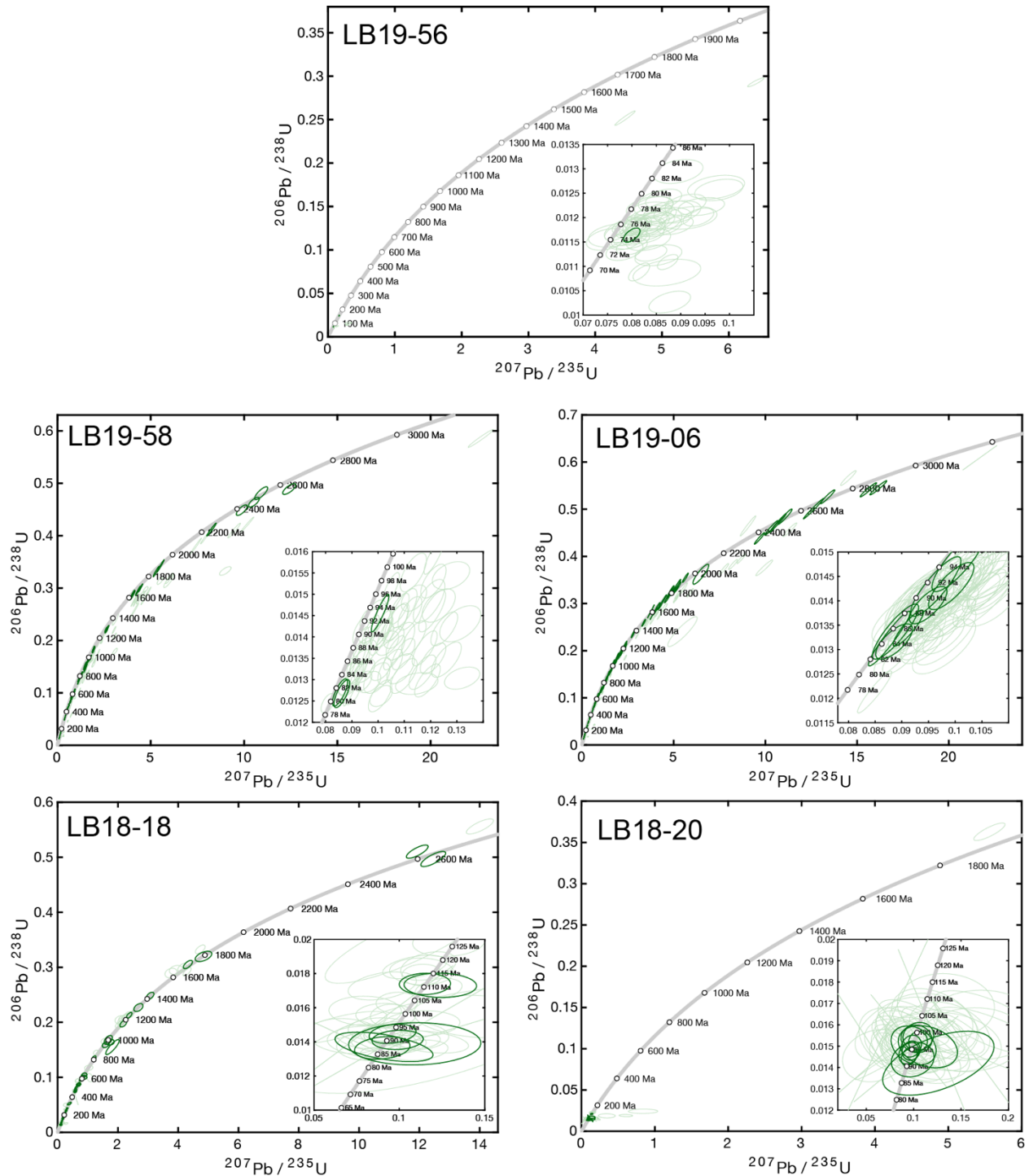


Figure 4-3: U-Pb isotopic data presented using Wetherill concordia diagrams with 2σ uncertainties (95% confidence limits). Smaller inlay Wetherill concordia diagrams show the youngest populations of grains in each sample. Dark green symbols indicate zircons that passed the filtration criteria ($\leq 5\%$ discordance and $^{206}\text{Pb}/^{204}\text{Pb} \leq 0.001$) while light green symbols indicate zircons that were excluded based on their failure to meet the same criterion.

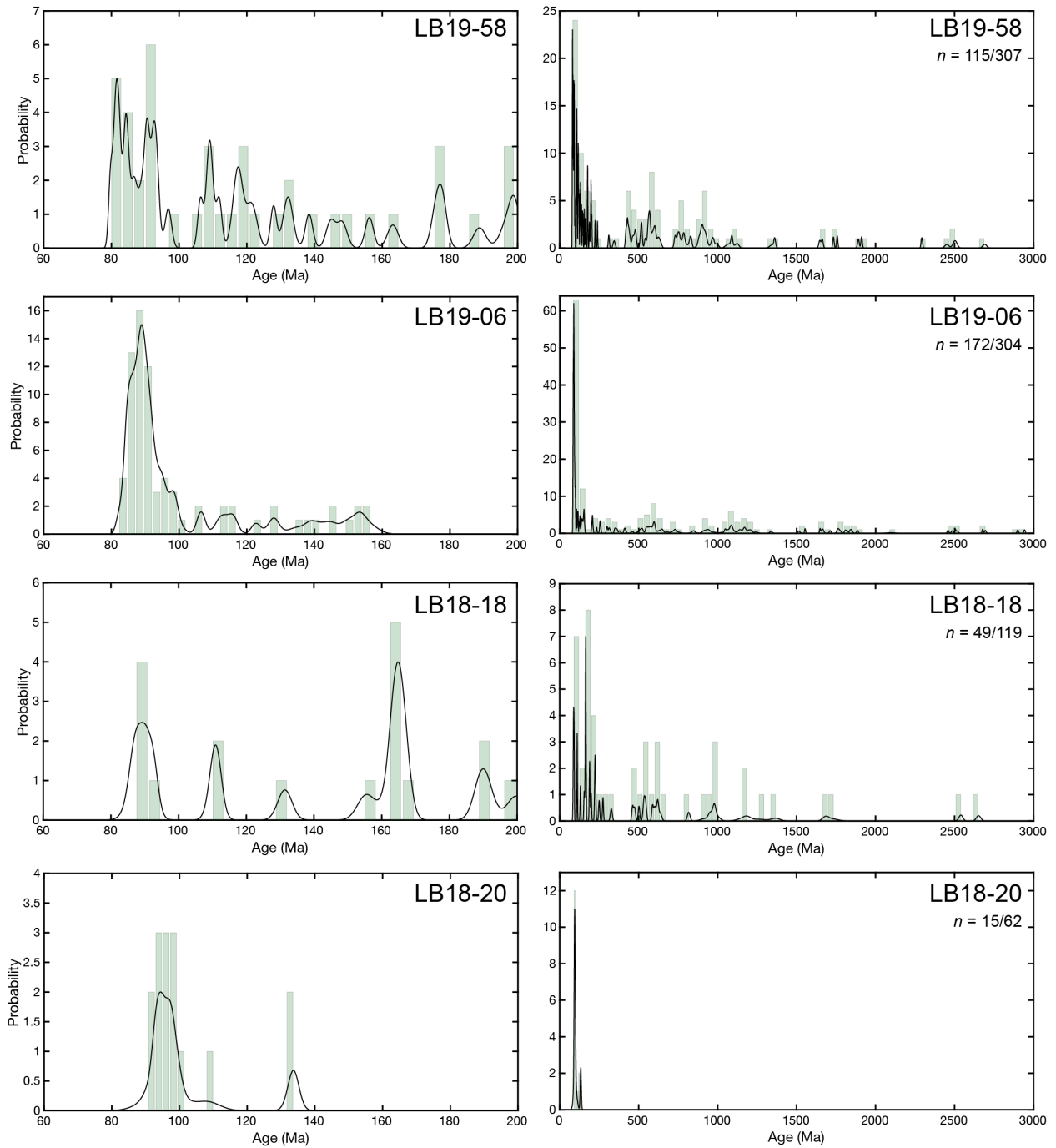


Figure 4-4: Histograms and probability density distributions of detrital zircon U-Pb ages that passed the <5% discordance criterion. Right panels show the full detrital age spectrum including all the grains present in the sample, left panel shows just the grains with U-Pb ages < 200 Ma.

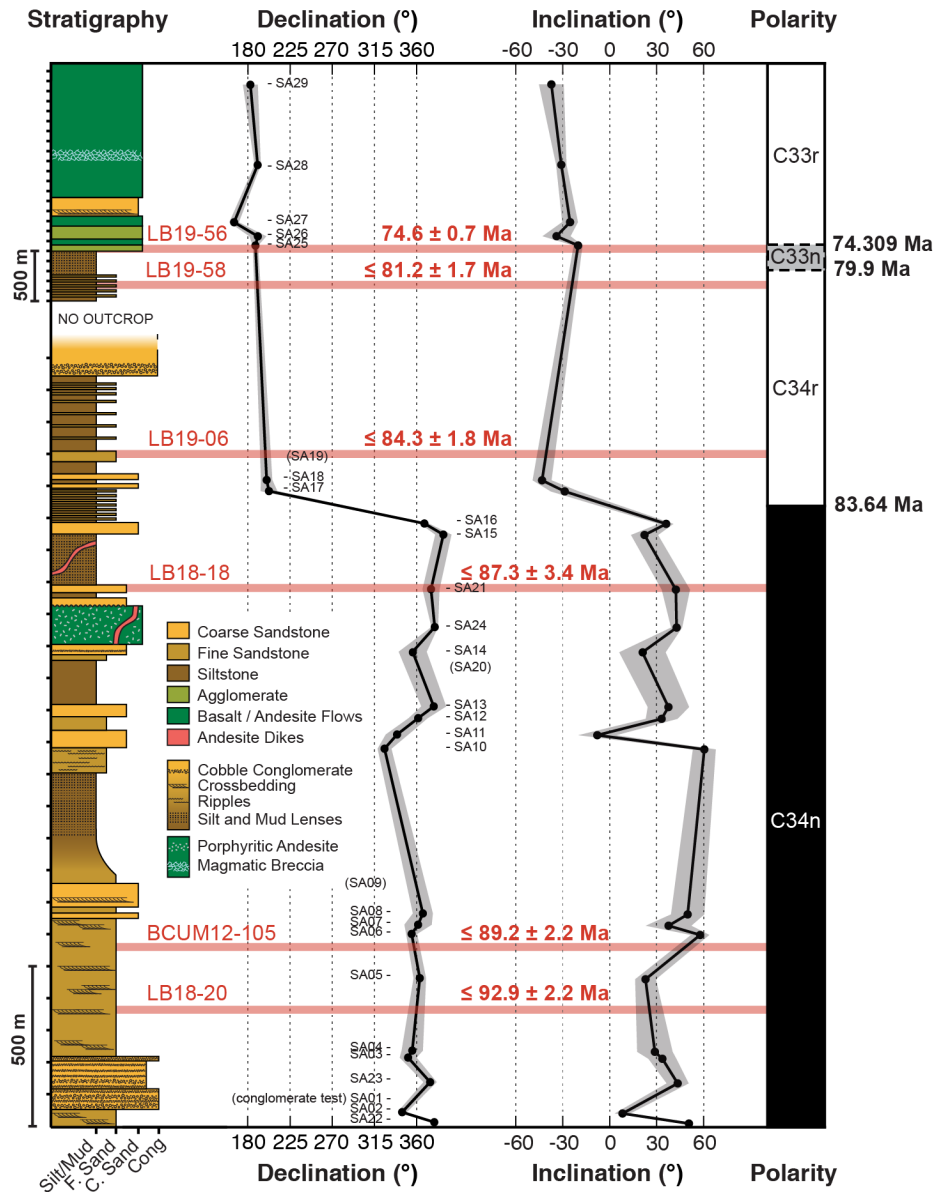


Figure 4-5: Stratigraphic column of the Saltoro Formation showing the change in lithology with increasing stratigraphic height. Red bars indicate U-Pb zircon ages from this study and the recalculated age from sample BCUM12-105 of Borneman et al. (2015). The black lines and points show the inclination and declination of our paleomagnetic sites with the 95% uncertainty displayed using shading around the line. The ages were used to correlate the magnetic declination and inclination of our paleomagnetic sites with the known geodynamo reversal C34n to C34r, shown using the chronostratigraphic bar on the right.

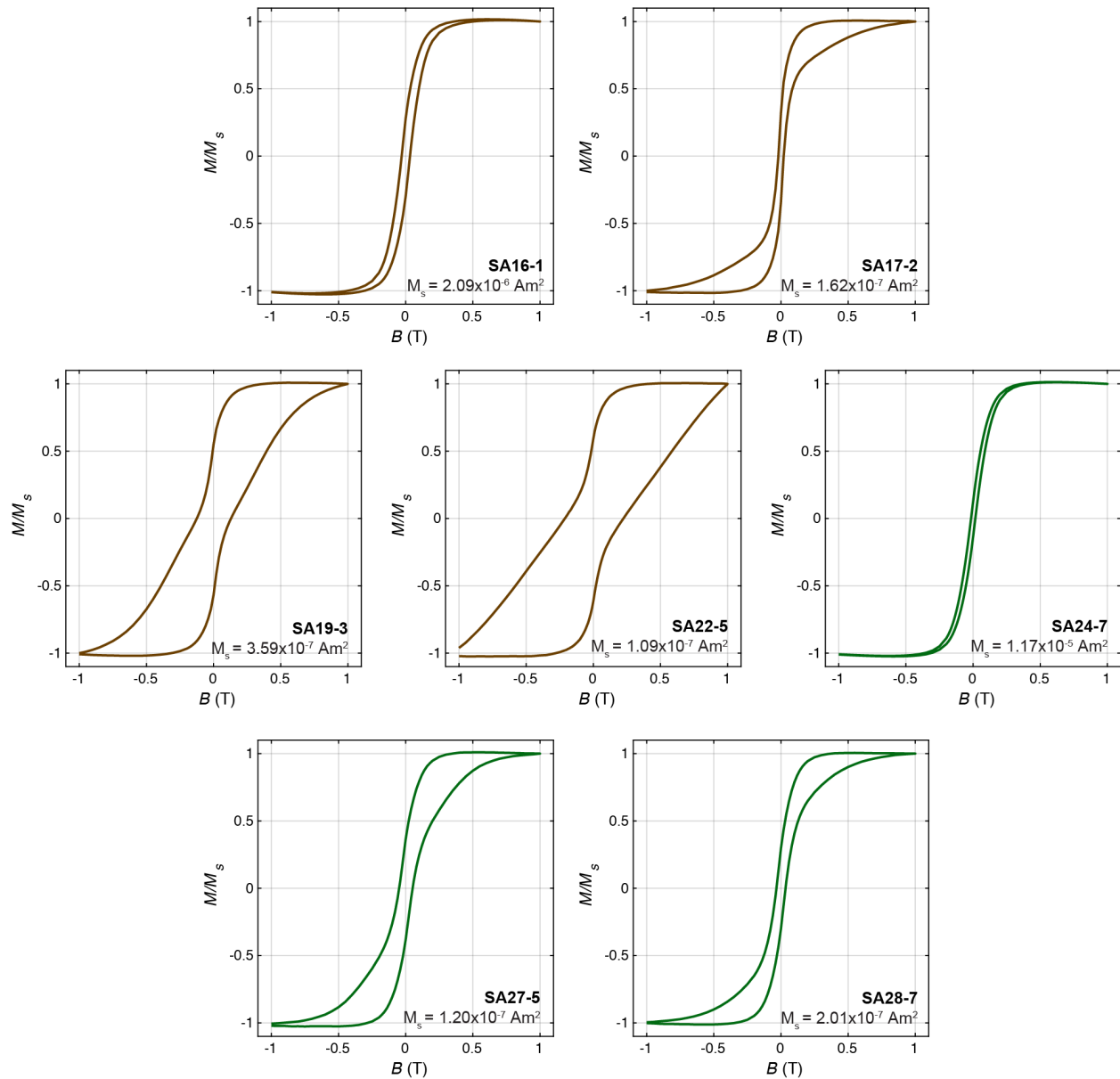


Figure 4-6: Hysteresis curves for four representative sediment samples (brown curves) and three representative volcanic samples (green curves). Hysteresis loops were acquired for applied fields of $B = -1.0 - 1.0$ T and were corrected by removing any paramagnetic or diamagnetic signals. The corrected curves were used to ascertain the saturation magnetization (M_s), the saturation remanent magnetization (M_{rs}), the coercivity of remanence (H_{cr}) and the coercivity (H_c) for each sample.

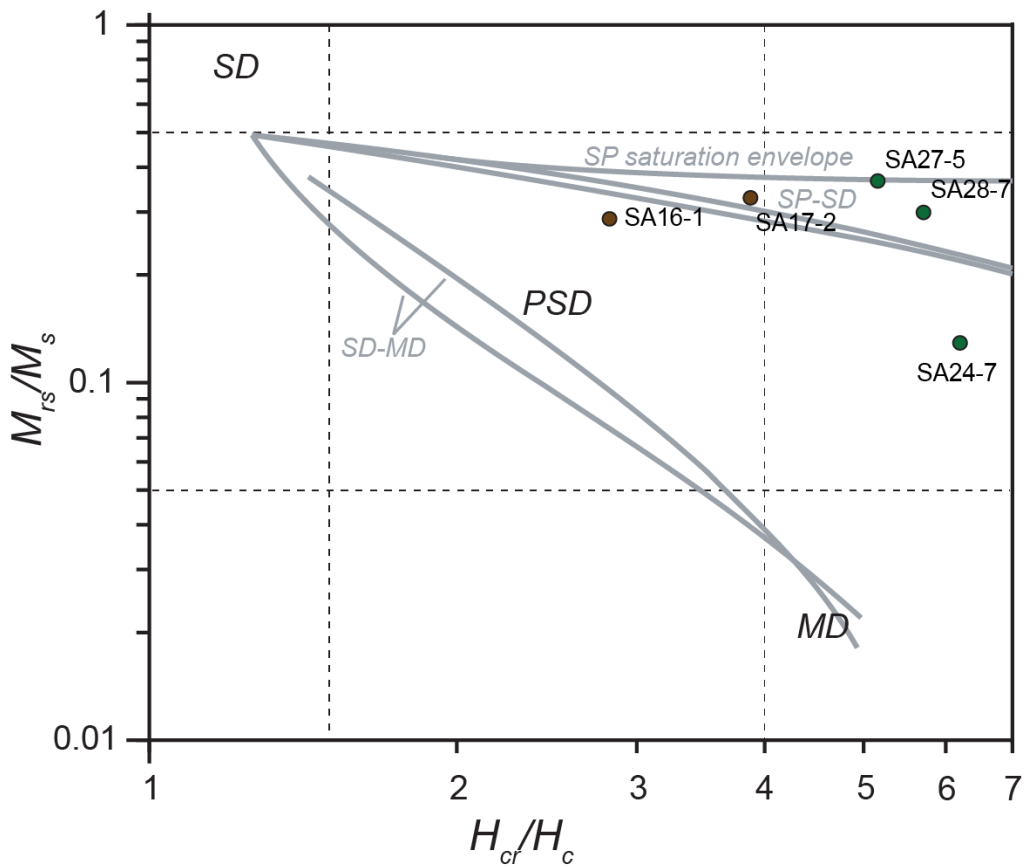


Figure 4-7: Day plot showing the ratio of saturation remanent magnetization (M_{rs}) over saturation magnetization (M_s), and the ratio of coercivity of remanence (H_{cr}) and coercive force (H_c) determined from hysteresis data for the representative samples. Regions are denoted to show the different domain state's magnetite: MD = multidomain, PSD = pseudo-single domain, SD = Single domain. Representative sedimentary samples are shown with brown symbols and representative volcanic samples are shown in green.

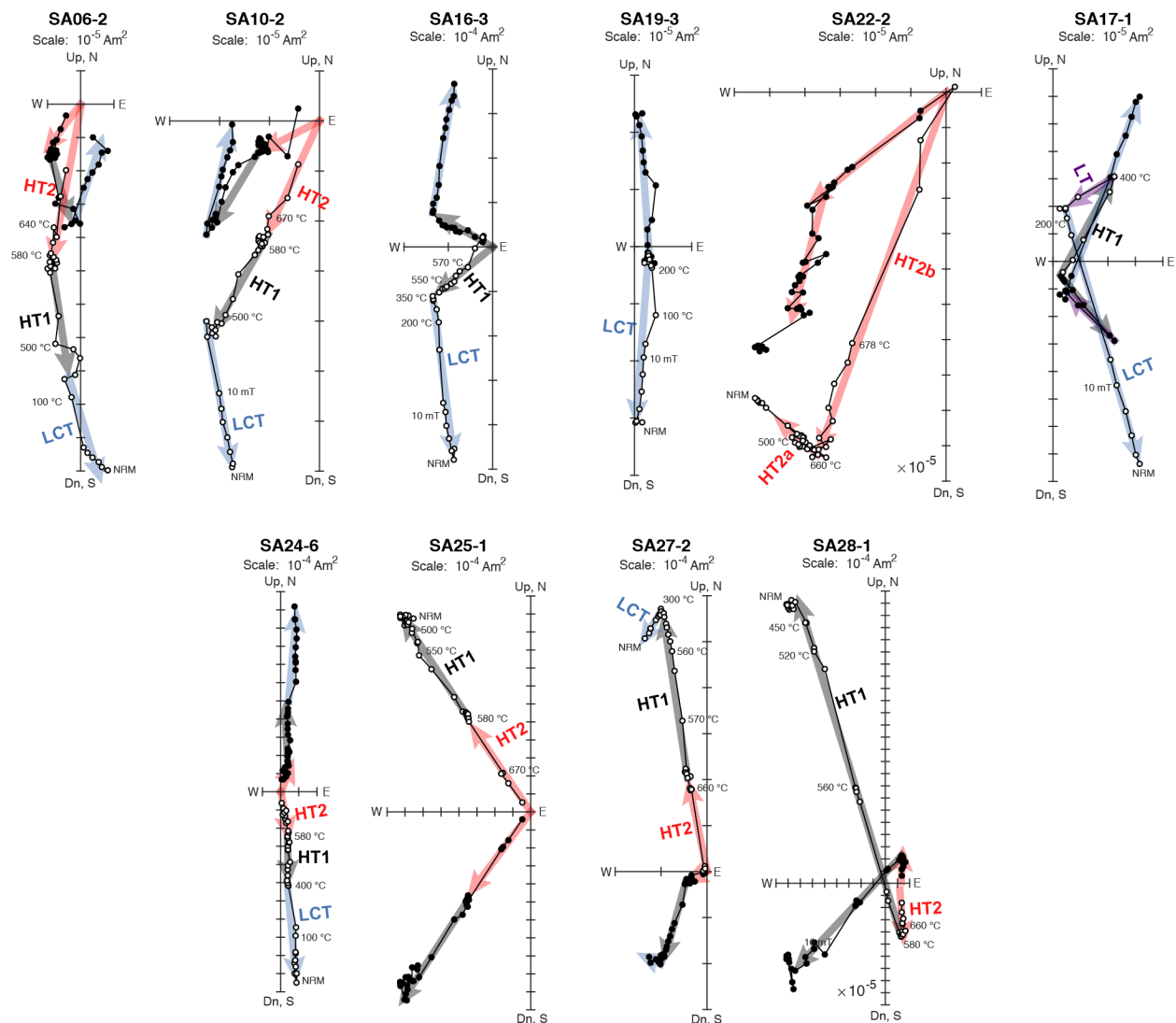


Figure 4-8: Orthographic projection diagrams showing AF and thermal demagnetization data from a suite of representative samples. The top row of diagrams shows demagnetization data from sedimentary samples; the bottom row shows demagnetization data from volcanic samples. Data are presented in geographic coordinates; closed symbols represent north–south–east–west projections and open symbols represent up–down–east–west projections. Interpretations are shown with colored arrows; each arrow reflects a direction vector corresponding to components inferred from principal component analysis (PCA). Low coercivity and low temperature overprint (LCT) is shown with blue arrows, low temperature overprint (LT) is shown with purple arrows, high temperature component associated with magnetite is shown with black arrows and high temperature components associated with hematite are shown with red arrows.

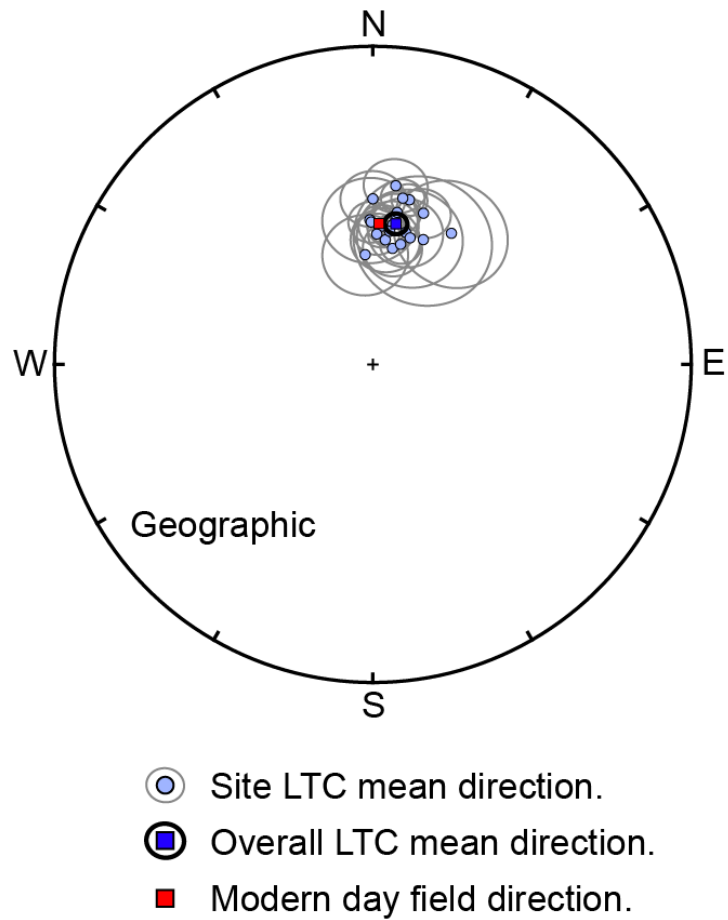


Figure 4-9: Equal area projection showing the LCT site-mean directions and their α_{95} uncertainty ellipses. The mean direction of the LCT components is almost equivalent to the modern-day field direction. Negative inclinations are projected onto the upper hemisphere and shown with open symbols; filled symbols represent positive inclinations.

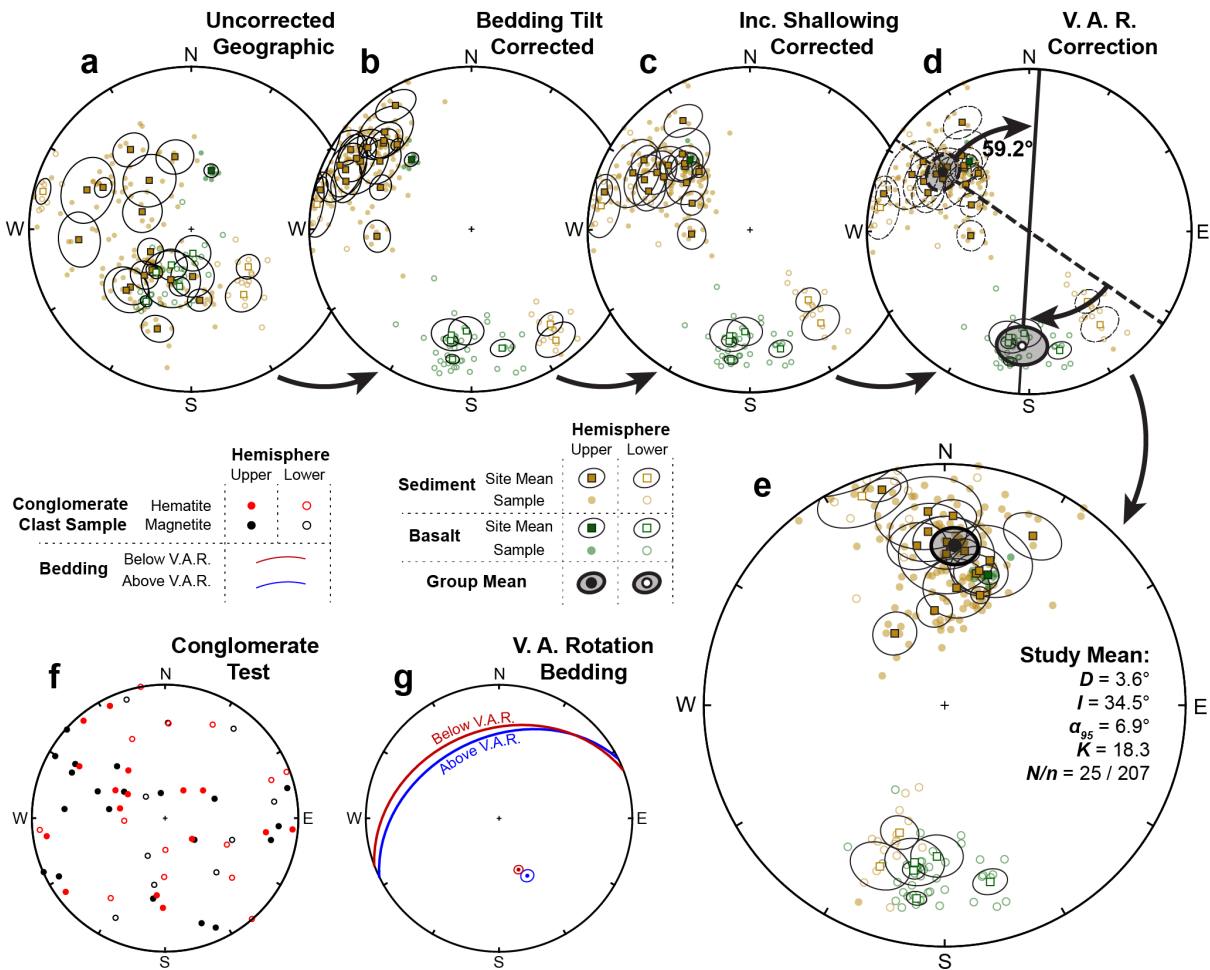


Figure 4-10: Stereographic projections showing paleomagnetic results from the Saltoro Formation with each panel showing successive corrections that have been applied to the data. Measurements from volcanic samples are shown with green symbols and sedimentary samples with brown symbols; open symbols indicate upper hemisphere projections while filled symbols indicate lower hemisphere projections. Circular symbols represent sample ChRM directions; square symbols represent site-mean ChRM directions with their α_{95} uncertainty ellipse displayed as a black curve. **a)** Paleomagnetic results shown in geographic coordinates. **b)** Paleomagnetic results after bedding tilt correction. **c)** Paleomagnetic results after sedimentary sites have been corrected for inclination flattening. **d)** Means of each sub-population before vertical axis rotation correction was applied. **e)** Final fully corrected paleomagnetic dataset with the study mean direction displayed using a solid black circle and shaded α_{95} uncertainty ellipse. **f)** Magnetization directions associated with magnetite (black symbols) and hematite (red symbols) in samples from conglomerate clasts from near the base of the Saltoro stratigraphy. The random distribution of magnetic directions demonstrates that neither hematite nor magnetite magnetization in the Saltoro Formation have been overprinted. **g)** Stereographic projection of the mean of bedding planes from horizons close to the stratigraphic height of the vertical axis rotation in the paleomagnetic results, with bedding

from the rotated stratigraphy shown in blue and bedding from the unrotated stratigraphy shown in red. The bedding is almost identical above and below the rotation, providing strong evidence that the rotation took place along a vertical axis.

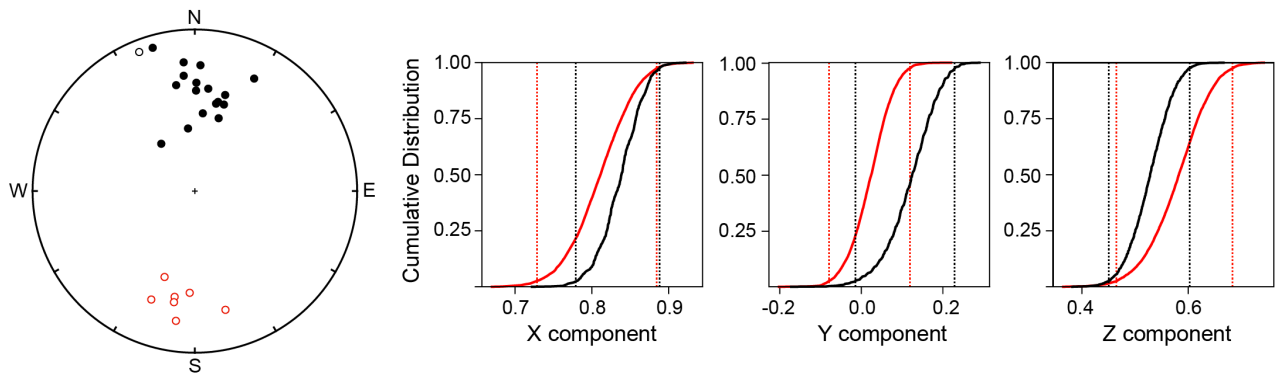


Figure 4-11: Cumulative distributions of Cartesian components of bootstrapped means from 1000 pseudo-samples from tilt-corrected, E/I corrected and VAR corrected site-mean direction data. The 95% confidence intervals for the two populations overlap in X, Y and Z. The two populations can be considered antipodal to one another because they share a common mean, passing a reversal test.

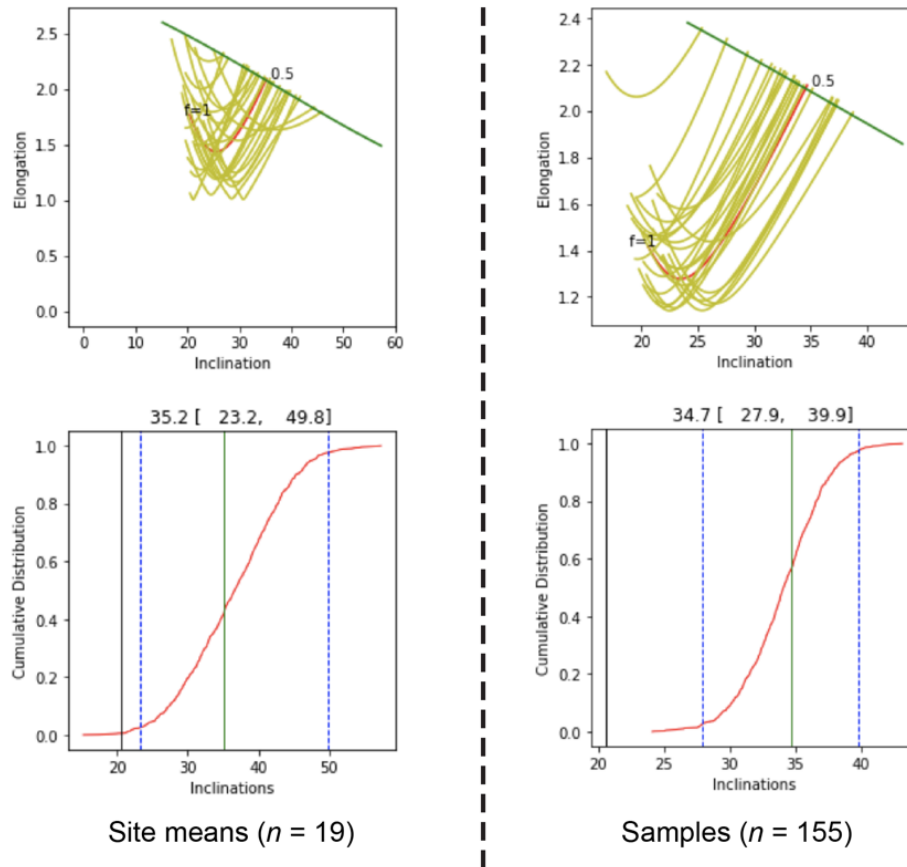


Figure 4-12: Results of Tauxe and Kent (2004) E/I method to determine flattening factor for $n = 19$ sedimentary site-mean directions on the left and $n = 155$ sedimentary sample directions on the right. The upper figures show elongation versus inclination predicted by the TK03 geocentric axial dipole model (green curve), elongation versus inclination upon stepwise unflattening of the data set by decreasing the flattening factor (f) (red curve) and the results of stepwise unflattening of 25 out of the 1000 bootstrap pseudosamples (yellow curves). The intersection between the red and green curves is used to determine the flattening factor that is then used to correct the sedimentary site-mean directions for inclination shallowing. The lower figures show a cumulative distribution of the 1000 bootstrap runs (red curve) along with the uncorrected inclination (black line) and the corrected inclination (blue line) as well as its 95% uncertainty (blue dashed lines).

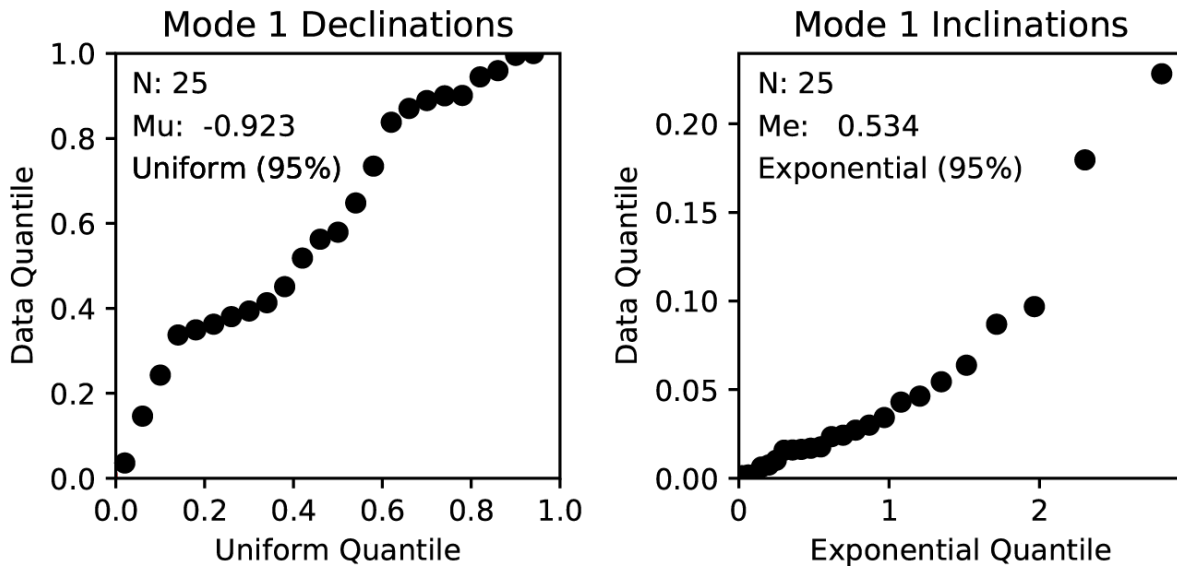


Figure 4-13: Quantile-quantile plots of VGP longitudes and latitudes plotted against an assumed uniform and exponential distribution respectively. The data are Fisher distributed because the statistical parameters μ and m are both less than the critical values.

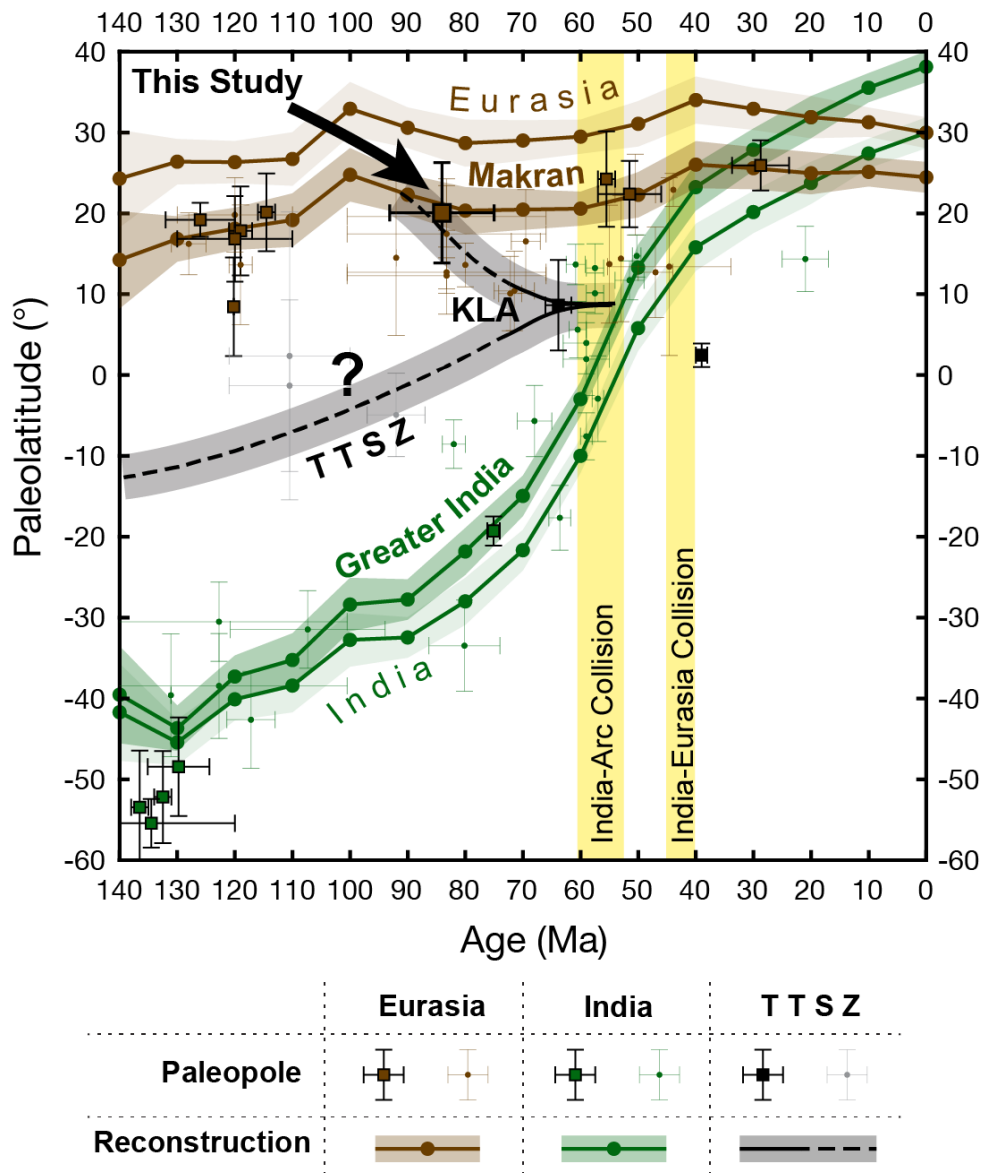


Figure 4-14: Plot of paleolatitude against age showing reconstructed motions of India (green) and Eurasia (brown) along with all the available paleomagnetic constraints from the Tethys Himalaya (green), Eurasian margin terranes (brown) and intra-oceanic arc remnants (grey/black). The most robust paleopoles are shown with square symbols and the least reliable poles are shown with small circle symbols. The reconstruction of Makran (part of the modern Eurasian margin minimally affected by India-Eurasia collision) is in good agreement with the results of this study and reliable paleomagnetic data. The paleolatitude of a point in north-central Greater India is predicted based on an assumed linear northern margin of Gondwana between Arabia and northern Australia. The pre-Paleocene paleogeography of the KLA is poorly constrained, so two possible models are shown using dashed black lines.

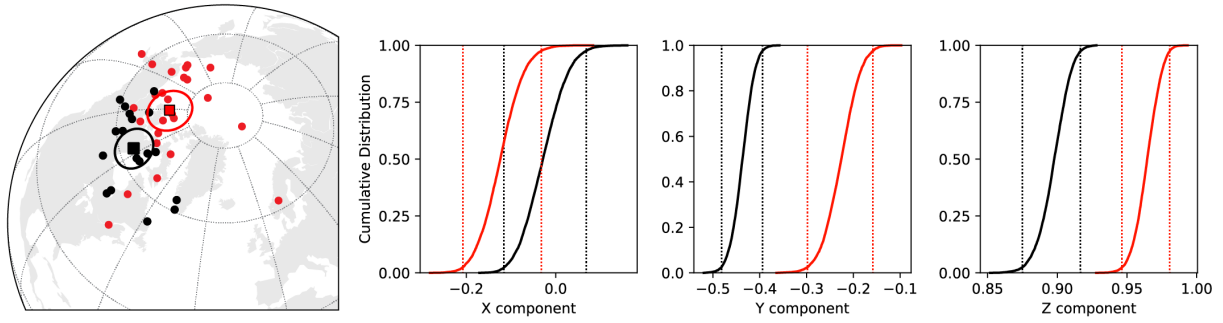


Figure 4-15: Cumulative distributions of Cartesian components of bootstrapped means from 1000 pseudo-samples from Saltero Formation VGP distribution (red) and Khardung Formation VGP distribution (black). The 95% confidence intervals for the two populations do not overlap in Y and Z. Therefore, the two populations cannot be considered to share a common mean direction.

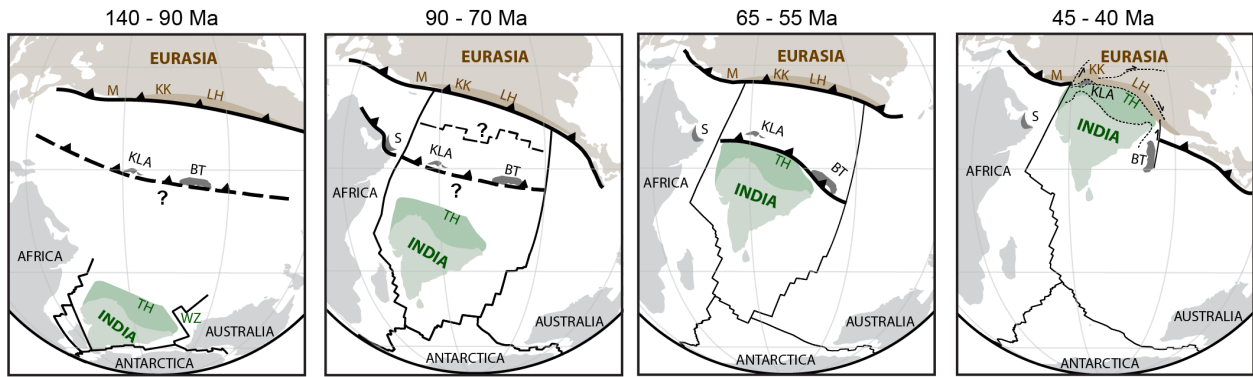


Figure 4-16: Reconstructions of the Neotethys ocean based on only the most robust paleomagnetic data for four time periods since the Early Cretaceous. Divergent and transverse plate boundaries are shown with solid black lines, and subduction zones are displayed with thick lines with triangular ticks indicating the direction of subduction and dashed lines where the paleogeography is poorly constrained. Major terranes and relevant locations are indicated with letter codes: BT = Burma terrane, KK = Karakoram terrane, KLA = Kohistan-Ladakh arc, LH = Lhasa terrane, M = Makran, S = Semail ophiolite (Oman), TH = Tethyan Himalaya, WZ = Wallaby-Zenith Fracture Zone.

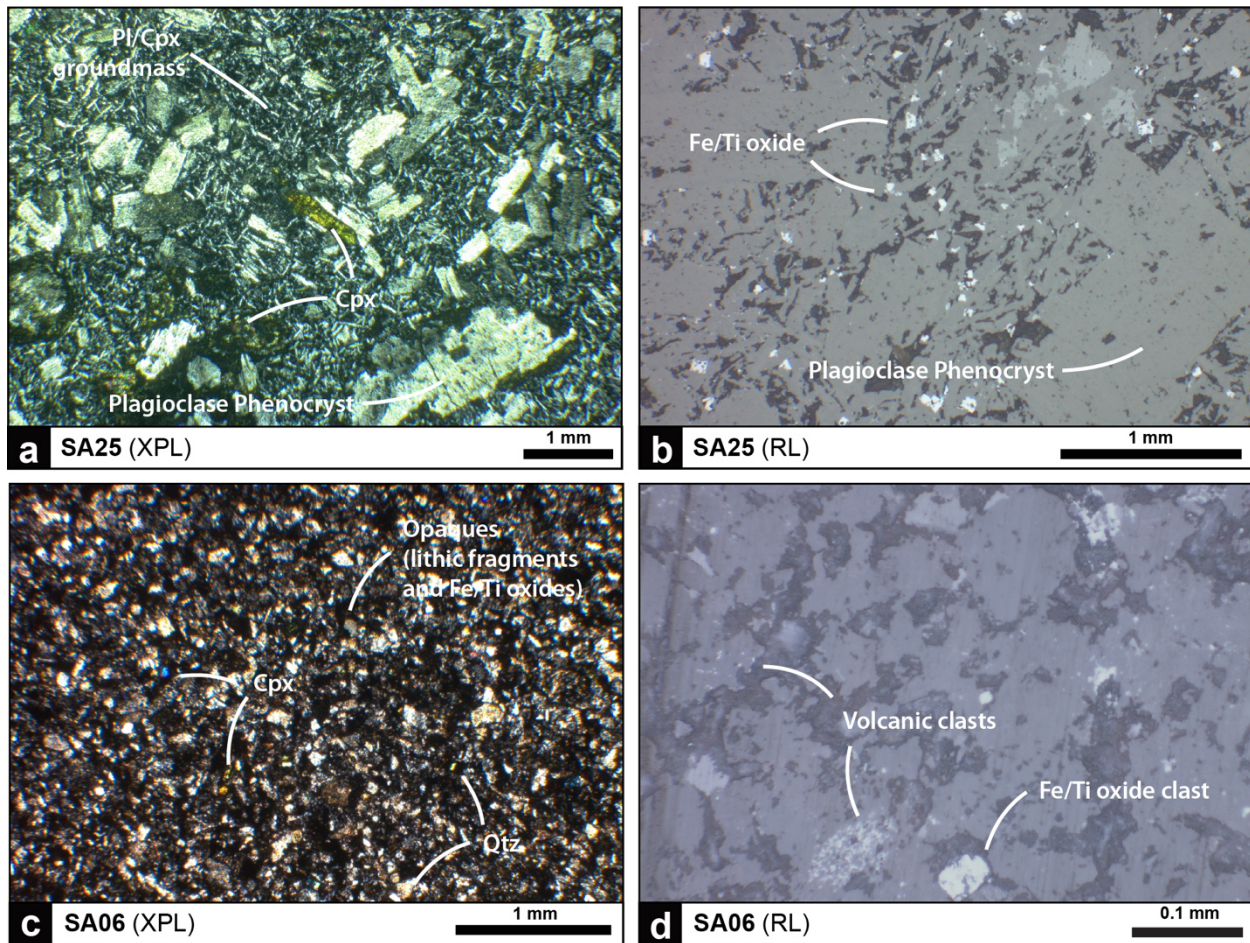


Figure 4-17: Optical micrographs of Saltoro Formation samples. **a)** Cross-polarized transmitted light (XPL) image of andesite volcanic from site SA25. **b)** Reflected light (RL) image of andesite volcanic from site SA25. **c)** Cross-polarized transmitted light (XPL) image of siltstone from site SA06. **d)** Reflected light (RL) image of siltstone from site SA06.

References

- Achache, J., Courtillot, V., & Xiu, Z. Y. (1984). Paleogeographic and tectonic evolution of southern Tibet since middle Cretaceous time: New paleomagnetic data and synthesis. *Journal of Geophysical Research: Solid Earth*, 89(B12), 10311-10339.
- Ahmad, M. N., Fujiwara, Y., & Paudel, L. P. (2001). Remagnetization of igneous rocks in Gupis area of Kohistan arc, northern Pakistan. *Earth, planets and space*, 53(5), 373-384.
- Ahmad, M. N., Yoshida, M., & Fujiwara, Y. (2000). Paleomagnetic study of Utror Volcanic Formation: Remagnetizations and postfolding rotations in Utror area, Kohistan arc, northern Pakistan. *Earth, planets and space*, 52(6), 425-436.
- Aitchison, J. C., & Davis, A. M. (2004). Evidence for the multiphase nature of the India-Asia collision from the Yarlung Tsangpo suture zone, Tibet. *Geological Society, London, Special Publications*, 226(1), 217-233.
- Aitchison, J. C., Davis, A. M., Liu, J., Luo, H., Malpas, J. G., McDermid, I. R., . . . Zhou, M.-f. (2000). Remnants of a Cretaceous intra-oceanic subduction system within the Yarlung–Zangbo suture (southern Tibet). *Earth and Planetary Science Letters*, 183(1-2), 231-244.
- Ali, J. R., & Aitchison, J. C. (2005). Greater India. *Earth-Science Reviews*, 72(3-4), 169-188.
- An, W., Hu, X., Garzanti, E., Wang, J. G., & Liu, Q. (2021). New precise dating of the India-Asia collision in the Tibetan Himalaya at 61 Ma. *Geophysical Research Letters*, 48(3), e2020GL090641.
- Andrews-Speed, C., & Brookfield, M. (1982). Middle Paleozoic to Cenozoic geology and tectonic evolution of the northwestern Himalaya. *Tectonophysics*, 82(3-4), 253-275.
- Appel, E., Crouzet, C., & Schill, E. (2012). Pyrrhotite remagnetizations in the Himalaya: a review. *Geological Society, London, Special Publications*, 371(1), 163-180.
- Barham, M., Kirkland, C., Reynolds, S., O’Leary, M., Evans, N., Allen, H., . . . Belousova, E. (2016). The answers are blowin’ in the wind: ultra-distal ashfall zircons, indicators of Cretaceous super-eruptions in eastern Gondwana. *Geology*, 44(8), 643-646.
- Beck, R. A., Burbank, D. W., Sercombe, W. J., Riley, G. W., Barndt, J. K., Berry, J. R., . . . Metje, J. (1995). Stratigraphic evidence for an early collision between northwest India and Asia. *Nature*, 373(6509), 55.
- Besse, J., Courtillot, V., Pozzi, J., Westphal, M., & Zhou, Y. (1984). Palaeomagnetic estimates of crustal shortening in the Himalayan thrusts and Zangbo suture. *Nature*, 311(5987), 621-626.
- Bhutani, R., Pande, K., & Venkatesan, T. (2009). ⁴⁰Ar–³⁹Ar dating of volcanic rocks of the Shyok suture zone in north–west trans-Himalaya: Implications for the post-collision evolution of the Shyok suture zone. *Journal of Asian Earth Sciences*, 34(2), 168-177.
- Bian, W., Yang, T., Ma, Y., Jin, J., Gao, F., Wang, S., . . . Li, H. (2019). Paleomagnetic and geochronological results from the Zhela and Weimei Formations lava flows of the eastern Tethyan Himalaya: New insights into the breakup of eastern Gondwana. *Journal of Geophysical Research: Solid Earth*, 124(1), 44-64.
- Bian, W., Yang, T., Ma, Y., Jin, J., Gao, F., Zhang, S., . . . Li, H. (2017). New Early Cretaceous palaeomagnetic and geochronological results from the far western Lhasa terrane: Contributions to the Lhasa-Qiangtang collision. *Scientific Reports*, 7(1), 1-14.
- Borneman, N. L., Hodges, K. V., Van Soest, M. C., Bohon, W., Wartho, J. A., Cronk, S. S., & Ahmad, T. (2015). Age and structure of the Shyok suture in the Ladakh region of

- northwestern India: implications for slip on the Karakoram fault system. *Tectonics*, 34(10), 2011-2033.
- Bouilhol, P., Jagoutz, O., Hanchar, J. M., & Dudas, F. O. (2013). Dating the India–Eurasia collision through arc magmatic records. *Earth and Planetary Science Letters*, 366, 163-175.
- Brookfield, M., & Reynolds, P. (1981). Late Cretaceous emplacement of the Indus suture zone ophiolitic melanges and an Eocene-Oligocene magmatic arc on the northern edge of the Indian plate. *Earth and Planetary Science Letters*, 55(1), 157-162.
- Burg, J., & Chen, G. (1984). Tectonics and structural zonation of southern Tibet, China. *Nature*, 311(5983), 219-223.
- Burg, J.-P., & Bouilhol, P. (2019). Timeline of the South Tibet–Himalayan belt: the geochronological record of subduction, collision, and underthrusting from zircon and monazite U–Pb ages. *Canadian Journal of Earth Sciences*, 56(12), 1318-1332.
- Cao, Y., Sun, Z., Li, H., Pei, J., Jiang, W., Xu, W., . . . Ye, X. (2017). New Late Cretaceous paleomagnetic data from volcanic rocks and red beds from the Lhasa terrane and its implications for the paleolatitude of the southern margin of Asia prior to the collision with India. *Gondwana Research*, 41, 337-351.
- Chapman, J. B., Scoggin, S. H., Kapp, P., Carrapa, B., Ducea, M. N., Worthington, J., . . . Gadoev, M. (2018). Mesozoic to Cenozoic magmatic history of the Pamir. *Earth and Planetary Science Letters*, 482, 181-192.
- Chen, J., Huang, B., & Sun, L. (2010). New constraints to the onset of the India–Asia collision: paleomagnetic reconnaissance on the Linzizong Group in the Lhasa Block, China. *Tectonophysics*, 489(1-4), 189-209.
- Chen, J., Huang, B., Yi, Z., Yang, L., & Chen, L. (2014). Paleomagnetic and $^{40}\text{Ar}/^{39}\text{Ar}$ geochronological results from the Linzizong Group, Linzhou Basin, Lhasa Terrane, Tibet: Implications to Paleogene paleolatitude and onset of the India–Asia collision. *Journal of Asian Earth Sciences*, 96, 162-177.
- Chen, W., Yang, T., Zhang, S., Yang, Z., Li, H., Wu, H., . . . Cai, F. (2012). Paleomagnetic results from the Early Cretaceous Zenong Group volcanic rocks, Cuoqin, Tibet, and their paleogeographic implications. *Gondwana Research*, 22(2), 461-469.
- Cloos, M. (1993). Lithospheric buoyancy and collisional orogenesis: Subduction of oceanic plateaus, continental margins, island arcs, spreading ridges, and seamounts. *Geological Society of America Bulletin*, 105(6), 715-737.
- Coutts, D. S., Matthews, W. A., & Hubbard, S. M. (2019). Assessment of widely used methods to derive depositional ages from detrital zircon populations. *Geoscience Frontiers*, 10(4), 1421-1435.
- Coward, M. P., Rex, D. C., Khan, M. A., Windley, B. F., Broughton, R. D., Luff, I. W., . . . Pudsey, C. J. (1986). Collision tectonics in the NW Himalayas. *Geological Society, London, Special Publications*, 19(1), 203-219.
- Cowgill, E., Yin, A., Harrison, T. M., & Xiao-Feng, W. (2003). Reconstruction of the Altyn Tagh fault based on U-Pb geochronology: Role of back thrusts, mantle sutures, and heterogeneous crustal strength in forming the Tibetan Plateau. *Journal of Geophysical Research: Solid Earth*, 108(B7).
- Crouzet, C., Gautam, P., Schill, E., & Appel, E. (2003). Multicomponent magnetization in western Dolpo (Tethyan Himalaya, Nepal): tectonic implications. *Tectonophysics*, 377(1-2), 179-196.

- Dannemann, S., Appel, E., Rösler, W., Neumann, U., Liebke, U., & Nag, D. (2022). Palaeomagnetic indication for India–Asia collision at 12° N and maximum 810 km Greater India extent in the western suture zone. *Geophysical Journal International*, 229(2), 1193-1211.
- Day, R., Fuller, M., & Schmidt, V. (1977). Hysteresis properties of titanomagnetites: grain-size and compositional dependence. *Physics of the Earth and planetary interiors*, 13(4), 260-267.
- DeCelles, P., Kapp, P., Gehrels, G., & Ding, L. (2014). Paleocene-Eocene foreland basin evolution in the Himalaya of southern Tibet and Nepal: Implications for the age of initial India-Asia collision. *Tectonics*, 33(5), 824-849.
- DeCelles, P. G., Robinson, D. M., & Zandt, G. (2002). Implications of shortening in the Himalayan fold-thrust belt for uplift of the Tibetan Plateau. *Tectonics*, 21(6), 12-11-12-25.
- Deenen, M. H., Langereis, C. G., van Hinsbergen, D. J., & Biggin, A. J. (2011). Geomagnetic secular variation and the statistics of palaeomagnetic directions. *Geophysical Journal International*, 186(2), 509-520.
- Deenen, M. H., Langereis, C. G., van Hinsbergen, D. J., & Biggin, A. J. (2014). Erratum: Geomagnetic secular variation and the statistics of palaeomagnetic directions. *Geophysical Journal International*, 197(1), 643-643.
- Dickinson, W. R., & Gehrels, G. E. (2009). Use of U–Pb ages of detrital zircons to infer maximum depositional ages of strata: a test against a Colorado Plateau Mesozoic database. *Earth and Planetary Science Letters*, 288(1-2), 115-125.
- Dunlap, W. J., & Wysoczanski, R. (2002). Thermal evidence for early Cretaceous metamorphism in the Shyok suture zone and age of the Khardung volcanic rocks, Ladakh, India. *Journal of Asian Earth Sciences*, 20(5), 481-490.
- Dunlop, D. J. (2002). Theory and application of the Day plot (Mrs/Ms versus Hcr/Hc) 1. Theoretical curves and tests using titanomagnetite data. *Journal of Geophysical Research: Solid Earth*, 107(B3), EPM 4-1-EPM 4-22.
- Dupont-Nivet, G., Lippert, P. C., Van Hinsbergen, D. J., Meijers, M. J., & Kapp, P. (2010). Palaeolatitude and age of the Indo–Asia collision: palaeomagnetic constraints. *Geophysical Journal International*, 182(3), 1189-1198.
- Fisher, N. I., & Lewis, T. (1983). Estimating the common mean direction of several circular or spherical distributions with differing dispersions. *Biometrika*, 70(2), 333-341.
- Fisher, R. A. (1953). Dispersion on a sphere. *Proceedings of the Royal Society of London. Series A. Mathematical and Physical Sciences*, 217(1130), 295-305.
- Gaetani, M., Garzanti, E., Jadoul, F., Nicora, A., Tintori, A., Pasini, M., & Khan, K. S. A. (1990). The North Karakorum Side of the Central Asia Geopuzzle. *Geological Society of America Bulletin*, 102(1), 54-62. doi:Doi 10.1130/0016-7606(1990)102<0054:Tnksot>2.3.Co;2
- Gaetani, M., Jadoul, F., Erba, E., & Garzanti, E. (1993). Jurassic and Cretaceous Orogenic Events in the North Karakoram - Age Constraints from Sedimentary-Rocks. *Himalayan Tectonics*, 74, 39-52. doi:Doi 10.1144/Gsl.Sp.1993.074.01.04
- Gansser, A. (1964). Geology of the Himalayas.
- Garzanti, E., Baud, A., & Mascle, G. (1987). Sedimentary record of the northward flight of India and its collision with Eurasia (Ladakh Himalaya, India). *Geodinamica Acta*, 1(4-5), 297-312.

- Gradstein, F. M., Ogg, J. G., Schmitz, M. D., & Ogg, G. M. (2020). *Geologic time scale 2020*: Elsevier.
- Huang, W., Dupont-Nivet, G., Lippert, P. C., van Hinsbergen, D. J., & Hallot, E. (2013). Inclination shallowing in Eocene Linzizong sedimentary rocks from Southern Tibet: correction, possible causes and implications for reconstructing the India–Asia collision. *Geophysical Journal International*, *194*(3), 1390-1411.
- Huang, W., Lippert, P. C., Jackson, M. J., Dekkers, M. J., Zhang, Y., Li, J., . . . van Hinsbergen, D. J. (2017). Remagnetization of the Paleogene Tibetan Himalayan carbonate rocks in the Gamba area: Implications for reconstructing the lower plate in the India-Asia collision. *Journal of Geophysical Research: Solid Earth*, *122*(2), 808-825.
- Huang, W. T., van Hinsbergen, D. J. J., Dekkers, M. J., Garzanti, E., Dupont-Nivet, G., Lippert, P. C., . . . Kapp, P. (2015). Paleolatitudes of the Tibetan Himalaya from primary and secondary magnetizations of Jurassic to Lower Cretaceous sedimentary rocks. *Geochemistry Geophysics Geosystems*, *16*(1), 77-100. doi:10.1002/2014gc005624
- Jagoutz, O., Bouilhol, P., Schaltegger, U., & Müntener, O. (2019). The isotopic evolution of the Kohistan Ladakh arc from subduction initiation to continent arc collision. *Geological Society, London, Special Publications*, *483*(1), 165-182.
- Jagoutz, O., Royden, L., Holt, A. F., & Becker, T. W. (2015). Anomalously fast convergence of India and Eurasia caused by double subduction. *Nature Geoscience*, *8*(6), 475-478.
- Jagoutz, O. E., Burg, J. P., Hussain, S., Dawood, H., Pettke, T., Iizuka, T., & Maruyama, S. (2009). Construction of the granitoid crust of an island arc part I: geochronological and geochemical constraints from the plutonic Kohistan (NW Pakistan). *Contributions to Mineralogy and Petrology*, *158*(6), 739-755. doi:10.1007/s00410-009-0408-3
- Kaneko, Y., Katayama, I., Yamamoto, H., Misawa, K., Ishikawa, M., Rehman, H., . . . Shiraishi, K. (2003). Timing of Himalayan ultrahigh-pressure metamorphism: Sinking rate and subduction angle of the Indian continental crust beneath Asia. *Journal of Metamorphic Geology*, *21*(6), 589-599.
- Kapp, P., & DeCelles, P. G. (2019). Mesozoic–Cenozoic geological evolution of the Himalayan–Tibetan orogen and working tectonic hypotheses. *American Journal of Science*, *319*(3), 159-254.
- Kirschvink, J. (1980). The least-squares line and plane and the analysis of palaeomagnetic data. *Geophysical Journal International*, *62*(3), 699-718.
- Kirschvink, J. L., Kopp, R. E., Raub, T. D., Baumgartner, C. T., & Holt, J. W. (2008). Rapid, precise, and high-sensitivity acquisition of paleomagnetic and rock-magnetic data: Development of a low-noise automatic sample changing system for superconducting rock magnetometers. *Geochemistry, Geophysics, Geosystems*, *9*(5).
- Klootwijk, C., Sharma, M. L., Gergan, J., Shah, S., & Turkey, B. (1984). The Indus-Tsangpo suture zone in Ladakh, Northwest Himalaya: Further palaeomagnetic data and implications. *Tectonophysics*, *106*(3-4), 215-238.
- Klootwijk, C., Sharma, M. L., Gergan, J., Turkey, B., Shah, S., & Agarwal, V. (1979). The extent of Greater India, II. Palaeomagnetic data from the Ladakh intrusives at Kargil, northwestern Himalayas. *Earth and Planetary Science Letters*, *44*(1), 47-64.
- Lakhan, N., Singh, A. K., Singh, B. P., Sen, K., Singh, M. R., Khogenkumar, S., . . . Oinam, G. (2020). Zircon U–Pb geochronology, mineral and whole-rock geochemistry of the Khardung volcanics, Ladakh Himalaya, India: Implications for Late Cretaceous to Palaeogene continental arc magmatism. *Geological Journal*, *55*(5), 3297-3320.

- Leloup, P. H., Arnaud, N., Lacassin, R., Kienast, J. R., Harrison, T. M., Trong, T. T. P., . . . Tapponnier, P. (2001). New constraints on the structure, thermochronology, and timing of the Ailao Shan-Red River shear zone, SE Asia. *Journal of Geophysical Research-Solid Earth*, *106*(B4), 6683-6732. doi:Doi 10.1029/2000jb900322
- Li, Z., Ding, L., Song, P., Fu, J., & Yue, Y. (2017). Paleomagnetic constraints on the paleolatitude of the Lhasa block during the Early Cretaceous: implications for the onset of India–Asia collision and latitudinal shortening estimates across Tibet and stable Asia. *Gondwana Research*, *41*, 352-372.
- Licht, A., Win, Z., Westerweel, J., Cogné, N., Morley, C. K., Chantraprasert, S., . . . Aung, D. W. (2020). Magmatic history of central Myanmar and implications for the evolution of the Burma Terrane. *Gondwana Research*, *87*, 303-319.
- Liebke, U., Appel, E., Ding, L., Neumann, U., Antolin, B., & Xu, Q. (2010). Position of the Lhasa terrane prior to India–Asia collision derived from palaeomagnetic inclinations of 53 Ma old dykes of the Linzhou Basin: constraints on the age of collision and post-collisional shortening within the Tibetan Plateau. *Geophysical Journal International*, *182*(3), 1199-1215.
- Liebke, U., Appel, E., Ding, L., & Zhang, Q. (2013). Age constraints on the India–Asia collision derived from secondary remanences of Tethyan Himalayan sediments from the Tingri area. *Journal of Asian Earth Sciences*, *62*, 329-340.
- Lippert, P. C., Van Hinsbergen, D. J., & Dupont-Nivet, G. (2014). Early Cretaceous to present latitude of the central proto-Tibetan Plateau: A paleomagnetic synthesis with implications for Cenozoic tectonics, paleogeography, and climate of Asia. *Geological Society of America Special Papers*, *507*, 1-21.
- Ma, Y., Yang, T., Bian, W., Jin, J., Wang, Q., Zhang, S., . . . Yuan, H. (2017). Paleomagnetic and geochronologic results of latest Cretaceous lava flows from the Lhasa terrane and their tectonic implications. *Journal of Geophysical Research: Solid Earth*, *122*(11), 8786-8809.
- Ma, Y., Yang, T., Bian, W., Jin, J., Zhang, S., Wu, H., & Li, H. (2016). Early Cretaceous paleomagnetic and geochronologic results from the Tethyan Himalaya: Insights into the Neotethyan paleogeography and the India–Asia collision. *Scientific Reports*, *6*(1), 1-11.
- Ma, Y., Yang, T., Yang, Z., Zhang, S., Wu, H., Li, H., . . . Ding, J. (2014). Paleomagnetism and U-Pb zircon geochronology of Lower Cretaceous lava flows from the western Lhasa terrane: New constraints on the India-Asia collision process and intracontinental deformation within Asia. *Journal of Geophysical Research: Solid Earth*, *119*(10), 7404-7424.
- Malatesta, C., Gerya, T., Crispini, L., Federico, L., & Capponi, G. (2013). Oblique subduction modelling indicates along-trench tectonic transport of sediments. *Nature Communications*, *4*(1), 1-6.
- Martin, C. R., Jagoutz, O., Upadhyay, R., Royden, L. H., Eddy, M. P., Bailey, E., . . . Weiss, B. P. (2020). Paleocene latitude of the Kohistan–Ladakh arc indicates multistage India–Eurasia collision. *Proceedings of the National Academy of Sciences*, *117*(47), 29487-29494.
- Meert, J. G., Pivarunas, A. F., Evans, D. A., Pisarevsky, S. A., Pesonen, L. J., Li, Z.-X., . . . Salminen, J. M. (2020). The magnificent seven: a proposal for modest revision of the quality index. *Tectonophysics*, *790*, 228549.

- Meng, J., Wang, C., Zhao, X., Coe, R., Li, Y., & Finn, D. (2012). India-Asia collision was at 24 N and 50 Ma: palaeomagnetic proof from southernmost Asia. *Scientific Reports*, 2(1), 1-11.
- Molnar, P., & Stock, J. M. (2009). Slowing of India's convergence with Eurasia since 20 Ma and its implications for Tibetan mantle dynamics. *Tectonics*, 28(3).
- Mueller, P. A., Kamenov, G. D., Heatherington, A. L., & Richards, J. (2008). Crustal evolution in the southern Appalachian orogen: Evidence from Hf isotopes in detrital zircons. *The Journal of Geology*, 116(4), 414-422.
- Najman, Y., Jenks, D., Godin, L., Boudagher-Fadel, M., Millar, I., Garzanti, E., . . . Bracciali, L. (2017). The Tethyan Himalayan detrital record shows that India–Asia terminal collision occurred by 54 Ma in the Western Himalaya. *Earth and Planetary Science Letters*, 459, 301-310.
- Paton, C., Hellstrom, J., Paul, B., Woodhead, J., & Hergt, J. (2011). Iolite: Freeware for the visualisation and processing of mass spectrometric data. *Journal of Analytical Atomic Spectrometry*, 26(12), 2508-2518.
- Patzelt, A., Li, H., Wang, J., & Appel, E. (1996). Palaeomagnetism of Cretaceous to Tertiary sediments from southern Tibet: evidence for the extent of the northern margin of India prior to the collision with Eurasia. *Tectonophysics*, 259(4), 259-284.
- Petterson, M. G., & Windley, B. F. (1985). RbSr dating of the Kohistan arc-batholith in the Trans-Himalaya of north Pakistan, and tectonic implications. *Earth and Planetary Science Letters*, 74(1), 45-57.
- Pullaiah, G., Irving, E., Buchan, K., & Dunlop, D. (1975). Magnetization changes caused by burial and uplift. *Earth and Planetary Science Letters*, 28(2), 133-143.
- Pundir, S., Adlakha, V., Kumar, S., & Singhal, S. (2020). Closure of India–Asia collision margin along the Shyok Suture Zone in the eastern Karakoram: new geochemical and zircon U–Pb geochronological observations. *Geological Magazine*, 157(9), 1451-1472.
- Rai, H. (1982). Geological evidence against the Shyok palaeo-suture, Ladakh Himalaya. *Nature*, 297(5862), 142-144.
- Rex, A. J., Searle, M. P., Tirrul, R., Crawford, M. B., Prior, D. J., Rex, D. C., & Barnicoat, A. (1988). The Geochemical and Tectonic Evolution of the Central Karakoram, North Pakistan. *Philosophical Transactions of the Royal Society a-Mathematical Physical and Engineering Sciences*, 326(1589), 229-255. doi:DOI 10.1098/rsta.1988.0086
- Rolland, Y., Pecher, A., & Picard, C. (2000). Middle Cretaceous back-arc formation and arc evolution along the Asian margin: the Shyok Suture Zone in northern Ladakh (NW Himalaya). *Tectonophysics*, 325(1-2), 145-173.
- Rolland, Y., Picard, C., Pecher, A., Lapierre, H., Bosch, D., & Keller, F. (2002). The cretaceous Ladakh arc of NW himalaya—slab melting and melt–mantle interaction during fast northward drift of Indian Plate. *Chemical Geology*, 182(2-4), 139-178.
- Rowley, D. B. (2019). Comparing paleomagnetic study means with apparent wander paths: A case study and paleomagnetic test of the Greater India versus Greater Indian Basin hypotheses. *Tectonics*, 38(2), 722-740.
- Saktura, W. M., Buckman, S., Aitchison, J. C., & Zhou, R. (2021). Paleogene magmatic flex and flux in the Ladakh Arc, NW Himalaya: chronostratigraphy of the Khardung Formation. *Lithos*, 388, 106053.

- Saktura, W. M., Buckman, S., Nutman, A. P., & Bennett, V. C. (2021). Late Jurassic Changmar complex from the Shyok ophiolite, NW Himalaya: A prelude to the Ladakh arc. *Geological Magazine*, 158(2), 239-260.
- Schill, E., Appel, E., & Gautam, P. (2002). Towards pyrrhotite/magnetite geothermometry in low-grade metamorphic carbonates of the Tethyan Himalayas (Shiar Khola, Central Nepal). *Journal of Asian Earth Sciences*, 20(3), 195-201.
- Searle, M., Rex, A., Tirrul, R., Rex, D., Barnicoat, A., & Windley, B. (1989). Metamorphic, magmatic, and tectonic evolution of the central Karakoram in the Biafo-Baltoro-Hushe regions of northern Pakistan.
- Searle, M. P. (2019). Timing of subduction initiation, arc formation, ophiolite obduction and India–Asia collision in the Himalaya. *Geological Society, London, Special Publications*, 483(1), 19-37.
- Sharma, K. K. (1987). Crustal growth and two-stage India-Eurasia collision in Ladakh. *Tectonophysics*, 134(1-3), 17-28.
- Srimal, N. (1986). India-Asia collision: Implications from the geology of the eastern Karakoram. *Geology*, 14(6), 523-527.
- Sun, Z., Jiang, W., Li, H., Pei, J., & Zhu, Z. (2010). New paleomagnetic results of Paleocene volcanic rocks from the Lhasa block: Tectonic implications for the collision of India and Asia. *Tectonophysics*, 490(3-4), 257-266.
- Sun, Z., Pei, J., Li, H., Xu, W., Jiang, W., Zhu, Z., . . . Yang, Z. (2012). Palaeomagnetism of late Cretaceous sediments from southern Tibet: Evidence for the consistent palaeolatitudes of the southern margin of Eurasia prior to the collision with India. *Gondwana Research*, 21(1), 53-63.
- Sundell, K. E., Gehrels, G. E., & Pecha, M. E. (2021). Rapid U-Pb geochronology by laser ablation multi-collector ICP-MS. *Geostandards and Geoanalytical Research*, 45(1), 37-57.
- Tahirkheli, R. K. (1979). Geology of Kohistan and adjoining Eurasian and Indo-Pakistan continents, Pakistan. *Geol. Bull. Univ. Peshawar*, 11(1), 1-30.
- Tan, X., Gilder, S., Kodama, K. P., Jiang, W., Han, Y., Zhang, H., . . . Zhou, D. (2010). New paleomagnetic results from the Lhasa block: revised estimation of latitudinal shortening across Tibet and implications for dating the India–Asia collision. *Earth and Planetary Science Letters*, 293(3-4), 396-404.
- Tapponnier, P., Mattauer, M., Proust, F., & Cassaigneau, C. (1981). Mesozoic ophiolites, sutures, and large-scale tectonic movements in Afghanistan. *Earth and Planetary Science Letters*, 52(2), 355-371.
- Tauxe, L. (2010). *Essentials of paleomagnetism*: Univ of California Press.
- Tauxe, L., & Kent, D. V. (2004). A simplified statistical model for the geomagnetic field and the detection of shallow bias in paleomagnetic inclinations: was the ancient magnetic field dipolar?
- Tauxe, L., Kylstra, N., & Constable, C. (1991). Bootstrap statistics for paleomagnetic data. *Journal of Geophysical Research: Solid Earth*, 96(B7), 11723-11740.
- Tauxe, L., Shaar, R., Jonestrask, L., Swanson-Hysell, N., Minnett, R., Koppers, A., . . . Fairchild, L. (2016). PmagPy: Software package for paleomagnetic data analysis and a bridge to the Magnetics Information Consortium (MagIC) Database. *Geochemistry, Geophysics, Geosystems*, 17(6), 2450-2463.

- Thanh, N. X., Rajesh, V., Itaya, T., Windley, B., Kwon, S., & Park, C.-S. (2012). A Cretaceous forearc ophiolite in the Shyok suture zone, Ladakh, NW India: Implications for the tectonic evolution of the Northwest Himalaya. *Lithos*, *155*, 81-93.
- Tong, Y., Yang, Z., Pei, J., Li, J., Jin, S., Hou, L., . . . Zhang, Z. (2022). New Late Cretaceous paleomagnetic results from the Lhasa terrane and their implications for the suturing of India and Eurasia and the closure of the Neo-Tethys Ocean. *GSA Bulletin*.
- Tong, Y., Yang, Z., Zheng, L., Yang, T., Shi, L., Sun, Z., & Pei, J. (2008). Early Paleocene paleomagnetic results from southern Tibet, and tectonic implications. *International Geology Review*, *50*(6), 546-562.
- Torsvik, T. H., Van der Voo, R., Preeden, U., Mac Niocaill, C., Steinberger, B., Doubrovine, P. V., . . . Tohver, E. (2012). Phanerozoic polar wander, palaeogeography and dynamics. *Earth-Science Reviews*, *114*(3-4), 325-368.
- Upadhyay, R. (2014). Palaeogeographic significance of Yasin-type rudist and orbitolinid fauna of the Shyok Suture Zone, Saltoro Hills, northern Ladakh, India. *Current Science*, 223-228.
- Upadhyay, R., Sinha, A. K., Chandra, R., & Rai, H. (1999). Tectonic and magmatic evolution of the eastern Karakoram, India. *Geodinamica Acta*, *12*(6), 341-358.
- Vaes, B., Li, S., Langereis, C. G., & van Hinsbergen, D. J. (2021). Reliability of palaeomagnetic poles from sedimentary rocks. *Geophysical Journal International*, *225*(2), 1281-1303.
- Van der Voo, R. (1990). The reliability of paleomagnetic data.
- Van Hinsbergen, D. J., Kapp, P., Dupont-Nivet, G., Lippert, P. C., DeCelles, P. G., & Torsvik, T. H. (2011). Restoration of Cenozoic deformation in Asia and the size of Greater India. *Tectonics*, *30*(5).
- Van Hinsbergen, D. J., Lippert, P. C., Dupont-Nivet, G., McQuarrie, N., Doubrovine, P. V., Spakman, W., & Torsvik, T. H. (2012). Greater India Basin hypothesis and a two-stage Cenozoic collision between India and Asia. *Proceedings of the National Academy of Sciences*, *109*(20), 7659-7664. Retrieved from <https://www.ncbi.nlm.nih.gov/pmc/articles/PMC3356651/pdf/pnas.1117262109.pdf>
- van Hinsbergen, D. J., Lippert, P. C., Li, S., Huang, W., Advokaat, E. L., & Spakman, W. (2019). Reconstructing Greater India: Paleogeographic, kinematic, and geodynamic perspectives. *Tectonophysics*, *760*, 69-94.
- Vermeesch, P. (2021). Maximum depositional age estimation revisited. *Geoscience Frontiers*, *12*(2), 843-850.
- Waldron, J. W., McCausland, P. J., Barr, S. M., Schofield, D. I., Reusch, D., & Wu, L. (2022). Terrane history of the Iapetus Ocean as preserved in the northern Appalachians and western Caledonides. *Earth-Science Reviews*, 104163.
- Wang, J. G., Hu, X. M., Garzanti, E., An, W., & Liu, X. C. (2017). The birth of the Xigaze forearc basin in southern Tibet. *Earth and Planetary Science Letters*, *465*, 38-47. doi:10.1016/j.epsl.2017.02.036
- Watson, G. (1956). A test for randomness of directions. *Geophysical Supplements to the Monthly Notices of the Royal Astronomical Society*, *7*(4), 160-161.
- Westerweel, J., Roperch, P., Licht, A., Dupont-Nivet, G., Win, Z., Poblete, F., . . . Aung, D. W. (2019). Burma Terrane part of the Trans-Tethyan arc during collision with India according to palaeomagnetic data. *Nature Geoscience*, *12*(10), 863-868.
- Xu, Y., Tan, X., Li, S., Li, Y., Ran, B., Han, Y., . . . Ma, Z. (2022). Paleomagnetism of the Greater Indian passive margin sediments from the Upper Cretaceous succession:

- Evidence for long-delayed remagnetizations and implication for the India-Asia collision. *Journal of Asian Earth Sciences*, 229, 105165.
- Yang, T., Ma, Y., Bian, W., Jin, J., Zhang, S., Wu, H., . . . Ding, J. (2015). Paleomagnetic results from the Early Cretaceous Lakang Formation lavas: Constraints on the paleolatitude of the Tethyan Himalaya and the India–Asia collision. *Earth and Planetary Science Letters*, 428, 120-133.
- Yang, T., Ma, Y., Zhang, S., Bian, W., Yang, Z., Wu, H., . . . Ding, J. (2015). New insights into the India–Asia collision process from Cretaceous paleomagnetic and geochronologic results in the Lhasa terrane. *Gondwana Research*, 28(2), 625-641.
- Yi, Z., Huang, B., Chen, J., Chen, L., & Wang, H. (2011). Paleomagnetism of early Paleogene marine sediments in southern Tibet, China: implications to onset of the India–Asia collision and size of Greater India. *Earth and Planetary Science Letters*, 309(1-2), 153-165.
- Yi, Z., Wang, T., Meert, J. G., Zhao, Q., & Liu, Y. (2021). An initial collision of India and Asia in the equatorial humid belt. *Geophysical Research Letters*, 48(9), e2021GL093408.
- Yin, A., Harrison, T. M., Murphy, M., Grove, M., Nie, S., Ryerson, F., . . . Zeng Le, C. (1999). Tertiary deformation history of southeastern and southwestern Tibet during the Indo-Asian collision. *Geological Society of America Bulletin*, 111(11), 1644-1664.
- Yuan, J., Deng, C., Yang, Z., Krijgsman, W., Qin, H., Shen, Z., . . . Zhao, P. (2022). Triple-stage India-Asia collision involving arc-continent collision and subsequent two-stage continent-continent collision. *Global and Planetary Change*, 212, 103821.
- Yuan, J., Yang, Z., Deng, C., Krijgsman, W., Hu, X., Li, S., . . . He, H. (2021). Rapid drift of the Tethyan Himalaya terrane before two-stage India-Asia collision. *National Science Review*, 8(7), nwaal173.
- Zaman, H., Otofujii, Y.-i., Khan, S. R., & Ahmad, M. N. (2013). New paleomagnetic results from the northern margin of the Kohistan Island Arc. *Arabian Journal of Geosciences*, 6(4), 1041-1054.
- Zaman, H., & Torii, M. (1999). Palaeomagnetic study of Cretaceous red beds from the eastern Hindukush ranges, northern Pakistan: palaeoreconstruction of the Kohistan–Karakoram composite unit before the India–Asia collision. *Geophysical Journal International*, 136(3), 719-738.
- Zanchi, A., Poli, S., Fumagalli, P., & Gaetani, M. (2000). Mantle exhumation along the Tirich Mir Fault Zone, NW Pakistan: pre-mid-Cretaceous accretion of the Karakoram terrane to the Asian margin. *Geological Society, London, Special Publications*, 170(1), 237-252.
- Zhang, Y., & Huang, B. (2017). The influence of Cretaceous paleolatitude variation of the Tethyan Himalaya on the India-Asia collision pattern. *Science China Earth Sciences*, 60(6), 1057-1066.

Appendix A

Ammonia-water Freezing in Pluto's Subsurface Ocean as a Mechanism for Recent Cryovolcanism

Material from:

Martin and Binzel, "Ammonia-water Freezing in Pluto's Subsurface Ocean as a Mechanism for Recent Cryovolcanism," Icarus, published online 26 March 2020, copyright Elsevier B.V. 2020. Reprinted with permission of Elsevier.

A.1 Abstract

NASA's New Horizons flyby of the Pluto-Charon system in 2015 exposed a multitude of geologically active terrains on the surface of Pluto. At the edge of the New Horizons closest approach hemisphere, there are two large circular mountains, informally referred to as Wright Mons and Piccard Mons. They are largely crater-free, which suggests that they have a younger relative age compared with Pluto's 4.5 billion year history. Their relative age, along with their circular mounded shapes and central depressions, suggests that they may have been formed by recent volcanism. Detailed geologic mapping of Wright Mons and the surrounding region reveals additional circular mounds overlying the main edifice and narrow ravines emanating from the summit, possibly produced by liquid flow. The dominance of extensional tectonic structures predating and postdating Wright Mons also suggests that Pluto's ice crust has been under extension throughout its geologic past. In order to explain these observations, we model the overpressure generated during freezing inside a mixed ammonia-water ocean beneath an elastic ice crust. We

consider two end-member scenarios spanning the possible range of Pluto's ammonia abundance and conclude that for both cases the tangential stresses generated in the crust due to ocean pressurization will exceed the tensile strength of ice after less than 2% freezing. We show that the volume of melt predicted to erupt once the ice crust fractures is comparable to the observed volume of Wright Mons. These findings suggest that subsurface ocean freezing is a viable mechanism for cryovolcanism on Pluto.

A.2 Introduction

Cryovolcanism is volcanism involving volatile ices and fluids rather than silicate rocks and melts. Active cryovolcanic eruptions, in the form of geyser-like plumes, have been observed on the icy moons of the gas giants since the early exploration of the outer solar system (Smith et al., 1989; Soderblom et al., 1990; Porco et al., 2006; Sparks et al., 2016). In addition, geomorphic evidence of past cryovolcanism has been identified on icy worlds throughout the solar system. For example, on Europa, chaotic dome structures containing blocks of older ice appear to have formed from liquid water that erupted onto and spread radially over the surrounding ice sheet (Fagents, 2003). On Saturn's moon, Titan, water-ice flow features extend down the flanks the mountain Doom Mons (Lopes et al., 2007). On Ceres, the cracked flat top and steep flanks of Ahuna Mons suggest that it may have formed due to an eruption of a viscous ice-silicate mixture, similar to rhyolite dome emplacement on Earth (Ruesch et al., 2016). A cryovolcanic landform has even been documented on Earth; the Yamal crater in Siberia is hypothesized to have formed by the explosion of pressurized water from the freezing of trapped subsurface aquifers (Buldovicz et al., 2018).

Recently, the New Horizons Mission extended the known occurrence of cryovolcanism to include the Kuiper belt. During its flyby of Pluto in 2015, New Horizons discovered a spectacular complexity of young and active terrains (Stern et al., 2015). These include a vast convecting nitrogen ice cap (McKinnon et al., 2016), networks of nitrogen ice glaciers (Howard et al., 2017), methane ice dunes (Telfer et al., 2018), and huge penitente-like spires of methane ice (Moores et al., 2017). In particular, two circular mounds were observed at the southern edge of the New Horizons Pluto encounter hemisphere. These features, informally referred to as Wright Mons and Piccard Mons, are approximately 150 km and 200 km in diameter respectively and both have over

4 - 6 km of relief (Schenk et al., 2018). The lack of observable impact craters suggests that these mounds are geologically young which has led to the hypothesis that they formed during recent cryovolcanism (Stern et al., 2015; Moore et al., 2016; Singer et al., 2016).

In order to assess this hypothesis, we used the New Horizons Ralph and Long-Range Reconnaissance Imager (LORRI) imagery and the digital terrain model of Schenk et al. (2018) to compile a detailed geological map of Wright Mons and the surrounding terrains. We present new supporting evidence for the interpretation that Wright Mons formed due to recent cryovolcanism and show that the region surrounding Wright Mons has experienced multiple phases of crustal extension that continued into Pluto's recent past. To explain these observations, we explore whether pressurization due to the freezing of Pluto's subsurface ocean is capable of generating extensional stresses in the overlying ice crust large enough to result in fracture and eruption of liquid at the surface. We adopt a similar modelling approach to that developed by Manga and Wang (2007) for Enceladus and Europa and modify their model to account for the effects of ammonia in the subsurface ocean. Ammonia is a powerful antifreeze that may be important for maintaining liquid water in the cold conditions of the outer solar system. The presence of ammonia can also affect the density evolution of the liquid and change the amount of overpressure generated from a given amount of freezing (Croft et al., 1988). Our results suggest that overpressure due to freezing in Pluto's subsurface ocean is a viable mechanism for cryovolcanism because only a small fraction of the subsurface ocean needs to freeze in order to produce stresses in the ice crust that exceed the crust's tensile strength. In addition, the volume of liquid predicted to erupt when the ice crust fractures is consistent with the volume of Wright Mons, implying that the mechanism presented here is capable of producing landforms on a scale that matches the observations.

A.3 Geology of Wright Mons, Hyecho Palus, and Cthulhu Regio

Using the New Horizons Ralph and LORRI data and the digital terrain model of Schenk et al. (2018), we have extended the geological map of Sputnik Planitia of White et al. (2017) westward to include Wright Mons, Hyecho Palus, and the higher elevation terrain of Cthulhu Regio (see Figure A-1). Cthulhu Regio, is heavily cratered and eroded suggesting that it is relatively old (see Figure A-1) (Schenk et al., 2018). Dendritic networks of glaciated valleys, channels, and scours emanate from scarps and mountains, converging eastward with the gradual decrease in elevation towards Sputnik Planitia (Howard et al., 2017). Around these channels, the flat plateau-like terrain is strewn with boulders and blocky mountains (see Figure A-2). These are presumed to be detritus from Pluto's water ice crust that have been transported and deposited by nitrogen ice that has since receded, similar to the glacial erratics and moraines on Earth (Howard et al., 2017; Umurhan et al., 2017). It is plausible that in its geological past this region resembled the western edge of Sputnik Planitia where chains of blocky mountains have been interpreted to be floating in the denser nitrogen ice (Trowbridge et al., 2016). Cthulhu Regio is also transected by a network of extensional fault systems with multiple orientations (see Figure A-2). One set of faults is oriented broadly east-west while others extend radially from Sputnik Planitia. Previous studies have related this radial faulting to the stresses induced by true polar wander during the reorientation of Sputnik Planitia to Pluto's anti-Charon tidal axis (Keane et al., 2016). The north-south oriented faults at the western edge of the mapped area could also be related to the "major north-south ridge-trough system" identified by Schenk et al. (2018). They interpreted this structure to be old because it appears to be crosscut by the edge of the Sputnik Planitia basin, which is thought to have formed early in Pluto's history, either during a giant impact or due to nitrogen loading (Nimmo et al., 2016; Hamilton et al., 2016; Schenk et al., 2018). Some of the east-west

oriented faults extend into Hyecho Palus, crosscutting the 4 km high north-south trending scarp that defines the boundary between the two terrains. Landslide features can also be identified along this escarpment (see Figure A-1).

Hyecho Palus is the lowest region on Pluto with a minimum elevation ~ 2 km below mean radius (Figure A-2) (Schenk et al., 2018). Its floor is craggy and cut by fissures as well as deep troughs that are sometimes infilled with pitted plains of nitrogen ice, similar to those at the edges of SP (White et al., 2017). The low-lying terrain is increasingly covered by the nitrogen ice towards the east and there is evidence of nitrogen ice flowing westward into the region from SP (White et al., 2017; Howard et al., 2017). Between Hyecho Palus and Sputnik Planitia there is a region of closely packed blocky mountains known as Norgay Montes (Stern et al., 2015). The western edge of Norgay Montes protrudes directly from the craggy low elevation plains of Hyecho Palus while its eastern flank is defined by a chaotic terrain of small blocks which are entrained within the nitrogen ice of Sputnik Planitia (White et al., 2017).

The region around Wright Mons is dominated by hummocky terrain which is defined by 5 - 10 km wide overlapping mounds (Schenk et al., 2018). This terrain also contains multiple large conical pits and flat-topped mountains, and appears to overlie the surrounding topography of Hyecho Palus (see Figure A-2). It is almost completely devoid of impact craters implying that it must be considerably younger than the heavily cratered landscape of Cthulu Regio (Stern et al., 2015). Beyond the southern boundary of the mapped area the hummocky terrain extends to the edge of the observation hemisphere surrounding Piccard Mons. The hummocks continue on the flanks of Wright Mons upwards to a circular crest which surrounds a 50 km wide and 6 km deep central depression (see Figure A-1). The central depression has a steep conical shape with a flat base that is almost as low as the surrounding plains of Hyecho Palus and Sputnik Planitia (see

topographic profile in Figure A-1). Two roughly circular summit mounds at the top of Wright Mons to the north and south-east of the central depression appear to have been emplaced on top of the hummocky terrain, similar to secondary cinder cones on terrestrial volcanoes. It is possible to trace multiple narrow ravines emanating from the tops of these summit mounds into the deep central depression and also outwards over the undulating flanks of the mountain. These could be formed by the flow of cryovolcanic fluids over the surface (see Figure A-1b). Wright Mons is also bisected by a major north-south oriented fault structure that displaces the eastern side of the mountain downwards relative to the western side, resulting in an east-west asymmetry in the mountain's height (see the topographic profile in Figure A-1). The fact that this fault crosscuts the crater-free hummocky terrain suggests that large-scale regional extension continued to affect the region even more recently than the formation of Wright Mons.

A.4 Modelling Freezing and Overpressure

Unlike the melts in silicate volcanic systems, cryovolcanic fluids do not naturally rise to the surface through diapiric or conduit ascent because liquid water is denser than ice (Fagents et al., 2003). Instead, subsurface reservoirs must become pressurized in order to overcome the negative buoyancy and force the liquid upward (Fagents et al., 2003; Manga and Wang, 2007). Since the ice is less dense than water, this overpressure can be generated by freezing if it occurs in a trapped reservoir where pressure is able to build (Fagents et al., 2003; Manga and Wang, 2007). If the pressure is capable of propelling water to the surface via a crack or conduit in the overlying crust, then this could result in a cryovolcanic eruption (Fagents et al., 2003; Manga and Wang, 2007; Neveu et al., 2015).

Consider the scenario in which an enclosed chamber of water freezes (Fagents, 2003). The volume of the ice formed after a certain amount of freezing is given by:

$$V_I = f \frac{\rho_w}{\rho_i} V_T$$

where ρ_w and ρ_i are the density of the liquid and the solid phases respectively, V_T is the total volume of the chamber, and f is the fraction of the water in the chamber that has frozen ($0 \leq f \leq 1$) (Fagents, 2003). The volume of liquid water remaining after freezing is:

$$V_w = (1 - f)V_T$$

and the volume left in the chamber to store that water is:

$$V = V_T - V_I$$

(Fagents, 2003). The volume of the new ice is greater than that of the water it formed from because the density difference between the solid and liquid phases is positive (i.e. $\rho_i < \rho_w$) (Fagents, 2003). This means that the space left after freezing is less than that which is required to store the remaining water ($V < V_w$) (Fagents, 2003). The water must be compressed to fit, producing an overpressure equal to:

$$\Delta P_{Rigid} = \frac{V_w - V}{\beta V_w} = \frac{f}{\beta(1 - f)} \left(\frac{\rho_w}{\rho_i} - 1 \right)$$

where β is the compressibility of the liquid (Fagents, 2003).

Supposing that all the excess water ($V_w - V$) is displaced from a rigid chamber and erupted at the surface, this liquid will only ever represent a very small fraction (maximum $\sim 9\%$) of the total chamber volume in the subsurface (Fagents et al., 2003). Integrating between the topographic surface defined by the New Horizons digital terrain model of Wright Mons and a flat surface at the approximate basement elevation of Hyecho Palus (1500 km below mean elevation) yields an estimate for the volume of Wright Mons of $\sim 5200 \text{ km}^3$ (see Figure A-1c). Even if it freezes

entirely, a spherical crustal chamber would have to be extremely large (~ 215 km in diameter) in order to produce the volume of liquid required to form Wright Mons. Therefore, it is much more likely that cryovolcanic liquids on Pluto are derived from a global subsurface ocean rather than a small trapped pocket of liquid. The presence of such an ocean is predicted by planetary evolution models and has been invoked to explain the proximity of the Sputnik Planitia basin to the anti-Charon tidal axis (Hussman et al., 2006; Desch et al., 2009; Robuchon and Nimmo, 2011; Hammond et al., 2016; Nimmo et al., 2016; Johnson et al., 2016; Keane et al., 2016; Bierson et al., 2018).

For simplicity, we consider a spherically symmetrical three-phase Pluto which has a rocky core, a subsurface ocean, and a linear-elastic ice crust. Unlike Manga and Wang (2007), we treat the entire crust as an elastic material and do not vary the elastic thickness. The initial volume of the subsurface ocean is given by:

$$V_T = \frac{4\pi}{3} (r_i^3 - r_c^3)$$

where r_c is the radius of the incompressible rocky core (889 km, 300 km below the surface) and r_i is the boundary between the ice crust and the liquid ocean (989 km, assumed crustal thickness of 200 km and an ocean thickness of 100 km, see Figure A-3). As with the enclosed chamber, freezing in the subsurface ocean will generate an overpressure (Fagents, 2003; Manga and Wang, 2007). The pressurized ocean will impart radial stresses on the base of the ice crust which will cause it to expand outwards. The expansion will increase the volume of the subsurface ocean, decreasing the excess pressure (Manga and Wang, 2007). We follow the approach of Manga and Wang, (2007) who use a solution to the Navier equations for the radial and tangential stresses in a thick hollow elastic sphere under internal and external pressure (Sokolnikoff, 1956; Manga and Wang, 2007).

$$\sigma_r = \frac{\Delta P r_i^3}{R^3 - r_i^3} \left(\frac{R^3}{r^3} - 1 \right) \quad (\sigma_r = \Delta P \text{ at } r = r_i)$$

$$\sigma_t = \frac{\Delta P r_i^3}{R^3 - r_i^3} \left(\frac{R^3}{2r^3} + 1 \right)$$

R is the outer radius (1189 km, Stern et al., 2018) and $r_i < r < R$. It is assumed that the surface pressures on Pluto are negligible. The ice crust will move outward under the applied stress by a radial displacement of:

$$u_r = -\frac{r}{E} (\sigma_r - 2\nu\sigma_t)$$

where E is Young's modulus for ice ($E = 5 \times 10^9$ Pa, Nimmo, 2004) and ν is Poisson's ratio ($\nu = 0.33$, Schulson, 2001) (Manga and Wang, 2007). Due to this expansion, the volume of the ocean increases by:

$$\Delta V = \frac{4\pi}{3} ((r_i + u_r)^3 - r_i^3)$$

where u_r is evaluated for the base of the ice crust ($r = r_i$). Incorporating the expansion of the ice shell, the overpressure in the ocean becomes:

$$\Delta P_{Elastic} = \frac{V_w - (V + \Delta V)}{\beta V_w}$$

$$\Delta P_{Elastic} = \frac{(1-f)(r_i^3 - r_c^3) - \left[\left(1 - f \frac{\rho_w}{\rho_i}\right) (r_i^3 - r_c^3) + ((r_i + u_r)^3 - r_i^3) \right]}{\beta(1-f)(r_i^3 - r_c^3)}$$

Due to the global expansion of the ice crust, more freezing in the subsurface ocean will be required to produce a given overpressure than would be required to reach the same overpressure in a rigid chamber (Manga and Wang, 2007). Once the extensional stresses in the ice crust exceed the tensile strength of the ice, the crust will fracture and a conduit will be created for the liquid to ascend (Neveu et al., 2015; Manga and Wang, 2007). Water will rise to the surface if the overpressure in

the chamber is greater than the negative buoyancy force (Fagents, 2003). The critical overpressure required for water to ascend to the surface is given by:

$$\Delta P_{Critical} = (\rho_w - \rho_i)(R - r_i)g$$

where g is the surface gravity on Pluto ($g = 0.62 \text{ ms}^{-2}$) (Manga and Wang, 2007). During eruption, the crust will relax and the water will decompress so the maximum volume of liquid erupted at the surface will be:

$$V_{Erupted} = \frac{4\pi}{3}\beta(\Delta P_{Elastic} - \Delta P_{Critical})(r_i + u_r)^3 - r_c^3 + \frac{4\pi}{3}((r_i + u_r)^3 - r_c^3)$$

assuming that all the water evacuated from the chamber reaches the surface (Manga and Wang, 2007).

A.5 The Effects of Ammonia

The eutectic temperature of the ammonia-water system is 176 K, so the presence of ammonia will allow a small fraction of the liquid to persist at temperatures almost 100 K below the normal freezing point of pure water (see Figure A-4) (Croft et al., 1988). For this reason, many previous studies have highlighted the importance of ammonia in maintaining liquid water in the outer solar system and its potential role in cryovolcanism (e.g. Desch et al., 2009; Robuchon and Nimmo, 2011; Neveu et al., 2015; Bierson et al., 2018). This inference is supported by the association of ammonia hydrates with regions of possible cryovolcanic resurfacing (Grundy et al., 2016; Cruikshank et al., 2019). In order to understand the potential implications of the presence of ammonia in Pluto's subsurface ocean for cryovolcanism, we use the equation of state from Croft et al. (1988) to track the evolution of the ammonia-water system during freezing.

As an ammonia-water mixture cools, for initial ammonia compositions of $X_0 < 0.3$, pure H₂O ice will form in equilibrium with an increasingly ammonia rich melt until the eutectic composition ($X = 0.3$) is reached (see Figure A-4; Croft et al., 1988). At this point, the remaining liquid will solidify to form ammonia dihydrate ice (NH₃·2H₂O) (Croft et al., 1988). The formation of ammonia dihydrate ice at the eutectic will not produce additional overpressure because the dihydrate ice is denser than the liquid phase (Leliwa-Kopystyński et al., 2002). As the concentration of ammonia increases, the density of the liquid mixture decreases – eventually approaching the density of pure H₂O ice (Croft et al., 1988). This has two important ramifications for cryovolcanism. First, the small density difference between the solid and liquid phases at high ammonia concentrations will reduce the amount of overpressure that can be generated for a given freeze fraction (Desch et al., 2009). Second, the smaller density difference will also reduce the

negative buoyancy of the melt, making it easier to transport upward towards the surface (Mitri et al., 2008).

The primordial abundance of ammonia in the outer solar system is uncertain, but it is likely that Pluto accreted with around 1–5 % (McKinnon et al., 2008; Desch et al., 2009). Assuming that no ammonia is stored in the rocky core and is instead concentrated in the subsurface ocean, the formation of the 200 km thick pure H₂O ice crust used as an initial condition in our model would raise the ammonia concentration in the remaining subsurface ocean to between 4 – 20 %. In order to bracket the plausible range of feasible initial subsurface ocean ammonia concentrations in our freezing model, we consider two end-member cases: $X_0 = 0.04$ and $X_0 = 0.2$. Each of these end-member ammonia concentrations results in very different thermal evolutions and liquid density paths for the system (see Figure A-5). An ocean with $X_0 = 0.04$ will remain above 250 K for freeze fractions of up to $f = 0.6$ and will not begin to form ammonia dihydrate ice until almost all of the water has frozen. Conversely, an ocean with $X_0 = 0.2$ will start to freeze at ~ 225 K and cool significantly until it reaches the eutectic temperature at $f = 0.4$. The high ammonia system will maintain a density difference of around 20 – 30 kg m⁻³ during freezing while the low ammonia system will have a density difference of around 90 – 100 kg m⁻³ throughout most of its evolution, only reaching lower values at very high freeze fractions ($f > 0.6$) (see Figure A-5). We track the density evolution of the liquid throughout freezing and include it in our calculation of the overpressure (see Section 3).

A.6 Results

The solid-liquid density differences between the two end-member ammonia scenarios have a significant effect on the overpressures that can be generated by freezing in the subsurface ocean (see Figure A-6). For a given freeze fraction, the low ammonia end-member scenario ($X_0 = 0.04$) will produce ~ 3 times the overpressure in the subsurface ocean compared to the high ammonia case ($X_0 = 0.2$). However, in both scenarios it is possible to reach significant overpressures in the subsurface ocean (between 1 – 10 MPa with less than 10% freezing). Overpressures of this magnitude will induce extensional stresses in the ice crust large enough to fracture the ice (see Figure A-6).

There are no experimental constraints on the tensile strength of ice at the extremely low temperatures on Pluto and the tensile strength of ice is highly dependent on other factors such as impurities, the grain size, and porosity (Litwin et al., 2012). However, extrapolating fits to experimental data between 110 – 270 K down to Pluto's surface temperatures (40 K) yields a conservatively broad range of possible tensile strengths between 0.3 – 2 MPa (Litwin et al., 2012). Both ammonia end-member cases can generate extensional stresses exceeding the upper limit of this range after a very small amount of freezing in the subsurface ocean (0.8% for $X_0 = 0.04$ and 2% for $X_0 = 0.2$). This means that freezing in Pluto's subsurface ocean, for a wide range of possible ammonia concentrations, is capable of fracturing the overlying ice crust and creating conduits for liquid to ascend. Furthermore, for both the high and low ammonia scenarios, the overpressures that are generated due to freezing will exceed the critical value required to overcome the negative buoyancy of the liquid for any appreciable freeze fraction (see Figure A-6). As a consequence, this means cryovolcanism on Pluto is not limited by negative buoyancy and the pressurized liquid will travel to the surface once cracks form in the crust.

In both cases, the freeze fractions that are capable of generating extensional stresses in the crust within the range of tensile strengths of ice coincide closely with the freeze fractions that are required to produce the same volume of liquid that froze to form Wright Mons (see Figure A-6). To form Wright Mons, $\sim 0.5\%$ subsurface ocean freezing is required for $X_0 = 0.04$ and $\sim 2\%$ freezing for $X_0 = 0.2$. These freeze fractions will induce extensional stresses of around 1 MPa and 4 MPa respectively (see Figure A-6). These stresses imply that overpressure due to freezing in Pluto's subsurface ocean could produce surface expressions of cryovolcanism that are a similar in volume to Wright Mons. The correlation is closer for the low ammonia end-member than the high ammonia case, possibly suggesting that Pluto's subsurface ocean has an ammonia concentration closer to 4% than 20%.

A.7 Conclusion

The exploration of Pluto by NASA's New Horizons mission has revealed an incredibly complex world with diverse and young geological terrains and evidence of active geologic processes (Stern et al., 2015). Despite its location in the frigid outer reaches of the solar system there is a growing body of evidence suggesting that Pluto experienced recent cryovolcanic activity (e.g Schenk et al., 2018; Cruikshank et al., 2019). Our geologic mapping of the region surrounding Wright Mons, at the southern edge of the New Horizons encounter hemisphere, supports the previous interpretation that it is a recently active cryovolcano. Wright Mons is a large, circular, mounded edifice with an almost crater-free surface and a deep central depression (Schenk et al., 2018). Its flanks overlie the surrounding terrains of Norgay Montes and Hyecho Palus and the summit rim has two subsidiary circular peaks that appear have been emplaced on top of the primary edifice. Narrow channels emanating from these subsidiary summit mounds could be evidence of liquid flow across the surface during cryovolcanic eruption. Our mapping also shows that the region around Wright Mons has experienced extensional tectonics throughout its history. Large-scale systems of extensional faults and fissures in multiple orientations crosscut Cthulhu Regio and Hyecho Palus as well as the major scarp which defines the terrain boundary between them. In addition, Wright Mons itself is crosscut by a major north-south oriented structure which must post-date the edifice as well as the young hummocky terrain around it. This crosscutting relationship implies that extension continued after the formation of Wright Mons and was likely the dominant tectonic regime during its formation.

Explaining these observations, and understanding the mechanism for cryovolcanism on Pluto, requires consideration of an important difference between cryovolcanic liquids and silicate melts. Unlike melts in silicate systems, water-based cryovolcanic liquids are denser than the solid

ice that they formed from. This means that while silicate melts would naturally rise to the surface, cryovolcanic melts should sink (Neveu et al., 2015). However, if enough pressure builds in a subsurface chamber so as to overcome the melt's negative buoyancy and fracture the overlying crust, it is possible to erupt cryovolcanic liquids at the surface (Fagents, 2003; Manga and Wang, 2007; Neveu et al., 2015). The same liquid-ice density difference that hinders the ascent of cryovolcanic melts also provides the mechanism to pressurize the liquid because trapped chambers of water will pressurize as they freeze (Fagents, 2003).

On Pluto and other KBOs, the necessary liquid persistence required for cryovolcanism is aided by antifreezes such as ammonia that enable cryovolcanic fluids to persist well below the freezing point of pure water (Desch et al., 2009; Robuchon and Nimmo, 2011; Neveu et al., 2015; Bierson et al., 2018, Cruikshank et al., 2019). The presence of ammonia reduces the density difference between the liquid and solid phases, resulting in less negatively buoyant cryovolcanic liquids, but also less overpressure during freezing (Mitri et al., 2008; Desch et al., 2009). The results of our modelling indicate that the thermal, compositional, and density evolution during freezing will be very different, dependent on the initial ammonia concentration of the liquid. The difference in density evolution will result in a factor of 3 difference in the overpressure that can be generated during freezing in Pluto's subsurface ocean. Despite this, even in the high ammonia end-member case, less than 2% freezing in Pluto's subsurface ocean will produce extensional stresses in the overlying ice crust that exceed the tensile strength of the ice (0.3 – 2 MPa, Litwin et al., 2012). Furthermore, at the freeze fractions at which the ice crust should fracture, the volume of melt predicted to erupt is comparable to that which formed Wright Mons. These results suggest that, within the bounds of our simple model, not only is overpressure due to freezing in a

subsurface ocean a viable first-order mechanism for cryovolcanism on Pluto, but it will produce cryovolcanic edifices that are the same size as those observed by New Horizons.

A.8 Acknowledgements

This work was supported by the NASA New Horizons Mission to Pluto.

A.9 Figures and Captions

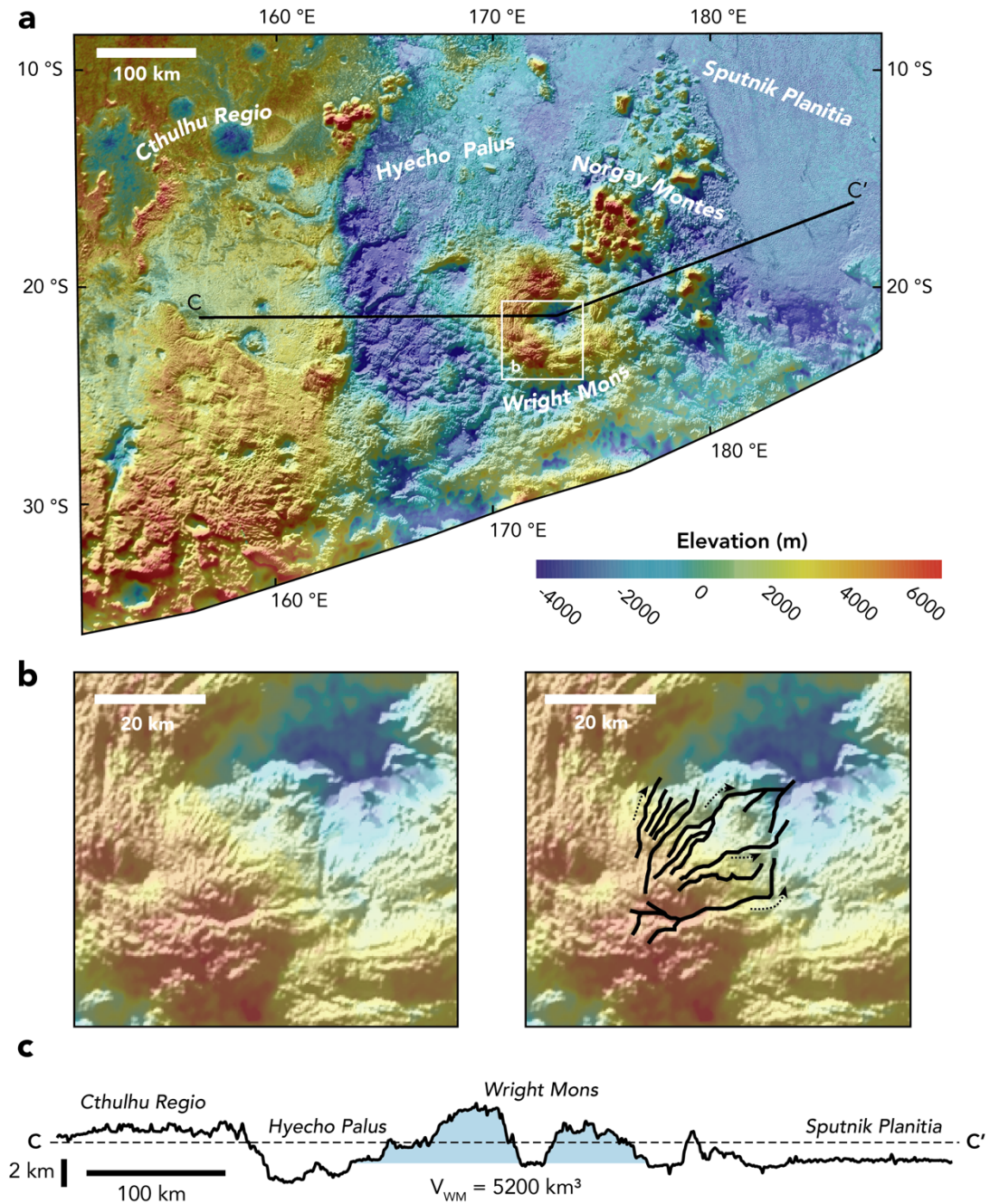


Figure A-1: **a)** Topography map of Wright Mons and surrounding terrains using New Horizons LORRI imagery and MVIC data at 320–386 m/pixel (White et al., 2017). The digital elevation model has a horizontal resolution of ~ 2 km across and a vertical precision of 115 m (White et al., 2017). **b)** Blow up of elevation map showing small channels emanating from the southern summit edifice of Wright Mons. **c)** Vertically exaggerated topographic profile C – C’ showing the high

plateau terrain of Cthulhu Regio terminating at a steep escarpment into the very low elevation Hyecho Palus basin. Wright Mons is higher in the west than the east and has a deep, steep sided central pit and two circular summit mounds.

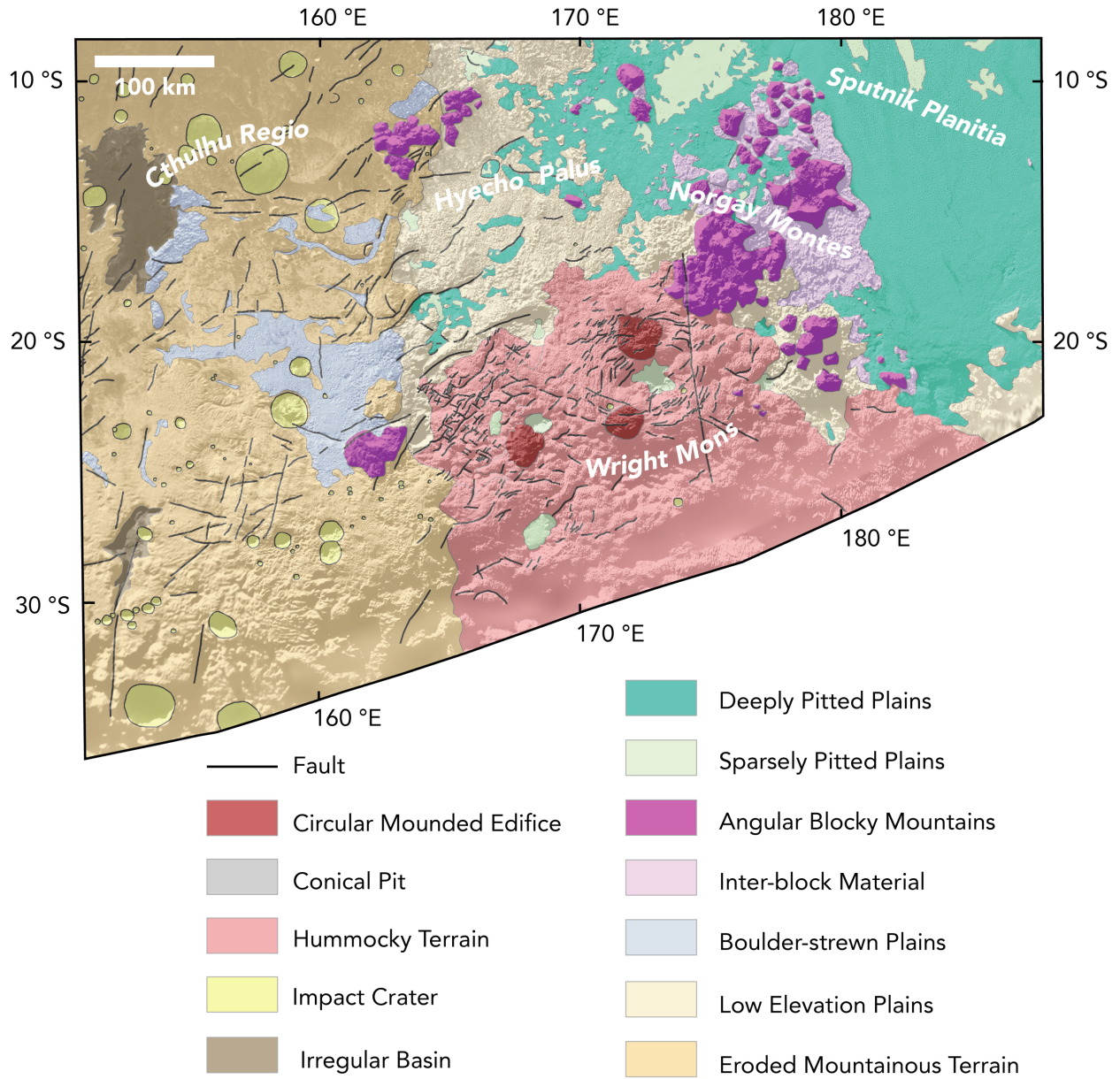


Figure A-2: Geological map of Wright Mons, Hyecho Palus, and Cthulu Regio. Unit definitions and color conventions for Sputnik Planitia units follow White et al., (2017).

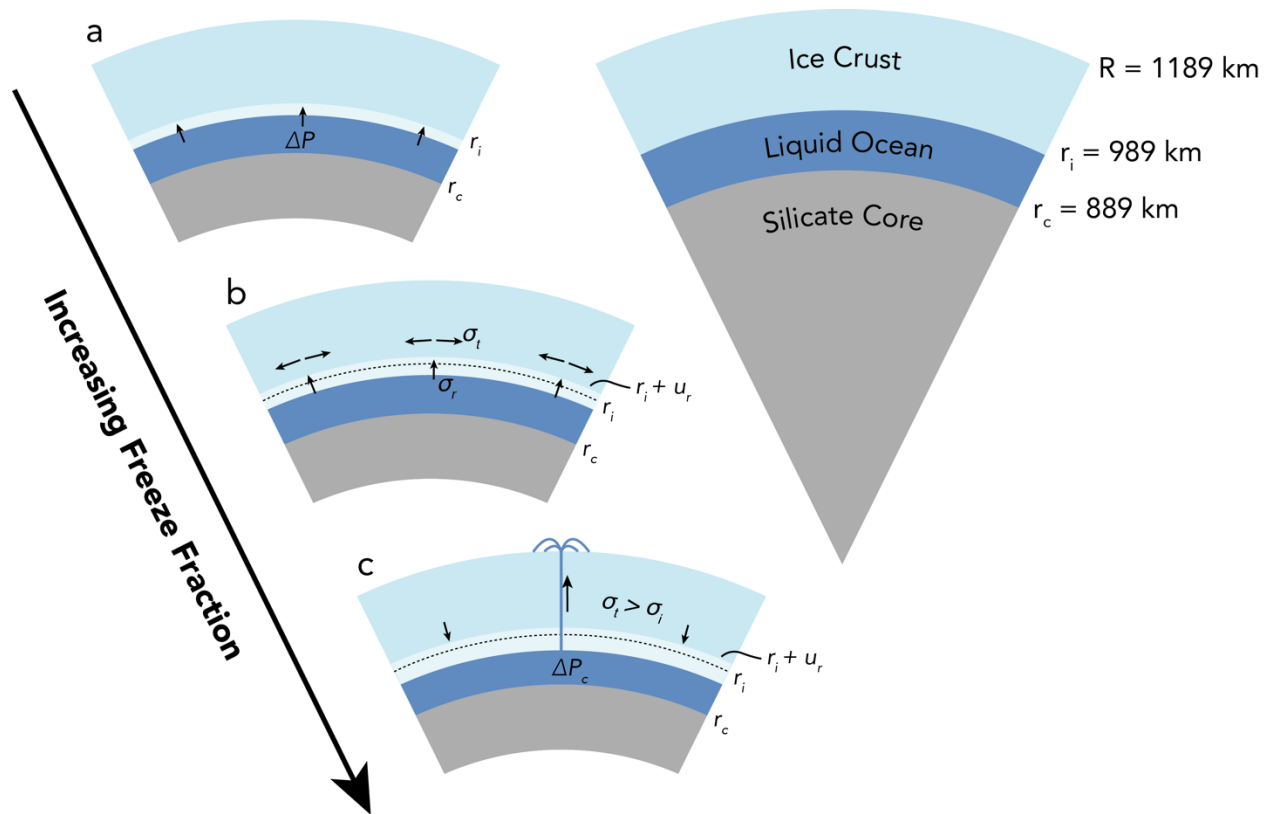


Figure A-3: Schematic diagram of the elastic crust model of overpressure and cryovolcanism as well as the assumed initial structure of Pluto. **a)** Freezing generates an overpressure in the subsurface ocean (newly formed ice is shown using an additional pale blue layer). **b)** The radial and tangential stresses cause the crust to expand outwards by a distance u_r above the initial base of the ice crust r_i (shown using a dashed line). The increase in volume in the subsurface ocean in turn reduces the overpressure. **c)** Once the tangential stress in the crust exceeds the tensile strength of ice, the crust will fracture and create a conduit for liquid to escape upwards, this releases the pressure and causes the crust to relax. Eruption will end when the pressure in the chamber is no longer large enough to overcome the negative buoyancy of the liquid.

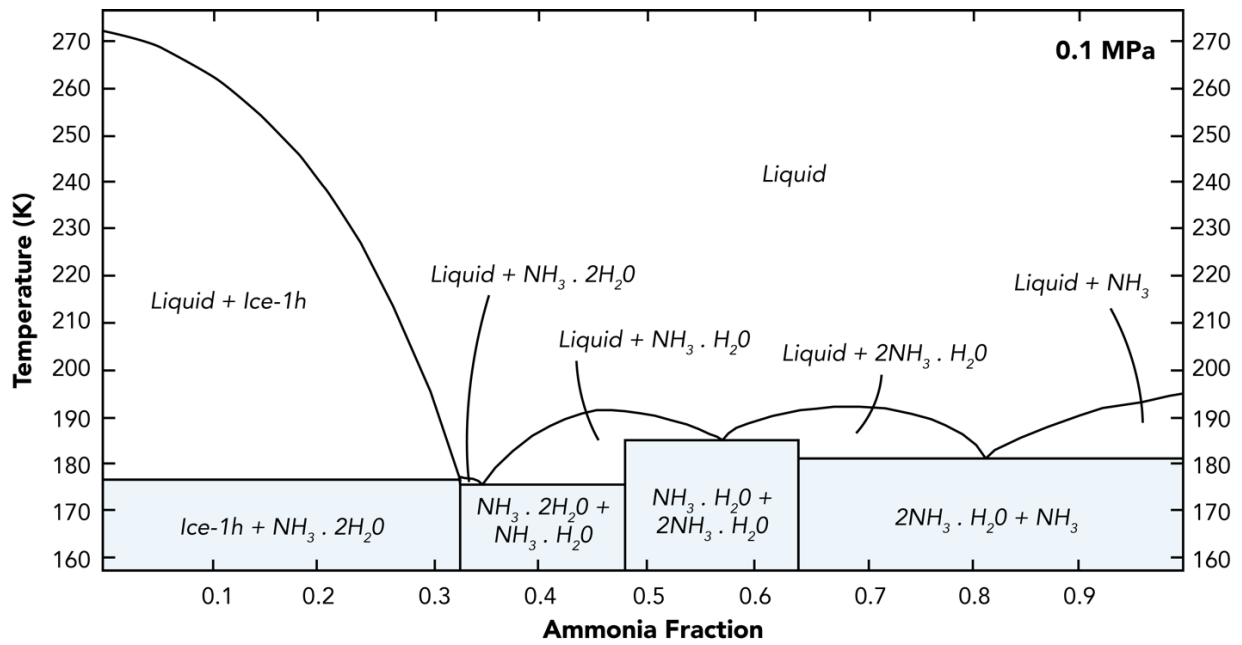


Figure A-4: Ammonia-water phase diagram at Earth atmospheric pressure modified from (Leliwa-Kopystyński et al., 2002; Kargel, 1992). For realistic ammonia concentrations on Pluto ($X < 0.3$) the relevant solid phases that can crystallize from the melt are water ice-1h and ammonia dihydrate ice ($\text{NH}_3 \cdot 2\text{H}_2\text{O}$).

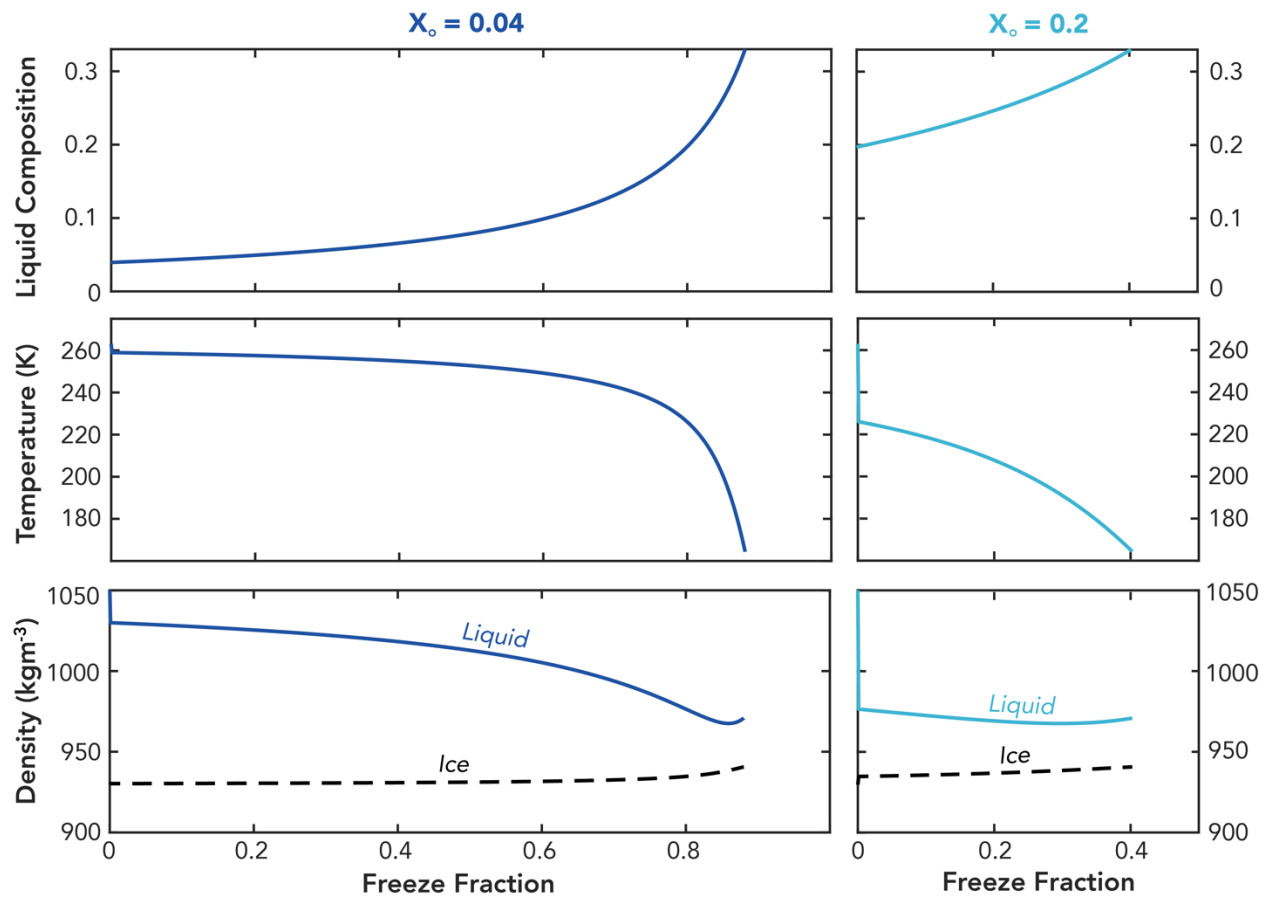


Figure A-5: Evolution during freezing of two end-member ammonia-water mixtures. Small density increases in the solid phase are caused by contraction due to cooling. The density evolution of the liquid is dominantly controlled by the ammonia concentration but thermal effects also play a role, increasing the density fractionally over the large decrease in temperature near the eutectic.

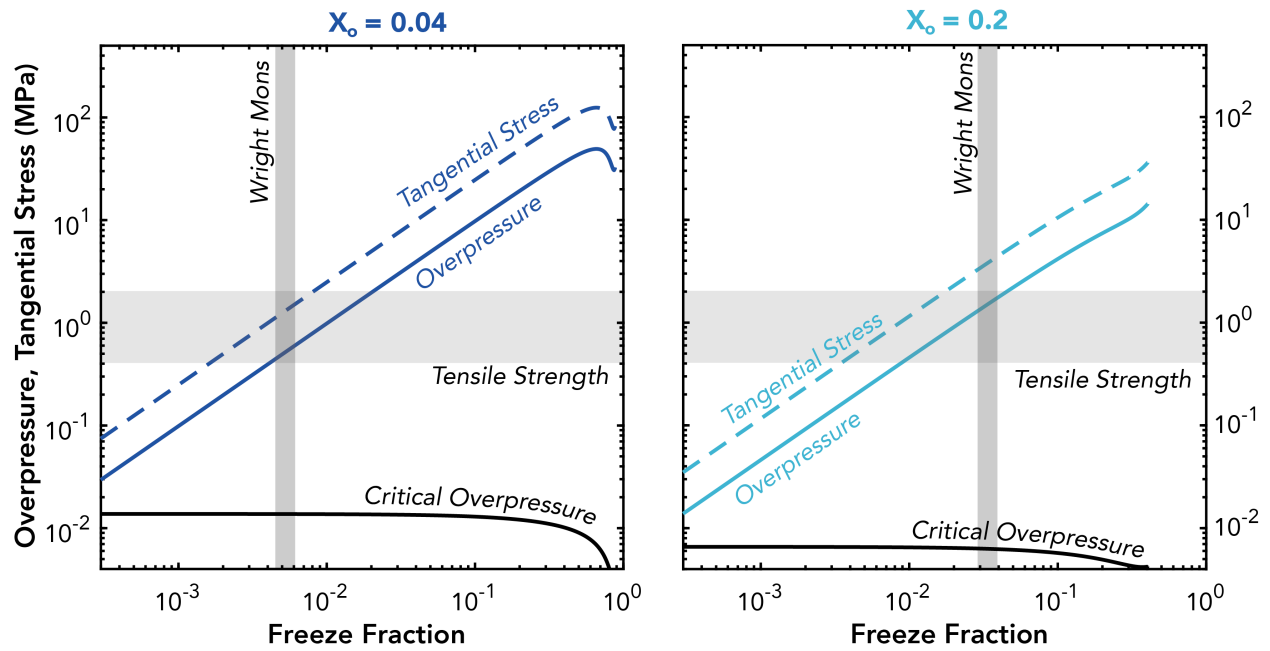


Figure A-6: Excess pressures generated during freezing subsurface ocean for each end-member ammonia concentration. Solid curves represent excess pressures (or radial stresses), dashed curves are the tangential stresses at the ocean-shell boundary ($r = r_i$).

References

- Bierson, C.J., Nimmo, F. and McKinnon, W.B., 2018. Implications of the observed Pluto–Charon density contrast. *Icarus*, 309, pp.207-219.
- Buldovicz, S.N., Khilimonyuk, V.Z., Bychkov, A.Y., Ospennikov, E.N., Vorobyev, S.A., Gunar, A.Y., Gorshkov, E.I., Chuvilin, E.M., Cherbunina, M.Y., Kotov, P.I. and Lubnina, N.V., 2018. Cryovolcanism on the Earth: Origin of a spectacular crater in the Yamal peninsula (Russia). *Scientific reports*, 8(1), p.13534.
- Croft, S.K., Lunine, J.I. and Kargel, J., 1988. Equation of state of ammonia-water liquid: Derivation and planetological applications. *Icarus*, 73(2), pp.279-293.
- Cruikshank, D.P., Umurhan, O.M., Beyer, R.A., Schmitt, B., Keane, J.T., Runyon, K.D., Atri, D., White, O.L., Matsuyama, I., Moore, J.M. and McKinnon, W.B., 2019. Recent cryovolcanism in Virgil Fossae on Pluto. *Icarus*.
- Desch, S.J., Cook, J.C., Doggett, T.C. and Porter, S.B., 2009. Thermal evolution of Kuiper belt objects, with implications for cryovolcanism. *Icarus*, 202(2), pp.694-714.
- Fagents, S.A., 2003. Returning to Europa: can traces of surficial life be detected. *J. Geophys. Res.*, 108, p.5139.
- Grundy, W.M., Binzel, R.P., Buratti, B.J., Cook, J.C., Cruikshank, D.P., Dalle Ore, C.M., Earle, A.M., Ennico, K., Howett, C.J.A., Lunsford, A.W. and Olkin, C.B., 2016. Surface compositions across Pluto and Charon. *Science*, 351(6279), p.aad9189.
- Hamilton, D.P., Stern, S.A., Moore, J.M., Young, L.A., Binzel, R.P., Buie, M.W., Buratti, B.J., Cheng, A.F., Ennico, K., Grundy, W.M. and Linscott, I.R., 2016. The rapid formation of Sputnik Planitia early in Pluto's history. *Nature*, 540(7631), p.97.
- Hammond, N.P., Barr, A.C. and Parmentier, E.M., 2016. Recent tectonic activity on Pluto driven by phase changes in the ice shell. *Geophysical Research Letters*, 43(13), pp.6775-6782.
- Howard, A.D., Moore, J.M., Umurhan, O.M., White, O.L., Anderson, R.S., McKinnon, W.B., Spencer, J.R., Schenk, P.M., Beyer, R.A., Stern, S.A. and Ennico, K., 2017. Present and past glaciation on Pluto. *Icarus*, 287, pp.287-300.
- Johnson, B.C., Bowling, T.J., Trowbridge, A.J. and Freed, A.M., 2016. Formation of the Sputnik Planum basin and the thickness of Pluto's subsurface ocean. *Geophysical Research Letters*, 43(19), pp.10-068.
- Kargel, J.S., 1992. Ammonia-water volcanism on icy satellites: Phase relations at 1 atmosphere. *Icarus*, 100(2), pp.556-574.
- Keane, J.T., Matsuyama, I., Kamata, S. and Steckloff, J.K., 2016. Reorientation and faulting of Pluto due to volatile loading within Sputnik Planitia. *Nature*, 540(7631), p.90.
- Leliwa-Kopystyński, J., Maruyama, M. and Nakajima, T., 2002. The water–ammonia phase diagram up to 300 MPa: Application to icy satellites. *Icarus*, 159(2), pp.518-528.
- Litwin, K.L., Zygielbaum, B.R., Polito, P.J., Sklar, L.S. and Collins, G.C., 2012. Influence of temperature, composition, and grain size on the tensile failure of water ice: Implications for erosion on Titan. *Journal of Geophysical Research: Planets*, 117(E8).
- Lopes, R.M., Mitchell, K.L., Stofan, E.R., Lunine, J.I., Lorenz, R., Paganelli, F., Kirk, R.L., Wood, C.A., Wall, S.D., Robshaw, L.E. and Fortes, A.D., 2007. Cryovolcanic features on Titan's surface as revealed by the Cassini Titan Radar Mapper. *Icarus*, 186(2), pp.395-412.
- Manga, M. and Wang, C.Y., 2007. Pressurized oceans and the eruption of liquid water on Europa and Enceladus. *Geophysical Research Letters*, 34(7).

- McKinnon, W.B., Nimmo, F., Wong, T., Schenk, P.M., White, O.L., Roberts, J.H., Moore, J.M., Spencer, J.R., Howard, A.D., Umurhan, O.M. and Stern, S.A., 2016. Convection in a volatile nitrogen-ice-rich layer drives Pluto's geological vigour. *Nature*, 534(7605), p.82.
- McKinnon, W.B., Prialnik, D., Stern, S.A. and Coradini, A., 2008. Structure and evolution of Kuiper belt objects and dwarf planets. *The Solar System Beyond Neptune*, 1, pp.213-241.
- Mitri, G., Showman, A.P., Lunine, J.I. and Lopes, R.M., 2008. Resurfacing of Titan by ammonia-water cryomagma. *Icarus*, 196(1), pp.216-224.
- Moore, J.M., McKinnon, W.B., Spencer, J.R., Howard, A.D., Schenk, P.M., Beyer, R.A., Nimmo, F., Singer, K.N., Umurhan, O.M., White, O.L. and Stern, S.A., 2016. The geology of Pluto and Charon through the eyes of New Horizons. *Science*, 351(6279), pp.1284-1293.
- Moore, J.E., Smith, C.L., Toigo, A.D. and Guzewich, S.D., 2017. Penitentes as the origin of the bladed terrain of Tartarus Dorsa on Pluto. *Nature*, 541(7636), p.188.
- Neveu, M., Desch, S.J., Shock, E.L. and Glein, C.R., 2015. Prerequisites for explosive cryovolcanism on dwarf planet-class Kuiper belt objects. *Icarus*, 246, pp.48-64.
- Nimmo, F., 2004. Stresses generated in cooling viscoelastic ice shells: Application to Europa. *Journal of Geophysical Research: Planets*, 109(E12).
- Nimmo, F., Hamilton, D.P., McKinnon, W.B., Schenk, P.M., Binzel, R.P., Bierson, C.J., Beyer, R.A., Moore, J.M., Stern, S.A., Weaver, H.A. and Olkin, C.B., 2016. Reorientation of Sputnik Planitia implies a subsurface ocean on Pluto. *Nature*, 540(7631), p.94.
- Porco, C.C., Helfenstein, P., Thomas, P.C., Ingersoll, A.P., Wisdom, J., West, R., Neukum, G., Denk, T., Wagner, R., Roatsch, T. and Kieffer, S., 2006. Cassini observes the active south pole of Enceladus. *science*, 311(5766), pp.1393-1401.
- Robuchon, G. and Nimmo, F., 2011. Thermal evolution of Pluto and implications for surface tectonics and a subsurface ocean. *Icarus*, 216(2), pp.426-439.
- Ruesch, O., Platz, T., Schenk, P., McFadden, L.A., Castillo-Rogez, J.C., Quick, L.C., Byrne, S., Preusker, F., O'Brien, D.P., Schmedemann, N. and Williams, D.A., 2016. Cryovolcanism on Ceres. *Science*, 353(6303), p.aaf4286.
- Schenk, P.M., Beyer, R.A., McKinnon, W.B., Moore, J.M., Spencer, J.R., White, O.L., Singer, K., Nimmo, F., Thomason, C., Lauer, T.R. and Robbins, S., 2018. Basins, fractures and volcanoes: Global cartography and topography of Pluto from New Horizons. *Icarus*, 314, pp.400-433.
- Schulson, E.M., 2001. Brittle failure of ice. *Engineering fracture mechanics*, 68(17-18), pp.1839-1887.
- Singer, K.N., White, O.L., Schenk, P.M., Moore, J.M., Spencer, J.R., McKinnon, W.B., Howard, A.D., Stern, A.S., Cook, J.C., Grundy, W.M. and Cruikshank, D.P., 2016, June. Pluto's putative cryovolcanic constructs. In *Annual Planetary Geologic Mappers Meeting (Vol. 1920)*.
- Smith, B.A., Soderblom, L.A., Banfield, D., Basilevsky, A.T., Beebe, R.F., Bollinger, K., Boyce, J.M., Brahic, A., Briggs, G.A., Brown, R.H. and Colvin, T., 1989. Voyager 2 at Neptune: Imaging science results. *Science*, 246(4936), pp.1422-1449.
- Soderblom, L.A., Kieffer, S.W., Becker, T.L., Brown, R.H., Cook, A.F., Hansen, C.J., Johnson, T.V., Kirk, R.L. and Shoemaker, E.M., 1990. Triton's geyser-like plumes: Discovery and basic characterization. *Science*, 250(4979), pp.410-415.
- Sokolnikoff, I.S., 1956. *Mathematical theory of elasticity*. McGraw-Hill book company.

- Sparks, W.B., Hand, K.P., McGrath, M.A., Bergeron, E., Cracraft, M. and Deustua, S.E., 2016. Probing for evidence of plumes on Europa with HST/STIS. *The Astrophysical Journal*, 829(2), p.121.
- Stern, S.A., Bagenal, F., Ennico, K., Gladstone, G.R., Grundy, W.M., McKinnon, W.B., Moore, J.M., Olkin, C.B., Spencer, J.R., Weaver, H.A. and Young, L.A., 2015. The Pluto system: Initial results from its exploration by New Horizons. *Science*, 350(6258), p.aad1815.
- Stern, S.A., Grundy, W.M., McKinnon, W.B., Weaver, H.A. and Young, L.A., 2018. The Pluto system after New Horizons. *Annual Review of Astronomy and Astrophysics*, 56, pp.357-392.
- Telfer, M.W., Parteli, E.J., Radebaugh, J., Beyer, R.A., Bertrand, T., Forget, F., Nimmo, F., Grundy, W.M., Moore, J.M., Stern, S.A. and Spencer, J., 2018. Dunes on Pluto. *Science*, 360(6392), pp.992-997.
- Trowbridge, A.J., Melosh, H.J., Steckloff, J.K. and Freed, A.M., 2016. Vigorous convection as the explanation for Pluto's polygonal terrain. *Nature*, 534(7605), p.79.
- Umurhan, O.M., Howard, A.D., Moore, J.M., Earle, A.M., White, O.L., Schenk, P.M., Binzel, R.P., Stern, S.A., Beyer, R.A., Nimmo, F. and McKinnon, W.B., 2017. Modeling glacial flow on and onto Pluto's Sputnik Planitia. *Icarus*, 287, pp.301-319.
- White, O.L., Moore, J.M., McKinnon, W.B., Spencer, J.R., Howard, A.D., Schenk, P.M., Beyer, R.A., Nimmo, F., Singer, K.N., Umurhan, O.M. and Stern, S.A., 2017. Geological mapping of Sputnik Planitia on Pluto. *Icarus*, 287, pp.261-286.

Geological Map of the Shyok Suture Zone Ladakh, NW India

Scale: 1:200,000 (Kilometers)



Measurements

- Inclined beds
- Vertical beds
- Overturned beds
- Inclined foliation
- Vertical foliation
- Overturned foliation
- Igneous foliation
- Mineral elong. lineation
- Slickenside lineation
- Fold axis lineation

- Settlement
- Glacier
- Modern alluvium
- Quaternary
- River
- Road

Karakoram Terrane

- Mylonite
 - Warshi Leucogranite
 - Nubra-Siachen Granite
 - Granodiorite
 - Calc-silicate
 - Marble
 - Psammite
 - Metavolcanic
 - Metaplutonic
- } Karakoram Batholith
- } Karakoram Metamorphic Complex

Shyok Suture Zone

- Murgic Conglomerate
 - Andesite
 - Conglomerate
 - Siltstone/mudstone
 - Tirit Granite
 - Gabbro
 - Diorite
 - Calcsilicate
 - Chert
 - Basalt (Shyok Volcanics)
 - Gabbro (Changmar Complex)
 - Serpentinite / Pyroxenite
- } Saltoro Fm.
- } Tirit / Hundar Intrusive Suite
- } Hundri Fm.

Kohistan-Ladakh Arc

- Khardung Volcanics (Upper)
 - Khardung Volcanics (Lower)
 - Undifferentiated Ladakh Volcanics
 - Marble/Psammite
 - Amphibolite
 - Granite
 - Tonalite
 - Undiff. Plutonic
 - Gabbro
 - Orthogneiss
- } Darnok Group
- } Ladakh Batholith
- } Turtuk Complex

Cross-section line

Structures

- Thrust/reverse fault
- Overturned thrust/reverse fault
- Normal fault
- Overturned Normal fault
- Strike-slip fault
- Fault traced with imagery
- F₁ Anticline fold axis
- F₁ Syncline fold axis
- F₂ Anticline fold axis
- F₂ Syncline fold axis
- Inferred fold axis

